

Understanding and Development of High Shear Technology for Liquid Metals Processing

A thesis submitted for the degree
of Doctor of Philosophy (PhD)

by

Agnieszka Dybalska

Brunel Centre for Advanced Solidification Technology
(BCAST)

Brunel University 2016

Abstract:

Oxide films in aluminium melts are unavoidable. A new technology developed by BCAST suggests breaking films into small fragments or particles which play a role as the grain refiner. Mechanical breakage is realised by using a high-shear mixer (HSM) with the rotor-stator impeller. In the presented thesis, the positive role of small oxide particles is shown by the computer modelling. The defragmentation potency of HSM is demonstrated by physical modelling with powders checked by optical analyses (microscopy) and SEM (Scanning Electron Microscopy). The flow has been analysed by optical recording and by PIV (Particle Image Velocimetry) to find the best conditions to cause a satisfying oxides distribution in all volume of liquid metal processed by the HSM. A new model to estimate the mixed volume has been proposed and checked by experiments with liquid metals. The model was checked by the PIV observations and by direct experiments in the liquid metal and is found to be in good agreement with reality. Optimisation methods are considered and a new design of HSM is proposed according to the experimental findings. This design improves the uniformity of mixing in the pseudo-cavern volume and exhibits the dispersion efficiency better than the design used currently by BCAST.

Understanding and development of high shear technology for liquid metals processing is an important part of BCAST research and is of great interest for industry. Up to now, this method was found to give good experimental results but it was a lack of information about physical basics behind this process. The goal of this thesis is to answer why and how to apply HSM in metallurgy and to propose new condition and design solutions associated with the specific requirements of the liquid metal process.

Contents:

Title.....	1
Abstract.....	2
Contents.....	3
List of Tables.....	6
List of Figures.....	8
Preface.....	18
Acknowledgement.....	19
Author's declaration.....	21
List of commonly used symbols.....	22
Introduction.....	23
Chapter 1. Literature Review.....	25
1.1. Process and design parameters of high-shear devices.....	25
1.1.1 Design of high-shear mixers.....	25
1.1.2. Reynolds and Newton numbers in stirred vessels.	33
1.1.3. Shear forces due to rotor-stator mixing.....	36
1.2. Behaviour of liquid stirred by rotor-stator devices.....	38
1.2.1. Flow description.....	38
1.2.2. Pseudo-cavern effect.....	48
1.3. Oxides present in the mixed fluid and their role.....	53
1.3.1. Agglomerates of oxides present in melts.....	53
1.3.2. Epitaxial nucleation model.....	56
1.4. Applications of high-shear impellers.....	61
1.5. Alloys structure improvement by shearing processing.....	63
Chapter 2. Methods.....	71
2.1. Physical modelling.....	71
2.1.1 HSMs setup equipment	71

2.1.2 Flow recording (PIV)	79
2.1.3 Silicon dioxide model.....	83
2.1.4 Argon-gas model	87
2.2. Processing of liquid metal	89
2.3. Optical microscopy analyses	92
2.4. Scanning Electron Microscopy.....	94
2.5. Image analyses.....	96
Chapter 3. Computer Simulation Of The Liquid Ordering On The Interface –	
Role Of Oxides In Liquid Metals.....	97
3.1. The purpose of computer simulation of atomic ordering	97
3.2. The computer simulation methodology.....	99
3.3. Physical quantities used in the simulation.....	101
3.4. Results.....	103
Chapter 4. Fragmentation Potency Of High Shear Devices For Metallic Oxides –	
Powder Analyses.....	110
4.1. Observation of defragmentation powders after HSM-RS processing.....	110
4.2. The defragmentation efficiency for different head designs.....	117
4.2.1. The stator with round holes (RH).....	117
4.2.2. The stator with square holes (SqH).....	119
4.2.3. New design of head – crossH.....	126
4.2.4. Gap increasing.....	128
4.3. Time influence on alumina shearing process.....	130
4.4. Validation of defragmentation pictures analyses.....	132
Chapter 5. Distributive Characterisation Of Mixing.....	137
5.1. Pseudo cavern size modelling.....	137
5.1.1. Pseudo-cavern radius.....	137
5.1.2. Measured pseudo-cavern height (argon gas model).....	141
5.1.3. Calculated pseudo-cavern height (the SiO ₂ model).....	145

5.1.4. Pseudo-cavern volume calculations.....	148
5.1.5. Model validation by PIV experiments.....	150
5.2. Universal model - scale up rules.	155
Chapter 6. Optimisation Of Design And Process Conditions.....	157
6.1. Impeller position.....	157
6.2. Mixing head design.....	164
6.2.1. Gap size modifications.....	164
6.2.2. Stator design.....	172
6.2.2.1 Flow instabilities with different stator designs.....	173
6.2.2.2. Pseudo-cavern sizes with different stator holes designs.....	175
6.2.3. Stator holes arrangement.....	185
6.3. Shearing time influence.....	195
Chapter 7. Proof Of Concept With Liquid Metal.....	199
7.1. Not fully agitated conditions – a verification.....	201
7.2. Not fully agitated conditions – a verification in different vessel.....	203
Chapter 8. Conclusions.....	205
Chapter 9. Future work.....	206
References.....	207

List of Tables:

- Table 1.1. Different stator designs and proposed applications.
- Table 1.2. Microstructures of different alloys cast without and after shearing.
- Table 1.3. Grain size reduction after MCAST-RS alloy treatment.
- Table 2.1. Dimensions of HSM setup.
- Table 2.2. Density differences for liquids and particles [Brandes, 1983; Hildebrand et al., 1976, Jakse et al., 2013].
- Table 2.3. The composition of the prepared alloy given in wt %
- Table 2.4. The crucibles size chart.
- Table 3.1. A static order parameter at 1100K .
- Table 4.1. The FDPA of the alumina after the HSM processing with the RH.
- Table 4.2. The FDPA of the alumina after shearing by the square-holes head.
- Table 4.3. The FDPA of the alumina after the HSM processing with the crossH.
- Table 4.4. The FDPA of alumina particles after shearing with an increased gap.
- Table 4.5. The FDPA of the alumina processed for 10 minutes.
- Table 5.1. SiO₂ pseudo-cavern radii for a different N (crossH).
- Table 5.2. Argon gas pseudo-cavern sizes for the different N.
- Table 5.3. Radii of the pseudo-cavern measured for both models, the sizes comparison.
- Table 5.4. The ratio of both pseudo-cavern half-axis.
- Table 5.5. SiO₂ pseudo-cavern sizes measured (size a) and calculated (size b) for the different N.
- Table 5.6. The measured pseudo-cavern size from PIV results (given as a) and in the SiO₂ model (given as R).
- Table 6.1. The vortex presence in a cylindrical vessel with T=84 mm , h=120 mm for different clearances C, 1 – presence of vortex / turbulence, 0 – vortex not observed.

Table 6.2. Pseudo-cavern radii for different N (SiO₂ system, crossH) and established from PIV photos.

Table 6.3. Recorded average (V_{ave}) and maximum (V_{max}) velocities for different gap sizes with the crossH stator.

Table 6.4. Values of the pseudo-cavern size a measured with a different gap (crossH).

Table 6.5. The observed maximal speed possible to use without the air vortex formation for different heads.

Table 6.6. Values of the pseudo-cavern size a measured with different stator holes.

Table 6.7. Mean velocities for different heads (RH and SqH) and comparison between them in percent's.

Table 6.8. The amount of energy dissipated in various regions in the vessel calculated by the computer simulation [Utomo, 2009].

Table 6.9. Averaged velocities around the RH and the crossH and comparison between them in percent's.

Table 6.10. The nonuniformity coefficient ΔR measured experimentally (SiO₂ model system) with different stator designs in a wide range of the N.

Table 6.11. A grain sizes of Al-3%Mg alloy dependence on a time of shearing at N = 3000 rpm after shearing without full agitation (N = 500 rpm).

Table 6.12. A grain sizes of Al-3%Mg alloy dependence on time of shearing.

Table 7.1 Measured grain sizes after the 3 min s shearing with and without a full volume agitation (crucible A20).

Table 7.2. Measured grain sizes after the 4 min shearing without and with a full volume agitation (crucible A16, Al-3%Mg alloy).

List of Figures:

Figure 1.1.

The HSM design. The shaft is connected to the rotor and the stator will be placed around the rotor after mounting.

Figure 1.2.

Silverson: in-line unit (left) and batch mixer (right) [www.silverson.co.uk].

Figure 1.3.

Ross in-line mixers [www.mixers.com] used to disperse injected powder (point 2) into the flow of fluid (point 1) by one pass of them by HSM. Well mixed materials are expelled centrifugally through the stator openings (point 3).

Figure 1.4.

Different designs of the in-line rotor-stator. a,b) multistage rotor-stator and its components [www.bematek.com], c) toothed device [www.quadroliquids.com], d) colloid mill [www.ikausa.com].

Figure 1.5.

Axial flow impellers. a) Axial rotor-stator design [www.greaves.co.uk], b) axial rotor shape with twisted blades, c) axial flow is shown schematically in the vessel, d) flow visualisation in cross-section of the vessel [Rielly et al., 2007].

Figure 1.6.

Radial flow impellers. a) radial rotor-stator design (Silverson), b) radial rotor shape, c) radial flow is shown schematically in the vessel, d) flow visualisation in cross-section of the vessel [Singh et al., 2007].

Figure 1.7.

Computer simulation of 3D flow lines around rotor-stator with a rotational speed $N = 3000$ rpm [Barailler et al., 2006].

Figure 1.8.

Axial-radial velocity vectors in cross-section at 2000 rpm (a) computationally calculated, (b) LDA measurements. Dimensions are in m. Points A and B represent the centres of circulation loops. The sucking force direction is drawn by green colour and the jets position is shown by red colour [Utomo, 2009].

Figure 1.9.

Vortexing. The central vortex along the impeller shaft changes the surface shape and sucks air into the bulk liquid [Busciglio et al., 2011].

Figure 1.10.

Tangential velocities contours in fully agitated and baffled vessel. Baffles changing the flow direction and prevent too strong vortexing. [Vlček et al., 2016].

Figure 1.11.

Flow pattern in a stirred vessel with an eccentrically positioned radial impeller, vertical cross-section plane (top row), horizontal cross-section plane on the liquid free surface (bottom row), [Karcz and Szoplik, 2004].

Figure 1.12.

The different flow instabilities present in the flow. The vessel is unbaffled and the impeller is placed off-centre [Galletti and Brunazzi, 2011].

Figure 1.13.

Liquid flows within the vessel as viewed on the vertical plane. (a) $C=T/3$, two-loops flow pattern, (b) $C=T/8$, one-loop flow pattern.

Figure 1.14.

Observed the pseudo-cavern effect around a rotor-stator head [Doucet et al., 2003].

Figure 1.15.

Evolution of cavern shapes with the Newtonian fluids [Doucet et al., 2003].

Figure. 1.16.

Evolution of the numerical pseudo-cavern with the Re [Barailler et al., 2006].

Figure 1.17.

The vortex with a torus shape is created by the fluid lines [Reza, 2015].

Figure 1.18.

The cavern observed around the open impeller. The visible ellipsoid shape is caused by both sides of the torus overlapping, the torus is compressed into ellipsoid shape [Sossa, 2007].

Figure.1.19.

Formation of a folded oxide bifilm by surface (schematic view),[Campbell, 2003].

Figure 1.20.

Schematic illustration of the epitaxial nucleation model (a) before the growth (b) layer-by-layer growth (c) introduction of the misfit dislocation [after Fan, 2012].

Figure 1.21.

a) HRTEM images of a liquid Al drop formed on α -Al₂O₃. b) HRTEM image of the Al/ α -Al₂O₃ interface. We can see also an overlay of intensity line scan perpendicular to the interface (red line). The inset is the result of a simulation, an image of α -Al₂O₃/vacuum interface [Lee and Kim, 2011].

Figure 1.22.

Micrograph of the semi-coherent interface between MgO and the α -Mg matrix in AZ91D alloy [Li et al., 2011].

Figure 1.23.

Macrographs of the longitudinal sections of the TP-1 samples of CP Al showing effects of melt shearing (a) non-sheared sample (b) sheared sample [Li et al., 2012b].

Figure 1.24.

Microstructures of sand cast LM25 components (a) without shearing, (b) with intensive melt shearing [Li et al., 2011].

Figure 1.25.

The average grain size of CP Al as a function of processing temperature [Li et al., 2011], (a) without intensive melt shearing, (b) with intensive melt shearing.

Figure 2.1.

HSM setup.

Figure 2.2.

a) Standard Silverson head, b) simplified tubular head (Silverson rotor) before mounting, c) mounted tubular head (crossH stator).

Figure 2.3.

The RH stator.

Figure 2.4.

The SqH stator.

Figure 2.5.

The crossH stator.

Figure 2.6.

PIV setup consists of a laser and a camera. Produced laser sheet illuminates tracing particles in the observed flow. The camera captures a sequence of images (www.berkeley-nucleonics.com).

Figure 2.7.

Two recorded pictures are cross-correlated to find the displacement values in each interrogation area. The displacement field is produced. (www.berkeley-nucleonics.com).

Figure 2.8.

Instantaneous wake visualization of vortices produced by the symmetrical tail of a freely swimming fish. The velocities vector are shown against vortices visualised by colours [Brook et al., 2011].

Figure 2.9.

The laser sheet in a tank, picture taken in a dark room.

Figure 2.10.

Laser light sheet placed before the HSM head, scattered light made visible tracing particles, picture taken in daylight to show the head position.

Figure 2.11.

Trace of a cavern diameter on the bottom of the tank obtained with SiO₂; a) schematic representation of flow and pseudo-cavern diameter measurements; (1) the trace of pseudo-cavern on the bottom, (2) the lines represents the flow in cross section, (3) the shaft, (4) the stator, (5) the tank, (6) the observation angle used to take pictures of the pseudo-cavern shape. b) a photograph taken during experiments, view on the pseudo-cavern trace shown in Figure 2.10 a.

Figure 2.12.

Pseudo-cavern shape observed with the argon-gas model. The line visualises estimated pseudo-cavern borders. (1) The gas purging, (2) observed the pseudo-cavern shape is an effect of the gas dispersion and distribution by the mixing head (3). Bubbles travel to the water surface (4).

Figure 2.13.

Al-Mg phase diagram [Brandes, 1983].

Figure 2.14.

The ceramic rotor-stator impeller.

Figure 2.15.

Cold mounted powders a) without a reference probe, b) with a reference probe.

Figure 2.16.

A basic SEM design.

Figure 2.17.

MgO particles after shearing in the water. SEM picture with magnification 60 000×

Figure 2.18.

The calibration photograph made before experiments with the argon gas.

Figure 3.1.

An illustration of the simulation cell. The fixed substrate atoms are visualised by purple balls and adjacent Al atoms are represented by green balls. The orientation of cell (z-axis) is comparable with the orientation of z-axis presented on the atomic density graphs given further.

Figure 3.2.

The density profile $r(z)$ of the substrate and the liquid as a function of z at $T=1100$ K. The positions of 5 layers observed in liquid aluminium are marked on the graph.

Figure 3.3.

The peak number density, ρ_{peak} , of the liquid as a function of the distance (z) from the interface at $T_e = 1000$ to 1400 K for two z ranges (shown above and below).

Figure 3.4

The peak number density, ρ_{peak} , of the liquid as a function of a distance (z) from the interface for the systems with misfits from 0% - -8%, at 1000 K [Men and Fan, 2012].

Figure 3.5.

The order parameter $S(z)$ of the liquid as a function of z ; $T_e=1000-1400$ K

Figure 3.6.

The static structural parameter of the Al atoms as a function of z in the systems with misfits from 0 to -8% at 1000 K [Men and Fan, 2012].

Figure. 4.1.

A sequence of pictures from the recorded video showing the clusters dispersion.

Figure 4.2.

Oxide powder before (a) and (b) after shearing by the HSM with the original tubular head and the Silverson square holes stator.

Figure 4.3.

The histogram of the FDPA for alumina – a maximum size reduction against to the FDPA before 15-min shearing.

Figure 4.4.

The histogram of the FDPA for the alumina – a maximum size reduction (enlarged portion of Fig. 4.3.).

Figure 4.5.

The histogram of the FDPA for the alumina after processing by the RH stator for 4 min.

Figure 4.6.

The histogram of the FDPA for sheared alumina particles with the SqH head for 4 min.

Figure 4.7.

SEM micrographs showing the morphology of the MgO particles collected at 650°C by the pressurised filtration of (a) non-sheared and (b) sheared AZ91 alloy melt. Films and agglomerates are broken into fine particles [Men and Fan, 2010].

Figure 4.8.

The measured size distribution of the MgO particles in the sheared AZ91 alloy melt collected by pressurised filtration from image analysis of SEM micrographs [Men and Fan, 2010].

Figure 4.9.

The histogram of the FDPA of the alumina after processing by the HSM with the crossH (4 min) against results obtained with the RH (4 min) and the FDPA of a non-sheared powder.

Figure 4.10.

The histogram of the FDPA of the alumina after processing (4 min) with the increased gap (gap+; gap size 0.8 mm). The used stator was the crossH. The inlet shows results for the crossH with a typical gap size (4 min).

Figure 4.11.

The histogram of the FDPA of the alumina after 10 minutes of shearing by the HSM. The used stator was the crossH. The inlet shows results obtained after 4 min.

Figure 4.12.

SEM picture of sheared alumina powder. We can observe some non-sheared particles of alumina and broken parts of spheres. As there are well defined so in cross-section of samples we observed sizes of single particles.

Figure 4.13.

SEM picture of a non-sheared MgO powder. We can observe different sizes of particles.

Figure 4.14.

SEM picture of a sheared MgO powder. The size decrease is well visible.

Figure 4.15.

The histogram of the FDPA of MgO particles before and after shearing (results obtained with crossH, 4 min shearing).

Figure 5.1.

The measured pseudo-cavern radius as a function of the rotational speed.

Figure 5.3.

(a) Argon gas bubbles without mixing forces present in the system move upwards due to the buoyancy force with velocity equal v_a (b) The resultant velocity of the bubble in the presence of mixing forces is the effect of movement with a flow velocity v_f , scaled by the vector v_a .

Figure 5.4.

The cross-section of the ellipsoid (the pseudo-cavern shape around the blue head). Light blue circles show circulation loops (a compressed torus). Measured sizes R and H are compared with conventional half-axis symbols a and b.

Figure 5.5.

The pseudo-cavern volume for the crossH as a function of the rotational speed N [rpm].

Figure 5.6.

The a size measurement rules from PIV photos. (1) the ellipse starts where the jets are emerging from the top stator holes, (2) the point where the jet is reflected by the bottom of the tank belongs to the ellipse border, (3) one of the ellipse axes is known to be equal to the head main axis, (4) the full ellipse shape is drawn to fulfil the rules 1-3 and to mimic in the best way the natural shape of the jet recorded by PIV system, (5) the tank walls are far enough to avoid the jet scattering from the walls, (6) the size a is measured from drawn elliptical shapes

Figure 5.7.

The pseudo-cavern development with the N increases. Velocities are given in m/s. Pseudo-cavern shapes are approximated by ellipses and sizes a were found.

Figure 5.8.

The pseudo-cavern development with N in the same scale.

Figure 5.9.

The pseudo-cavern size a as the function $a(N)$ estimated from PIV results.

Figure 6.1.

A flow pattern around the crossH (shown by the red rectangular). The clearance $C = 30$ mm, $N = 5\ 000$ rpm. The circulation loop and the jet are shown by white lines, the sucking force direction is shown by the purple arrow.

Figure 6.2.

A flow pattern close to the crossH (shown by the red rectangular). The clearance $C = 50$ mm, $N = 5\ 000$ rpm. The circulation loop and the jet are shown by white lines, the sucking force direction is shown by the purple line.

Figure 6.3.

A flow around the crossH with the 0.4 mm gap, $N = 8\ 000$ rpm. The head position is shown by the red rectangular and flow loops are shown by white round shapes. The purple line is drawn across the loop to show the analysed direction.

Figure 6.4.

The velocities profile along the loop axis for the 0.4 mm gap (crossH).

Figure 6.5.

Flow around the crossH with the 0.6 mm gap, $N=8\ 000$ rpm. The head position is shown by the red rectangular and flow loops are shown by white round shapes. The purple line is drawn across the loop to show the analysed direction.

Figure 6.6.

The velocities profile along the loop axis for the 0.6 mm gap (crossH).

Figure 6.7.

A flow around the crossH with the 0.8 mm gap, $N=8\ 000$ rpm. The head position is shown by the red rectangular and flow loops are shown by white round shapes. The purple line is drawn across the loop to show the analysed direction.

Figure 6.8.

The velocities profile along the loop axis for the 0.8 mm gap (crossH).

Figure. 6.9.

The pseudo-cavern observed with the argon gas ($N = 6000$ rpm, crossH) for the (a) 0.4 mm, (b) 0.8 mm gap size.

Figure 6.10.

The pseudo-cavern diameter dependence on the N for stators with round and square holes with linear estimation.

Figure 6.11.

Plate I of Rayleigh's 'some applications of photography' showing the destabilization of a jet of air into water (a) and of a water jet in air (b,c,d); [Rayleigh, 1891].

Figure 6.12

Abbot Nollet demonstrating how a charged water jet disintegrates [from Abbé Nollet, 1749].

Figure 6.13.

Isosurfaces of the velocity gradient tensor for circular and square jets at a Reynolds number of 1000 and 2000. The turbulence in the end of the jet occurs earlier in the case of the square jet.

Figure 6.14.

A flow around the head with square holes, $N = 7\ 000$ rpm. The head position is shown by the red rectangular.

Figure 6.15.

A flow around the head with round holes, $N = 7\ 000$ rpm. The head position is shown by the red rectangular.

Figure 6.16.

The flow close to the slotted head (the stator is light grey, the rotor is dark grey), visible reversed velocities behind the jet. The jet is strong and well concentrated [Mortensen et al., 2011]. Top view of the head horizontal cross-section is shown. The point of view used in this thesis is shown by an arrow.

Figure 6.17.

Positions of jets around a stator with round holes arranged in rows (RH) and around a crossH design. Additional red positions of jets are the effect of the holes rearrangement on the stator what improves uniformity.

Figure 6.18.

Jets around a new stator (crossH) are arranged uniformly in the space what improves the uniformity of a fluid agitation.

Figure 6.19.

A flow around the head with round holes arranged in cross lines (crossH), $N = 7\ 000$ rpm. The head position is shown by the red rectangular.

Figure 6.20.

The laser light overexposes one plane and reflects existence 4 jets in one plane. Visible red jets and a green observation plane.

Figure 6.21.

The laser light overexposes one plane and reflects existence 2 jets in one plane. Visible red jets and a green observation plane. Two yellow jets are relocated into another plane.

Figure 6.22.

Flow patterns around (a) disintegrating head, (b) slotted head. [Utomo, 2009]

Figure 6.23.

The „star” shape observed as the nonuniformity of mixing effect. The difference between measured radii is taken as the nonuniformity coefficient $\Delta R = R_1 - R_2$.

Figure 6.24.

The nonuniformity of mixing observed for RH and crossH stator.

Figure 6.25.

Predicted volumes of the pseudo-cavern observed with different stators for a wide range of the N .

Figure 6.25.

The grain size of Al-3%Mg alloy decrease with a time (pictures are given for two magnifications); (a) after 2 minutes of shearing (b) after 4 minutes of shearing.

Figure 7.1.

The volume as a function of N predicted the physical model for the 32 mm ceramic rotor.

Figure 7.2.

Grain sizes of Al-3%Mg alloy observed after 3 min shearing (crucible A20) (a) without a full agitation ($N = 700$ rpm) and (b) with a full agitation ($N = 3000$ rpm)

Figure 7.3.

Grain sizes of Al-3%Mg alloy observed after 4 min shearing (a) without a full agitation ($N = 500$ rpm) and (b) with a full agitation ($N = 2500$ rpm, crucible A16)

**He has made everything beautiful (*) in its time. He has even put eternity
in their heart; yet mankind will never find out the work that the true God
has made from start to finish.**

(Ecclesiastes 3: 11, NW Bible)

(*) Or “well-arranged; proper; appropriate.”

Acknowledgement:

I would like to thank my supervisor, Prof. Dmitry Eskin, for the patient guidance, encouragement and advice he has provided throughout my time as his student. I have been extremely lucky to have a supervisor who cared so much about my work and who teach me how to analyse and describe my results. Without him, this work will never be finished. He helps me to leave the difficulties behind. He always had a supportive attitude, even if I wish to give up, and always let me take responsibility for my thesis.

I would also like to thank all the members of staff and PhD students at BCAST on Brunel University who helped me during years of studies. In particular, I would like to thank Dr Kawther Al-Helal, Dr Nilam Barekar, Dr Hu-Tian Li, Dr Yun Wang, Dr Ian Stone, Dr Markus Köhler, Dr Iakovos Tzanakis for all forms of support. Thank you for a first advice how to start and what to read and for all support in the laboratory. Especially I would like to thank Mr Edward Djan for his advice how to grind and polish the metal samples.

The thesis will be never done without the help of Dr Hua Men and Prof. Zhongyun Fan which give me the first direction in my research. Dr Hua Men share with my own knowledge about computer simulations. Prof. Zhongyun Fan decided about the form of my thesis when I found an explanation of the pseudo-cavern effect and he told me to keep that direction.

The help of my unofficial laboratory supervisor, Dr Jayesh Patel is even difficult to describe. He teaches me everything that I know now about experimental procedures with melts, even if my lack of knowledge in material chemistry sometimes make him laugh. Unfortunately, the Optical Engineering studies do not prepare me to be good metallurgist but I believe that everything is possible, sometimes only needs more time. Thank you, Jayesh, for your time and help with melt shearing experiments.

Other important advice I received from Prof. Peter Quested and Prof. Jack Silver. The good questions and simple tips really help me during difficulties which I encountered in the research process. Sometimes few words opened my mind to new possibilities.

It is really important for me to say thank you to all people which were involved in an extension of this thesis. Those people help me when my way on Brunel was dark and really difficult. Their decisions or advice changed my situation and I get enough time to finish my thesis. Without you, this research never will be submitted.

Let me show appreciation for: Ingrid Samuels from ADE, Prof. Dmitry Eskin, Dr Giulio Alfano , Dr.Philip Collins, Prof. Geoff Scamans, Prof. Robert Macredie.

Completing this work would have been all the more difficult were it not for the support provided by my friends and family. The best greetings I owe my parents, which left everything to give me emotional support.

Finally, I would like to thank the Institute of Materials and Manufacturing, not only for providing the funding which allowed me to undertake this research, but also for giving me the opportunity to attend conferences and the university courses.

Author's declaration

I hereby declare that I am the sole author of this thesis. This is a true copy of the thesis, including any required final revisions, as accepted by my examiners.

I understand that my thesis may be made electronically available to the public; therefore I authorise Brunel University to make available electronically to individual or institutions for the purpose of scholarly research.

List of commonly used symbols

[and SI dimensions]:

μ – the dynamic viscosity of the fluid [Pa·s]

ρ – the density of the fluid [kg/m³]

d – the impeller diameter [m]

N – the rotational speed of impeller [s⁻¹]

P – the shaft power for the impeller [W].

Re – the Reynolds number

Ne – the Newton number, often called the power number

τ – the shear stress [N/m²],

$\dot{\gamma}$ – the shear rate [s⁻¹]

q – the gap width [m]

C – the clearance between the tank bottom and the impeller [m]

T – the tank (vessel) diameter [m]

h – the tank (vessel height) [m]

R – the pseudo-cavern radius (measured) [m]

H – the pseudo-cavern height (measured) [m]

a, b – the ellipsoidal pseudo-cavern half-axis [m]

v – velocity [m/s]

V – volume [m³]

Introduction.

The removal of harmful oxide films from aluminium melts has been a key research field for many years as their formation is unavoidable. Instead of removing them from liquid metals a new technology developed by BCAST suggests breaking films into small fragments or particles. Usually, entrained oxides and films are distributed non-uniformly in the melt. They are frequently large and have poor wettability. Thus, the naturally present oxides are not effective as the grain refiner. It is possible to change this situation by mechanical breakage of clusters or films and dispersion of them in the liquid metal.

BCAST proposed to realise those goals by using a high-shear mixer (HSM). During intensive melt shearing, the defragmentation, as well as dispersion of individual oxide particles happens. Finally, after processing by HSM they can play a role of nuclei when the nucleation process occurs.

In the presented thesis, the positive role of small oxide particles is shown by the computer modelling. The defragmentation potency of HSM is demonstrated by physical modelling with powder. To observe the flow of liquid around the HSM a model situation with a transparent fluid has been used in presented research. The flow has been analysed to find the best conditions to cause a satisfying oxides distribution in all volume of liquid metal processed by the HSM. A new model to estimate the mixed volume has been proposed and checked by experiments with liquid metals. The model was checked by the PIV observations and by direct experiments in the liquid metal and is found to be in good agreement with reality. Optimisation methods are considered and a new design of HSM is proposed according to the experimental findings. This design improves the uniformity of mixing in the pseudo-cavern volume and exhibits the dispersion efficiency better than the design used currently by BCAST.

Understanding and development of high shear technology for liquid metals processing is an important part of BCAST research and is of great interest for industry. Up to now, this method was found to give good experimental results but it was a lack of information about physical basics behind this process. The goal of this thesis is to answer why and how to apply HSM in metallurgy and to propose

new condition and design solutions associated with the specific requirements of liquid metal process.

In Chapter 1 the literature review is given. The first, the high-shear devices are described. The process and design parameters, the applications, as well as the behaviour of fluid stirred by those devices, are presented. The second, the role of oxides present in melts and their influence on the alloys structure after high-shear processing is outlined.

Chapter 2 is giving a brief overview on used in the presented research materials and methods.

As the alloy improvement by high-shear processing is believed to be the effect of the liquid ordering on the interface in Chapter 3 the role of oxides in liquid metals is discussed. The liquid ordering is proven by the computer simulation. Presented results indicate that the uniformly dispersed oxides can play a positive role during nucleation.

Next chapters are focused on the uniform dispersion of oxides. In Chapter 4 the fragmentation potency of high-shear devices for metallic oxides is proven by the powder analyses. Presented results show that the clusters are easily broken by used impellers. The next question is how effective is the oxides distribution inside mixed volume. Chapter 5 describes a new physical model which estimates the maximum volume of mixed liquid metal which can be processed with given rotational speed.

In Chapter 6 those findings are completed by the analyses of different design and process conditions. Proposed a new design of stator is checked and compared with other designs.

Chapter 7 presents the results of melt shearing in conditions established by this thesis findings. The presented model is verified in two different conditions and proven to be in good agreement with reality.

Chapter 8 outlines the final conclusions from the research described in this thesis.

Chapter 1. Literature review.

1.1. Process and design parameters of high-shear devices.

1.1.1. Design of high-shear mixers.

The idea of rotor-stator mixers is quite simple and really functional. Traditionally agitation of a vessel and mixing is done by using different types of open impellers as the Rushton turbine or the marine propeller [Kresta et al., 2004]. Rotor-stator devices have a rotor which works similar as open impeller but this rotor is surrounded closely by the stator with holes. This design allows one to use the high speed, i.e. rotors rotate at an order of magnitude higher speed than open impellers in a stirred tank. The typical tip of the blade (rotor) speed ranges from 10 to 50 m/s (Kresta et al., 2004). Open impellers operating in a unbaffled vessel cause a strong vortex which results in turbulence on the surface of the liquid. In the case of rotor-stator devices, the most turbulent flow exists in the swept volume of a mixing head in the gap between the rotor and the stator and inside the stator holes. The gap varies from 100 to 3000 μm (Karbstein and Schubert, 1995) and, as the locally mixed volume inside the head or in the gap is really small, the local energy dissipation rate can be three orders of magnitude higher than in a conventional stirred vessel (Kresta et al., 2004). This is why the mixers are usually called High-Shear Mixers (HSM) as the high shear rate in the gap can have values from 20,000 to 100,000 s^{-1} (Kresta et al., 2004).

The basic geometry of rotor-stator devices is shown in Figure 1. A “mixing head” is a commonly used term to describe the rotor-stator impeller. The motor with a suitable power rotates the shaft and the rotor surrounded by the stator, which agitates a flow to circulation in the vessel. The flow in each circulation time passes the gap and stator openings. The rotating agitator (rotor) acts as a centrifugal pump which sucks the fluid in. When the fluid passes the HSM head, high-shear forces inside cause deagglomeration processes or the droplets breakage.

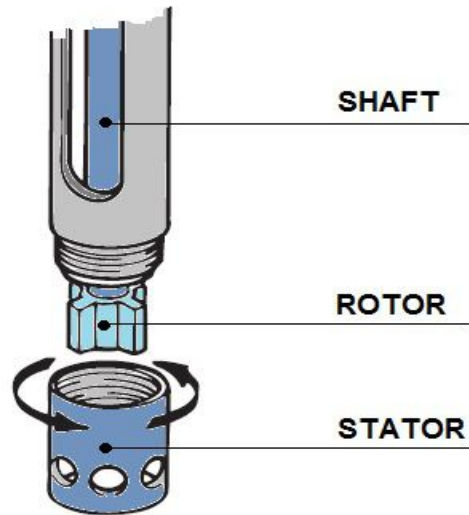


Figure 1.1. The HSM design. The shaft is connected to the rotor and the stator will be placed around the rotor after mounting.



Figure 1.2. Silverson: in-line unit (left) and batch mixer (right) [www.silverson.co.uk].

The idea of rotor-stator mixers is quite simple and really functional. According to the working setup, we can define batch rotor-stator mixers or in-line rotor-stator mixers (Figure 1.2). The main difference is that in the case of the in-line rotor-stator mixers the fluid is not only agitated by the rotor-stator itself but the fluid motion is improved by using external pumps. In this case, the rotor-stator can have more complicated shapes and the design is concentrated mostly on the effective deagglomeration or dispersion of materials. The in-line rotor-stator mixers can have complicated designs and have many applications in the industry. In-line mixers are used mostly in systems which require an only single pass of materials, for example, to effectively mix the fine powder with fluid (Figure 1.3). To make the shearing more effective different designs of rotor-stator are used, as in colloid mills or toothed devices (Figure 1.4).

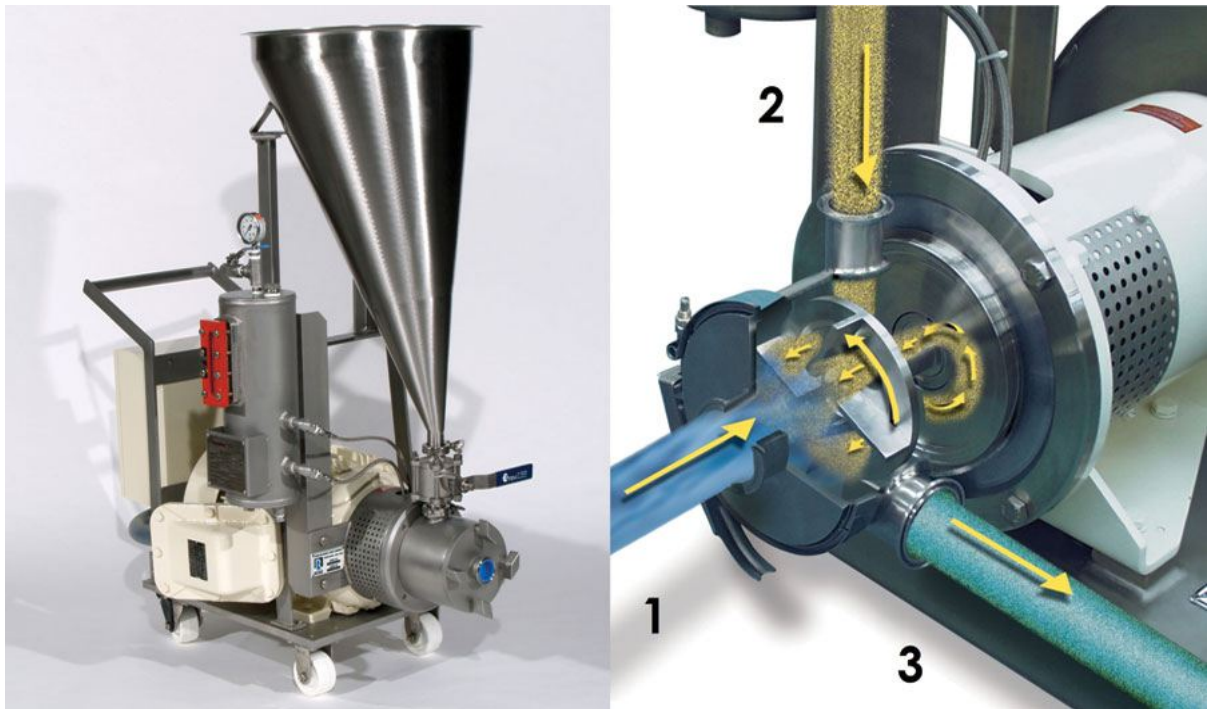


Figure 1.3. Ross in-line mixers [www.mixers.com] used to disperse injected powder (point 2) into the flow of fluid (point 1) by one pass of them by HSM. Well mixed materials are expelled centrifugally through the stator openings (point 3).



a)



b)



c)



d)

Figure 1.4. Different designs of the in-line rotor-stator.

*a,b) multistage rotor-stator and its components [www.bematek.com],
c) toothed device [www.quadroliquids.com], d) colloid mill [www.ikausa.com].*

When more passes are required to achieve product specification the batch mixers are used. The simple batch rotor-stator mixers have the pumping ability still big enough to use them in some systems without the external pumps [Myers et al., 1999]. Depending on the design and shape the batch rotor-stator mixers can handle even 30 000 litres of fluid like water (large scale batch mixer with a diameter comparable to the open impellers diameter) [www.silverson.com]. To agitate a big volume of liquid or liquids with a higher viscosity the process can be optimised by using an additional impeller which enhances bulk mixing. Another way to improve the spatial homogeneity in a large vessel is a creation of full circulation and a longer processing time.

The batch rotor-stator devices can be used in liquid metal processing. In-line mixers require a longer way passed by liquid than batch ones as fluid have to go through the additional pump. From this reason, it can be difficult to use them without the energy (temperature) loss. The liquid metal processing usually must be done at a constant temperature so using of batch mixers is more common. Therefore, batch rotor-stator devices are in focus of this work. Generally, when mixing in batch mixers is optimised, this knowledge can be used to optimise the in-line process too.

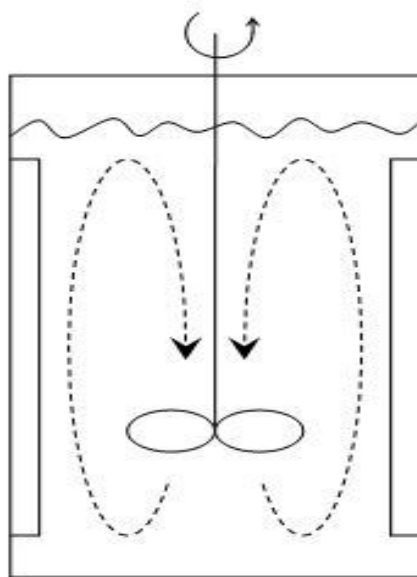
In addition to different operating conditions (presence of external pump), the design of the rotor can be different too. We can find two types of HSM according to the type of rotor. There are axial and radial discharge rotor-stator mixers (Fig. 1.5 and Fig. 1.6) [Kresta, 2004]. This is similar to the case of open impellers. An axial or a radial open impeller results in a different flow pattern in the vessel. The axial flow pattern is mainly down and up oriented and a radial flow pattern is a side to side oriented. The radial and axial flow impellers have different designs (compare with Fig 1.5 and 1.6) of blades, the blades of an axial flow rotor are twisted. The axial impellers are used in an application where bulk mixing plays more important role than shear forces. The radial impellers provide more shear stress so are used in applications where the higher shear rates are necessary. In batch mixers mostly for practical reasons (a simplified design), the radial rotors are used.



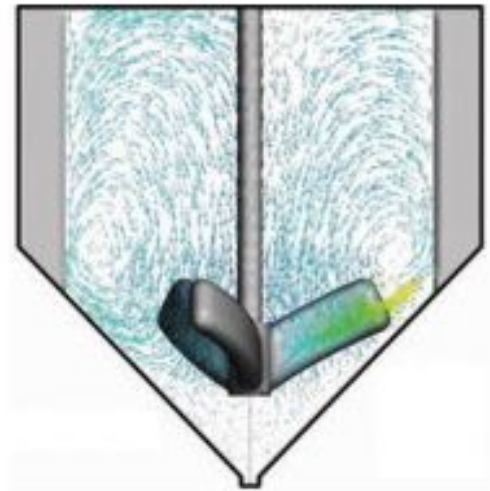
a)



b)



c)



d)

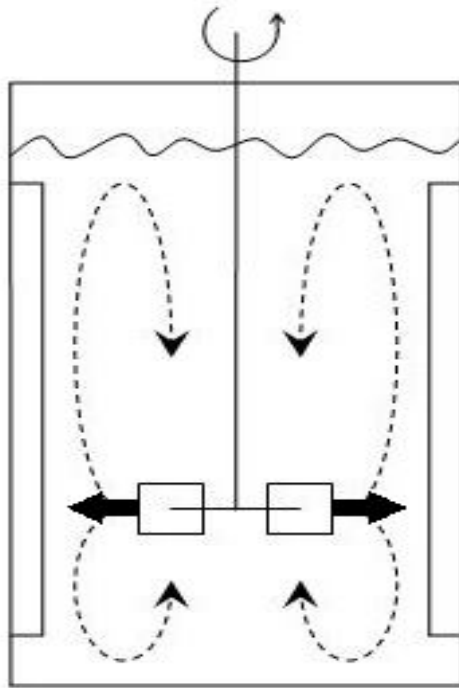
Figure 1.5. Axial flow impellers. a) Axial rotor-stator design [www.greaves.co.uk], b) axial rotor shape with twisted blades, c) axial flow is shown schematically in the vessel, d) flow visualisation in cross-section of the vessel [Rielly et al., 2007].



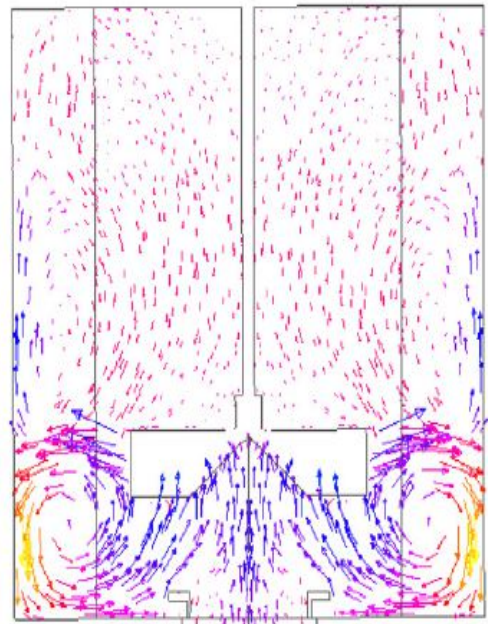
a)



b)



c)


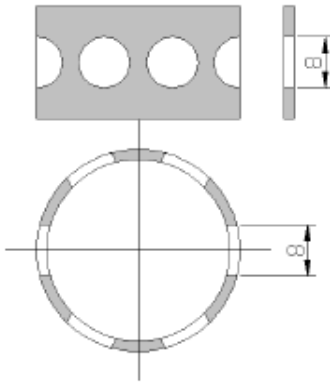

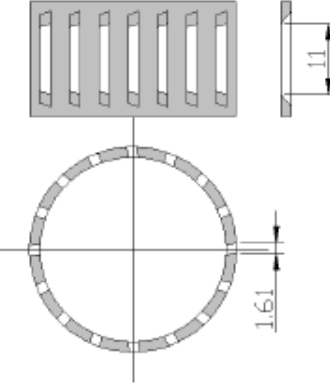



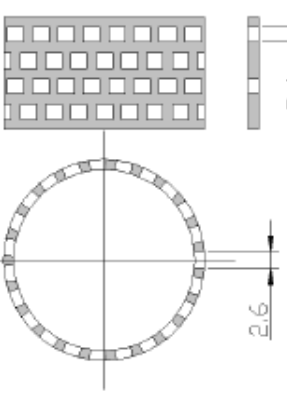

d)

Figure 1.6. Radial flow impellers. a) radial rotor-stator design (Silverston), b) radial rotor shape, c) radial flow is shown schematically in the vessel, d) flow visualisation in cross-section of the vessel [Singh et al., 2007].

Another classification of rotor-stator devices is based on the stator design. There are a lot of different designs available from vendors. According to different applications, usually the stators are variations of shapes shown in Table 1.1 (for standard diameter 31 mm) where proposed applications from Silverson are also given [www.silverson.co.uk; Utomo, 2009].

Table 1.1. Different stator designs and proposed applications.

Stator name	Stator design	Stator holes geometries	Typical application (from Silverson)
General Purpose Disintegrating Head			<p>This stator is giving an exceptionally vigorous mixing action and is ideal for general mixing applications and the disintegration of solids.</p>
Slotted Disintegrating Head			<p>Advised for the disintegration of fibrous materials and “elastic” materials such as rubbers and polymers</p>

Square Hole High Shear Screen™			The configuration provides exceptionally high shear rates. It is designated for the rapid size reduction of granular solids. Can be used for the preparation of emulsions.
Emulsor Screen		288 round holes with diameter 1.25 mm arranged in 8 horizontal rows in the same way as in Square Hole HS Screen	Suitable for liquid/liquid preparations of emulsions.

1.1.2. Reynolds and Newton numbers in stirred vessels by rotor-stator devices.

A number of dimensionless numbers describe the mixing parameters in a stirred vessel. Two commonly used are the Reynolds number and the Newton (power) number.

As the exact flow description is usually complicated, to describe similar mixing conditions the Reynolds number is used. The concept was introduced by G. Stokes in 1851, [Stokes, 1851] and is consistent with the Stokes equations of fluid motion. Using of the Reynolds number was popularised by Osborne Reynolds in 1883 [Reynolds, 1883; Rott, 1990] and the number was named after him. This number is really useful for scaling problems, for example when the airflow around cars is checked with the smaller model. If the same geometrical proportions are kept, the same Reynolds number will describe flow behaviour around the model of car and around the real car. The main problem, when using the Reynolds number, it is making the situations comparable. In the case of identical proportions of geometrical sizes of the system, the description is simple. But the

Reynolds number can be the same in two different situations, for example, equal 1000 inside the flow in the pipe or in the stirred vessel. Thus, the Reynolds number is described by the equations dependent on system geometries and the similar systems are usually compared. Anyway, as the describing of a turbulent flow is really complicated, the Reynolds number (Re) in fluid dynamics is used to help predict similar flow patterns in different fluid flow situations. Of course, the system is different but some similarity usually can be found. This similarity is easier to explain by using the specific terms describing the flow pattern. The Reynolds number does not give full information about a flow movement, but describes what a flow behaviour we can expect. The flow pattern is considered as laminar or turbulent (transitional flow is sometimes described too) dependent of Re. Usually, high Re (over 10 000) are a good indication of the turbulent behaviour of flow. Turbulent flow is dominated by inertial forces, which tend to produce chaotic flow instabilities as eddies and vortices. Laminar flow occurs at low Reynolds numbers, where viscous forces are dominant, and is characterised by a smooth, constant fluid motion.

As the behaviour of flow is governed by two types of forces, the Reynolds number is defined as the ratio of inertial forces to viscous forces for given flow conditions. It can be described by Equation 1.1 [Falkovich, 2011].

$$\text{Re} = \frac{\text{inertial forces}}{\text{viscous forces}} = \frac{\rho v L}{\mu} \quad \text{(Equation 1.1)}$$

Where: v – the maximum velocity of the object relative to the fluid or characteristic velocity in the fluid;

L – a characteristic linear dimension, (the travelled length of the fluid).

μ – the dynamic viscosity of the fluid

ρ – the density of the fluid

The problem is to define the characteristic length L in the classical definition of Reynolds number (Equation 1.1). If we compare with Padron [2001] the Reynolds number can be correlated to different dimensions e.g. rotor diameter, gap width and total hydraulic radius of stator holes. Further studies for example from Doucet et al. [2005] suggest that the definitions of Reynolds numbers based on rotor diameter can be used

with good results to describe the power draw in a batch rotor-stator. This definition (Equation 1.2) of Reynolds number has been used widely as it is similar to that in a stirred vessel [Kowalski et al., 2011] and gives a good prediction to describe flow pattern in a mixed vessel.

$$\text{Re} = \frac{\rho N d^2}{\mu} \quad \text{(Equation 1.2)}$$

Where: N – the rotational speed of impeller,
 d – the impeller diameter
 μ – the dynamic viscosity of the fluid
 ρ – the density of the fluid

Another dimensionless number used to describe what happens inside the agitated vessel is Newton number. For Newtonian fluids the power consumption in a stirred vessel can be normalised as [Ulbrecht, 1985; Wei, 1991]:

$$\text{Ne} = \frac{P}{\rho N^3 d^5} \quad \text{(Equation 1.3)}$$

Where: N – the rotational speed of impeller,
 d – the impeller diameter
 P – the shaft power for the impeller.
 ρ – the density of the fluid

Ne it is the Newton number, often called the power number as it describes the power consumption. Both, the Reynolds number and the Newton number are dependent on ρ, N, d . Thus, there exists a dependence between this numbers. The power number it is inversely proportional to the Reynolds number in the laminar regime and relatively constant in the turbulent regime. It was unclear for the stator of rotor-stator devices how to predict the laminar and turbulent regimes by specific Reynolds numbers [Calabrese and Padron, 2008; Doucet et al., 2005]. One reason was the existence of several

definitions of the Reynolds number as mentioned before. The Reynolds number given by the Equation 1.2 is based on a rotor diameter seems to be the best tool to predict both, a flow behaviour and power consumption, as described by Doucet et al. [2005]. Secondly, if this definition is chosen, the power number in a batch rotor-stator mixer will be similar to that in the stirred tank.

Up to date it has been stated that the fully turbulent regime for a tank agitated by rotor-stator starts at Re above 10 000 similar to tanks stirred by the open impeller. The laminar regime extends up to $Re = 100$ for rotor-stator instead of $Re = 10$ for the stirred tank (Padron, 2001; Doucet et al., 2005). The dispersion of oxide should be done in fully agitated conditions, which means that we expect the turbulent flow.

Power number and power draw are characteristic parameters fundamental to the motor selection. The connected motor power should be higher since it takes into account the electrical and mechanical losses. The power consumed by the motor and gearbox as well as the energy losses are not considered for process design or scale-up and can be represented as the percentage of the overall power input [Bader, 1987]. For an in-line rotor-stator mixer Kowalski et al. [2011] found that the power transmitted by the rotor consists of a power term and a flow term and has to be calculated more exactly.

A power consumption depends on the mixed volume. Increasing of N will increase both Re and decrease Ne . To describe the power changes the power draw is used. Power draw is defined as the amount of energy necessary for a period of time, in order to generate the movement of the known amount of fluid within a container. The power draw is calculated from Equation 1.3, usually with respect to mixed volume [compare Das et al., 2014] or Reynolds number [compare Doucet et al., 2005]. Power draw influences heat and mass transfer processes, mixing and circulation times. Power draw has been used as a criterion for process scale-up and a system design [Kresta et al., 2004]. Usually, the power draw is subject to a further investigation since geometries of the impellers and tanks influence the power draw calculated from the Equation 1.3 more than can be predicted from this formula. In the case of rotor-stator devices, we can refer to the research done by Doucet [2005]. It has been found that formulas presented above are in good correlation with measured power draw. Thus, for simple rotor-stator design used in metallurgy, those formulas should be enough for efficient motor selection or tank scale-up.

1.1.3. Shear forces due to rotor-stator mixing.

A shear stress in physics is defined as the component of stress coplanar with a material cross section. Shear stress is related to the force vector component parallel to the cross section. From the definition of a fluid, this substance deforms continuously, when subjected to shearing forces. If the particles of the fluid are in movement relative one to another there exists a shear stress in the fluid as adjacent particles have different velocities. A fluid movement with the same velocity in each point means that the shear stress is not produced inside the flow. When flow moves relatively to the constant surface the shear stress exists close to boundaries. Fluids behaviour under stress is different as it depends on the fluid atomic arrangement. Different fluids deform at different rates under the same shear stress as the natural resistance to sheer deformation occurs due to cohesion and interaction between molecules. This resistance is measured by the viscosity, which is a property of the fluid. A fluid with a high viscosity deforms more slowly than the fluid with a low viscosity.

The deformation can be linearly or not linearly dependent on the shear forces. The fluids are usually called “Newtonian fluids” or “non-Newtonian fluids” dependent on behaviour. Newtonian fluids obey the linear relationship given by Newton’s law of viscosity (Equation 1.4) [Smith,1994; Nash, 1998; Morrison, 2012].

$$\tau = \mu \frac{dv}{dy} \quad \text{(Equation 1.4)}$$

Where: dv/dy is the velocity gradient

If we consider the velocity vector with one non-zero component (v_x), the shear is named a simple shear [Morrison, 2012]. For Newtonian fluids, the gradient of velocity is constant and perpendicular to the velocity itself. It is called the shear rate and given by:

$$\dot{\gamma} = \frac{dv_x}{dy} \quad \text{(Equation 1.5)}$$

The shear rate is the velocity change along the flow direction and can be measured for different systems. Because the shear rate depends on the velocities change, it can be described in terms of velocity of the impeller in the case of stirred vessels, since the velocities inside fluid are produced by the impeller movement. A lot of effort has been taken to establish usable equations to calculate expected shear rate without velocity measurements. Some authors correlated shear ratio with the rotational speed [Metzner and Otto, 1957; Calderbank et al. ,1959; Bowen, 1986; Robertson et al., 1987], others with power input [Hoffmann et al., 1995; Candia et al., 1999]. Since the power draw has been described for many open impellers so shear rates for them can be usually calculated. For rotor-stator devices, the power draw has been estimated by Doucet et al. [2005] by applying the rules used for open impellers.

The rotor-stator design provides high shear rates, what means that a velocity gradient is high. The highest shear rates are expected inside the gap between the rotor and stator. The rotor movement is giving the velocities to the fluid which passes through the stator. If the fluid contains the agglomerates or films, those can be broken due to high relative velocities and the shear rate in the fluid.

The nominal shear rate inside gap is given by the following formula (Eq.1.6) [Couper et al., 2005]:

$$\dot{\gamma} = \frac{\pi N d}{q} \quad \text{(Equation 1.6)}$$

The velocity change is equal to the velocity of the rotor blade tip. It is the maximum possible velocity in the system. The velocity changes take place on the way equal to the gap width. The minimum fluid velocity is equal zero and maximum possible velocity in the setup is the tip of blade velocity equal ($\pi N d$). Thus, the nominal shear rate in the gap is given by Equation 1.6.

From this description, the shear rate is inversely proportional to the gap size. Thus, the gap increase will decrease shear forces inside a gap. The optimal gap size is an open question as depends on the process requirements. Higher shear rates are necessary for particles joined by relatively high forces. The solid milling requires higher shear rates to occur than emulsification. Practically, gap sizes are usually kept relatively small (100 to 3000 μm) in the commercial multipurpose mixers [Karbstein and Schubert, 1995].

1.2. Behaviour of liquid stirred by rotor-stator devices.

1.2.1. Flow description.

To describe a viscous fluid motion in physics Navier-Stokes equations are used. These balance equations are a form of Newton's second law applied to fluid motion. The laminar flow occurs when a fluid flows in parallel layers, with no disruption between the layers and for this situation there are solutions of Navier-Stokes equations. A turbulent flow is a flow regime characterised by chaotic changes and by recirculation, eddies, and apparent randomness. Unfortunately, the numerical solution of the Navier-Stokes equations for turbulent flow is extremely difficult. This is why a well-known physicist, Nobel laureate, Richard Feynman described turbulence as "the most important unsolved problem of classical physics" [Vergano, 2006]. Even the computational time becomes significantly infeasible for calculation. Usually, the problems of turbulences are solved by using a laminar solver with time-averaged equations such as the Reynolds-averaged Navier-Stokes equations (RANS), supplemented with turbulence models [Reynolds, 1895, Tennekes and Lumley, 1992, Temam, 2001; Wang, 1991].

Agitation means forcing a fluid mechanically such that it flows creating any type of flow pattern inside a vessel. Agitation includes mixing as a special case. Mixing can be defined as a distribution of two or more separate phases together up to the moment when they are randomly distributed inside the vessel [Geankoplis, 2003]. The geometry of setup (impeller and vessel) is so important that the agitation and mixing processes can be considered geometry specific. In a stirred vessel we can expect existence of both, laminar and turbulent regions. Since the motion of flow is three-dimensional (3D), the laminar flow can not describe conditions in the vessel. Even in low Reynold numbers the flow pattern is complicated due to eddy creation around the mixing head (a fluid vortex, which is the effect of the fluid circulation by the impeller). The numerical predictions of the flow show the velocity pattern (Figure 1.7) which cannot be described by simple mathematical formulas [Barailler et al., 2006].

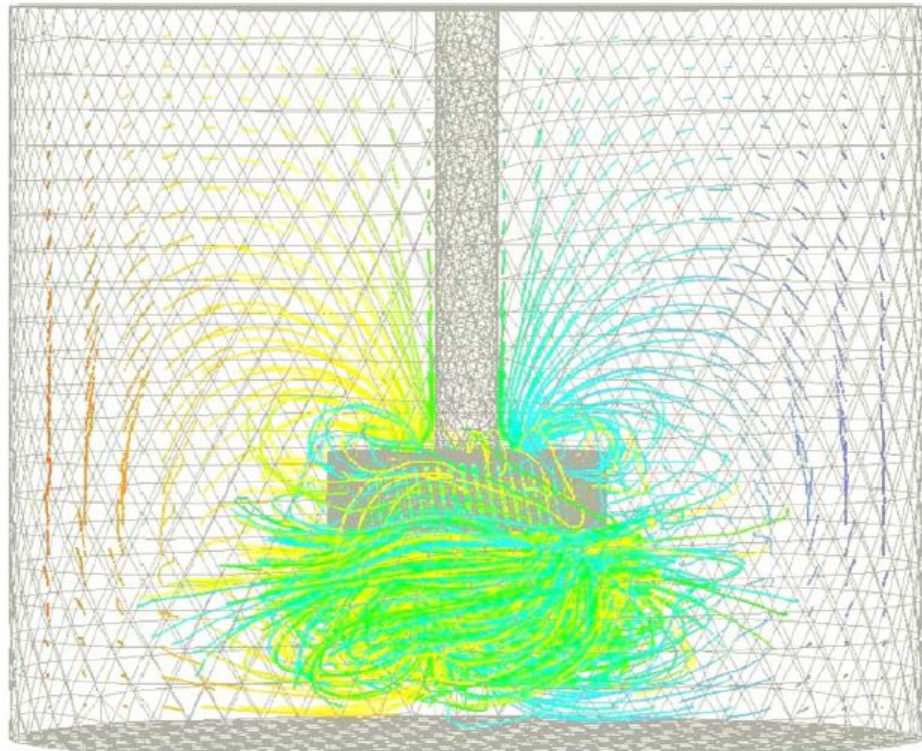


Figure 1.7. Computer simulation of 3D flow lines around rotor-stator with a rotational speed $N = 3000$ rpm [Barailler et al., 2006].

From a simulated flow pattern around the mixing head (Figure 1.7), we can predict that a flow pattern is rather complex. The presence of high-velocity jets travelling from the head to the walls cause recirculation loops. It has been predicted by CFD simulation that the jets velocity is a few orders of magnitude higher than in other parts of the vessel [Utomo, 2009]. The jets emerging from the holes extend up to the tank wall where the radial velocity is converted back into tangential velocity by tank wall. In the case of simulated stirring, the liquid is fully agitated, what means that jets hit the vessel wall. Without disturbing, the velocity of jets will decrease along the way and flow will be recirculated due to centrifugal action of the rotor which acts as pump [Paipetis, Kostopoulos, 2012; Gülich, 2014]. In simulated figures, we can observe this pumping force below the head (Figure 1.8). Rotations of rotor suck the liquid up into mixing head where the pumped amount of liquid is exposed to shear forces and later pushed by the stator holes as the jets (shown by red colour in Figure 1.8). Behind the jets vortices occur and part of the flow can be reversed into the head so it is possible to observe reversed velocities (Figure 1.8).

When the fluid is pushed out through rotor blades and leaves the rotor-stator head

as the jet, the local pressure inside the head decreases. The pressure difference is a source of the “pumping” or “sucking” force and a centrifugal action of the impeller [Utomo, 2009]. The agitation is dependent on the vessel geometry [Geankoplis, 2003] and the presence of the wall in the way of jets will change the flow pattern. If the velocity of jet flow is high enough, the flow will be scattered up and down improving the fluid agitation in other parts of the vessel.

Figure 1.8 shows the flow pattern in a cross section along a vessel axis with the central position of the head. The velocity pattern consists two recirculation loops with centres in points A and B. Upper circulation loop is the effect of agitation which occurs when the flow is scattered by the wall.

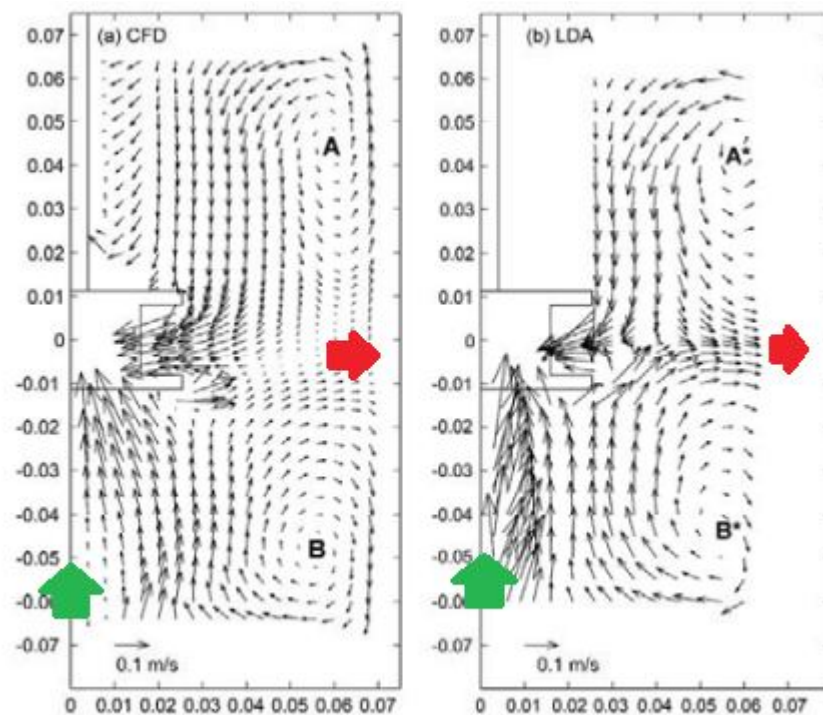


Figure 1.8. Axial-radial velocity vectors in cross-section at 2000 rpm (a) computationally calculated, (b) LDA measurements. Dimensions are in m. Points A and B represent the centres of circulation loops. The sucking force direction is drawn by green colour and the jets position is shown by red colour [Utomo, 2009].

If the shape of the vessel is cylindrical as on the simulated picture, the radial velocity is converted into tangential velocity and the vortexing [Figure 1.9] can happen if the energy dissipated in the vessel is high. Agitation in the vessel can lead to swirling flow and the surface vortex creation.



Figure 1.9. Vortexing. The central vortex along the impeller shaft changes the surface shape and sucks air into the bulk liquid [Busciglio et al., 2011].

Vortexing is usually avoided by baffles mounting. Baffles change the tangential velocity to other direction by reflecting flow into the centre of the vessel. The flow pattern in a baffled vessel is shown in the Figure 1.10 [Viček et al., 2016]. If unbaffled vessels are used, the vortex creation can be avoided by off- centre agitator position. Flow patterns in unbaffled vessels with a shaft placed off-centre for different distances from the tank central axis are shown in Figure 1.11.

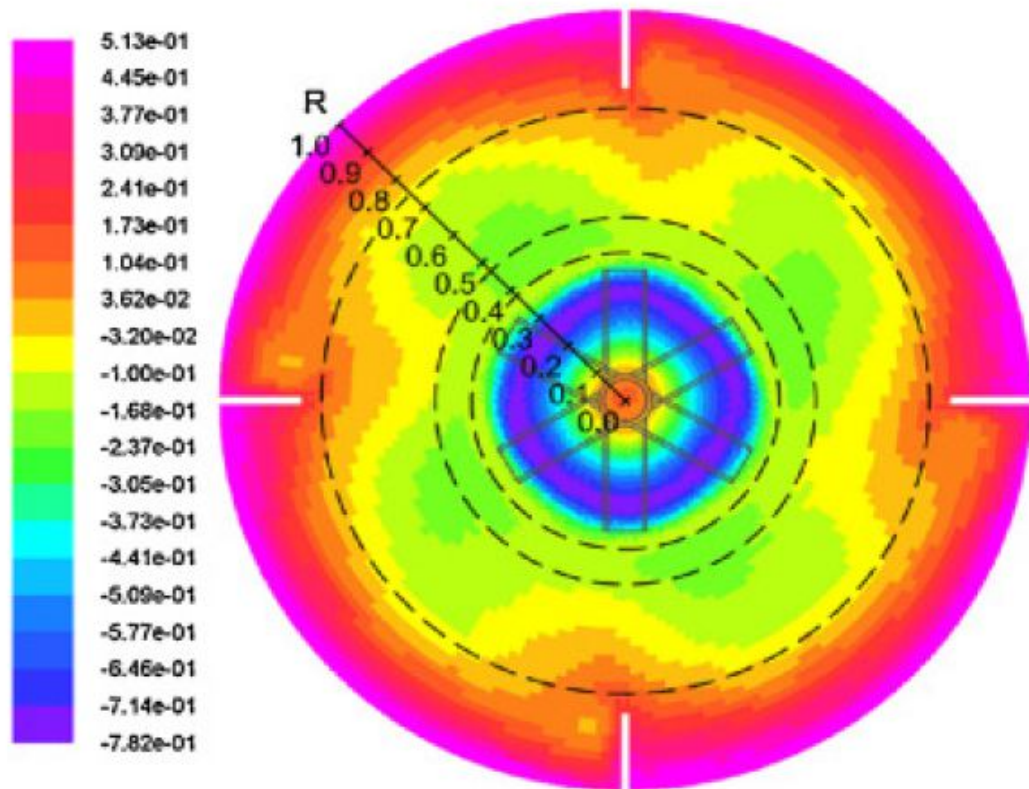


Figure 1.10. Tangential velocities contours in fully agitated and baffled vessel. Baffles changing the flow direction and prevent too strong vortexing [Vlček et al., 2016].

A vessel with cuboid shape can be also used to avoid vortexing [Myers et al., 2015]. The cuboid shape disturbs the tangential flow and baffles are not mounted in this kind of vessels. The simulated flow by Utomo [2009] was investigated in the unbaffled vessel. The vortexing effect for rotor-stator is not so strong since the movement of bulk liquid is much weaker than in the case of open impellers [Kresta et al., 2004].

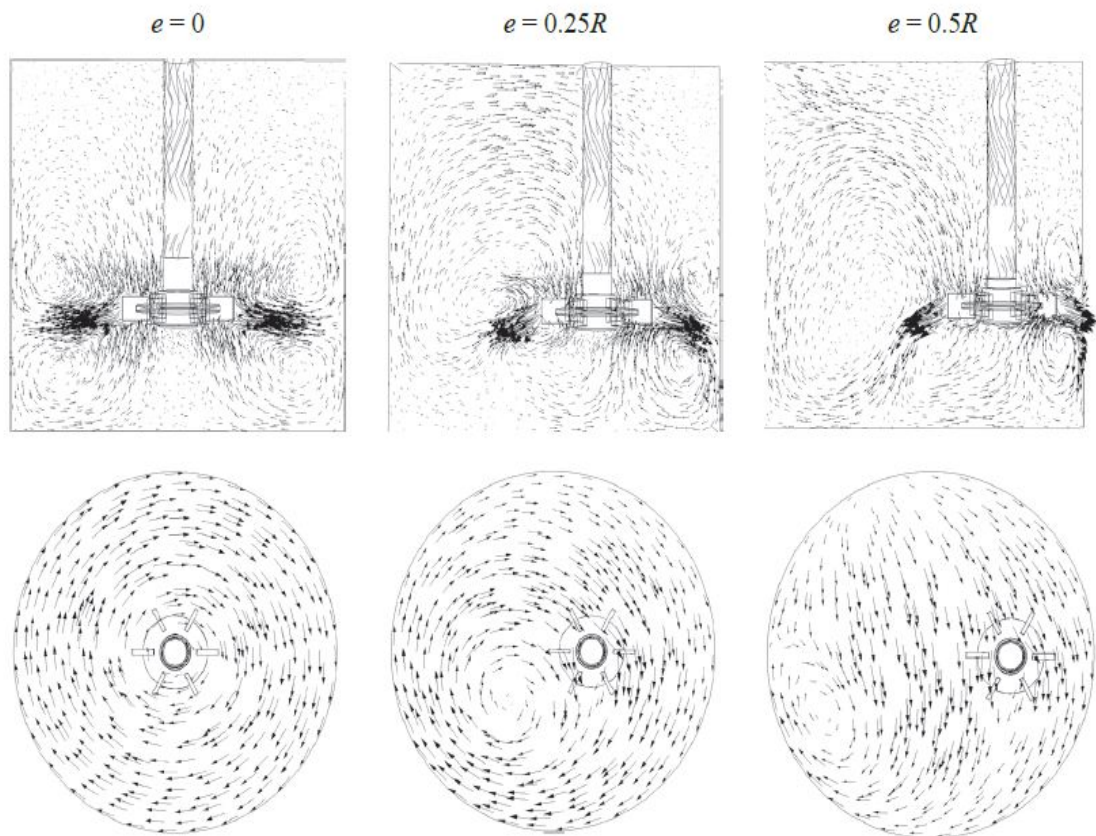


Figure 1.11. The flow pattern in a stirred vessel with an eccentrically positioned radial impeller, vertical cross-section plane (top row), horizontal cross-section plane on the liquid free surface (bottom row), [Karcz and Szoplik, 2004].

The eccentrically placed impeller reduces vortexing but if the rotational speed is increased still a lot of flow instabilities can occur. In the case of off-centre placed impellers, the vortex can occur on the side of the vessel. This side vortex usually is smaller than vortex located in the centre. Figure 1.12 shows different instabilities in the flow with eccentrically placed radial impeller [Galletti and Brunazzi, 2011].

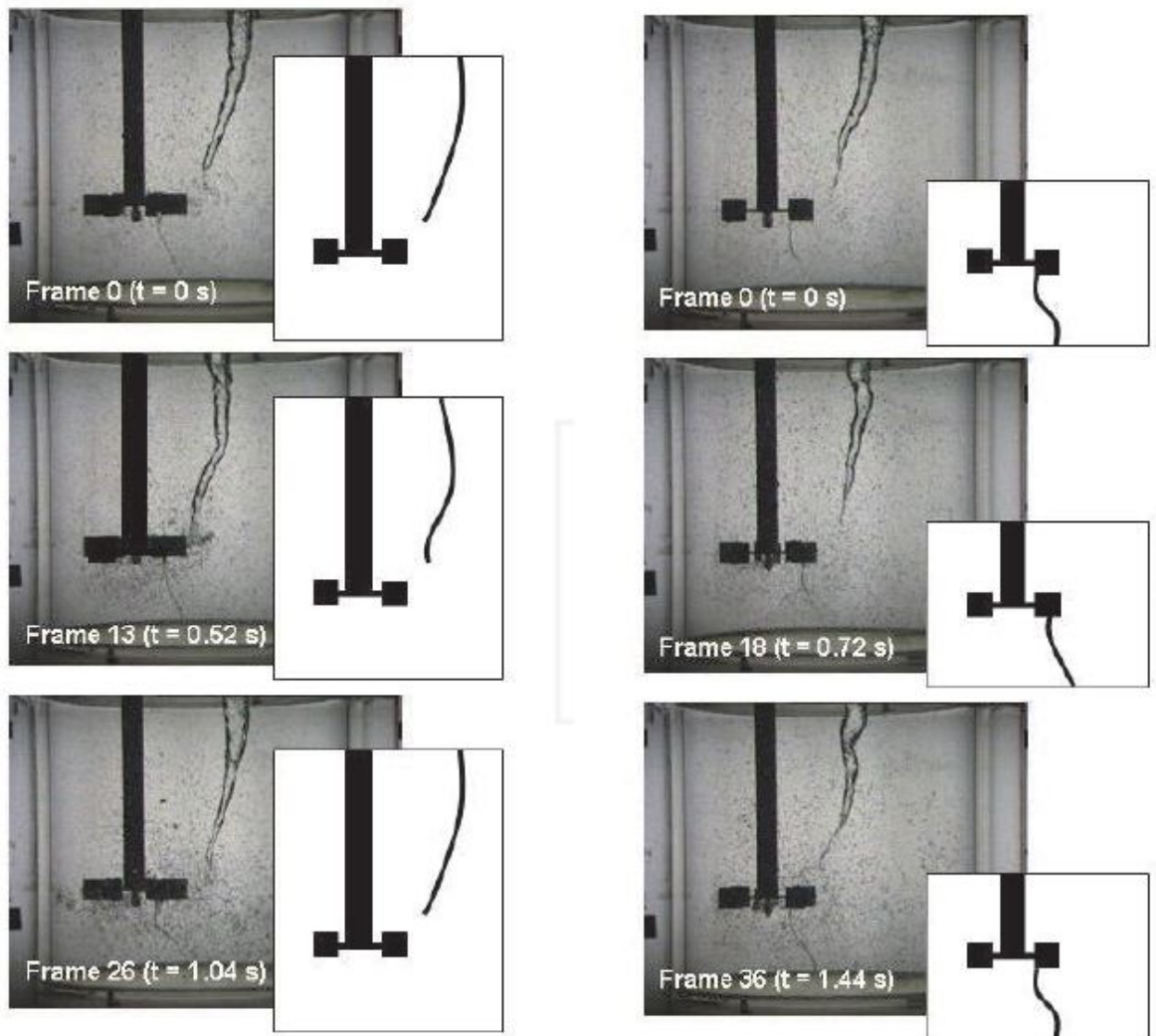


Figure 1.12. The different flow instabilities present in the flow. The vessel is un baffled and the impeller is placed off-centre [Galletti and Brunazzi, 2011].

The vortex is created on the side (“side vortex”) of mixing impeller and gives the way to air. The air is sucked into liquid by the pressure difference and with rotational speed increase can touch the head what results in the air dispersion into a bulk liquid. In most cases, vortexing is avoided by the off-center position of the impeller and by using the rotational speed from safe range established experimentally for the specific mixing conditions since it was found that the vortex depth is highly dependent on the rotational speed [Hayduk and Neale, 1978].

Another problem is the influence of the bottom on the flow pattern. The distance between the impeller and the bottom is named a clearance. Increasing of clearance (C) plays an important role, as depending on the C value either two (Figure 1.13 a) or one (Figure 1.13 b) circulation loops are observed. Galletti et al. [2003, 2005a, 2005b] found that the flow pattern transition (single- to double-loop pattern) occurred for $C/T = 0.17-0.2$. Nienow [1968] observed pattern transition for $C=T/6$. Typical radial flow over $T/6$ needs the higher rotational speed required to suspend the particles (N_{js}) than for smaller clearances. It has been explained by Sharma & Shaikh [2003] by the fact that the energy available for suspension decreased with the clearance increasing. When impellers were operating very close to the vessel base, the N_{js} was observed to be constant with C/T . Additionally, Myers et al. [1997] found that at the lower clearance, $C = 0.33T$ more stable flow fields are observed. Thus, the clearances increase will increase the probability of instabilities as a vortex creation. The vortex has a characteristic depth. If a vortex created close to the surface will be elongated with a rotational speed increase, it can touch the impeller and the air will be dispersed into the fluid. This can change the mixing conditions and should be avoided. If the impeller is positioned close to the liquid surface the way for oxygen from the surface to the impeller is short, so the vortex can easily touch the impeller. To avoid a vortex creation the impellers are located deeper under the surface, with smaller clearances to the bottom [Myers et al., 1997].

In Figure 1.13 we can observe a flow pattern created with clearances $T/8$ and $T/3$. As mentioned before the flow pattern is different and transition from the one-loop flow pattern to the double-loop pattern is expected about $C=T/6$.

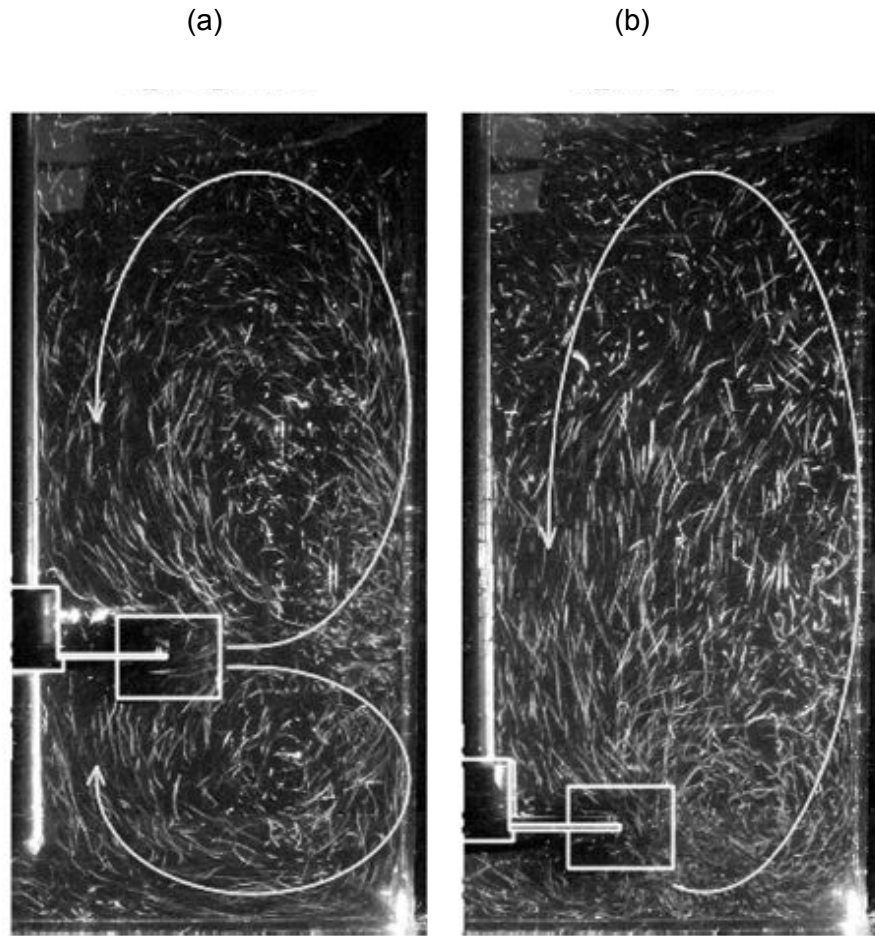


Figure 1.13. Liquid flows within the vessel as viewed on the vertical plane.
 (a) $C=T/3$, two-loops flow pattern, (b) $C=T/8$, one-loop flow pattern.

The flow pattern is different in both cases but if we compare the mixed areas in both cases they seem to be similar. Fig. 1.13 shows the loops borders which demonstrate that the vessel is agitated above open impeller to the same level. As mentioned before, the smaller clearances result in the more stable flow without a vortex creation. In the case of mixing two different substances, the smaller clearances are strongly advised as the substances with higher densities tend to settle down on the bottom and a sucking force has to be strong enough to bring them into the head. Thus, the clearance increase will increase minimum necessary rotational speed which will suspend a denser substance in the bulk liquid.

1.2.2. Pseudo-cavern effect.

In 1975 first time the cavern effect was described and defined as a well-mixed region around the impeller surrounded by a stagnant region [Wichterle and Wein, 1975]. It was observed that when moving away from the well-mixed region the fluid motion becomes laminar and nearly stagnant. The same phenomenon can be observed with shear-thinning fluids and has been named the 'pseudo-cavern' by Doucet et al. [2005]. The pseudo-cavern term describes this phenomenon if it occurs with both Newtonian and non-Newtonian fluids. The interesting fact is that Doucet used the rotor-stator devices to investigate and describe the pseudo-cavern existence. Previous observations have been done for open impellers. The main purpose of Doucet's research was to check viscosity influence on the shape of pseudo-cavern. Authors applied some rules developed for open impellers to predict pseudo-cavern sizes. Unfortunately, they state that "Correlations taken from literature (developed for Rushton turbine) to predict cavern diameter and height were unable to fit our experimental data due to the particular mixing behaviour of the rotor-stator impeller". Thus, authors correlate their results with previous models but were unable to predict a priori the cavern volume. The power draw was estimated by authors as correlated with the pseudo-cavern size. Authors used a flow visualisation technique based on a fast acid/base reaction described by Brennan and Lehrer [1976]. On Figure 1.14. we can see the pseudo-cavern photograph visualised in the vessel. The chemical reaction in the well-mixed region changed the pseudo-cavern colour and made it possible to further analyses. Sizes of the cavern have been named by authors: h_c (height) and d_c (diameter) and are shown in the picture. The rest of the fluid in vessel seems to be stagnant since only a pseudo-cavern volume changed the colour after mixing. Observations made by Doucet et al [2005] proves that the well-mixed region is separated from the rest of liquid by shear forces due to fast movement of a fluid flow.

Very interesting is the physical description of this phenomenon. If we will use the nomenclature used before in a flow description, we can conclude from recorded pictures few important facts.

1. The flow of a photographed pseudo-cavern is not disturbed by the presence of the walls or by reflections from the bottom of the tank.
2. The one loop flow is observed. The jets emerging from the stator holes are recirculated only by the pumping action of the head since on their way is no wall present.
3. In the picture (Fig. 1.14), we can observe the free fluid stirring. The influence of the vessel is not important as any part of the vessel doesn't disturb the flow. In this mixing conditions, the mixed pseudo-cavern volume is equal to the maximally mixed volume by the known impeller with a constant rotational speed.

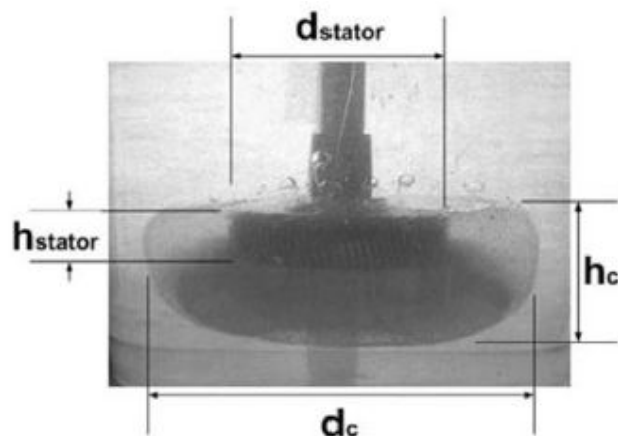


Figure 1.14. Observed the pseudo-cavern effect around a rotor-stator head (d_{stator}, h_{stator} – the stator dimensions, d_c, h_c – the pseudo-cavern dimensions [Doucet et al., 2003].

From the pseudo-cavern visualisation, Doucet et al. [2003] conclude that cavern size scales with the classical definition of Reynolds number for Newtonian fluids. There has been some irregularity in pseudo cavern shape observed. The pseudo-caverns observed in Newtonian fluids are shown in Figure 1.15. The non-Newtonian fluids behaviour differ slightly in terms of the pseudo-cavern creation, but since the molten aluminium and magnesium are believed to be Newtonian fluids [Geiger and Poirer, 1973]

they should behave similarly as has been described by Doucet et al. [2003]. In Figure 1.15, we can observe that a pseudo-cavern shape in the case of Newtonian liquids occupies more the bottom part of the vessel than top one. Even if the pseudo-cavern is changing the shape depending on the stirring conditions (influence of the walls and bottom) the volume is growing when the Re increases. Only in the case of small Re (2.3 and 2.8), we observe the free pseudo-cavern creation. The pseudo-cavern can touch the bottom and walls in the case of higher Re (presented on the pictures).

It can be concluded that in the case of undisturbed flow around the head the pseudo-cavern shape is an ellipsoid. In the process setup, a cylindrical vessel has been used and when the Re increases the pseudo-cavern occupied part of the vessel and had the cylindrical shape as mimicking the shape of the vessel. Thus, the pseudo-cavern shape has been approximated by Doucet et al. [2003] and others as a cylindrical shape with dimensions d_c and h_c [Barailler et al., 2006; Utomo, 2005]. Estimated pseudo-cavern volumes were calculated by Doucet et al. [2003]. The ellipsoid shape is indicated by the results of computer simulation presented in Figure 1.16.

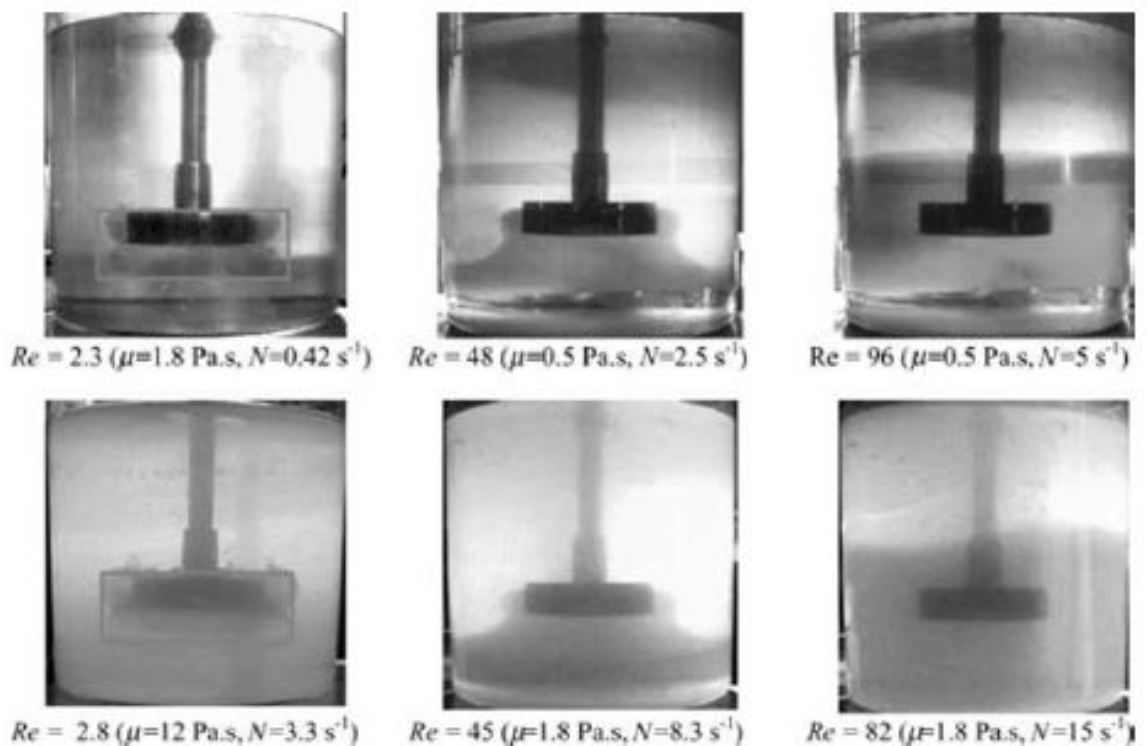


Figure 1.15. Evolution of cavern shapes with the Newtonian fluids [Doucet et al., 2003]

The pseudo-cavern creation has been proven by the computational modelling too and is shown in Figure 1.16. The simulated flow behaviour shows the same tendency to the pseudo-cavern creation. In the picture, the main part of pseudo-cavern is shown by colour points. Red flow around the colour points indicates that movement of fluid is strongly bordered since we can observe a small transitional (green and light blue) zone. The rest of bulk liquid is almost stagnant (a darker blue colour in Figure 1.16). Pseudo-cavern sizes are growing proportional in both dimensions when the N (and Re) increases. The ratio of both sizes seems to be constant. The cross-section of pseudo-cavern demonstrates that shape is more ellipsoid than cylindrical, as will be described in more detail further.

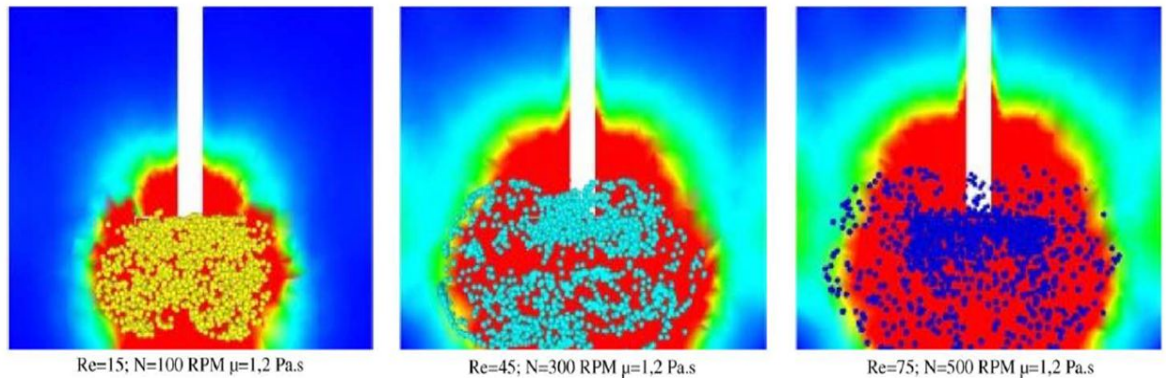


Figure. 1.16. Evolution of the numerical pseudo-cavern with the Re [Barailler et al., 2006].

The definition of the pseudo-cavern says, that it is a well-mixed region. If we compare this with the flow description we can find information, that jets emerging from head holes agitate the fluid (Section 1.2.1). As the head operates constantly, and the rotation of the rotor are responsible for the existence of a sucking force due to the pressure differences, thus jets are brought back into the head. The resultant flow has the shape of flow loops, as described in Section 1.2.1. Hence, the flow is moving around central points of loops as indicated by results of the simulation and experiment (compare with Fig. 1.8). Of course, the flow in the 3D space is more complicated but if we consider velocity components as shown in Figure 1.8 we can treat the flow as the simple circular motion of fluid particles around points A and B (loop centres). In the case of the free pseudo-cavern (when the jet flow is not scattered by the tank wall), there exists only one loop from each side of the head since the second loop is the effect of a jet scattering (see Section 1.2.1).

The velocity pattern in the 3D situation is the result of circular lines starting from stator openings and brought by a sucking force back. Those lines are not circular in the same planes (see Fig. 1.7). Each circulation happens in a slightly different plane, which results in an eddy around the head. A proper visualisation of this process (the vortex creation by the fluid lines) is shown in Figure 1.17:

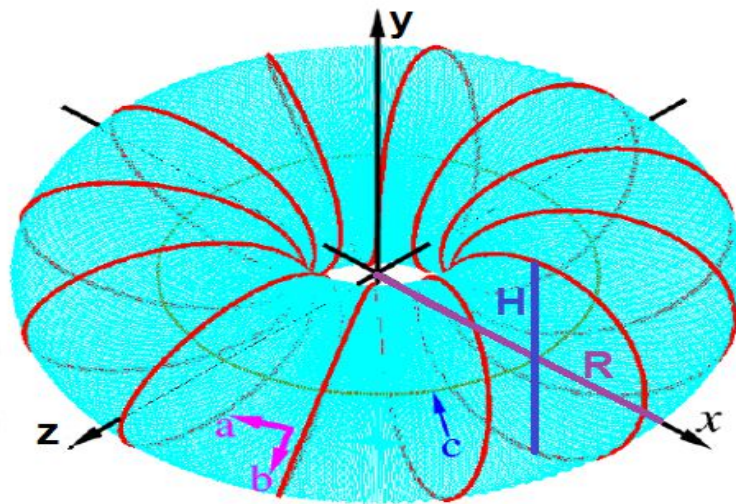


Figure 1.17. The vortex with a torus shape is created by the fluid lines [Reza, 2015].

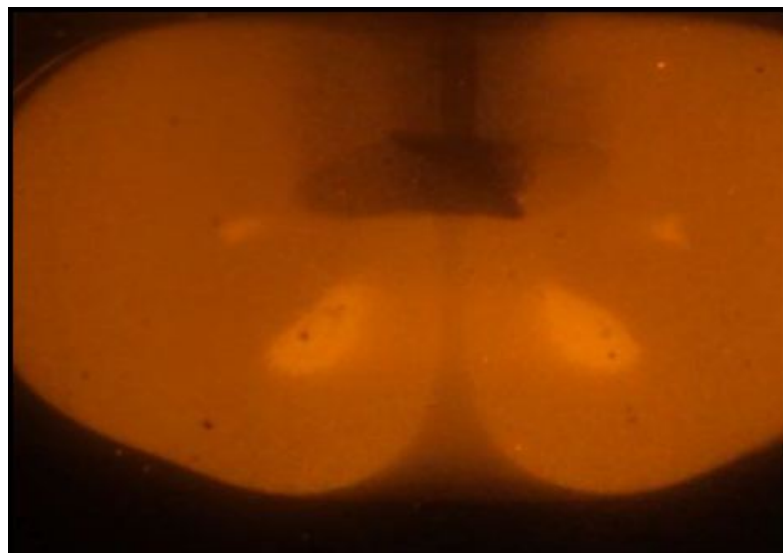


Figure 1.18. The cavern observed around the open impeller. The visible ellipsoid shape is caused by both sides of the torus overlapping, the torus is compressed into ellipsoid shape [Sossa, 2007].

The vortex around the HSM head is similar to that in Figure 1.17. The head is placed in the centre of this vortex. The vortex shape around open impellers is often approximated by the torus shape or described as an ellipsoid [Amanullah et al., 1998; Galindo and Nienow, 1992; Wilkens et al., 2005]. The ellipsoid shape of a vortex around the impeller is well proven by photographs of the cavern (see Fig.1.18). For rotor-stator devices, as given in Section 1.2.1, the fluid motion in the vessel is weaker than for open impellers but the velocity pattern is similar. Hence, the pseudo-cavern approximation should be considered as the torus or the ellipsoid shape. On Figure 1.17, two characteristic dimensions, the size R (pseudo-cavern radius) and the size H (pseudo-cavern height) are drawn. If the “hole” inside torus is small as compared with the rest of the torus volume, the torus volume is almost equal to calculated for the ellipsoid shape. For HSM mixers this central place is fulfilled by the head, so we do not expect that there will be a stagnant fluid inside the torus. Thus, the pseudo-cavern shape can be best described as an ellipsoid around the mixing head with equal radii in the jets plane (radius is equal jets length).

1.3. Oxides present in the mixed fluid and their role.

1.3.1. Agglomerates of oxides present in melts.

A surface oxide film covers liquid aluminium and prevents its further oxidation. However, the film can be entrained into the melt by, for example, surface turbulence. Entrained films can act as a crack during and after solidification. This is why mechanical properties of castings, particularly the tensile behaviour, in a presence of oxides films are unpredictable [Caceres and Selling, 1996; Liu et al., 2003]. Unfortunately, the presence of oxide film defects is practically unavoidable in the aluminium foundry. Even small amounts of air oxygen are sufficient to instantaneously form a layer of aluminium oxide [Grandfield et al., 2013]. Folded oxide films can be of different sizes and shapes. It is the reason why the crack in the alloy can be really serious. They can cause a major reduction in the strength or fatigue resistance [Campbell, 2000]. Additionally, oxide films lead to more problems in addition to the reduction in mechanical properties, such a decreased

fluidity and feeding [Eckert Jr., 1992], creation of leakage paths by connecting wall-to-wall in castings [Campbell, 2000], reduced machinability [Fuoco et al., 1999; Makarov et al., 1999]. As it is difficult to measure oxide film defects with any non-destructive testing methods, our understanding how to remove defects is limited.

The oxidation occurs naturally when a liquid metal is in a contact with the oxygen which is present in the atmosphere [Sleppy, 1961; Silva and Talbot, 1988; Impey et al., 1988; Jeurgens et al., 2002]. In the case of pure aluminium, an amorphous form of Al_2O_3 film protects liquid metal as diffusion of aluminium or oxygen in the film is very slow [Silva and Talbot, 1988]. It is almost impossible to avoid the films creation because of turbulences and other oxygen pathways into liquid. Once created the amorphous film may develop to crystalline forms of alumina rapidly after an incubation time [Haginoya and Fukusako, 1983; Impey et al., 1991; Dignam, 1962]. It has been found that the crystalline alumina grows by further oxidation of metal which requires open pathways between the atmosphere and the melt [Werfers and Misra, 1987]. The transformation to the final crystalline forms results in a reduction in oxide volume what can cause film cracks and expose the liquid metal to the atmosphere. The cracks allow for the growth of new oxide films [Impey et al., 1991]. Many factors influence the nucleation and growth of oxide films. The most important are temperature since it accelerates the oxidation of molten aluminium [Sleppy, 1961]. Increasing the temperature and time will strengthen formed films [Agema and Fray, 1989]. Aluminium oxides observed in the casting can form in different types with the density from 2.3 to 4 depending upon an oxidation temperature, time and thickness [Davis, 1993; Jeurgens et al., 2002]. The presence of alloying elements influences the strength and the oxidation reaction rate of oxide films. Magnesium commonly used in aluminium alloys rapidly increases the oxidising tendency of the liquid metal. The oxide film initially has a form of amorphous MgO , or MgAl_2O_4 , or Al_2O_3 depending on Mg content. The transformation to crystalline films causes cracks as described for pure aluminium and development of new oxide layer. The final oxide film consists of magnesia, spinel and alumina. The oxide film is chemically stable at the temperature commonly used in most cast aluminium alloy processes.

The rates of growth of protective films on liquid metals are an order of magnitude faster than on solid metals due to temperature influence [Campbell, 2000]. According to Campbell [2000], the morphology of oxide films is different for young and old oxide films.

The young oxide films are very thin – up to hundreds of nanometres, usually formed during pouring or mould filling and appear as fine wrinkles. Even early reports show that oxides films will thicken with time [Thiele, 1962] and turn into old oxide films with

thickness from few micrometres to even a millimetre [Campbell, 2000]. If not removed from melt they appear as massive, film-like, or dross-like inclusions in finished castings [Campbell, 2003]. Young films are delicate and thin. Old oxide films are initially flexible and later the thickening process decreases the flexibility. Time of typical treatment of liquid metal allows growing up old films, as they need about 10 s to 1 min to build up to a 10 μm thick layer. Thicker layers up to 100 μm need longer time to be build up, from 10 min to 1 hour [Campbell, 2000].

As mentioned before, the surface oxide film in principle plays a protective role. Problems happen when this film is broken or folded and immersed into a liquid metal. The film breakage can happen during pouring or stirring. It is also possible that film will be folded over with two dry sides lying one against another with trapped gas between them. Lack of bonds between that oxide films and gases will make material weak and after casting can act as cracks. As we have two layers of oxide films it has been named as a double oxide film defect or a bifilm [Cao and Campbell, 2002]. Mechanisms which submerge oxide films into the bulk liquid melt are quite simple. The most common – a surface turbulence – is shown in the Figure 1.19.

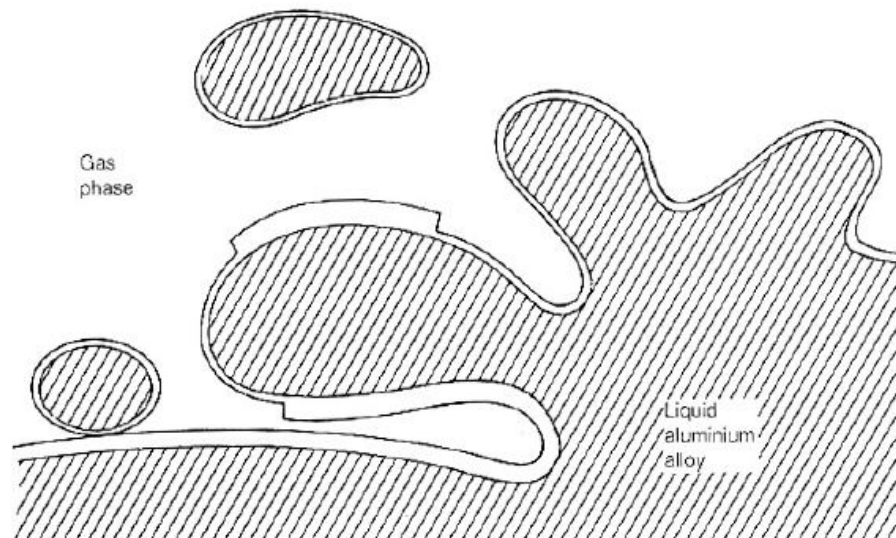


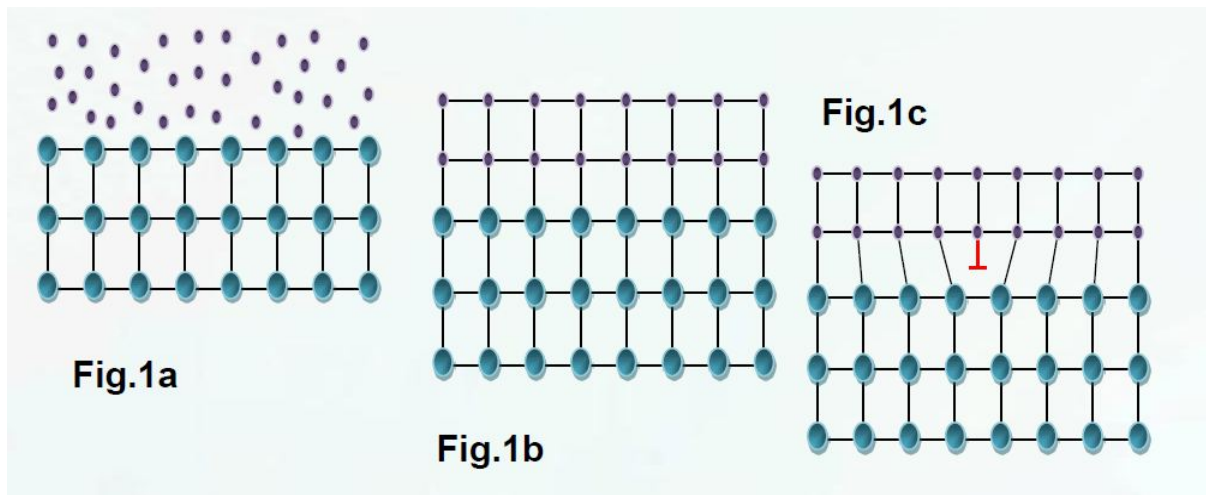
Figure.1.19. Formation of a folded oxide bifilm by surface (schematic view), [Campbell, 2003].

1.3.2. Epitaxial nucleation model.

In the classical approach, the heterogeneous nucleation [Volmer and Webber, 1926; Kelton and Greer, 2011] starts with the formation of a spherical cap on the substrate. Nucleation can start on some potent substrates as energy balance between the interfacial energy change and the volume free energy change is favourable for the formation of a new phase. The created cup will be in contact with the substrate and a contact angle between them is a measure of the substrate potency. But this classical approach cannot be used for potent nucleating substrates which have very small contact angle (effectively zero). In the case of this substrates, it is unphysical to consider a spherical cap [Cantor, 2003]. The principle of chemical and structural similarity as a basis for potent substrates has been suggested many years ago and is commonly used [Kainer, 2007]. The epitaxial model for heterogeneous nucleation on potent substrates tries to explain mechanisms of crystallisation on this substrate [Merwe and Frankand, 1949; Fan, 2012].

The epitaxial model suggests a layer-by-layer growth from the significantly ordered liquid atoms at the interface during the initial stage of the nucleation. The initial structure of the ordered solid mimics the crystal structure of the substrate. Naturally observed distances between atoms in crystal lattice depend on the type of material. Thus, the substrate atoms and liquid atoms tend to build specific and different distances between own atoms. When created layers on the interface mimic the structure of the substrate, this initially strained layer builds up (as it grows) elastic strain energy within the layer. As the layer thickness increases, this elastic strain energy will increase too.

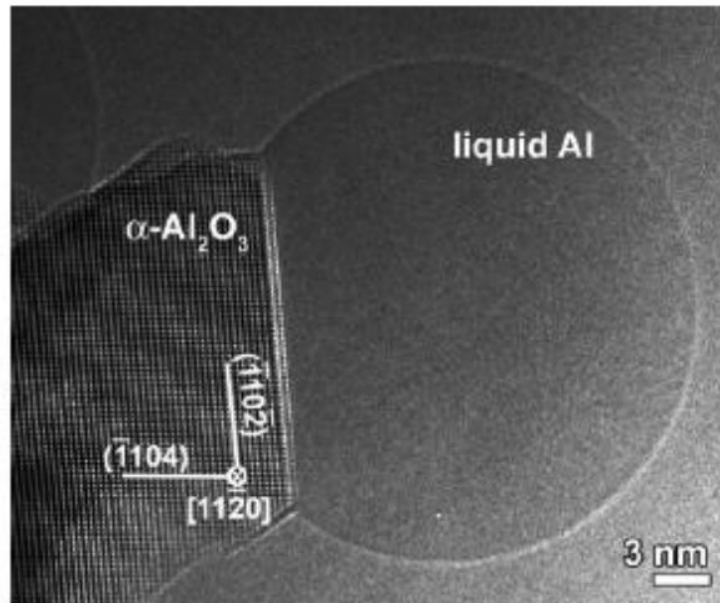
When the layer thickness reaches a critical level, the stress has to be released by, for example, misfit dislocations. In this particular moment, the strained layer becomes a strain-less solid and solidification enter the growth stage (Figure 1.20). Only a small undercooling is required to allow growth of the strained layer (epitaxial nucleation). The energy difference is necessary to give rise to a formation of the initial solid layer of a certain thickness. As described by a free growth model, further growth will lead to the formation of a new grain.



*Figure 1.20. Schematic illustration of the epitaxial nucleation model
 (a) before the growth (b) layer-by-layer growth
 (c) introduction of the misfit dislocation [after Fan, 2012].*

Very interesting experimental observations have been done by Lee and Kim in 2011. They found some ordering a liquid Al drop formed on $\alpha\text{-Al}_2\text{O}_3$ [Lee and Kim, 2011]. In Figure 1.21 we can see the liquid ordering on the interface visible through 5 ordered layers. As described by the epitaxial model for heterogeneous nucleation on potent substrates that ordering will start the nucleation and crystallisation. The picture indicates that aluminium oxide provides liquid ordering, so can be treated as potent substrate. Highly potent nucleating particles need to have a small lattice misfit and be well dispersed in the melt [Fan, 2012].

a)



b)

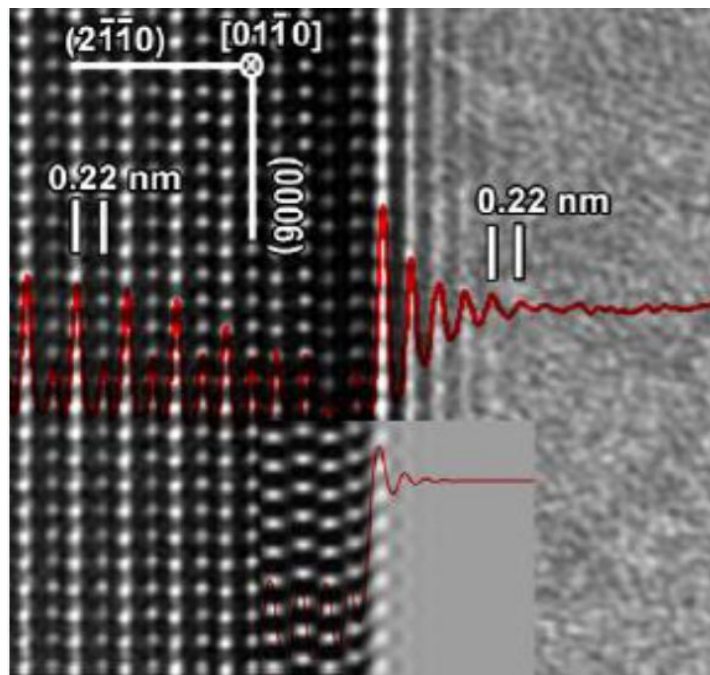


Figure 1.21. a) HRTEM images of a liquid Al drop formed on $\alpha\text{-Al}_2\text{O}_3$.
b) HRTEM image of the Al/ $\alpha\text{-Al}_2\text{O}_3$ interface. We can see also an overlay of intensity line of the atom density scan perpendicular to the interface (red line).
The inset is it result of a simulation, an image of $\alpha\text{-Al}_2\text{O}_3$ /vacuum interface [Lee and Kim, 2011].

The potency of a solid substrate in a liquid metal can be connected with the lattice misfit on the interface between the substrate and the solid phase [Merwe and Frankand, 1949 , Fan, 2011]. The lattice misfit f .is defined as:

$$f = \frac{dS-dN}{dS} \quad \text{(Equation 1.7)}$$

Where: dS – the atomic spacing along a close packed direction on a close-packed plane of the solid,
 dN – the atomic spacing along a close packed direction on a close-packed plane of the nucleating substrate.

Frequently computer simulation was done to prove that ordering exists on the interface. The simulation was done by Men and Fan [2012] and proved that in-plane ordering persisted in few atomic layers at the interface for substrates with misfit less than 3%. They found that with a further increase in the magnitude of the misfits (over 4%) only a certain in-plane atomic ordering persisted within the 1st atomic layer at the interface.

Results of such a simulation support the epitaxial model for heterogeneous nucleation on potent substrates and predicts liquid layering and in-plane ordering, as will be presented in following chapters of this work.

Well-known grain refiners have misfits equal -4.22% (TiB_2) and 0.09% (Al_3Ti). Since the calculated lattice misfit with solid Al at $660\text{ }^\circ\text{C}$ is 3.38% for $\gamma\text{-}Al_2O_3$, -0.48% for $\alpha\text{-}Al_2O_3$, and 1.41% for $MgAl_2O_4$ we can expect that those oxides are highly potent for nucleation of Al [Fan, 2011]. In the case of Mg, the calculated lattice misfit for MgO and Mg is 8.01% which seems to be larger than expected for potent substrates. Further investigation shows that experimentally measured lattice misfit in an AZ91D alloy was about 5.46% [Fan et al., 2009].

The existence of an orientation relationship between the solid Mg and the MgO substrate was demonstrated experimentally. A picture of the semi-coherent interface [Li

et al., 2011] obtained by high-resolution transmission electron microscopy (HRTEM) is the most direct evidence of heterogeneous nucleation on potent substrates (Fig. 1.22).

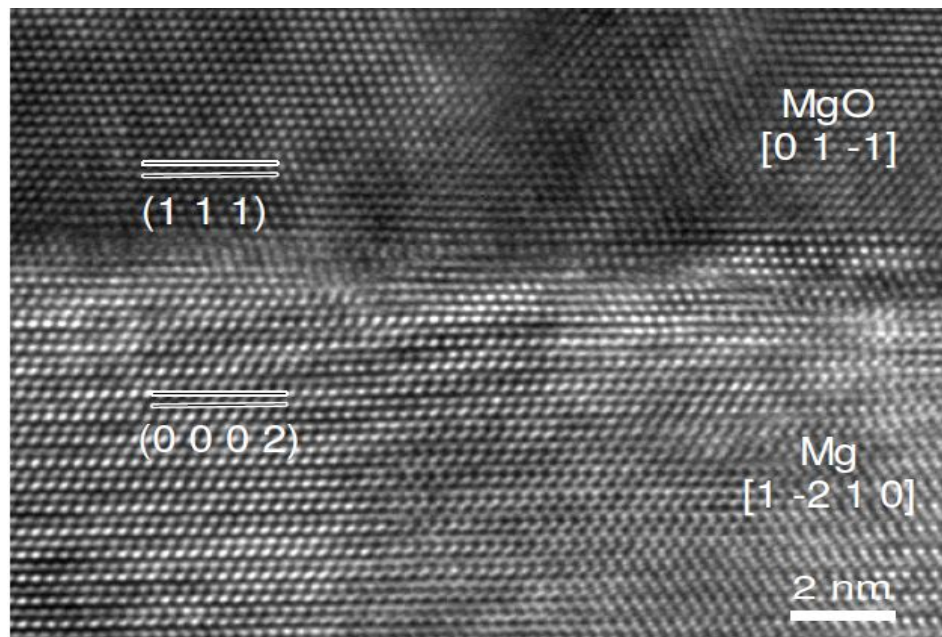


Figure 1.22. Micrograph of the semi-coherent interface between MgO and the α-Mg matrix in AZ91D alloy [Li et al., 2011].

As both, magnesium oxide and aluminium oxide seem to be very potent substrates, the following section will show some examples how dispersed oxides work as grain refiners in real alloys.

1.4. Applications of high-shear impellers.

HSMs are widely used in cosmetics, paint, food, pharmaceutical and chemical industry. It is even difficult to specify all types of industrial work where the rotor-stator mixers are applied. The main applications of the HSM include:

- liquid-liquid processing
- solid-liquid suspension
- chemical reactions

Emulsification, one of liquid-liquid processing methods, is really important in many industrial fields. Small droplets produced by shear forces in the narrow gap of the HSM are the major effect expected in a wide range of processes. The homogenisation, coagulation or emulsification is necessary to produce food, drugs or cosmetics. Thus, for rotor-stator mixers, the maximum droplet size has been an important subject of research. The process parameters, such a local power draw, can be related to this maximum size what facilitates the production process [Davies, 1987]. When the process is designed, it is understood that above some critical speed no further droplet size reduction can be expected [Thapar, 2004].

Since the batch HSMs can be applied in really wide range of processes and the flow in them is only dependent on the simple rotor-stator setup, the research is mostly based on applications of this kind of HSMs [Padron, 2005; Maa and Hsu, 1996; Adler-Nissen et al., 2004; Ouzineb et al., 2006; El-Jaby, 2008; Francis et al., 1999; Phongikaroon et al., 2001; Calabrese et al., 2002; Phongikaroon et al., 2004; Davies, 1985; Khopkar et al., 2009]. A number of in-line processes have been described and some basic process descriptions are available in the publications [Hall et al., 2011; Gingras et al., 2005; Averbukh et al., 1988; Thapar, 2004; Kevala et al., 2005; Hall et al., 2011]. The droplets breakage mechanism is not fully understood yet so researchers put a lot of effort to establish a droplet size dependence on mixing condition.

It is known that the effect of the stator geometry can play a more important role than the gap width [Padron, 2005; Francis et al., 1999; Phongikaroon et al., 2001;

Calabrese et al., 2002]. The micro-scale of droplets size suggests the existence of multiple breakage mechanisms [Francis et al., 1999; Calabrese et al., 2002].

Solid-liquid suspension applications are probably the most important as possibilities of HSMs are wider than other commonly used techniques. Powders are mixed with fluids in a chemical, pharmaceutical and food industry. High-shear forces provide the effective dispersion, even a nano-materials dispersion has been considered. The agglomerates breakup occurs through different mechanisms depending on the relative magnitude of the bonds between particles. Thus, the shear ratio of HSMs used as dispersers is kept on a high level as application conditions can differ. High-shear forces are responsible for the erosion of big agglomerates which results in the formation smaller and fairly equisized agglomerates. It is possible to use HSMs to provide shattering. In this process, large agglomerates are broken up into lots of small particles without the intermediate sizes [Özcan-Tas et al., 2009]. The solid-liquid suspension processing by HSMs has been widely used in pharmaceutical industry to improve a particle-size reduction of active pharmaceutical ingredients through the high-shear wet milling. It can be also used to improve fermentation recovery processes by rapid breakage of biological cells.

Another typical application is using HSMs to intensify chemical reactions. If reactions have relatively slow mass transfer rates [Patterson et al., 2004] the HS mixing can improve both, the mass and the heat transfer. Fine chemicals and intermediates production with using HSMs have been patented, for example, chlorobenzene [Hassan et al., 2010], nano-CaCO₃ [Guang-wen et al., 2005], etc.

It is impossible to describe all applications of HSMs in industries or laboratories. As this mechanical tool has been found so useful and yet there exists a lack of information about physical basics which stand behind the HSM process, it is important to find more information about them.

1.5. Alloy structure improvement by shearing processing.

There is a number of techniques developed to remove oxide films from the melt. The most popular are following: sedimentation, fluxing, degassing and filtration. To achieve the best results they are often applied simultaneously. The removal of films from aluminium melts has been a key research field for many years but the improvement of cleanliness is still an open problem [Cao and Campbell, 2002]. Much work has been done to remove existing oxide films as their formulation is unavoidable. Instead of removing harmful films from liquid metals a new technology developed by BCAST suggests breaking films into small fragments or particles.

The melt mixing is not a completely new idea as about 1960 started and later has been developed aluminium-alumina stirring with an impeller [Ray, 1993]. To improve the mixing effects reinforcement particles are added. The vortex created during stirring helps to suck externally added particles in and distribute them within the liquid metal [Harnby et al., 1997]. It has been reported that stirring causes the entrapment of air bubbles and other impurities from the surface of the melt. On the other hand, the reinforcement particles tend to agglomerate and settle down. It is possible that the reinforcement particles will react with the melt. Finally, macroscopic casting defects such as porosity and inclusions are present in the product [Rohatgi et al., 2005]. As this technology does not achieve a uniform distribution of particles, it has not been used in commercial applications. BCAST proposed to solve this problem by using a high-shear mixer instead of typical stirrers. This technique provides more benefits than conventional stirring. In past years, the solidification process has been better described and there is a reason to believe in the positive role of dispersed oxides (see the previous section). Thus, a high-shear device can be used to disperse oxides present in the melt with additional effects such as [Li et al., 2011]:

1. Increased fluidity of melt, hence an easier casting process with reduced energy consumption.
2. Reduced chances of large oxide films presence and inclusions in the castings, and improved ductility of castings.

3. Increased number density of potential nucleating particles with enhanced heterogeneous nucleation for grain refinement.
4. Lesser harmful effects of oxides and inclusions and increased allowed the content of scrap metals to be used.
5. Accelerated chemical reactions or phase transformations due to enhanced kinetic conditions for mass transport in the melt.

The newly developed technique is named MCAST-RS (Metal Casting Advanced Shear Technology – Rotor-Stator) or just HS (High Shear). Previously term MCAST has been used for a high-shear mixing using a twin-screw mechanism [Scamans et al., 2012].

In a conventional stir casting, we have just a rotor impeller which mixes all volume of liquid. At contrast, in the high-shear process, we have a rotor impeller surrounded by a stator with holes, which significantly increases the speed of liquid mixing between the rotor and the stator and introduces shear. In this technology, we do not use any additives. It has been predicted [Fan, 2011] and shown [Tzamtzis et al., 2011] that dispersion of naturally occurring oxides can act as heterogeneous nucleation sites and improve the cast product quality. A number of MCAST-RS effects have been observed and described by the BCAST team in recent years.

The mechanical properties of metallic alloys are highly affected by the grain size. This is based on the Hall-Petch equation (Eq. 1.8) [Hall, 1951; Petch, 1953]:

$$\sigma_y = \sigma_0 + \frac{k_y}{\sqrt{d}} \quad \text{(Equation 1.8)}$$

Where: σ_y – the yield stress, σ_0 – the resistance of the lattice to dislocation motion,
 k_y – the strengthening coefficient (a constant specific to each material, equal
 $\sim 1.4 \text{ MPa}\cdot\text{mm}^{1/2}$ for Aluminium [Armstrong, 2013]),
 d – the average grain diameter.

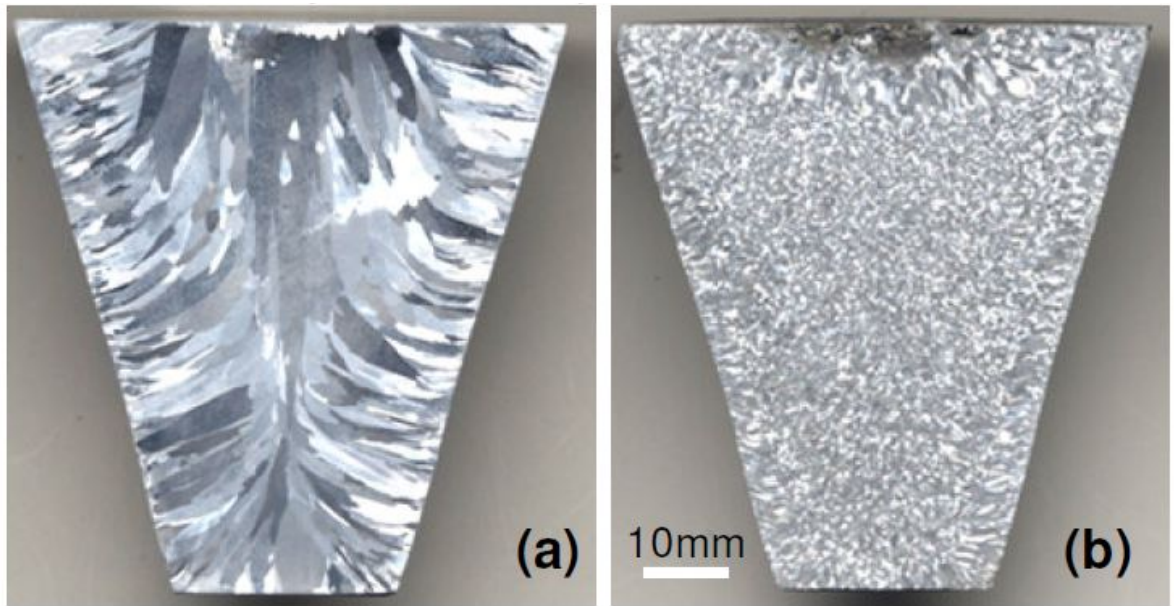


Figure.1.23. Macrographs of the longitudinal sections of the TP-1 samples of CP Al showing effects of melt shearing (a) non-sheared sample (b) sheared sample [Li et al., 2012b].

With intensive melt shearing, the grain size (measured conventionally in cross-sections of samples as shown in Fig. 1.23) of the CP Al was decreased from 1100 μm without shearing to 379 μm with shearing as given by authors, what means that the grain size decreases more than 65%.

If we look closer at the microstructures of an aluminium alloy we can observe reduction in grain sizes more clearly [Li et al., 2011]. Prepared samples were sand cast. Sand casting process requires a long time for cooling down of the melt, so grains observed afterwards can be really big and coarse. The experiment made by Li et al. [2011], prove that even in slow cooling processes, which allows dendritic structures to grow up (Figure 1.24 a), MCAST-RS results in dramatic reduction of grain sizes (Figure 1.24 b). The experiment has been done on a standard Al-Si7Mg alloy.

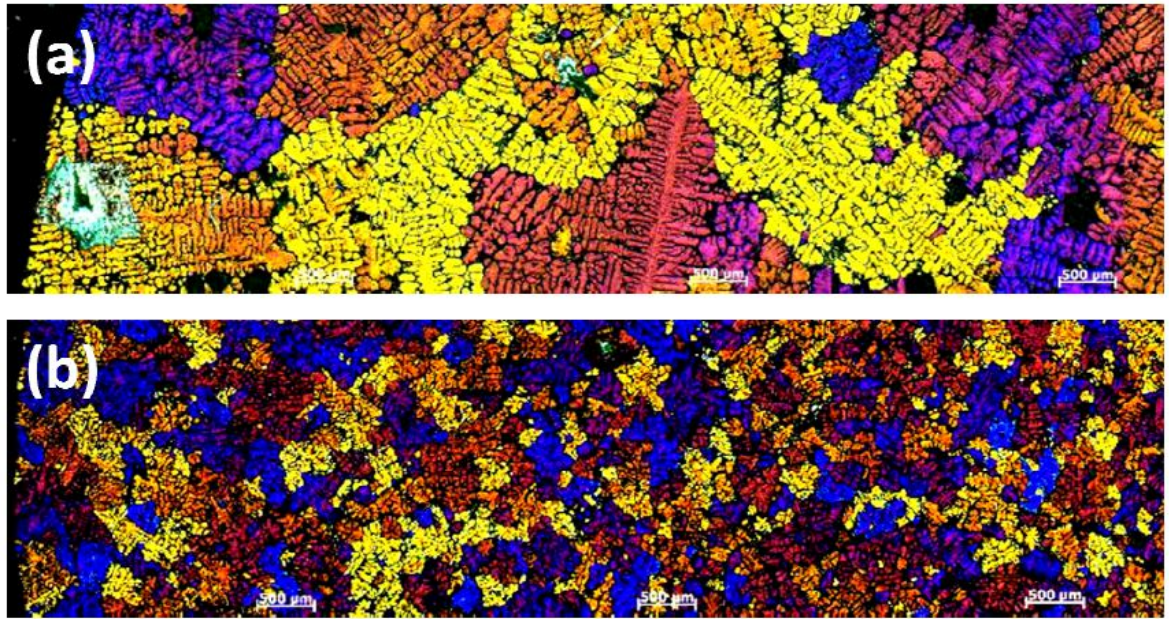
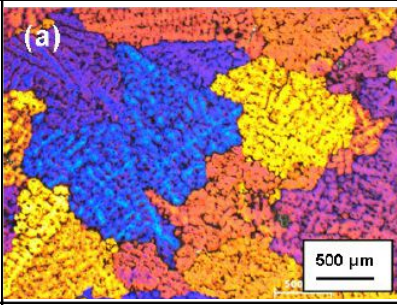
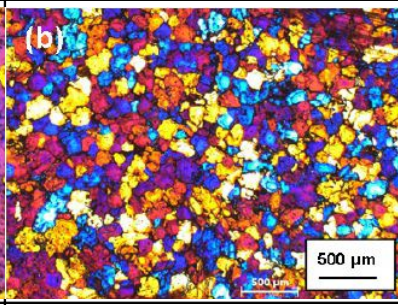
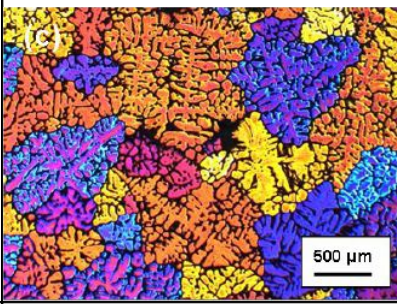
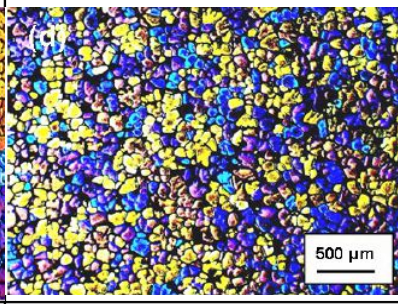
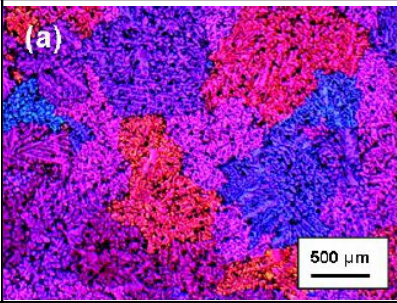
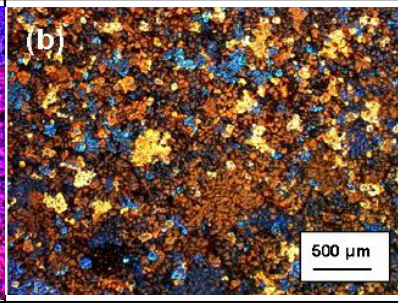
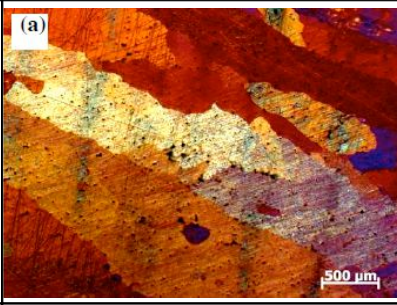
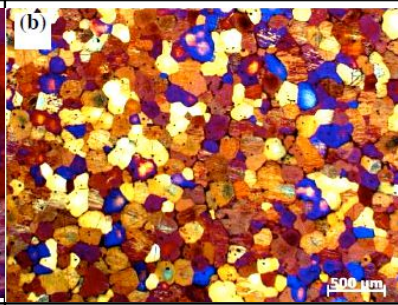

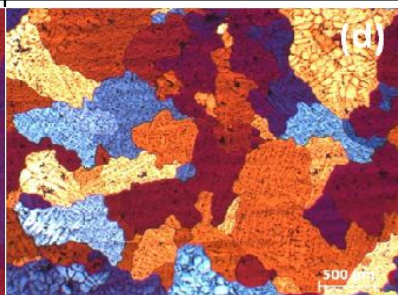
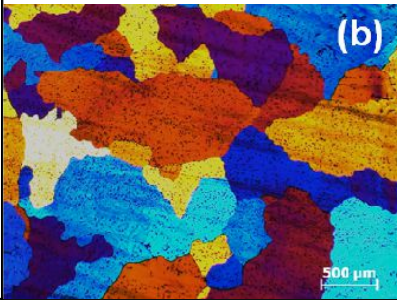
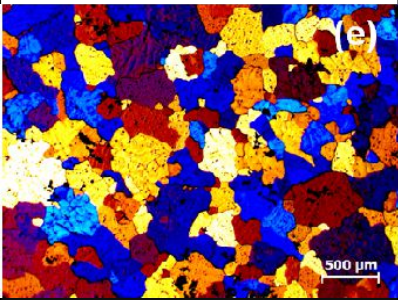
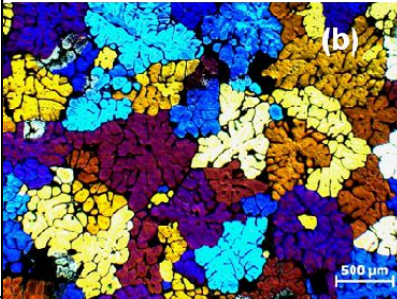
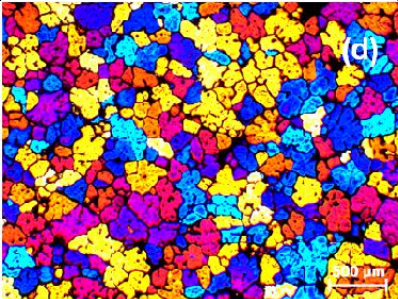
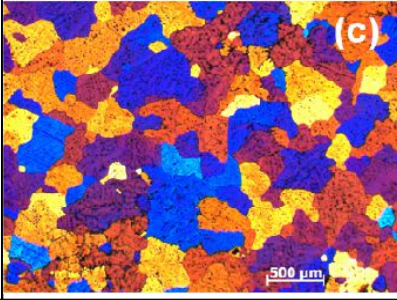
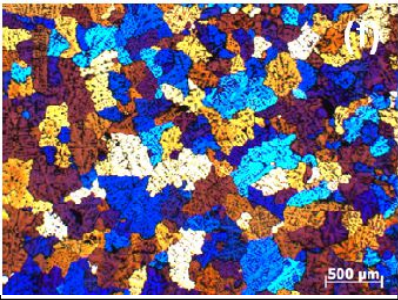


Figure 1.24. Microstructures of sand cast LM25 components (a) without shearing, (b) with intensive melt shearing [Li et al., 2011].

More results are given in Table 1.2 for several aluminium and magnesium alloys without and after shearing. All samples were poured into a TP-1 mould. Reference samples usually were air cooled to the desired pouring temperature to make samples comparable. More information about the specific procedure can be found in the references given in the table.

Table 1.2. Microstructures of different alloys cast without and after shearing.

Material; casting temperature	Without shearing	After shearing	Ref.
Aluminium alloy A6082; 730°C	 Micrograph (a) shows the microstructure of Al6082 alloy cast without shearing. It features large, irregularly shaped grains with a coarse, multi-colored appearance. A scale bar of 500 μm is visible in the bottom right corner.	 Micrograph (b) shows the microstructure of Al6082 alloy after shearing. The grains are significantly smaller and more uniform in size compared to the non-sheared sample. A scale bar of 500 μm is visible in the bottom right corner.	[Patel et al. 2013]
Aluminium alloy 7075; 700°C	 Micrograph (c) shows the microstructure of Al7075 alloy cast without shearing. It displays a coarse, multi-colored grain structure. A scale bar of 500 μm is visible in the bottom right corner.	 Micrograph (d) shows the microstructure of Al7075 alloy after shearing. The grains are much finer and more uniform. A scale bar of 500 μm is visible in the bottom right corner.	[Patel et al. 2013]
Mg alloy AZ91D; 650°C	 Micrograph (a) shows the microstructure of AZ91D alloy cast without shearing. It exhibits a coarse, multi-colored grain structure. A scale bar of 500 μm is visible in the bottom right corner.	 Micrograph (b) shows the microstructure of AZ91D alloy after shearing. The grains are significantly smaller and more uniform. A scale bar of 500 μm is visible in the bottom right corner.	[Patel et al. 2013]
AZ31 Mg- alloy; 680°C	 Micrograph (a) shows the microstructure of AZ31 Mg alloy cast without shearing. It features a coarse, multi-colored grain structure. A scale bar of 500 μm is visible in the bottom right corner.	 Micrograph (b) shows the microstructure of AZ31 Mg alloy after shearing. The grains are much finer and more uniform. A scale bar of 500 μm is visible in the bottom right corner.	[Zuo et al., 2012]
Al-0.2Mg; 700°C (*)	 Micrograph (a) shows the microstructure of Al-0.2Mg alloy cast without shearing. It displays a coarse, multi-colored grain structure. A scale bar of 500 μm is visible in the bottom right corner.	 Micrograph (d) shows the microstructure of Al-0.2Mg alloy after shearing. The grains are significantly smaller and more uniform. A scale bar of 500 μm is visible in the bottom right corner.	[Li et al., 2012b]

<p>Al-0.7Mg; 700°C (*)</p>	 <p>(b)</p> <p>500 μm</p>	 <p>(e)</p> <p>500 μm</p>	<p>[Li et al., 2012b]</p>
<p>Al-20Zn-0.05Ti; 650 °C (*)</p>	 <p>(b)</p> <p>500 μm</p>	 <p>(d)</p> <p>500 μm</p>	<p>[Li et al., 2011b]</p>
<p>Al-5.0Mg; 700°C (*)</p>	 <p>(c)</p> <p>500 μm</p>	 <p>(f)</p> <p>500 μm</p>	<p>[Li et al., 2012b]</p>

(*) Shearing by the twin-screw unit, using the similar rules as basic rotor stator unit, but with more complicated design (higher shear rates). Presented micrographs show that the applied shear decreases the grain sizes.

The example of the Al-5.0Mg [Li et al., 2012b] alloy shows that not always we can observe the reduction in grain sizes. Authors explain that if oxide particles are naturally dispersed into individual particles, melt shearing by HS device has the only small effect on the grain refinement [Li et al., 2012b]. Even if grain decrease is smaller than in other cases, we can expect to disperse of all impurities in the melt which will improve the alloy quality too. The positive role of shear treatment for an Al-Mg alloy with high added impurity content has been reported and is a proof that impurities are sheared too [Kumar et al., 2011] made the conclusion that high shear melt conditioning of an AA5754 alloy, with deliberate additions of iron, silicon, and copper, modifies the distribution of intermetallic particles in the as-cast ingot. They advised the MCAST-RS to increase the tolerance of AlMgMn alloys to impurities typical of those remelt from post-consumer scrap. To compare grain size reduction we can refer to past publications.

Table 1.3 gives some overview how significant can be the reduction of grain sizes

after MCAST-RS alloy treatment.

Table 1.3. Grain size reduction after MCAST-RS alloy treatment.

Material	Casting temperature	Grain size (without shearing)	Grain size (after shearing)	Grain size differences (*)	References
Mg alloy AZ91D	650°C	550 µm	170 µm	69%	[Patel et al., 2013]
Mg alloy AZ91D	605°C	180 µm	90 µm	50%	[Patel et al., 2013]
AZ31 Mg-alloy	680°C	few mm (min 2 mm)	200 µm	Min 90%	[Zuo et al., 2012]
Al-Mg alloys (**)	700°C	1115±134 µm	377±01 µm	66%	[Li et al., 2012b]
Al-7 Mg alloy (**)	700°C	240 ±44 µm	207±30 µm	no difference	[Li et al., 2012b]
Al-20Zn-0.05Ti (**)	650°C	620 µm	260 µm	58%	[Li et al., 2011a]

(*) Relatively, differences between grain sizes without and with shearing divided by the initial value (without shearing). (

(**) Shearing by the twin-screw unit, using the similar rules as basic rotor stator unit, but with more complicated design (higher shear rates). Presented micrographs show that the applied shear decreases the grain sizes.

As we can see in many causes the grain size reduction by an order of magnitude and occurs for different types of aluminium and magnesium alloys. As described by Li et al., [2012 b], grain refining of Al-Mg alloys with high Mg content (&% on the picture) by shearing treatment is not so effective since oxide particles have been naturally dispersed into individual particles by the increased Mg content.

The grain size dependence on temperature of casting and shearing has been presented in Figure 1.25. The average grain size of CP Al is shown as a function of casting temperature (or melt superheat) for sheared and non-sheared TP-1 samples. In

the case of non-sheared samples (Fig. 1.25 a) the grain size is at the millimetre level and increases with increasing melt superheat, then tends to decrease slightly. For sheared samples significant grain refinement can be observed and there is a complex grain size dependence on melt superheat (Fig. 1.25 b). The grain size increases initially with the increase in shearing temperature and decreases sharply at 740 °C. Concerning the sharp change in the grain size of alpha aluminium phase at about 740 °C, authors believe it is most likely to be due to a transition from γ alumina to α alumina at around this temperature. α alumina possesses smaller lattice misfit with aluminium compared with γ alumina based on their calculation [Li et al., 2012 b; private communication with H.T. Li]. Further increase of melt superheat results in the increase of grain sizes at a slower pace .

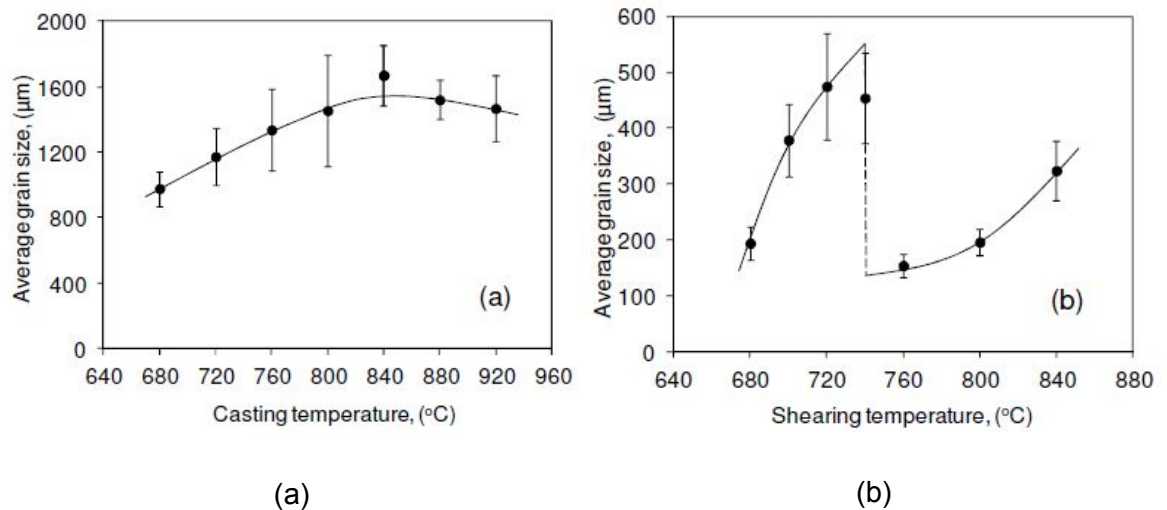


Figure 1.25. The average grain size of CP Al as a function of processing temperature [Li et al., 2011], (a) without intensive melt shearing, (b) with intensive melt shearing.

From Figure 1.25, we can conclude that independently on the shearing temperature the grain size is significantly reduced. The grain size refinement has been observed with different Al and Mg alloys processed in different ways, by the TP-1 procedure or by sand casting etc. Thus, it is necessary to understand and improve this technology with respect to application to liquid metal treatment. It is the main reason of this work which is focused on process explanation and development.

Chapter 2. Methods.

2.1. Physical modelling.

In some specific situations, the process parameters cannot be checked experimentally or the experimental procedure is difficult. In addition to a computer modelling, it is possible to mimic the process parameters in another physical setup. This procedure is called the physical modelling.

Liquid aluminium and its alloys are not optically transparent so direct observations of inside flow are impossible. Thus, to observe the flow of liquid around the HSM the model situation with a transparent fluid has been used in presented research. Basically, the setup consists the HSM, the working fluid and the tracing substance. In this section, the used methodology is described, starting from the types of used mixers (HSMs).

2.1.1. HSMs setup equipment.

The used mixer was Silverson L5M Laboratory Mixer. The motor has a power 750W and a nominal maximum speed of 8000 rpm (6000 rpm under full load). Figure 2.1 presents the dimensions of the HSM mixer setup. Used vessels were carefully chosen with respect to the setup dimensions given in Table 2.1.

Table 2.1. Dimensions of HSM setup (see Fig. 2.1).

Dimensions	A	B	C	D (max height)	E (min height)
Size [cm]	94	30	51	33	3

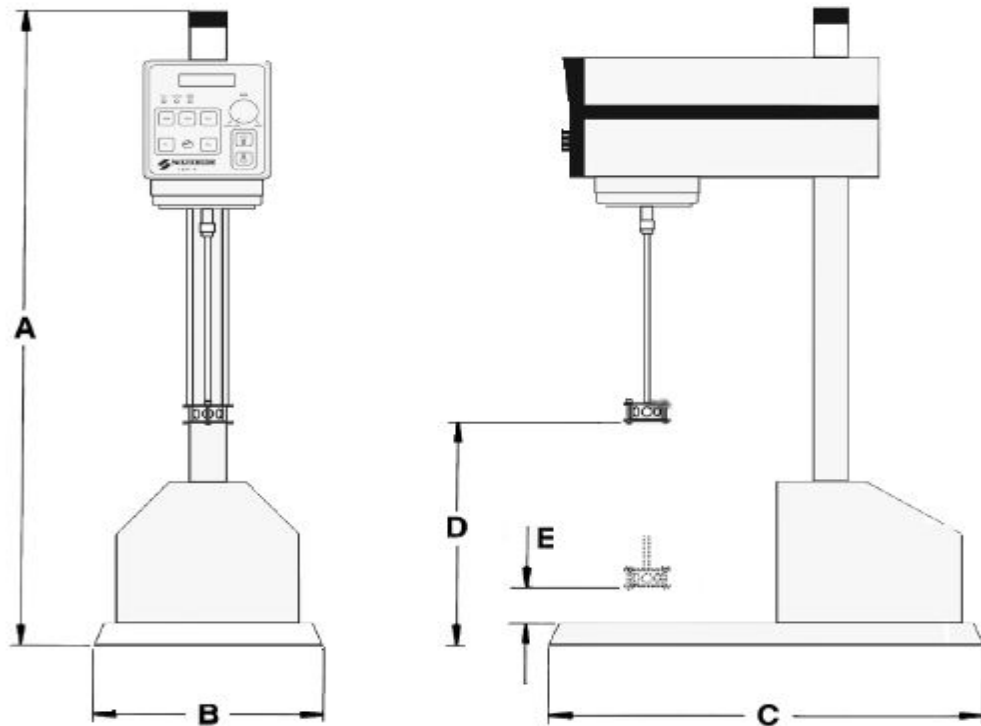


Figure 2.1. HSM setup.

For physical simulation purposes, two main impellers have been used. The first impeller has the diameter about 32 mm (the standard head). We used commercial Silverson stators. The specific gap between a rotor and the stator is 0.6 mm. Second mixing head, more similar in shape to those used by BCAST laboratory, has the diameter about 25 mm.

Exact sizes of Silverson heads:

- 1) Standard head: inner diameter 1.25" (31.75 mm), outer diameter 1.375" (34.925 mm), rotor diameter 1.23" (31.242 mm).
- 2) Tubular head: inner diameter 0.865" (21.717 mm), outer diameter 0.995" (25.273 mm), rotor diameter 0.852" (21.6408 mm).

With the standard impeller, original stators from Silverson have been used (compare Table 1.1). In experiments the following stators have been checked according to basic parameters important in liquid metal processing:

- General Purpose Disintegrating Head.
- Square Hole High Shear Screen™ .
- Emulsor Screen.

The optimal stator from those presented above has been chosen for further research. The first criterion it was an increased probability of turbulences and the Square Hole HS Screen has been found to be the best design from presented above. The square holes head was taken as a first approximation for a design improvement. Next changes of design were done with respect to the ceramic head design used in BCAST and to the actual needs. The smaller rotor (about 22 mm) was chosen for modelling. Specially designated stators similar to both, Silverson Square Hole HS Screen and ceramic head used in BCAST, were ordered.

The smaller rotor-stator impellers provide weaker but the same flow pattern as those with bigger diameters if the geometrical similarity is kept. The smaller impeller is giving more possibilities in modelling, to observe the flow up to a higher level of agitation in the vessel, as the tank dimensions are bordered. It was the main reason for our choice.

To choose and improve the stator properties special conditions present in melt have to be considered. High-shear heads are commonly made from steel. Since the aluminium and magnesium alloys are chemically active and aggressive for many materials, the head from steel after processing of liquid aluminium is eroded and cannot be used again. To solve this problem, the BCAST team is using specially designated ceramic heads for processing liquid Al.

For the same reason – high aggressive properties of liquid aluminium, the HSM head for metal processing purposes should be so simple in shape as possible. The ceramic head of BCAST is similar to the tubular assembly of Silverson without any unnecessary mounting parts which will be most exposed to erosion resulting in the HSM damage. To compare the mounting system design of tubular and typical mixing head both impellers (Silverson assembly) are shown in Figure 2.2.

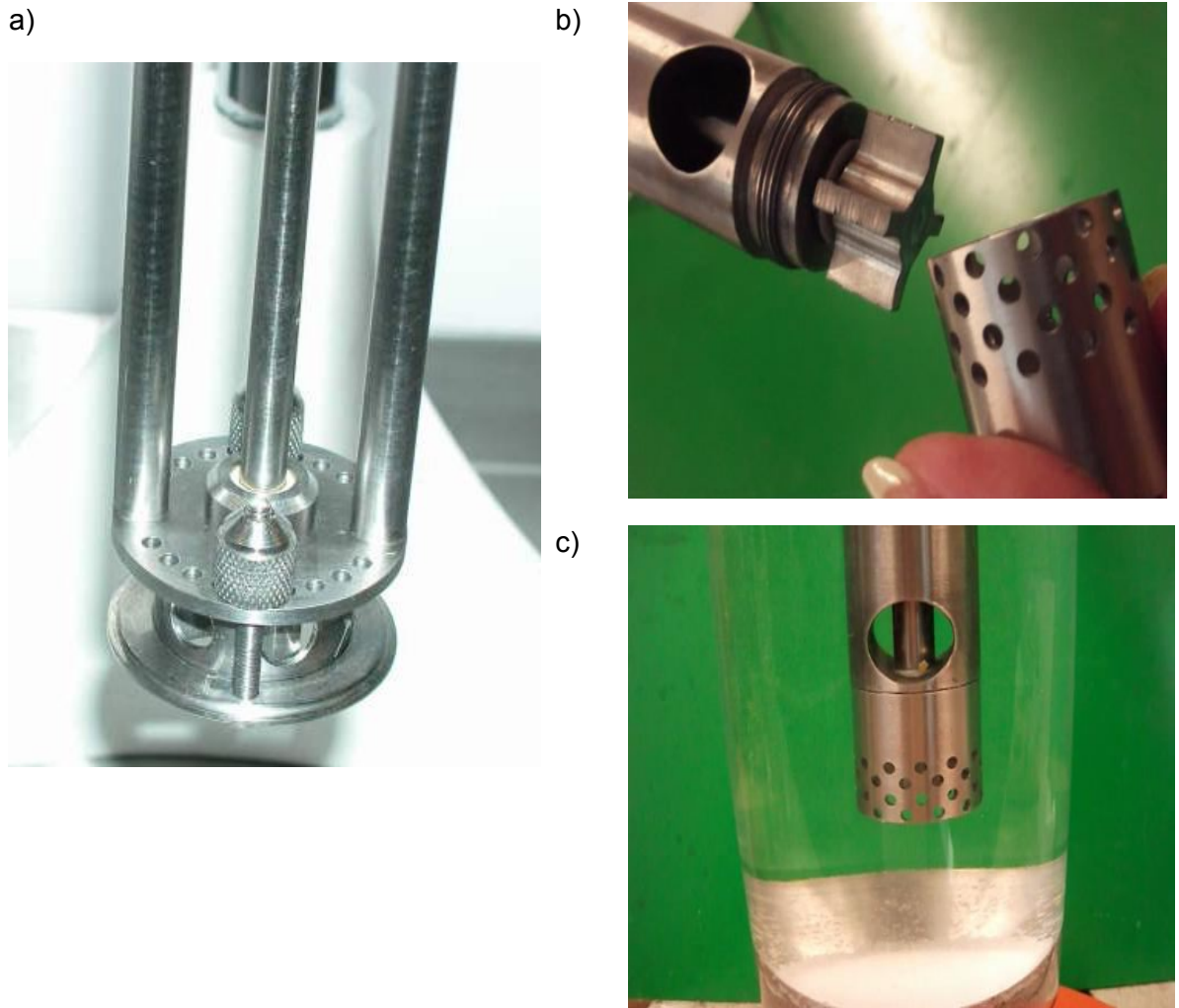
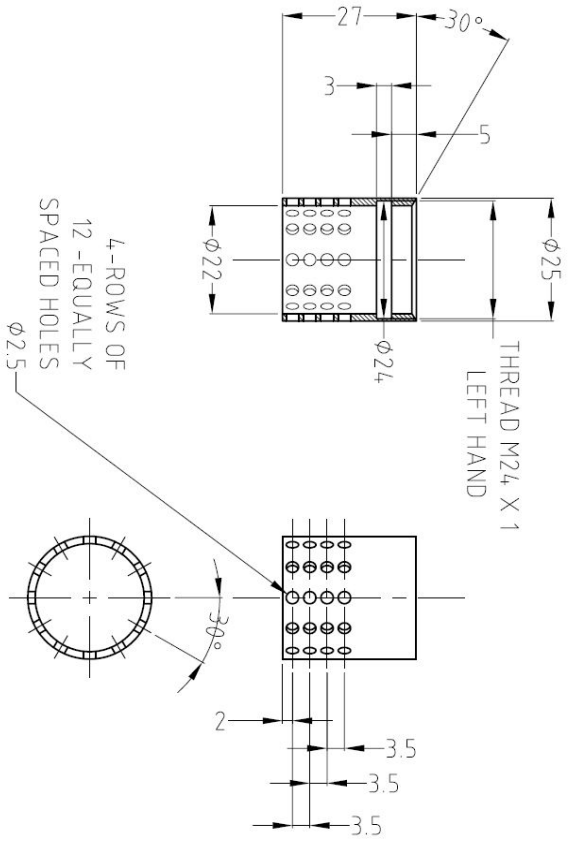


Figure 2.2. a) Standard Silverson head, b) simplified tubular head (Silverson rotor) before mounting, c) mounted tubular head (crossH stator).

Figure 2.2 b and c show the stator designated for this thesis purpose. The Silverson LM5 mixer has been used with standard head and with the smaller rotor (22 mm) mounted with specially prepared stators (as mentioned before). The specification of new stators is shown in Figures 2.3, 2.4 and 2.5. The first stator (RH) with round-holes is designated to repeat a design used by BCAST in liquid metal processing (Figure 2.3). The second stator (SqH) has a similar design except of the shape of holes which are square-shaped (Figure 2.4). The last one stator has other holes arrangement (in cross lines) then used before and round-holes (CrossH, Figure 2.5).

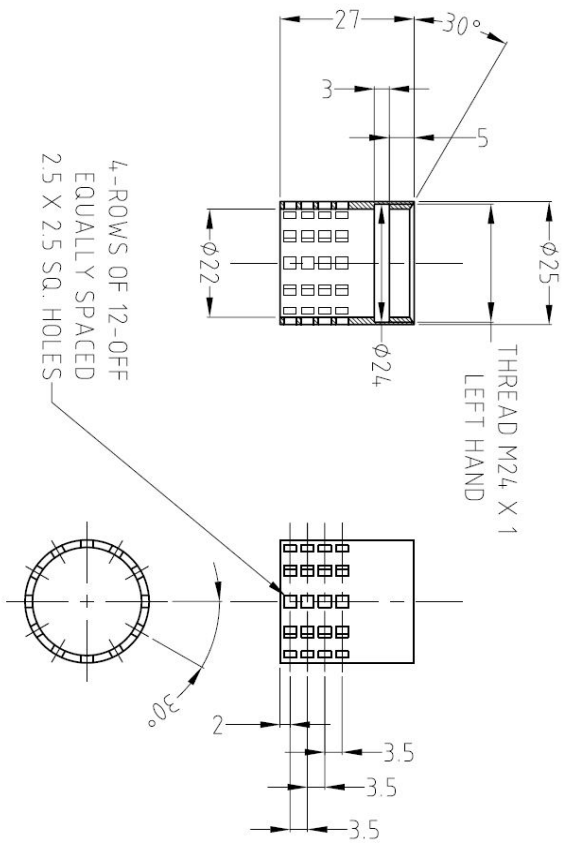
3rd ANGLE



<p>Zyomax Ltd</p> <p>THE COPYRIGHT IN THIS DRAWING & THE DESIGN SHOWN HEREIN BELONGS EXCLUSIVELY TO ZYOMAX LTD. NO DISCLOSURE OF ITS CONTENTS WITH ANY THIRD PARTY OR REPRODUCTION IN WHOLE OR IN PART IS ALLOWED WITHOUT PRIOR WRITTEN CONSENT</p>		<p>MACHINE FINISH UNLESS STATED OTHERWISE</p>		<p>MATERIAL</p>		<p>STAINLESS STEEL</p>		<p>TITLE</p>		<p>SCALE</p>		<p>DATE</p>		<p>ISSUE</p>	
<p>www.zyomax.com</p>		<p>16</p>		<p>STAINLESS STEEL</p>		<p>STATOR (Ø2.5 X 48 STR.)</p> <p>LAB HIGH SHEAR MIXER</p>		<p>1:1</p>		<p>10.04.14</p>		<p>1</p>			
<p>Zyomax</p>		<p>16</p>		<p>STAINLESS STEEL</p>		<p>STATOR (Ø2.5 X 48 STR.)</p> <p>LAB HIGH SHEAR MIXER</p>		<p>1:1</p>		<p>10.04.14</p>		<p>1</p>			
<p>www.zyomax.com</p>		<p>16</p>		<p>STAINLESS STEEL</p>		<p>STATOR (Ø2.5 X 48 STR.)</p> <p>LAB HIGH SHEAR MIXER</p>		<p>1:1</p>		<p>10.04.14</p>		<p>1</p>			

Figure 2.3. The RH stator.

3rd ANGLE 




		www.zyomax.com	
TITLE STATOR (2.5 SQ. X 48 STR.) LAB HIGH SHEAR MIXER		A4	
SCALE 1:1	Drawn BEC	Drawing No. LHSM/005/1	Issue 1
	Date 10.04.14		
MACHINE FINISH UNLESS STATED OTHERWISE	MATERIAL STAINLESS STEEL		
© ZYOMAX Ltd THE COPYRIGHT IN THE DRAWING & THE DESIGN IS RESERVED BY ZYOMAX LTD. ALL RIGHTS ARE RESERVED. NO PARTS OR REPRODUCTIONS IN WHOLE OR PART MAY BE MADE WITHOUT PRIOR WRITTEN CONSENT.			

Figure 2.4. The SqH stator.

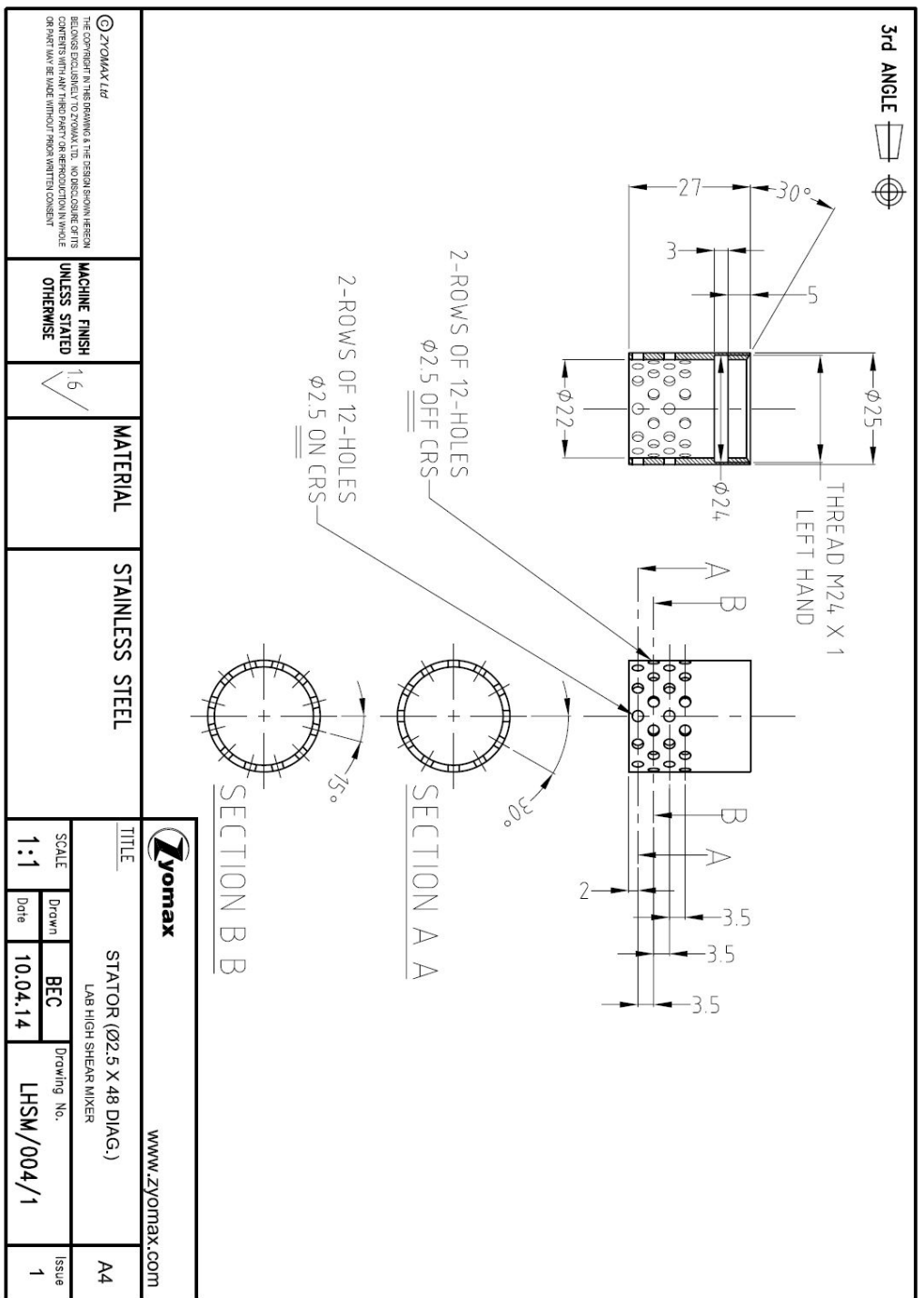


Figure 2.5. The crossH stator.

The head for experiments was immersed into a working fluid and flow parameters were checked. During experiments, different sizes of vessels were used. As in metal processing, it is difficult to use baffled vessels (crucibles) so all experiments have been done in unbaffled vessels. The cylindrical vessel with diameter 84 mm has been used to observe turbulences as the volume of water in the vessel should be fully agitated. The bottom of the vessel was rounded in shape, similar to commercially used crucibles.

To observe the mixing around the head without an influence of vessel walls (no scattered or reflected flow) the special tank was designed. A transparent, glass tank was ordered to experiments with sizes 260 mm (wide) on 260 mm (high) and 800 mm (length). The 260 mm width is the maximum (Figure 2.1, size $\frac{1}{2}$ C) possible to place in the mixer setup. The water level was kept on the 200 mm from the bottom. In this case, the water volume was about 40 l. It is much more than advised by Silverson, as maximum volume mixed by this setup can be 12 l according to their website. In this case, we were sure that the volume will be not fully agitated and the flow will be moved freely without reflections from walls (at least with smaller values of a rotational speed).

Each time the impeller was immersed to the position between 30 to 50 mm above the bottom of the tank for the SiO_2 model (description of the model can be found in Section 2.1.3). In the case of the full pseudo-cavern visualisation by an argon gas model (description of the model can be found in Section 2.1.4), the head was placed high enough to observe all effect. The position of the head was slightly off-centre to avoid unnecessary vortexing. The pictures or movies were taken with the Fuji digital camera and by the PIV system, which is described in the next section.

2.1.2. Flow recording (PIV).

Particle image velocimetry [PIV] is a very useful technique which allows velocity measurements over an entire two-dimensional plane. As the tool which gives possibilities to measure flow velocities without disturbing the flow, it is perfect for exploring flow velocities in research and development applications. Point measurement tools (for example popular laser Doppler velocimeters) use an invasive probe. PIV relies on sequential images of visible features within the flow, which is not invasive for the flow behaviour. To improve visibility fluid flows are seeded with particles that follow the fluid motion. To avoid alteration spherical particles are used, usually coated to reflect laser light. Particles are illuminated by laser sheet in the region of interest and scattered light produce tracer field for image capture (Figure 2.6), [Raffel et al., 2007].

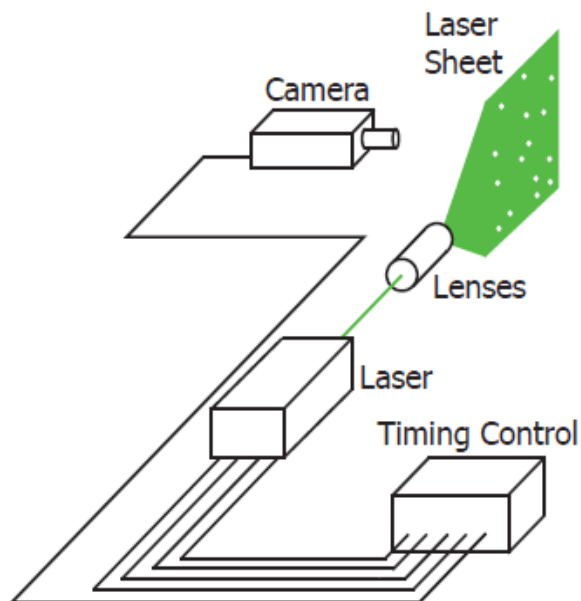


Figure 2.6. PIV setup consists of a laser and a camera. Produced laser sheet illuminates tracing particles in the observed flow. The camera captures a sequence of images (www.berkeleynucleonics.com).

The sequence of images is captured and the local velocity is determined statistically. The clue to effective capturing is to find the best value of the separation time with respect to flow velocities. Separation times must be short enough to record flow even with high velocities. It is achieved by using two laser pulses which are captured by a high-speed camera. The same visible features in each image have to be identifiable despite the displacement. From the sequential images of these tracer fields, the velocity of the fluid flow can be calculated using the known separation time and measured displacement (Figure 2.7).

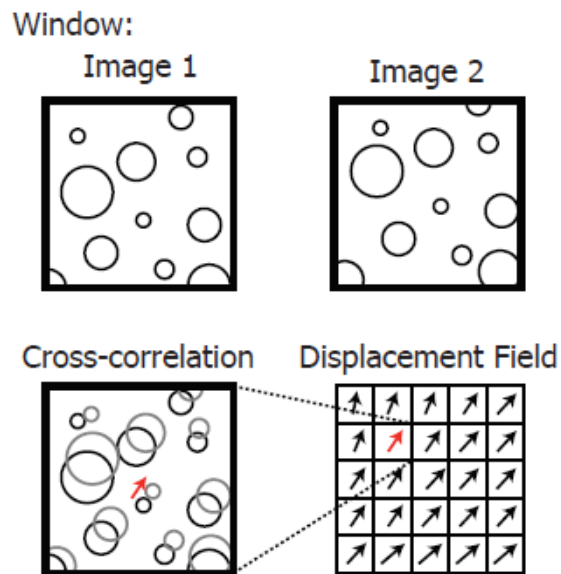


Figure 2.7. Two recorded pictures are cross-correlated to find the displacement values in each interrogation area. The displacement field is produced (www.berkeleyneuronics.com).

Statistical determination of displacement is done by dividing each image into a large number of subsections named interrogation areas and a cross-correlation of them. As the effect, the signal peak is generated indicating the average particle displacement. The calculated mean displacement is divided by the separation time to calculate a local mean velocity. In effect, the velocity field is given which usually needs further post-processing to filter the results. Velocity vector field and fluid vortices visualisations (example is shown in Figure 2.8) can be presented on graphs which are the base for the analyses of flow motion [Raffel et al., 2007].

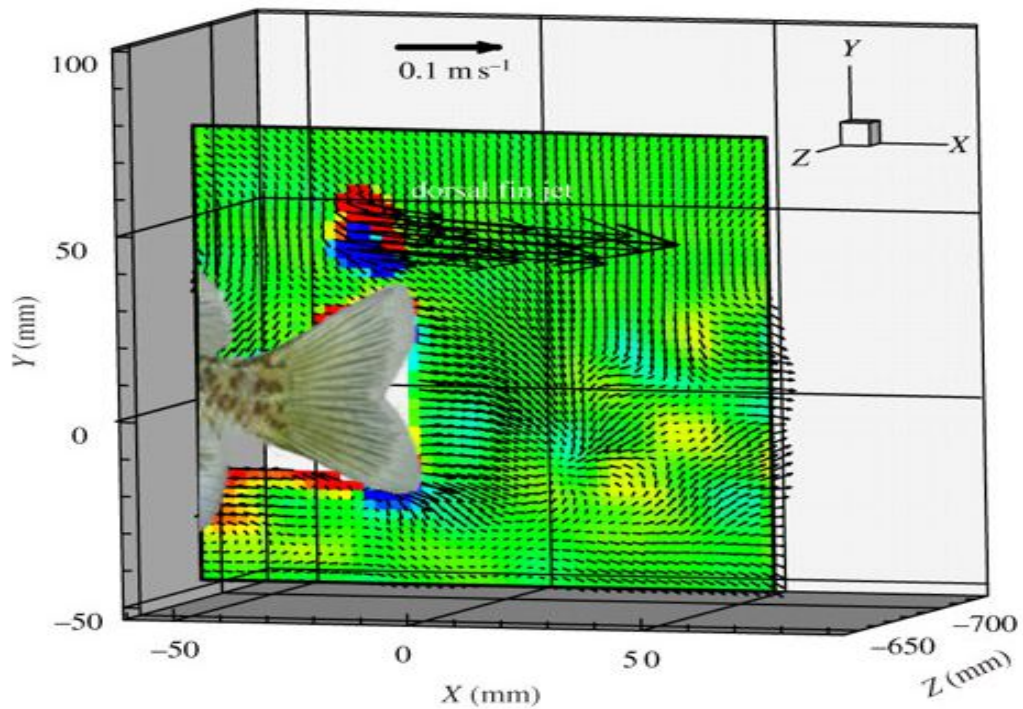


Figure 2.8. Instantaneous wake visualisation of vortices produced by the symmetrical tail of a freely swimming fish. The velocities vector are shown against vortices visualised by colours. It is a new approach in biological science which shows that volumetric imaging of biologically generated flow patterns can reveal new features of locomotor dynamics and provides an avenue for future investigations of the diversity of fish swimming patterns and their hydrodynamic consequences [Brook et al., 2011].

Velocity field measurements has been made with an TSI PIV system with high resolution. The system was loaned courtesy of EPSRC Engineering Instrument Pool and consisted of:

- 1) High Repetition Rate Nd:YAG laser; high power (120mJ), pulsed.
- 2) High Frame Rate CMOS camera Photron APX which provides full mega pixel resolution images at frame rates up to 3,000 frames per second (fps).
- 3) INSIGHT™ 4G Data Acquisition, Analysis and Display Software Package.
- 4) TecPlot 10 software for data display and analysis (with TSI Plot PIV add on).
- 5) Light sheet optics and the optical filter.
- 6) LaserPulse™ Model 610036 Synchronizer.

The water was seeded with TSI 8-12 μm hollow glass spheres [www.tsi.com] and scanned by the laser light sheet (Figure 2.9). Laser light sheet has to be placed just before the head of HSM to avoid scattering of light from the metal stator and shaft (Figure 2.10).

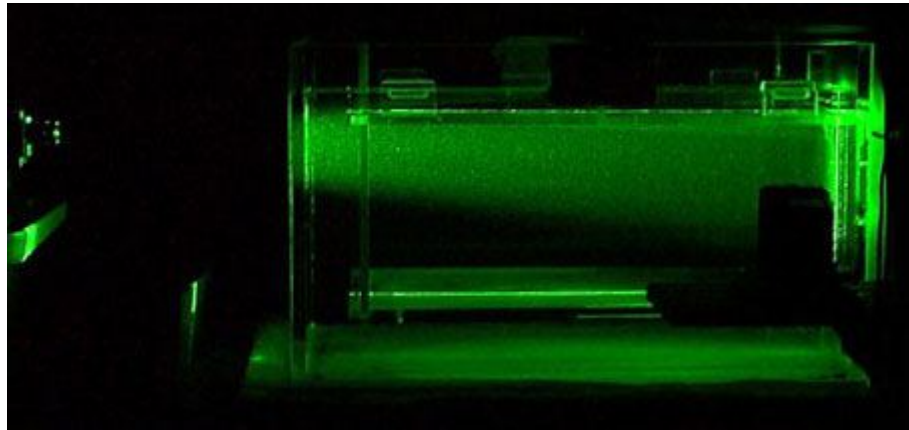


Figure 2.9. The laser sheet in a tank, picture taken in a dark room.

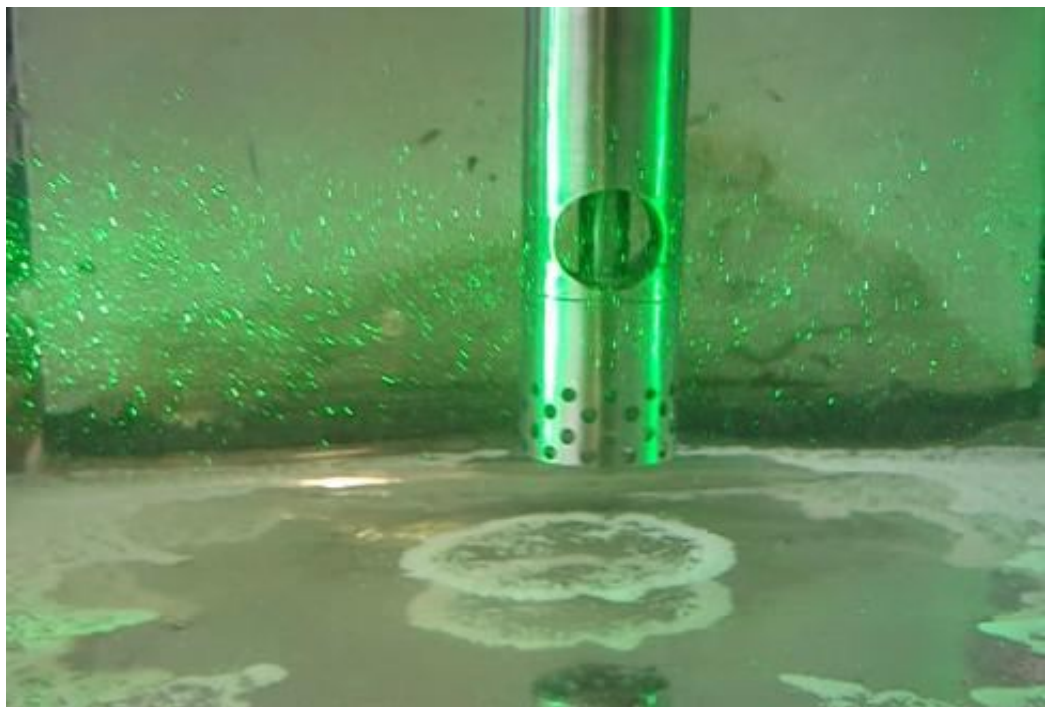


Figure 2.10. Laser light sheet placed before the HSM head, a scattered light made visible tracing particles, picture taken in daylight to show the head position.

The laser has been turned on when the head works for about 30 seconds to be sure that desired uniformity of seeding particles is present in the flow. When laser operates the photos has been taken minimum 50 times with the separation time 100 μ s by a high-speed camera. Before each experiment, the calibration has been made by taking the photo of metal metric scale. All results have been stored as vector files, and with Inside-6 software, we extracted the graphs of vectors of a fluid velocity field or flow (vortices) visualisation graphics. All fluid patterns were estimated from 50 to 150 measurements and the error is negligible [Raffel et al., 2007].

2.1.3. Silicon dioxide model.

Observation of the flow is difficult and usually needs a special equipment. To mimic situation which happens inside the liquid metal when it is processed by the batch HSM we have to design physically similar setup but with the transparent liquid to make the flow observable.

As the working liquid, water has been chosen. As the viscosity at room temperature is similar to liquid aluminium, the water is a reasonable medium which can mimic the aluminium flow behaviour. Water is often used as a modelling material for liquid metals (i.e. [Xu et al., 1998; Zhang et al., 2002; Zhang et al., 2007; Gupta, 1996]), because of practical reasons and because liquid metals behave as Newtonian fluids same as water at the room temperature.

The aluminium oxide or other aluminium-magnesium oxides are not usable to simulate the behaviour of oxides in liquid aluminium alloys as the density difference between water and those oxides is much higher, especially in comparison with liquid aluminium. So the physical simulation requires using some particles which are not so "heavy" and are possible to move much more freely by water than real aluminium and magnesium oxides. To find suitable particles density comparison was made and it is presented in Table 2.2. Oxides present in aluminium-magnesium alloys are described in Chapter 1.3. The main examples are alumina (Al_2O_3) and spinel (MgAl_2O_4).

Table 2.2. Density differences for liquids and particles
 [Brandes, 1983; Hildebrand et al.,1976, Jakse et al., 2013].

System : liquid / particles	Liquid density [g/cm ³]	Particles density [g/cm ³]	Density difference [g/cm ³]	Liquid viscosity [mPa·s]
Al / Al ₂ O ₃	2.375	4	1.625	1.03
Mg / MgO	1.584	3.58	1.996	1.25
Al / MgAl ₂ O ₄	2.375	3.58	1.205	1.03
H ₂ O / SiO ₂	1.010	2.56	1.640	0.89

From the table, we can see that density difference is between 1.205 to 1.996. In the centre of this range will be density difference about 1.6. To make model applicable for prediction of a behaviour for all oxides from Table 2.2 with good probability, we decided to use SiO₂ particles. As presented in Table 2.2 the density difference is equal 1.604 and chosen particles should model the behaviour of all presented oxides during processing liquid aluminium and its alloys.

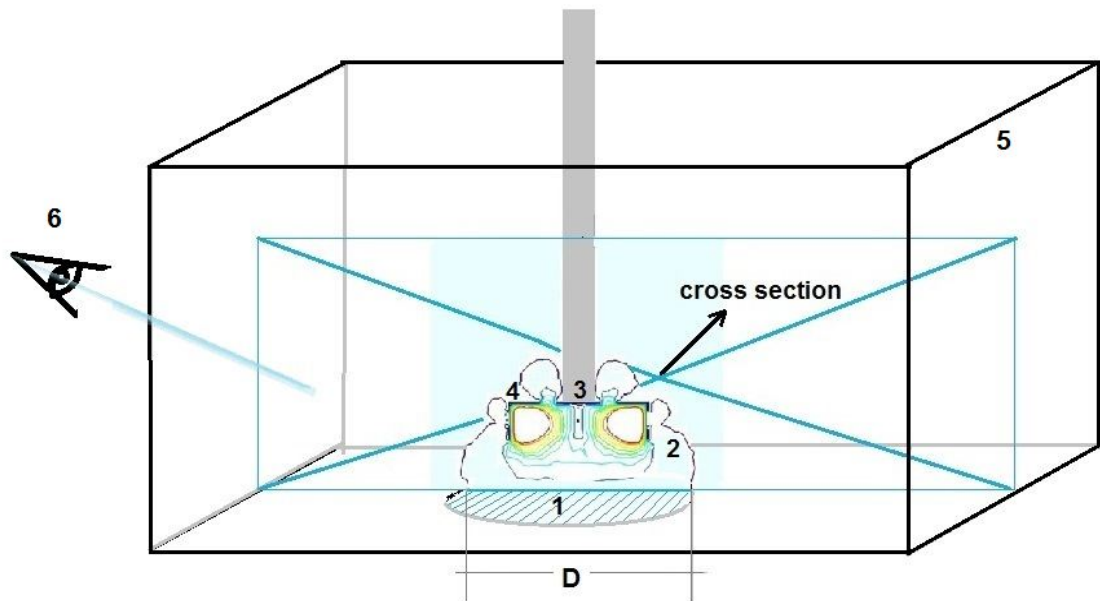
The difference between densities for an alumina / aluminium system is practically identical like in the model. For a Mg / MgO system, the density difference is bigger, but the difference will be about 0.3 g/cm³ and shouldn't change sizes of the cavern as the gravitational force is much smaller than mechanical forces applied to the system by the HSM head. The difference between liquid aluminium and spinel is 0.4 g/cm³ smaller than for the model. The liquid Al-Mg alloy should have the density smaller than clean aluminium.

Used particles have sizes 0.105 mm to 0.297 mm and the volume fraction which has been added was about 1%. As will be discussed further, the original oxide particles tend to join together and create the agglomerates or films, which can have different sizes. Thus, it is difficult to mimic exactly the situation in the melt. The chosen model particles had sizes from the range given above since the oxide agglomerates have different sizes too. The particles movement has been observed and photographed. Under the tank bottom, the length scale has been inserted and the measurements of the distance travelled by particles in specific conditions have been made.

To observe the movement caused by the HSM head it was necessary to avoid reflecting off the flow from the tank walls. As described in the previous chapter, experiments were done in the specially designated tank.

As silicon oxide particles are small with respect to the eye or the camera resolution, and the pseudo-cavern is localised mostly under the head, it was difficult to take any pictures of full pseudo-cavern shape. Instead, we were able to observe and measure the pseudo-cavern trace on the bottom of the tank. SiO₂ settled down outside of the well-mixed region (pseudo-cavern) and the pseudo-cavern diameter became visible as a clear place on the bottom of the tank (see Figure. 2.11). The rotational speed of HSM has been controlled and changed in the range, depending on the used head between 2000-7000 rpm. With a smaller rotational speed, the pseudo-cavern shape was usually not of a regular circle as the jets, in this case, travelled farther than the range of sucking force (Figure 2.11 b). The pseudo-cavern, from this reason and because of the stator properties, leaves a “flower” or a “star” shape, so it was necessary to measure sizes at least 10 times to determine the average radius.

a)



b)

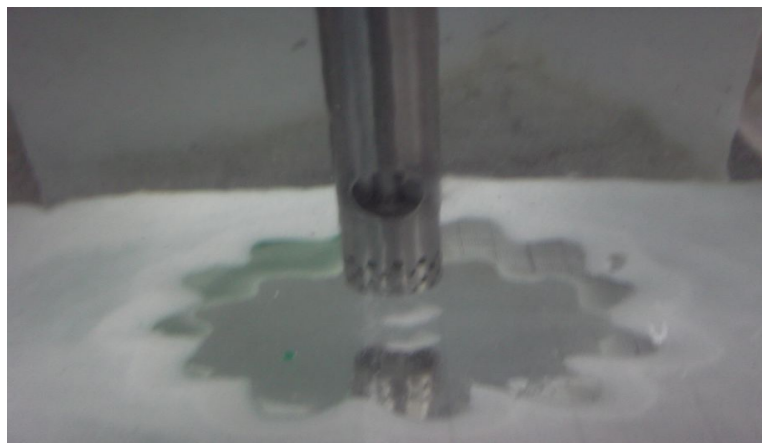


Figure 2.11. Trace of a cavern diameter on the bottom of the tank obtained with SiO_2 ;

a) schematic representation of flow and pseudo-cavern diameter measurements;

(1) the trace of pseudo-cavern on the bottom, (2) the lines represents the flow in cross section, (3) the shaft, (4) the stator, (5) the tank, (6) the observation angle used to take pictures of the pseudo-cavern shape.

b) a photograph taken during experiments, view on the pseudo-cavern trace shown in Figure 2.10 a.

2.1.4. Argon-gas model.

The SiO₂ model does not show the height of pseudo-cavern as the particles in the flow are not well visible. To visualise the full size of the well-mixed region the additional model was used. As argon gas bubbles are easier to observe, the second model was created with argon gas purging under the head. The pseudo-cavern was observed and the photographs have been taken. The measurement has been calibrated by placing a metal ruler on the calibration photograph as the size reference.

A similar flow of argon gas was used during experiments. This allows us to make results comparable each other. It improves the visibility too as if too much amount of gas is used, a shearing area will be covered by gas bubbles which escape from a pipe and moving up close to head. Both sizes of pseudo-cavern in directions x and y were measured and named respectively R (radius of pseudo-cavern) and h (height of pseudo-cavern). Figure 2.12 shows a visible pseudo-cavern area when the argon gas is sheared and dispersed into water by the HS device.

With changing the rotational speed (N) the cavern size became bigger and measurements were done for N in the range 2000-7000 rpm. With the higher rotational speed, sheared gas bubbles were too small which decreased the visibility and it was difficult to estimate the pseudo-cavern size for this model.

SiO₂ in water mimics closely the situation in Al melts as shown before by the density comparison, but measured dimensions of the pseudo-cavern observed with gas bubbles were different. Thus, both sizes of argon pseudo-cavern (R and h) have to be compared with the measured values previously obtained with SiO₂.

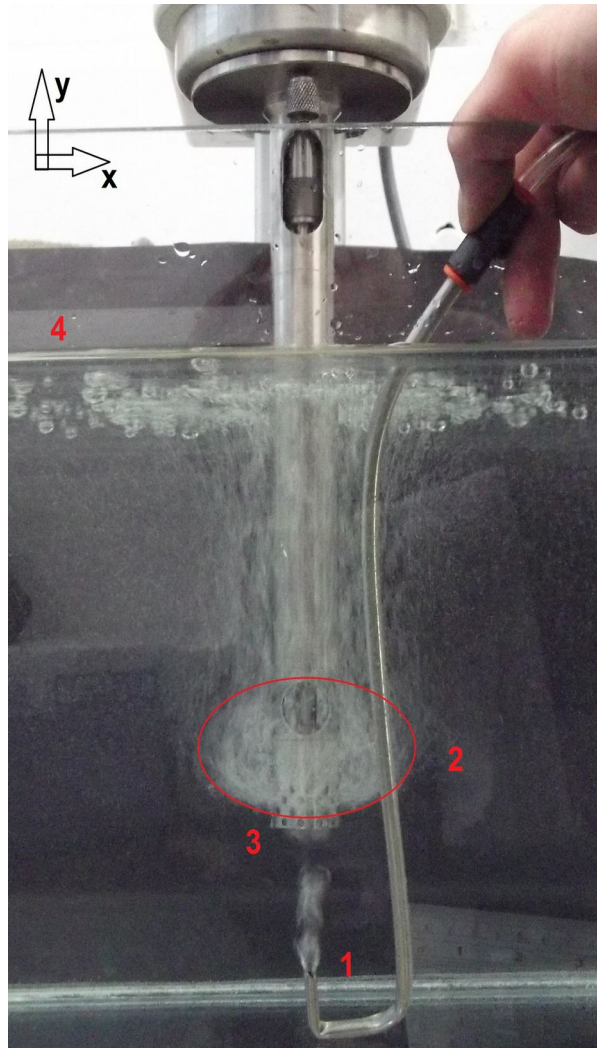


Figure 2.12. Pseudo-cavern shape observed with the argon-gas model. The line visualises estimated pseudo-cavern borders. (1) The gas purging, (2) observed the pseudo-cavern shape is an effect of the gas dispersion and distribution by the mixing head (3). Bubbles travel to the water surface (4).

2.2. Processing of a liquid metal

The physical modelling described before is expected to be applicable for aluminium and its alloys (see Section 2.1.3). The application of the best conditions determined from the modelling should give the best results of real alloys processing. As signalled in Section 1.5 with the high Mg content the grain refining effect of the shearing process is not so well visible as with a lower content. Thus, to make the observation easier, the Al alloy with a low content of Mg was chosen for experiments. A commercial purity Al and a pure Mg (99.95 wt.%) ingots were used to prepare the Al-3%Mg binary alloy. The prepared alloy has the composition presented in Table 2.3 (checked by the optical emission spectrometer – Foundry Master).

Table 2.3. The composition of the prepared alloy given in wt %

Al	Si	Fe	Cu	Mn	Mg	Zn
97.0	0.0145	0.0509	0.0019	0.0054	2.81	0.0072

From the phase diagram of Al-Mg alloys (Figure 2.13) the melting temperature of the prepared alloy was found as 643°C and the temperature for HSM processing was chosen above the liquidus (660°C).

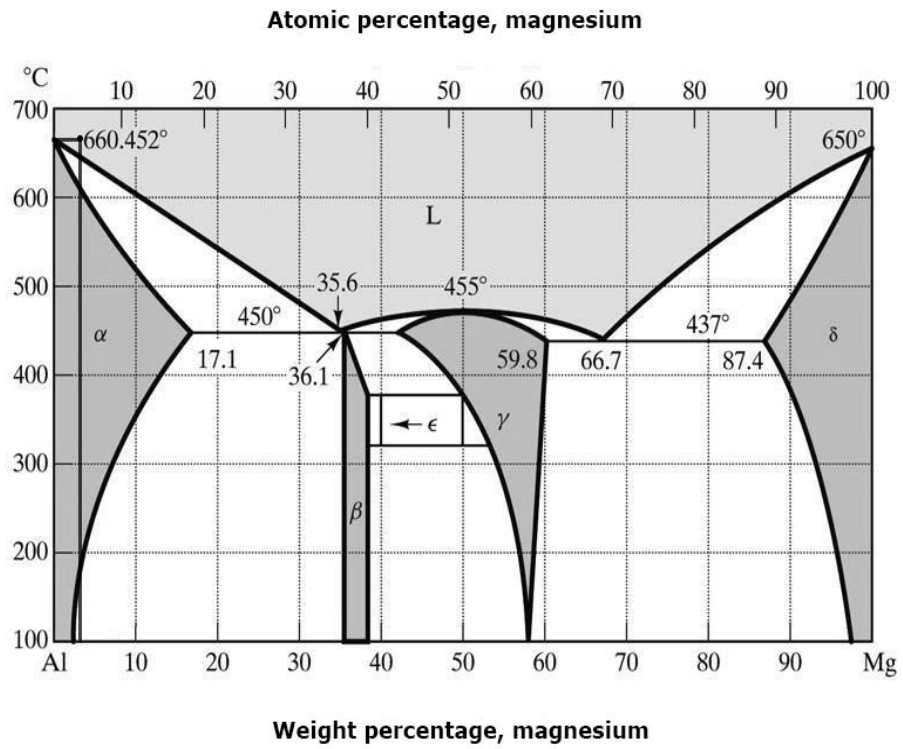


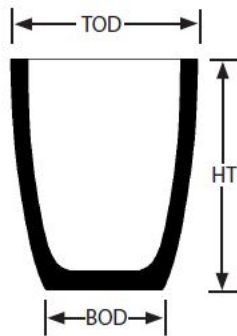
Figure 2.13. Al-Mg phase diagram [Brandes, 1983].



Figure 2.14. The ceramic rotor-stator impeller.

The ceramic mixer suitable for metal processing had outside diameter 42 mm. The rotor diameter was 32 mm and the gap between rotor and stator was 0.6 mm. The stator holes were round and arranged in rows (Figure 2.14) similar like in RH stator. The mixer was used for processing of a liquid alloy in crucibles A16 (diameter 184 mm), A20 (diameter 197 mm) and A30 (diameter 232 mm). The rotational speed was chosen for each experiment independently and kept at the constant level during the liquid metal processing. To avoid temperature change the crucible was placed in a heater. The mixing head, as well as the heater, were preheated to the desired temperature 660°C.

Table 2.4. The crucibles size chart.



Crucibles for Lift Out and Bale Out Furnaces					
SUPER A-SHAPES (A)	TOD	HT	BOD	Brass Capacity	Brimful capacity
	(mm)	(mm)	(mm)	(Kg)	(Litres)
A5/0	32	35	24	0.09	0.01
A3/0	46	52	30	0.22	0.03
A1/0	60	67	41	0.56	0.07
A0.5	68	78	48	1	0.13
A1	79	97	55	1.5	0.2
A1.5	90	92	55	1.9	0.25
A2	95	109	61	2.5	0.33
A3	105	127	70	3.7	0.49
A4	114	141	76	5.6	0.75
A5	124	152	86	6.8	0.9
A6	130	165	95	9	1.2
A7	140	175	105	11	1.5
A8	156	184	108	12.5	1.7
A10	160	200	110	18	2.4
A12	171	210	121	18	2.4
A16	184	232	130	23	3.1
A20	197	260	145	30	4
A25	210	280	155	36	4.8
A30	232	290	160	43	5.7

To examine the effect of HSM processing of the melts the Aluminium Association Test Procedure-1 (TP-1) mould was used, which allowed us to avoid the influence of a cooling rate as in the standard TP-1 procedure the cooling rate is constant. This technique starts with melting alloy inside a crucible in an electrical resistance furnace at chosen temperature. In mid-time, the TP-1 ladles are preheated in an electrical furnace at 350°C. The ladle with liquid alloy taken from crucible after each HSM processing was

water-cooled. The TP-1 mould quench tank with water flow rate 3.8 l/min has been used. Each ladle has been immersed in water up to 25 mm from the bottom of the ladle. The TP-1 samples were cut on the 50 mm level above the bottom.

Two main processing procedures were used and are given below.

The not full agitated conditions (N = 500 rpm) and fully agitated conditions (N = 3000 rpm) were checked. Several times of mixing were used to check time influence. The crucible A20 was used. Liquid metal was premixed with N = 700 rpm and later the rotational speed was increased. To check timing effect in full agitated conditions the rotational speed was increased to 3000 rpm. The shearing time influence was checked with 2 minutes step. The shearing temperature was kept above 660°C, liquid metal was poured to crucible at about 680°C and later to TP-1 mould at about 660°C.

Not full agitation conditions (N = 500 rpm) in the crucible A30 and full agitation conditions (N = 2500 rpm) in the crucible A16 were examined. Both crucibles were prepared separately to avoid the influence of premixing present in first processing conditions. The sample was taken by the ladle. The shearing temperature was kept above 660°C, liquid metal was poured to crucible at about 680°C and later to TP-1 mould at about 660°C.

2.3. Optical microscopy analyses.

Metal samples were cut from the cast alloy for microstructural characterization and hot mounted in Bakelite. The surface of metallographic specimens was prepared by grinding, polishing, and etching. Mechanical preparation help to remove a material from the sample surface until the desired surface quality was achieved. After mounting, the specimens were wet ground to reveal the surface with a finer and finer abrasive paper. We used 120, 500, 800, 1200, 2500 and 4000 grit SiC papers before polishing of samples. Polishing was performed to produce a scratch-free mirror finish with minimal

deformation remaining from the preparation process. Grain boundaries of the specimen were revealed by using the Baker's etchant in anodising conditions (about 80-90 s, 15-20 V). After preparation samples were examined by optical methods.

Prepared samples were examined by a Carl Zeiss Axioskop 2 MAT optical microscope equipped with image analysis software. The microscope is connected with a camera and a computer and installed AxioCam software is giving wide possibilities of observations and the quantitative measurements. This microscope has fitted objective and ocular lenses with the corresponding magnifications: 25×, 100×, 200× and 500×. Grain sizes measurements were done from photographs taken at various magnifications. To observe grain boundaries the polarised light was used as metal samples were anodised before examination.

To observe the sizes of the powder particles, the powders were cold mounted in the transparent epoxy resin (Figure 2.15). To improve visibility the samples were grinded with 120, 500, 800, 1200, 2500 grit SiC papers. The reference metal sample was placed inside resin to observe grinding effects. Prepared samples were observed under the microscope and photographs were taken.

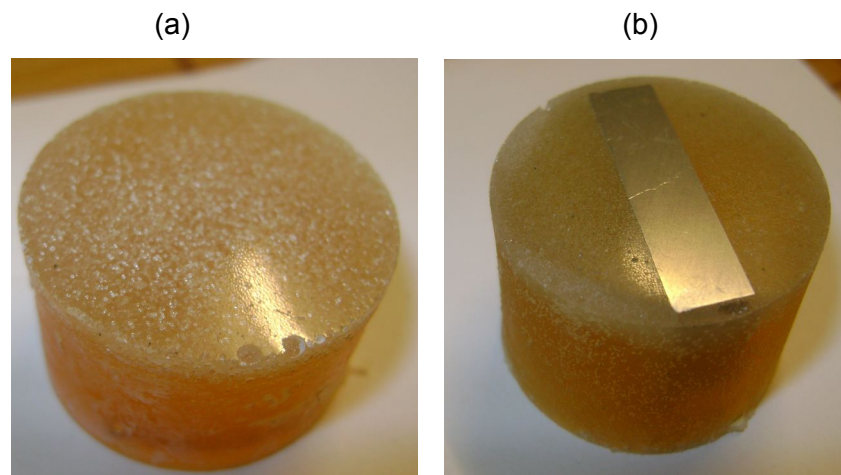


Figure 2.15. Cold mounted powders a) without a reference probe, b) with a reference probe.

2.4. Scanning electron microscopy.

A scanning electron microscope (SEM) is a type of the electron microscope that produces images of a sample by scanning it with a focused beam of electrons. Electrons interactions with atoms in the sample are producing various signals. From those signals, information about the sample's surface topography and composition can be extracted. When electron beam meets the specimen from the material surface the secondary electrons are emitted by atoms excited by the electron beam. The number of secondary electrons can be detected. As the secondary electron number and position depend on the angle between the beam and the surface of the specimen so the signal detected depends on specimen topography (Figure 2.16).

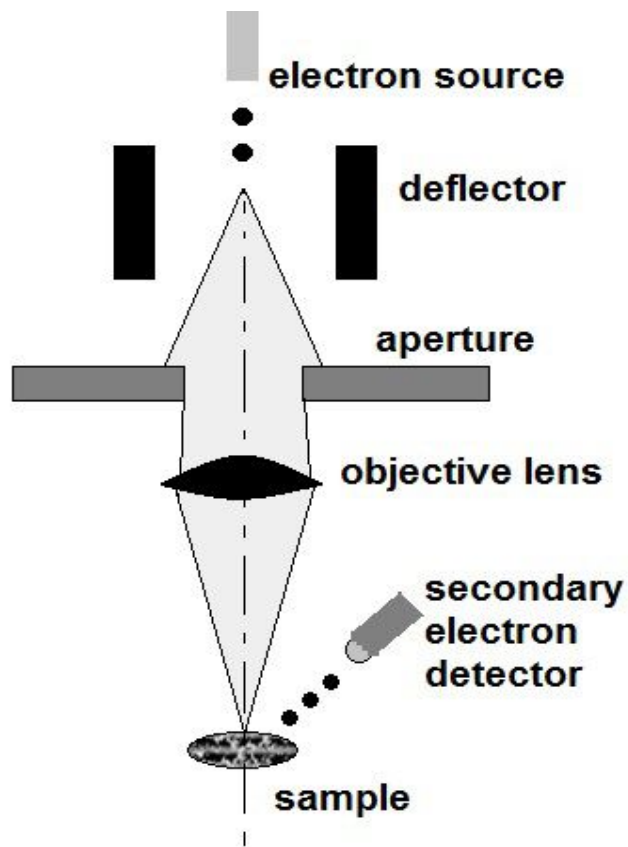


Figure 2.16. A basic SEM design.

All samples must be of an appropriate size to fit in the specimen chamber and specimens must be electrically conductive. Metal objects require little special preparation for SEM except for cleaning and mounting on a specimen stub. Non-conductive specimens are usually coated with an ultra-thin coating of electrically conducting material as gold or platinum.

Metal samples for grain counting are usually analysed by optical microscopy with no necessity to use the SEM. To observe some smaller structures the SEM pictures are used. The powder analyses made in this research needs both optical and SEM photographs especially in the case of MgO which is really fine after shearing. Powder specimens were placed on special glue tape and coated with gold by high-vacuum evaporation. The chosen voltage was 10 kV and allowed us to observe the specimen with high magnification and resolution. For experiment purposes, we used the working distance from range 6.4 - 8.9 mm. The magnification ranged from 100 to 60 000 times. Maximum magnification photographs reveal the reason of a strong agglomeration of MgO particles after shearing in the water. As shown in Figure 2.17 the structure is similar to aerogels (sponge-like) and particles tend to be joined after shearing. Thus, under the optical microscope, it is difficult to observe separated particles and measure their sizes.

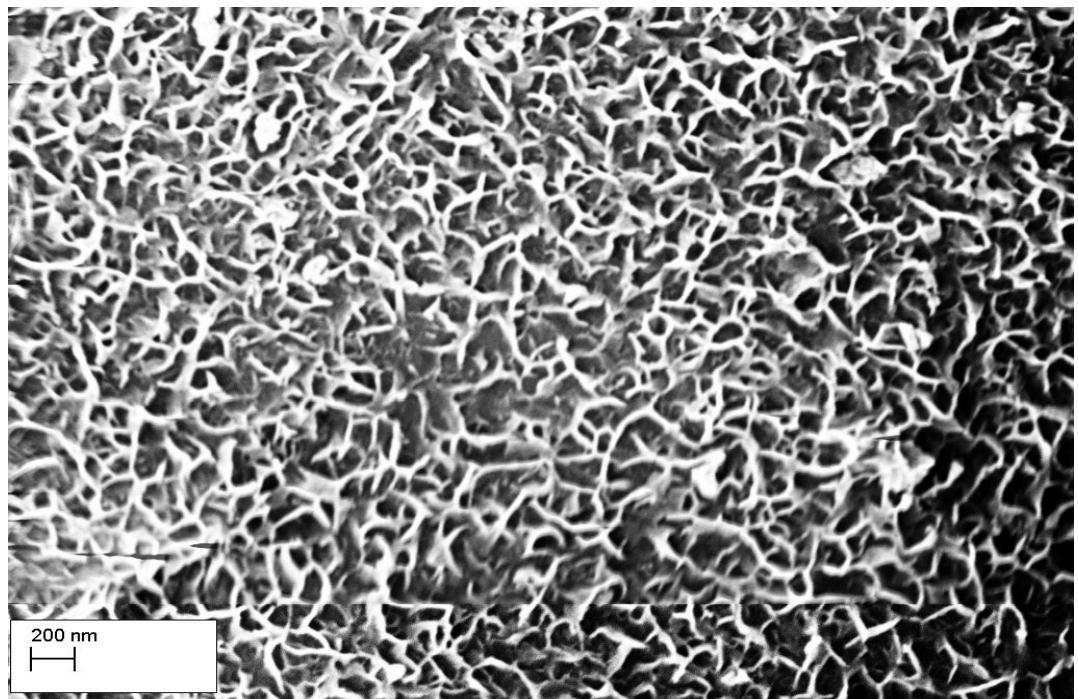


Figure 2.17. MgO particles after shearing in the water.

SEM picture with magnification 60 000×

2.5. Image analysis.

Images analysis was done by ImageJ software and by the software from TSI loaned with the PIV system (INSIGHT™ 4G, TecPlot 10) as well as attached to Zeiss optical microscope (AxioCam). Before each experiment in which the flow was recorded, the calibration photo was taken. The PIV system was calibrated before each run and the results were stored by the included software for analyses. The photographs of pseudo-cavern sizes taken during the modelling with argon gas or SiO₂ particles were calibrated by using a metal ruler and globally calibrated in ImageJ later. One of calibration photographs is shown in the Figure 2.18.

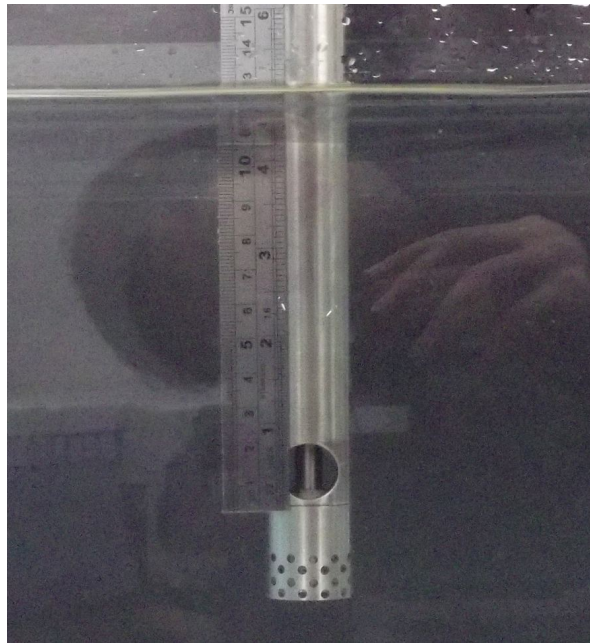


Figure 2.18. The calibration photograph made before experiments.

The powder particle size is difficult to determine as the sheared particles have irregular shapes. Thus, instead of one-dimensional measurements, the area measurements were done in ImageJ software. Areas of at least 100 measurements for each case were checked and the average area was calculated.

To determine the mean grain size the mean line intercept method was used. This method bases on measurements of line intercepts with grain boundaries. The grain size is approximated as the mean intercept length. The standard error is calculated as the standard deviation of the Student t-distribution.

Chapter 3. Computer Simulation Of The Liquid Ordering On The Interface – Role Of Oxides In Liquid Metals.

3.1. The purpose of computer simulation of atomic ordering.

This theoretical prediction is a base for the presented computer simulation. As the direct observations of the interface are difficult, the computer simulations are commonly used to model what happens in specific conditions at the interface. The layering effect at the interface with different substrates was previously studied by molecular dynamics simulations and a few experimental observations were described [Webb et al., 2003; Kauffmann et al., 2005; Oh et al., 2006; Geysers et al., 2000; Hashibon et al., 2001; Hashibon et al., 2002; Palafox and Laird, 2011]. One example was given in Section 1.3.2 where photographs of direct HRTEM observations are presented. This example is quite significant as the layering persisted up to 6 atomic layers from the interface adjacent to oxide surface (Al_2O_3) [Oh et al., 2006]. It is another proof of the potentially positive role of oxides present in the liquid Al. The high shear processing of the melts is used to shear oxides present in the melts as described in Section 1.5. Usually, entrained oxides and films are distributed non-uniformly in the melt. There is a small number of them and they have poor wettability. Thus, the naturally present oxides are not effective as the grain refiner even if they can play a role of nucleation sites to some extent. It is possible to change this situation by mechanical breakage of clusters or films. The substrates have to be well dispersed. During intensive melt shearing, the defragmentation, as well as dispersion of individual oxide particles, happens. Finally, after processing by HSM they can play a role of nuclei when the nucleation process occurs. It can be predicted by the misfit analyses and is described by the epitaxial nucleation theory (Section 1.3.2). The experimental observations confirm that grains are refined by application of HSMs

(Section 1.5). To complete this research and to be sure that oxide can play a role of nucleation sites, some additional computer modelling was done. The results show that at the interface between ceramic-like materials (in a real situation – oxides) and liquid metals the ordering happens. An arrangement of liquid metal atoms mimics ordering of the atoms in the ceramic-like material. Results of this simulation confirm the existence of 5 liquid layers adjacent to the interface which can start the nucleation process. As layers present in liquid close to the interface repeat ordering of another material (for example oxides), the forces between atoms in layers are not well balanced. The particles interactions can be described by Leonard Jones potential which indicates a strong tendency of atoms to take positions governed by a minimum of the energy law. At the beginning, the liquid atoms take positions which are the effect of forces exerted by substrate atoms. When with time next layers are growing, in each layer more strain energy is accumulated. The influence of substrate atoms decreases with distance from them and Al atoms will tend to take positions independently of substrate atoms positions. The distance correspondent to minimum energy of Al atoms is equal a crystal lattice parameter characteristic of solid Al. When a number of layers is growing, usually over 5, the stress due to forces between Al atoms is too big to be balanced by forces exerted by the substrate. The stress has to be released and the atoms will change positions. Thus, in the crystal structure after growth, the dislocation according to changed positions of atoms can be observed. The growth of the new atomic structure after a stress release can be continued.

The present knowledge suggests that the layering at the interface is not related to the structural property. For example, there are predictions that the layered structure of Al is independent of the surface orientation, as observed in the liquid Al/solid Cu system [Geysersmans et al., 2000; Hashibon et al., 2002]. On the other hand, there is a far greater in-plane ordering found for the liquid atoms in contact with a bcc [100] substrate than a [110] substrate [Hashibon et al., 2001], which suggests that the substrate orientation can play a role in the process of the in-plane atomic ordering.

The simulations which can be found in publications were performed for different conditions and materials. The authors choice of them was not determined by the misfit value. As the misfit can have a strong influence on the ordering, in current simulation the chosen misfit was equal to 0%. In this case, we can observe a behaviour of the atoms in a potentially ideal situation. Thus, we can observe the layering and in-plane ordering effects clearly. Further research was done by Men and Fan [2012], and they investigated how this ordering is influenced by the misfit increase. It is well-known fact that nucleation

happens on substrates with a small lattice misfit (less than 10%) [Zhang et al., 2005; Brandes, 1983] so with 0% misfit good conditions for nucleation are expected.

The interfacial atoms ordering plays a significant role in nucleation behaviour of alloy melts [Greer, 2006] as the layer which mimics substrate atoms is a template for a growth of a new phase. This growth was observed even for a small undercooling [Greer et al., 2000; Quested and Greer, 2004] or beyond a critical undercooling [Kim and Cantor, 1994; Reilly and Cantor, 1995]. Finally, the observation of ordering on the interface can be treated as the proof that the substrate can be used as the grain refiner. Presented below a computer simulations are intended to reveal this ordering.

3.2. The computer simulation methodology.

The MD (Molecular Dynamics) simulations were performed using the DL_POLY 4.03 and 4.04 packages. The simulated system was liquid Al and a substrate with an fcc structure and an [111] surface orientation. To make the simulation simpler the structure of the substrate was that of solid Al. My part of the research consisted of a simulation of ordering which happens at the interface when the misfit is 0%. It is a proof that layering and in-plane ordering occurs at the interface (results are presented below). This simulation was an important step of a wider research made to establish the effect of a lattice misfit on the degree of atomic layering at the interface.

A total number of atoms used in the simulation system was 5670, and a number of the substrate atoms was 4050 (Figure 3.1. shows the simulated cell, Men and Fan 2012). Periodic boundary conditions were applied in the x and the y dimensions and only the z-dimension was a dynamic variable. Around a sample a vacuum region was simulated with periodic boundary conditions in all directions as the simulated cell consists of a liquid phase. The periodic boundary conditions are commonly used for approximating a large (infinite) system by using a small part called a unit cell. To simulate a ceramic material (as an oxide), substrate atoms were frozen in positions to avoid interactions between atoms different than considered. In this way the model mimics behaviour of liquid close to a hard wall of a solid, such as the oxide with a much higher melting temperature (the

movement of substrate atoms was not expected in this temperature and those atoms were not included in the equations of motion, being frozen at constant positions). Influence of forces exerted by substrate atoms on liquid atoms was checked by the simulation. The liquid Al atoms were allowed to move freely during steps of the simulation. Under the different forces present and defined in the simulated system the movement of liquid atoms was predicted. To find displacements of Al atoms the movement equations were integrated [Hashibon et al., 2001, Smith et al., 2010].

In the DL-Poly software, the integration can be done by a few different algorithms. Some of them are more time consuming than others so a suitable algorithm has to be chosen. With our simulation cell, we chose the Verlet algorithm with a time step of 0.001 ps [Hashibon et al., 2001; Smith et al., 2010]. The software in each step was analysing the small integration bin with sizes from $-\frac{1}{2} dz$ to $\frac{1}{2} dz$, and dz it is the bin width. The temperature had to be controlled by special numerical thermostats which can be chosen from DL_POLY functions. In the presented simulation the Berendsen NVT ensemble was used [Hashibon et al., 2001, Smith et al., 2010].

First, 100 ps of simulation took the equilibration of the sample at 0 K. In each next 100 ps, the sample was heated by 50 K up to 1400 K. After heating the liquid Al the simulation cell was cooled to a desired temperature (for example 1100 K in the presented results). Again, the system needs 100 ps to cool down for each 50 K. When system reached the chosen temperature, 100 ps was given for the system equilibration.

The movement of atoms is governed by forces present in the system. In addition to the interaction of substrate atoms with liquid atoms, the liquid atoms interact with each other. To model all interatomic interactions the EAM potential [Smith et al., 2010] was used. This potential was applied with good results for Al systems by Zope and Mishin [Zope and Mishin, 2003]. To setup the initial data, an atomic radius of aluminium (half of the distance between two nearest atoms) equal to 0.142 nm was used (as predicted by previous EAM simulation) [Wang et al., 2010; Totten et al., 2003].

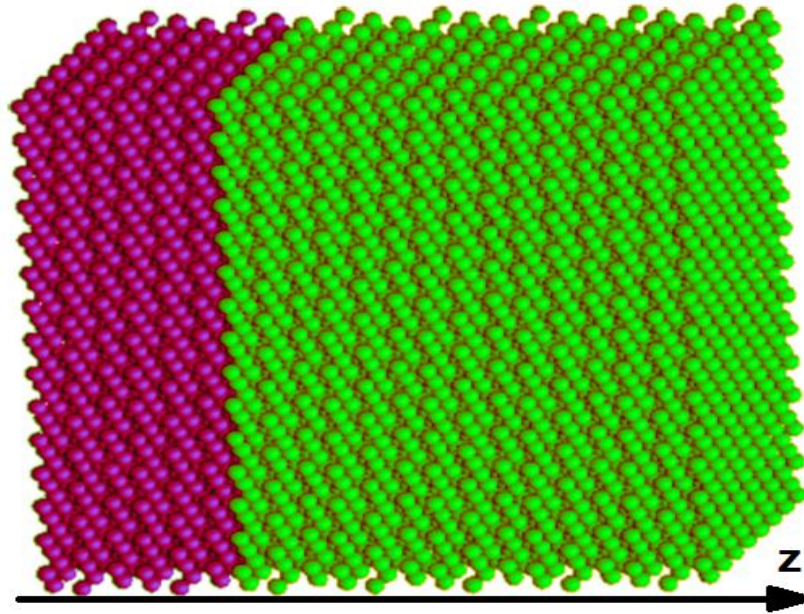


Figure 3.1. An illustration of the simulation cell. The fixed substrate atoms are visualised by purple balls and adjacent Al atoms are represented by green balls. The orientation of cell (z-axis) is comparable with the orientation of z-axis presented on the atomic density graphs given further.

3.3. Physical quantities used in the simulation.

A characterization of the interface was done by the density profile and the static structural parameter [Smith et al., 2010] which are described below.

To decide whether the ceramic-like materials, as oxides, can play a role in the nucleation, we are looking for two main signs. Solidification process can be described as an ordering of atoms of the liquid. Nucleation is the beginning of this process. In the simulation cell, two kinds of ordering were checked. First, the atomic density should oscillate close to the hard wall (a substrate) [McMullen and Oxtoby, 1987; Curtin, 1987; Sikkenk et al., 1987; Fisher, 1980]. As this oscillation is induced by the substrate, the density oscillation will decay and disappear with the distance from the substrate.

Secondly, positions of atoms inside the layers with high atomic density should mimic positions of substrate atoms.

During the solidification, the liquid atoms tend to take positions determined by the minimum energy rule. The effect of this rule is the atoms' location in the space with a characteristic length between them. Depending on atom types the distance between them can be found as a constant value. Atoms from the liquid mimic the substrate lattice. It is in-plane ordering which plays role in nucleation by ordering the liquid. The position of liquid atoms in relation to defined positions of substrate atoms is one of the results of each simulation run.

To describe two ordering types – in the atomic density, along with the z-axis and the in-plane ordering, two physical quantities are defined.

First, we have to check the layering effect. A layer consists close-packed atoms and no atoms present between layers. Layering happens in planes perpendicular to the z-axis (mimics the substrate atom planes). Thus, the density of atoms in the layers is higher than between them. If layers are not observed the density will be, approximately, constant. For this reason, we have to define the density profile along the z-axis of a simulation box.

The density profile is expressed as [Smith et al., 2010]:

$$\rho(z) = \frac{\langle N_z \rangle}{L_x L_y \Delta z} \quad \text{(Equation 3.1)}$$

where: N_z – number of atoms in the range from $-\frac{1}{2} \Delta z$ to $+\frac{1}{2} \Delta z$ at time t ,

L_x, L_y – the cell dimensions, Δz – width of an examination bin (a slice of the cell).

From the presented formula, the atoms density profile is calculated in each step, when the bin is analysed. The density average was calculated after 10 ps.

Even when we obtain regular density peaks close to the interface, we still do not know how atoms are arranged in XY plane. Thus, it is necessary to find a tool which describes the in-plane ordering. We expect that the liquid atoms mimic positions of the substrate atoms. In other words, there are not far from the position of the frozen atoms. The in-plane order parameter describes positions of Al atoms in each layer.

The static structural order parameter is defined as [Smith et al., 2010]:

$$S(\mathbf{K}, z) = \frac{\left| \sum_{j \in \Delta z} \exp(i\mathbf{K} \cdot \mathbf{r}_j) \right|^2}{N_z^2} \quad \text{(Equation 3.2)}$$

where: j – atoms index in the bin,
 \mathbf{r}_j – a position vector of the j -th atom in the Cartesian space,
 \mathbf{K} – a reciprocal lattice vector.

With respect to the fcc structure of a substrate, geometrical calculations show that if we choose:

$$\mathbf{K} = \pi a^{-1}[\sqrt{2}, 2\sqrt{6}, \sqrt{3}],$$

the $\exp(i\mathbf{K} \cdot \mathbf{r}_j) = 1$ for any \mathbf{r}_j in a perfect lattice with an [111] surface orientation. In this case, we have to count j -times the exponent value equal 1, which gives the number of atoms in the bin (N_z). This formulation lets us obtain values of the static structural order parameter equal 1 when Al atoms are in the same positions as substrate atoms. If the position of them will be different, the exponential value will be smaller and the static structural order parameter decreases. Thus, when the distance from frozen atoms increases, the static structural order parameter decreases and can be used to measure the level of ordering inside the XY plane.

3.4. Results.

Results extracted from the data generated by the DL_POLY and stored originally in the history file are used to draw the density profile as well as the $S(z)$ dependence. Presented results for 0% misfit (figures 3.2, 3.3) are obtained by my part of simulation work, the extended results for other misfits are effects of the simulation made by Dr H. Men which teach me about MD and made parallel simulation at the same time, published previously [Men and Fan, 2012].

The density profile describes how many atoms is present in a specific length along the chosen axis. In Figure 3.2. the calculated by the software density profile along the z-axis is presented.

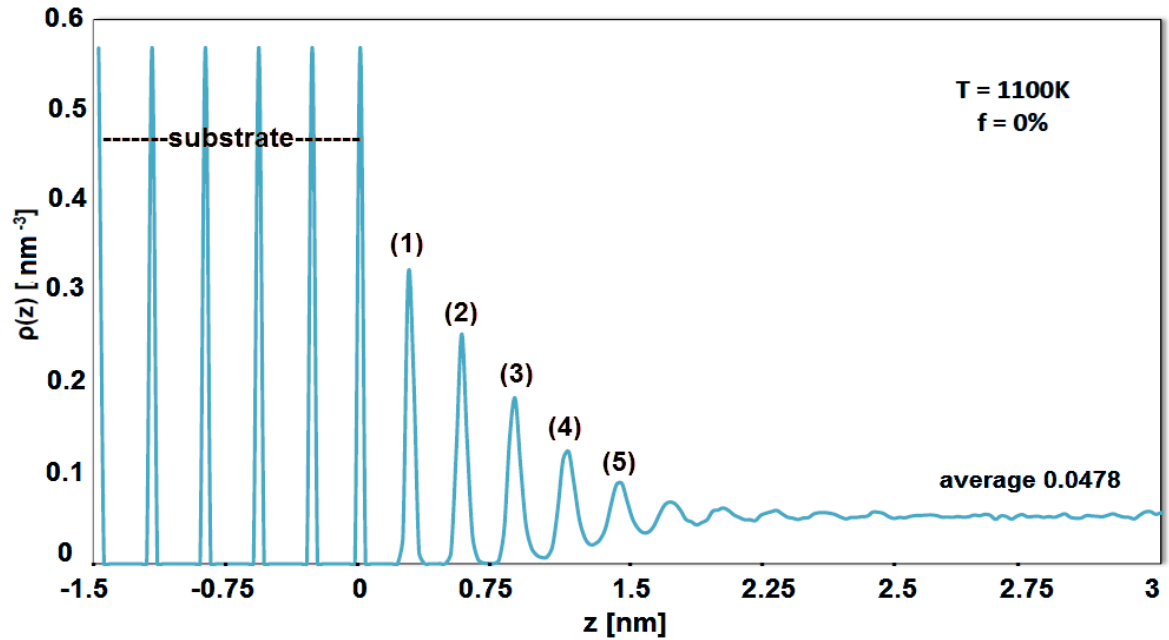


Figure 3.2. The density profile $\rho(z)$ of the substrate and the liquid as a function of z at $T=1100$ K. The positions of 5 layers observed in liquid aluminium are marked on the graph.

The density profile of the substrate atoms shows regular peaks with a fixed peak density of 0.575 atoms/nm^3 as we can observe in three first peaks in Fig. 3.2. The oscillations appear in the atomic density profile of liquid Al over 5 atomic layers at the interface as can be seen as smaller peaks to the right of the interface (along the z-axis). Between layers, the density decreases to zero what means that it is no atoms present in this plane. Thus, these oscillations in the atomic density show that atoms are located in layers. The simulation confirms the possibility of a layered structure of liquid close to the interface. Figure 3.2 can be compared with Figure 1.21 as direct HRTEM observation also revealed similar atomic density oscillations up to 6 atomic layers from the interface between liquid Al and $\alpha\text{-Al}_2\text{O}_3$ [Oh et al., 2006]. That experimental proof can be used as the validation of a presented simulation.

To compare density profiles at different temperatures the peak number density was obtained and presented in Figure 3.3.

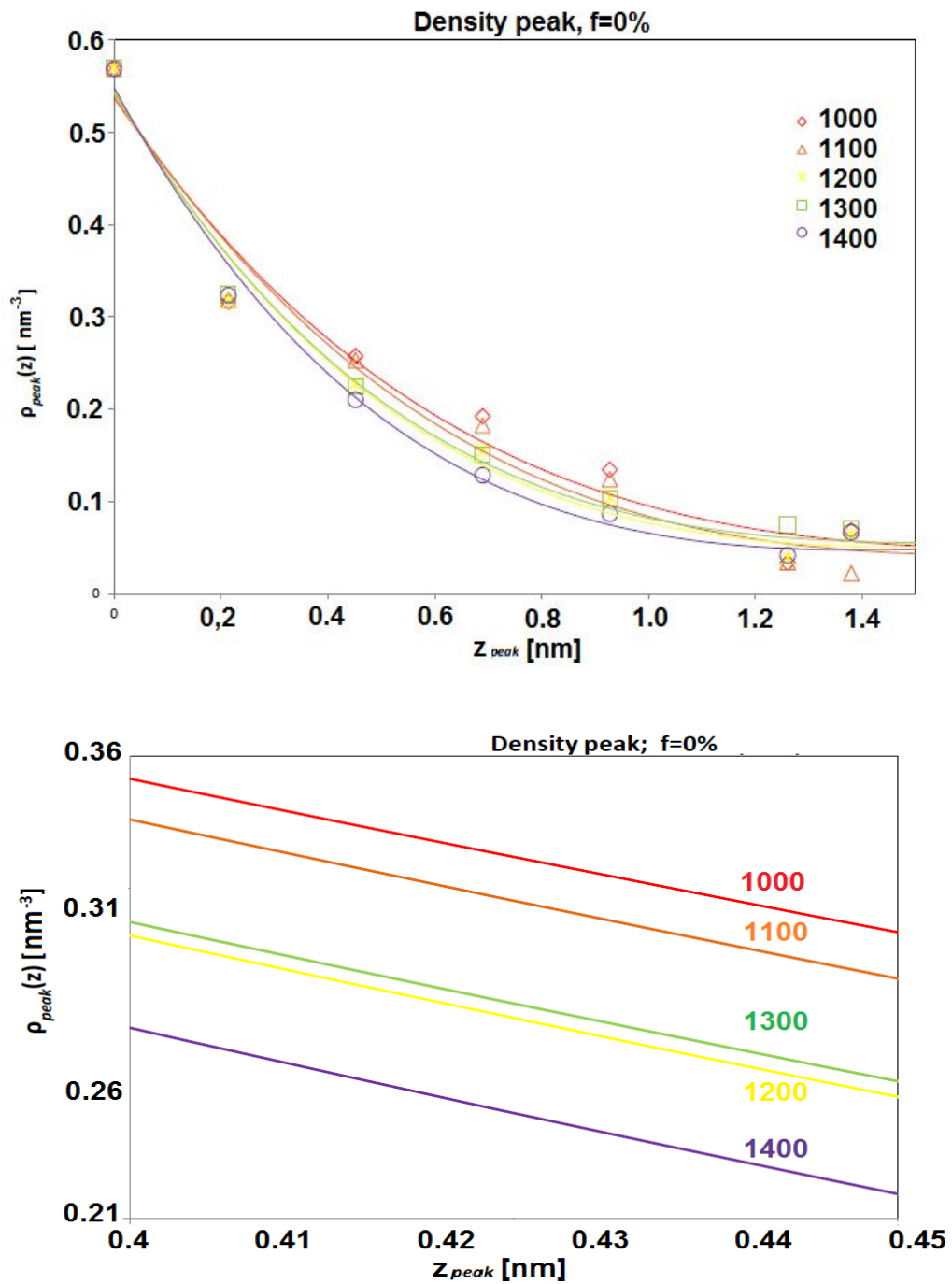


Figure 3.3. The peak number density, ρ_{peak} , of the liquid as a function of the distance (z) from the interface at $T_e = 1000$ to 1400 K for two z ranges (shown above and below).

We can observe the exponential decay of the peak density for all equilibration temperatures. Hashibon et al. [2002] also confirmed an exponential decay of the density profile of liquid Al at the interface in the previous research. With a temperature increase, the ordering (atomic density in the layers) decreases. The maximum difference between 1000 and 1400 K equals about 0.1 of $\rho_{\text{peak}}(z)$. That means that the atomic layering can be less significant at a higher temperature, what can be expected, as at higher temperatures atoms are moving more freely and faster. At the same time, the ordering decreases not much, maximally about 10%. Generally, the weak influence of temperature on layering is in a good agreement with previous publications and was mentioned before by Zhao and Rice [2011]. Another factor that can influence layering possibility is a misfit between atoms of a substrate and a liquid. In this case, we can refer to the further simulation [Men and Fan, 2012]. My simulation was a small part of whole research which proves that the misfit value does not have the influence on the layered structure of a liquid adjacent to a solid surface. As shown in Figure 3.4., the peak density decay is similar for substrates with misfits from range 0% to 8%. If the maximum difference of peak density function will be estimated from the presented graph, the value remains about 0.1. Similarly, as in the case of temperature dependence, the difference is maximally 10% and do not play a significant role.

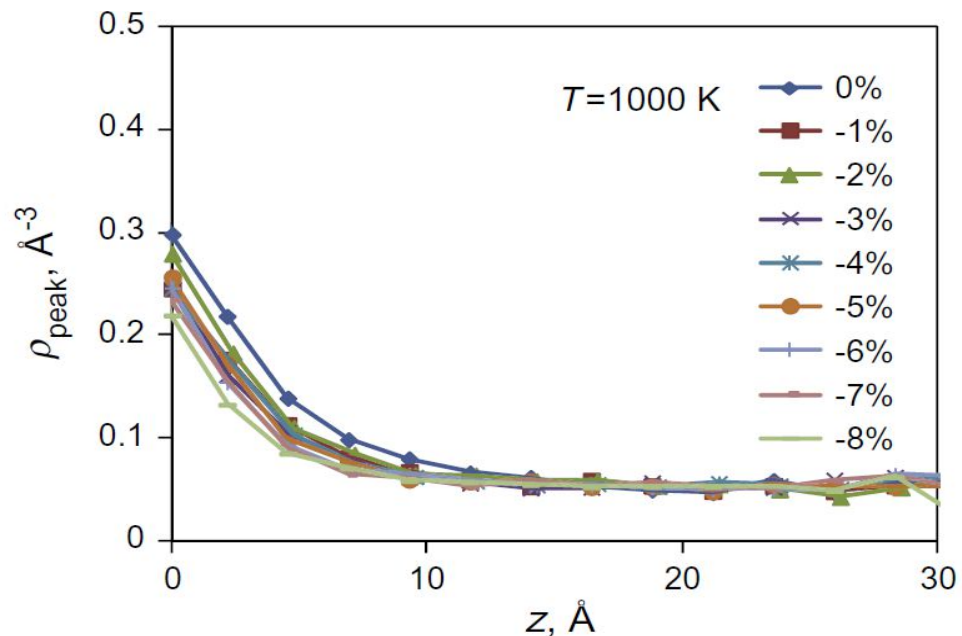


Figure 3.4 The peak number density, ρ_{peak} , of the liquid as a function of a distance (z) from the interface for the systems with misfits from 0% - -8%, at 1000 K [Men and Fan, 2012].

Finally, we can conclude that layering up to 5 layers occurs at the interface and this effect can be treated as independent from the temperature or misfits between two substances on the interface. It can be compared with previous studies. It has been found that the liquid Al is always layered within 5 atomic layers at the interface whatever the surface orientation is in the liquid Al/solid Cu system [Geysersmans et al., 2000; Hashibon et al., 2002].

Density profiles considered alone can not give us information about atomic in-plane ordering. To check what happens inside layers which are obtained by the density profile, we have to calculate and check the other parameter – the static order parameter. The order parameter $S(z)$ helps us to check how ordered is the structure of atoms after an each simulation run. As substrate atoms are in frozen positions they will exert constant forces on the liquid atoms. Liquid atoms will take positions which are governed by those atomic forces. In the effect, we should see that in layers exist some atomic ordering, indicated by an increase in the order parameter. The order parameter equal to 1 means full ordering similar to present in the frozen Al lattice. Figure 3.5 presents the order parameter $S(z)$ for different temperatures.

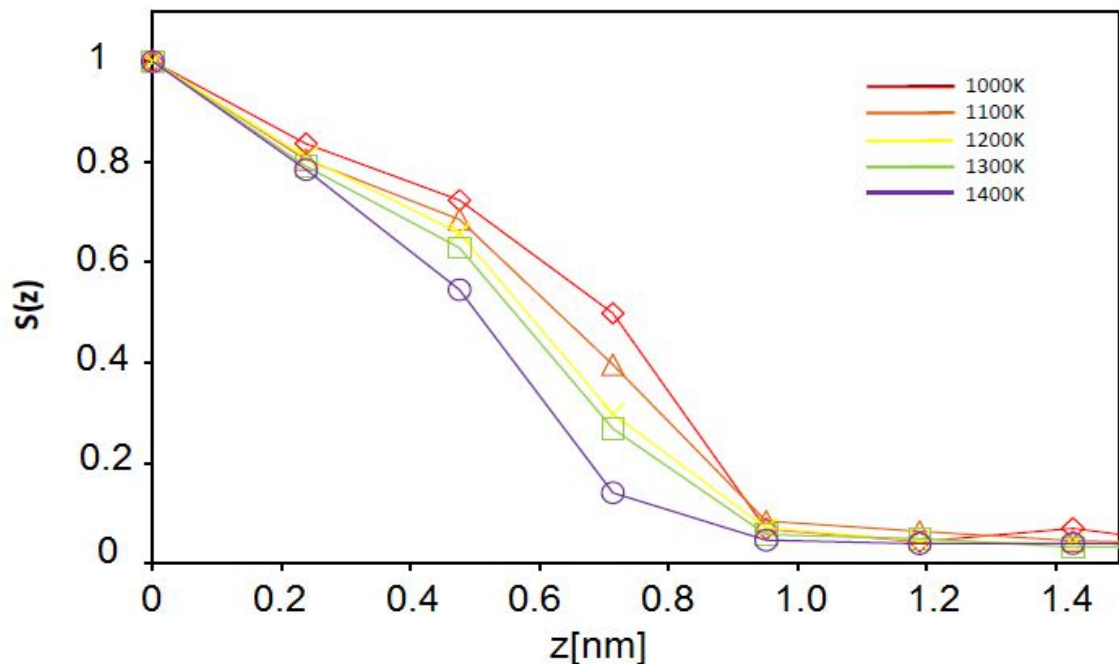


Figure 3.5. The order parameter $S(z)$ of the liquid as a function of z ;
 $T_e=1000-1400$ K.

$S(z) = 1$ for the substrate, as it is the fixed value. The average $S(z)$ in the bulk liquid is about 0.1. The values of a static order parameter for each layer shown in previous figures (Fig. 3.2, Fig.3.3) were checked in the results from DL_POLY software. Values of them for 1100 K are given in Table 3.1.

Table 3.1. A static order parameter at 1100K .

	Layer 1	Layer 2	Layer 3	Layer 4
$S(z)$	0.84	0.72	0.5	0.07

The last value is smaller than the order parameter in the bulk liquid indicates that in this layer no in-plane ordering exists. The first three layers are ordered and this ordering decreases from 1 to 0.5 at third layer. It means that atoms present in this layer mimic positions of the substrate but some of them (about 50% of atoms) changed positions. The atomic in-plane ordering decreases faster than layering at the interface. It is in agreement with previous studies [Kaplan and Kauffmann, 2006; Kauffmann and Koch, 2011]. Nevertheless, three ordered layers on the interface can induce the crystal growth.

If we look closer at Figure 3.5 we can see that the in-plane ordering decreases with increasing temperature. For example in the third layer, the $S(z)$ for 1000 K is about 0.5; what means that about 50% of atoms in this layer mimics positions of substrate atoms. But in the case of a temperature 1400 K the $S(z) = 0.1$, what is just slightly higher than $S(z) = 0.05$ for bulk liquid. Thus, the in-plane ordering on the interface is dependent on the temperature.

Another factor that can influence the ordering is the mentioned before misfit between atoms of a substrate and the Al. If we compare our results with findings of Men and Fan [2012], a strong influence of the misfit value on the in-plane ordering can be expected as shown in Figure 3.6.

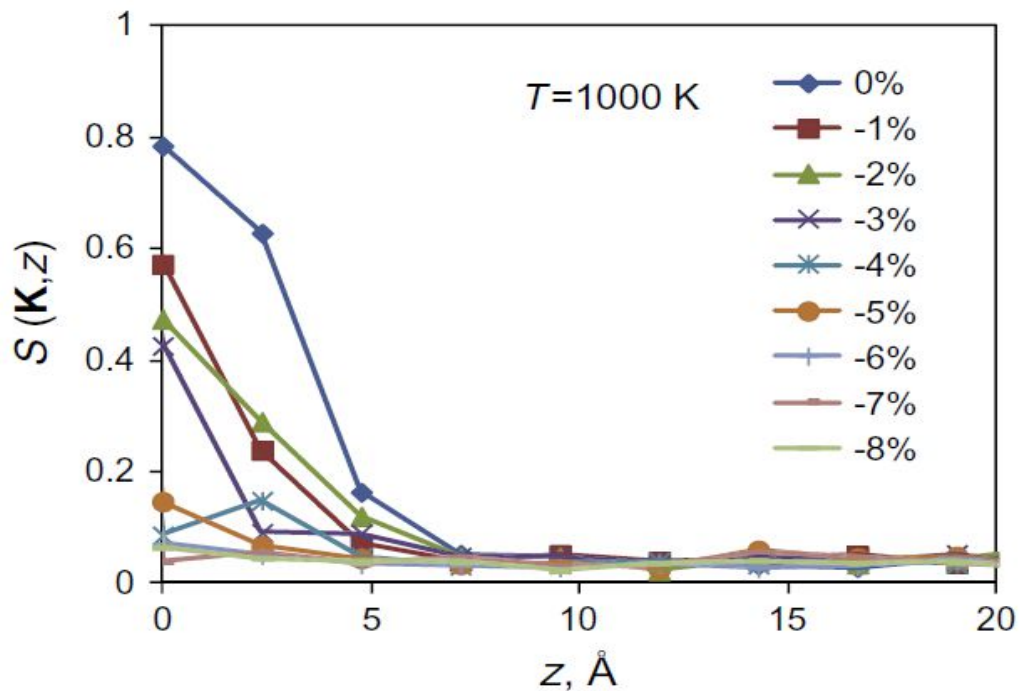


Figure 3.6. The static structural parameter of the Al atoms as a function of z in the systems with misfits from 0 to -8% at 1000 K [Men and Fan, 2012]. The maximal value is 0.8 in point $z=0$ where in previous Fig. 3.5 which is the result of my simulation, the maximum value at $z=0$ is taken 1 for the substrate. This difference should be pointed when comparison will be considered.

As can be seen in Figure 3.6 the in-plane ordering for misfits over 4% almost disappear. For the 5% misfit $S(z)$ is close to 0.15 even in the first layer at the interface. As $S(z)$ for bulk liquid is about 0.1 the system with 5% misfit do not exhibit the ordered structure inside the layered plane.

Results of MD give good fundamental background for developing new technology of liquid metal processing. Those results confirm clearly that oxides present in the melts can play role in nucleation. At the interface between ceramic-like oxides with small misfit and liquid aluminium, the ordering will happen. As this ordering is giving rise to a crystal growth, the oxides can be treated as grain refining particles. Thus, the uniform distribution of oxides should improve the quality of alloys.

Chapter 4. Fragmentation potency of high shear devices for metallic oxides – powder analyses.

4.1. Observation of defragmentation oxide powders after HSM-RS processing.

Direct observations of the dispersion of oxides in melts are impossible and really difficult to control. Usually, the dispersion is evaluated by indirect methods such as metallography and grain sizes reduction (Section 1.5). In the presented research, observations of the dispersion were made in a physical model system. Presented results show clearly that HSMs are really effective dispersers. To model the oxide behaviour firstly an indigotin dye was used. The dye was in a form of powder and tended to make films and clusters in the water, which was the reason for this material choice. The clusters are possible to observe by the naked eye and are shown in Figure 4.1 a. The indigotin has a density 1.199 g/cm^3 so just slightly higher than the liquid (water). This density difference allows us to observe the results of dispersion quickly and with low rotational speeds. An example of the observations of a dispersion process is shown in Figure 4.1.

As the density difference between the indigotin and water is much smaller than in the case of the alumina / liquid aluminium system, the clusters are easier to move by the flow. Of course, the forces between indigotin particles are likely to be different than those between oxide particles, as materials are chemically different, but in both cases, clusters and films are connected by van der Waals forces. The range of those forces depends strongly on the distance between particles and should be similar for both materials [Parsegian, 2006]. Thus, the dispersion of indigotin clusters is comparable with the oxides dispersion and with liquid metals processing by a rotor-stator high-shear mixer.



Clip 1. Clusters of the dye are localised under the head.



Clip 2. The sucking force brought clusters under the head into the one place on the impeller axis.



Clip 3. The pumping action causes the sucking force and the dye travels into the head. Jets start to be visible.



Clip 4. Dispersed and distributed by jets particles reduce the visibility, the dye amount under head decreases.



Clip 5. When few clusters together are passing through the head, the jets position is visible because the dye particles are present in jets emerging from stator holes.



Clip 6. Deagglomeration continues until all clusters localised under the head are well dispersed. Unfortunately, the dispersed powder dye – the indigotin – decreases the visibility and further observations are difficult.

Figure. 4.1. A sequence of pictures from the recorded video showing the clusters dispersion.

The view on the process shows that agglomerates can be easily dispersed by the device, even when the cluster pass the head only once. It is in good agreement with the latest findings of Tong [2016], as he predicts from a computer simulation a really short time necessary for oxides dispersion, the order of a ms. In the case of indigotin, the clusters are not strong enough to survive if they pass the head once. In the clip nr 4, we can see the big cluster under the head. Later, in the clip 5, the cluster, after passing the rotor-stator head, appears as separated particles which are thrown out the stator holes and distributed by jets around the head (clip 6).

This simple observation shows how effective is high-shear processing of the oxides present in the melts. To be a step closer to the liquid aluminium processing, in the next experiment we used alumina powder with different sizes to check how effective can be the high shear device in dispersing real alumina. A shearing process was done in a water. Again, as the density difference has the other value than in the alumina / liquid aluminium system, the time of shearing and the rotational speed necessary to shear particles are not comparable with a real situation. The alumina powder in water behaves as “heavier” particles than in the liquid aluminium because higher density difference between the solid and liquid. Thus, we used a maximum speed of the motor and extended the mixing time to about 4 minutes. The time choice is base on the observations. When hard alumina is processed by the metal head it causes strong noise. After about 3 minutes the noise disappears because of the sizes of particles, which are finer and moving easier through the head. To achieve good shearing effects, the shearing time was 4 minutes if is not otherwise given in the description. The same amount of powder was used each time (2 cm³).

To check fragmentation potency of HSM we take the photos of powder alumina particles before and after the high shear process. The main example of results is shown in the picture below (Fig. 4.2).

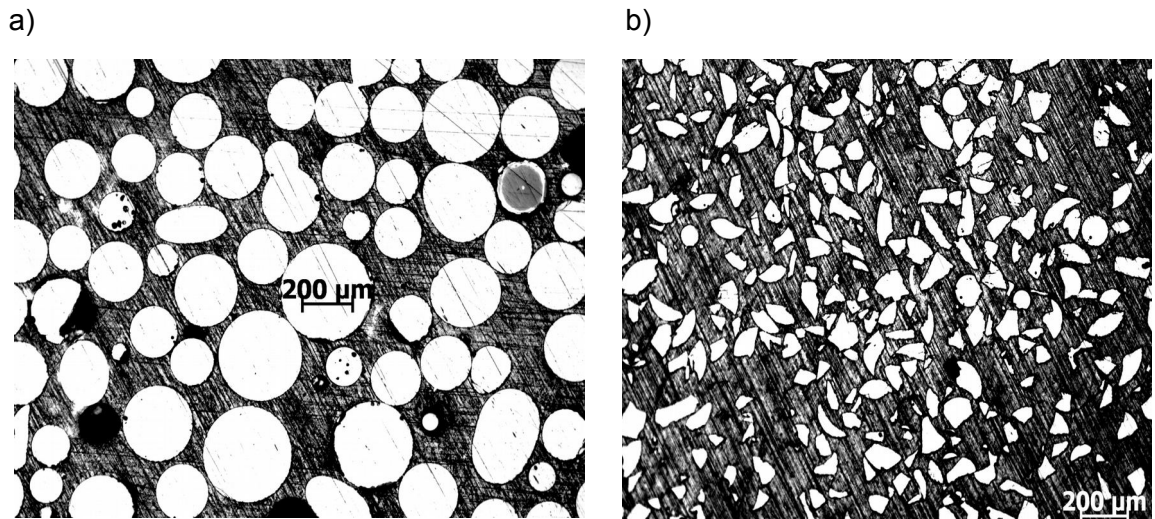


Figure 4.2. Oxide powder before (a) and (b) after shearing by the HSM with the original tubular head and the Silverson square holes stator.

The average particle size is difficult to establish. Before shearing, the particles were round shaped and afterwards, there are irregular shapes which are fragments of broken spheres. To find a particle size distribution we decided to measure the areas instead doing the one-dimensional analysis. Measurements were done for at least 200 particles in each case to find a particle area distribution. The results are given in Figure 4.3 (FDPA - the Frequency Distribution of Particles Area). We found that the average area after shearing decreases maximally to 7.7% from initial size (Figure 4.2). So the total decrease of a size is about 92% in the case of the original Silverson square holes stator. The time of processing was about 15 min so it is the example of a maximum size reduction achieved in this set of experiments.

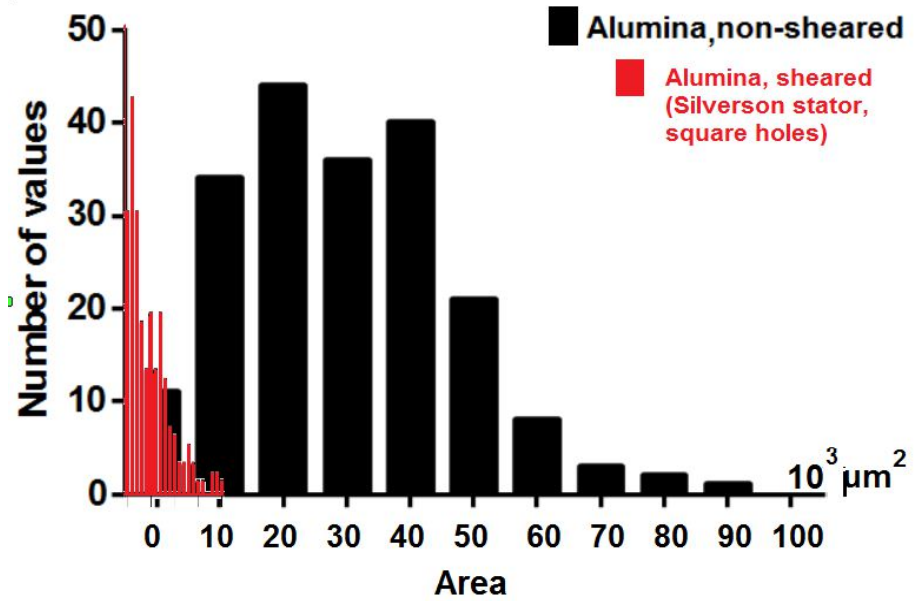


Figure 4.3. The histogram of the FDPA for alumina – a maximum size reduction against to the FDPA before 15-min shearing.

In Figure 4.3 is well visible that the size reduction achieved by MCAST-RS can be potentially about 90%. It is meaningful as alumina particles are bonded by strong ion bonds. The shear force has to be stronger than force responsible for bonding to break them into smaller parts. On Figure 4.4 the FDPA for the sheared powder is shown closer.

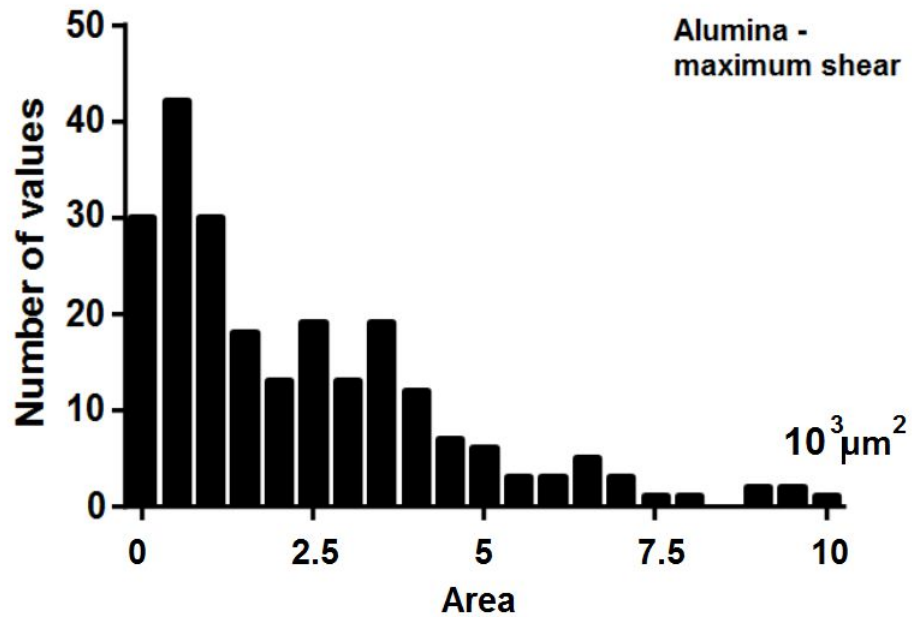


Figure 4.4. The histogram of the FDPA for the alumina – a maximum size reduction
(the enlarged portion of Fig. 4.3).

After shearing, particle surface areas decrease and are mostly in the range 0-3000 μm^2 . We do not observe clusters with sizes over 10 000 μm^2 that are dominant before shearing.

This first example shows clearly that the HSM processing can achieve a significant size reduction of particles. The presented defragmentation was done by using a commercial head with a small gap size (about 0.1 mm, the tubular assembly with square holes from Silverson). This design is not commonly used in BCAST. To check and compare other types of heads, the powder analyses was done with using the specially prepared heads (see Section 2.1.1).

4.2. The defragmentation efficiency for different head designs.

4.2.1. The stator with round holes (RH).

Typical rotor-stator used by a BCAST team is quite simple (see Fig. 2.4). The spherical holes are arranged in rows along stator axis. It is a special design ordered by BCAST laboratory and all published results of shearing (Section 1.5) were achieved by this type of head .

The particle fragmentation results are presented in Table 4.1 and in Figure 4.5.

Table 4.1. The FDPA of the alumina after the HSM processing with the RH.

Particle area (μm^2)	Frequency (%)
5000	20.7
10000	10.4
20000	9.6
25000	7
30000	7.4
35000	8.5
45000	3.3
50000	1.5
55000	1.5
60000	0.7
65000	0.4
70000	0.4
75000	0
80000	0
85000	0.4

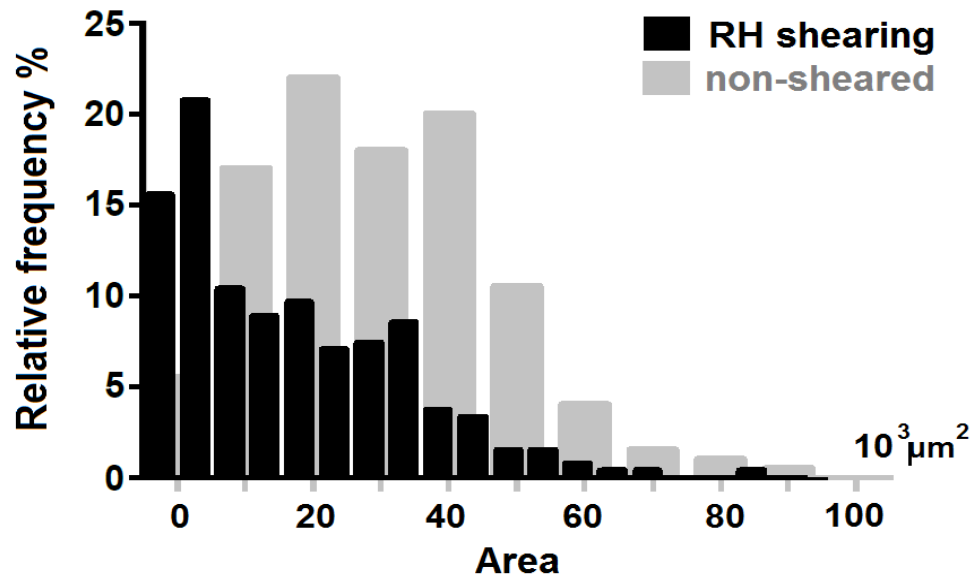


Figure 4.5. The histogram of the FDPA for the alumina after processing by the RH stator for 4 min.

Before shearing the particles, the surface area was mostly in the range from 10 000 μm^2 to 90 000 μm^2 and after shearing, we observe the higher amount of smaller particles (0-10 000 μm^2). Anyway, as we can see from the table (Tab. 4.1) mostly the area of particles is smaller than 50 000 μm^2 (about 67% of particles is in this range). About 30% of a particle areas is smaller than 20000 μm^2 . In the range from 20000- 45000 μm^2 is about 35% of all measured areas. For the non-sheared powder in that range (20000-45000 μm^2) it was more than 60% particles, so sizes of them definitely decrease.

The question is how potent are different heads, especially the dispersing head with square holes. Next experiments can give us an answer if the defragmentation potency depends on the shape of the holes.

4.2.2. The stator with square holes (SqH).

Square holes are often used for dispersion purposes (see Table 1.1 with the shapes of Silverston stators). As given in Chapter 2 the rotor-stator head used to improve liquid metal quality is made from different materials than commercially used steel. The rotor-stator devices are made from ceramic-like materials. Thus, the cost of one head is about £2,000 [the information from P. Lloyd, the laboratory technician]. Each significant change will increase the costs. As ceramic-like materials have high elastic modulus and hardness so the preparation of square-shaped holes is much more difficult and expensive than round-shaped holes. It is why a head typically used in BCAST has simple rows of circular holes. The main question is how we can improve this design to achieve the best results without unnecessary costs increase. To find the answer we have to compare the potency in defragmentation of both holes shapes in identical conditions.

Table 4.2 shows the results of the alumina shearing by the SqH and in Figure 4.6 these results are compared with results of shearing by the RH head. For convenience, both results are shown against the non-sheared FDPA.

Table 4.2. The FDAP of the alumina after shearing by the square-holes head.

Particle area (μm^2)	Frequency (%)
0	35
2000	16
4000	8.5
6000	4.2
8000	5.7
10000	4.2
12000	4.2
18000	1.2
20000	1.8
22000	1.2
24000	0.9
26000	1.2
28000	3
30000	1.5
32000	2.1
36000	0.3
38000	0.6
46000	0
48000	0
50000	0.3

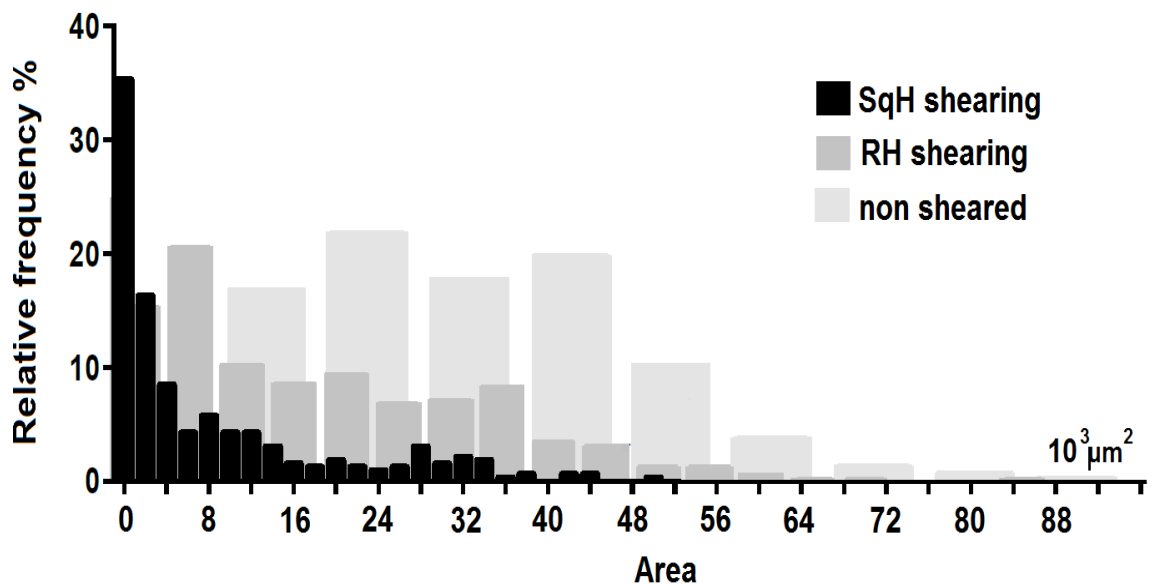


Figure 4.6. The histogram of the FDPA for sheared alumina particles with the SqH head for 4 min.

We can observe that square holes have a big influence on the sizes reduction. A number of holes, time and mixing speed were the same for both experiments. Thus, we observe the only effect of the holes shape change.

If we compare the percentage results recorded in Table 4.2 with presented before for the head with round holes, we can state, that for the square holes head over 70% particles are in the range 0 to 10 000 μm^2 . For the round holes head in this range is only 30% of particles. As analysed before, after shearing by the head with round holes the initial sizes of particles decreased. Measured particles processed by RH have surface areas up to 90 000 μm^2 while processed by SqH have maximum areas reduce to about 50 000 μm^2 . Secondly, there are about 50% more particles with sizes in the range below 10 000 μm^2 . This result is much better than achieved before (RH). It shows that square holes are really effective to shear even hard particles. Using of this holes shape would be beneficial.

However, costs of the square holes preparation are currently very high we have to use round holes in metallurgical experiments.

Let us compare the situations of the model and liquid metal processing. Of course, if we improve the head defragmentation potency, the forces exerted on particles

inside a rotor-stator will be stronger independently from the mixed system. If stronger forces are applied the defragmentation process will happen quicker and will be more effective. In a real situation, we have a little bit different process than in the model system. In the molten metal oxides are present as films and clusters (compare Section 1.3). Particles in agglomerates are joined by van der Waals attractive forces. To deagglomerate them it is necessary to apply forces which are stronger than those attractive forces.

In the model system, we are applying shear forces to alumina particles bonded with ion bonds in bigger granules. As shown in the previous sections (see Fig. 4.3), the alumina powder sizes after shearing decrease by 90%. Thus, applied shear forces are stronger than the bonding forces.

A deeper look at physical basic rules explains that the van der Waals bond is created when any two neutral nonpolar atoms or molecules are attracted to each other by inducing dipoles in each other. It is due to fluctuations of the charge distribution. A fluctuation in the charge distribution in the first particle produces a temporary dipole moment which induces a dipole moment in the second particle. The induced dipole moment is the reason of induction of dipole moment again in the first particle so the process continues. Both particles are attracted to each other due to the charge difference. The resulting force is known as van der Waals force. The attractive part of the bond potential goes as r^{-6} (r – distance between both charges localisation), [Naumann, 2008]. As the force decreases very fast when the distance increases, thus this force is known as a short-range force. The van der Waals bond is the weakest of all bond types, the strength of the van der Waals force is between 0.01eV and 0.1eV per the bond [Roesler et al., 2007; Smirnov, 1992].

The aluminium oxide molecules are bonded by ionic bonds. The bond energy is typically about 8-10eV [Il'inskii and Keldysh, 2013; Rita, 2014] what means that in the model situation we are breaking bonds about 100 -1000 times stronger than expected to bond oxide films and agglomerates in the melt (van der Waals forces).

Unfortunately, it is difficult to predict exact values of forces which join the agglomerates and films together as they depend on local and temporary conditions, as a presence of dipoles and distance between them as well as on the number of dipoles in agglomerates. Instead of predictions, we can refer to real shearing effects. As described before (Chapter 1.5), shearing forces applied when the liquid was processed by the RH were strong enough to break agglomerates of oxides. This is well proven as the processing of the liquid metal by the RH results in a grain size refinement. Thus, this is an

indirect evidence that the shear applied by this head is enough to broke agglomerates and films.

According to our modelling results, similar forces as were applied during real melt processing, in the model situation changed sizes of the crystal alumina from the initial one to smaller. The smaller size can be described by the FDPA with area sizes ranged below 50 000 μm^2 and with over 50% of a particle areas smaller than 30 000 μm^2 . Thus, this FDPA reflects the forces which definitely will cause the oxides deagglomeration.

Besides those experimental observations, there exists another evidence of the films breakage. Men et al. [2010] used both experiments and the theoretical modelling with based on the free growth model to investigate the mechanisms of a grain refinement by intensive melt shearing. They found that intensive melt shearing can effectively disperse MgO films into more individual particles. The MgO particle density was three orders of magnitude higher than without shearing. Additionally, the density of active nucleating MgO particles increased by a factor of 20 compared with those of the non-sheared melt. Men et al. [2010] attributed the refining effect of intensive melt shearing to the significantly increased refining efficiency of the naturally occurring MgO particles. The experimental part of their work includes image analysis of the MgO particle size and the size distribution in the pressurised filtration samples for the AZ91 alloy with and without intensive melt shearing (see Figure 4.7 and 4.8).

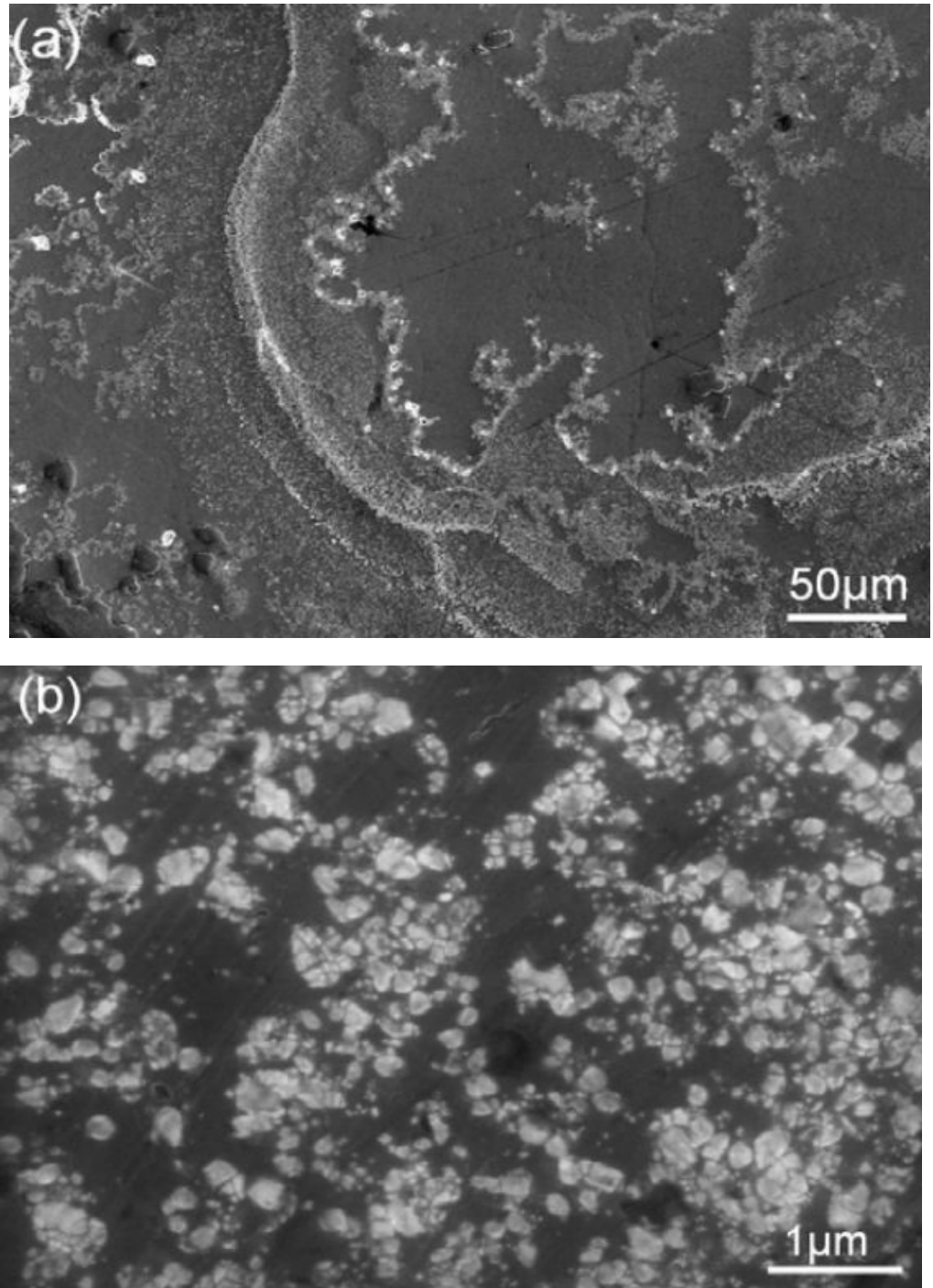


Figure 4.7. SEM micrographs showing the morphology of the MgO particles collected at 650°C by the pressurised filtration of (a) non-sheared and (b) sheared AZ91 alloy melt. Films and agglomerates are broken into fine particles [Men and Fan, 2010].

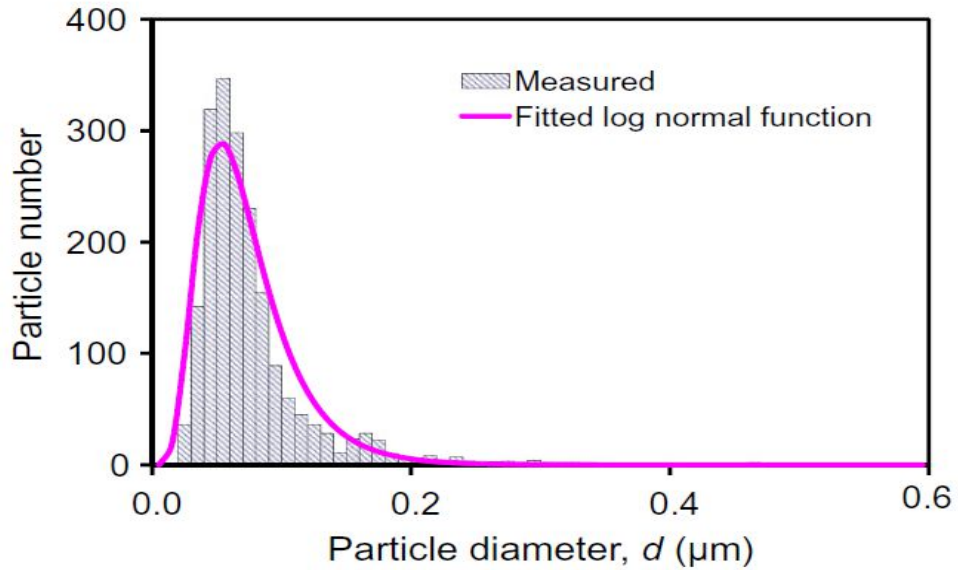


Figure 4.8. The measured size distribution of the MgO particles in the sheared AZ91 alloy melt collected by pressurised filtration from image analysis of SEM micrographs [Men and Fan, 2010].

Sizes of MgO particles were below 0.3 μm and are mostly localised around 0.07 μm . It is consistent with the reported narrow size distribution of potent nucleant particles in different systems. The sizes of described grain refiners are usually between 0.5 to 10.5 μm [Conrad, 2004; Armstrong, 1970; Schiötz et al., 1998; Hall, 1951]. The size of MgO particles after shearing is really small and their agglomerates can play a role in the nucleation. MgO particles are the one example of oxides present in Al-Mg melts and the grain refining effect of them has been reported (Section 1.5).

Results found by Men et al. [2010] can be compared with those presented in this work. The shear forces applied in work presented by Men et al. [2010] are comparable with forces applied in the experiment with alumina shearing by the RH. We can conclude, that if any kind of analysed designs of the head will give results comparable with achieved with the RH head, or the size reduction will be better, the applied shear is enough to break oxides films and agglomerates. If the simple change of design improves the results, this design can be considered as the optimal for liquid metal processing. Next part is showing results of shearing alumina by another head design.

4.2.3. The new design of head – crossH.

The main reason for a new design of the head is a mixing improvement and increase of the agitation uniformity as will be explained in Chapter 6.

To validate a new design the alumina powder was sheared by the new head. The change in holes arrangement results in the change of local pressure inside the head. In the case of the RH, the pressure exerted by the fluid on stator walls is stronger close to areas between rows, where holes are no present. Inside the new head, we expect smaller changes in the local pressure as the area between holes has more uniform sizes.

In the case of the RH, the jets emerging from stator openings are not distributed randomly around the head and there is a possibility that stagnation areas occur between them. To avoid this problem the proposed head has a cross-line arrangement of holes. Secondly, this change cost little as we just change places of holes on the stator without expensive shape changes. Results of the alumina powder shearing with the new design are presented in Table 4.3 and in Figure 4.9.

Table 4.3. The FDPA of the alumina after the HSM processing with the crossH.

Particle area (μm^2)	Frequency (%)
0	26.9
5000	15.3
10000	18.6
15000	9.1
20000	9.5
25000	6.6
30000	6.6
35000	3.7
40000	0.4
45000	0.8
50000	1.7
60000	0.8
65000	1.6

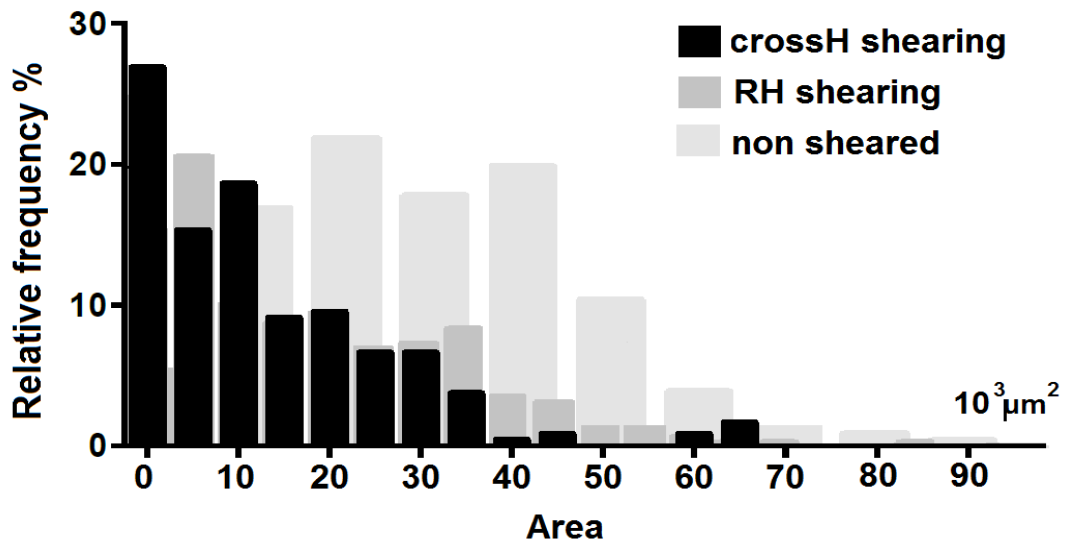


Figure 4.9. The histogram of the FDPA of the alumina after processing by the HSM with the crossH (4 min) against results obtained with the RH (4 min) and the FDPA of a non-sheared powder.

Figure 4.9 demonstrates a size distribution of alumina processed by the crossH. Particles have mostly areas below or equal $10\,000 \mu\text{m}^2$ – about 60% of them are in this range. In the case of the RH, it was only 30% of particles with the area smaller or equal $10\,000 \mu\text{m}^2$. Results are even better than the size reduction after the alumina processing by the RH. The design was changed to improve the uniformity of the agitation and this improvement is for the defragmentation potency is beneficial. Obviously, the uniformity of mixing inside the rotor-stator assembly improves the shear process as well as the agitation of the bulk liquid.

To apply the new design for liquid metals processing we need to be sure that the design changes will not decrease the shearing potency of the head. However, the RH is proven to apply enough shear to broke oxide films and agglomerates as discussed in the previous chapter. As results of shearing of alumina powder with a new design of the head (crossH) are even better, the new design is advised for the introduction to the melt shearing.

4.2.4. Gap increasing.

According to Equation 1.6, the shear ratio inside the gap depends strongly on the gap size. The gap increase should decrease a present shear ratio resulting in smaller shear forces. To compare what will be the influence of an increased gap size the alumina powder was sheared with the smaller rotor inside the previously used stator. The gap expanded from 0.4 to 0.8 mm. Results of experiments are presented below.

Table 4.4. The FDPA of alumina particles after shearing with an increased gap.

Particle area (μm^2)	Frequency (%)
0	26.3
5000	20.9
10000	10.4
15000	10.8
20000	8.1
25000	7.4
30000	5
35000	3.7
40000	3.7
45000	3.4

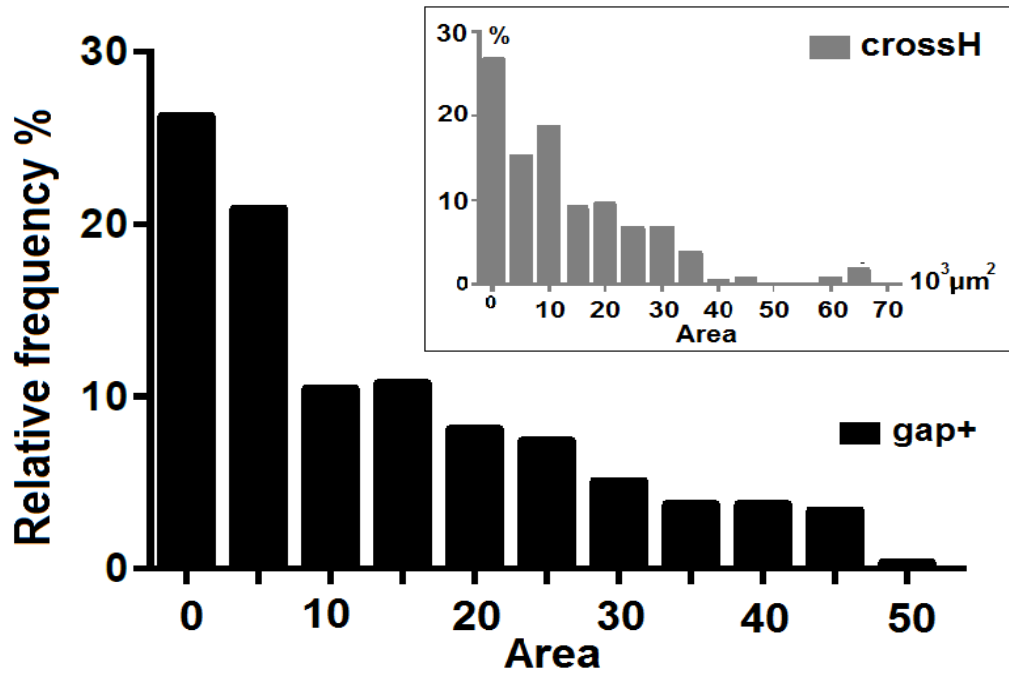


Figure 4.10. The histogram of the FDPA of the alumina after processing (4 min) with the increased gap (gap+; gap size 0.8 mm). The used stator was the crossH. The inset shows results for the crossH with a typical gap size (4 min).

The gap increase results in the following (Figure 4.10). A number of the particles up to $10\,000 \mu\text{m}^2$ is about 10 percent smaller than before. The gap was doubled and the resulting sizes distribution is similar to observed before. It is surprising as the shear in the gap is usually strongly dependent on a gap size (Eq. 1.6). One of the possible explanations is given by Calabrese et al. [2002]. His research showed that impeller with an enlarged gap ($d = 1 \text{ mm}$) produced smaller mean drop sizes in the turbulent flow regime than that with a smaller gap ($d = 0.5 \text{ mm}$). Authors concluded that shear in the gap was not the predominant droplets breakage mechanism in HSMs in the turbulence regime. The gap increase results in the flow rate increase and more effective mixing (more fluid will pass the head in the same time when the gap is enlarged). Thus, the purpose of their simulation was to find the dependence between the enlarged gap size (from 0.5 mm to 4 mm) and the dispersing and emulsification efficiency. The efficiency of dispersion (or emulsification) depends on the energy field inside the flow. They found that the most intense turbulent kinetic energy occurs on the leading edge of a downstream stator tooth. It happens when the stator slot was overlapped with the rotor tooth and a

flow rate began to fall. Thus, the maximum energy field was observed with a smaller flow rate of the HSM. Additionally, high flow rates (when the rotor and stator slots were aligned) were accompanied by the low energy field. The main application of HSMs is not agitation of fluid (dependent on the flow rate), but the dispersion mostly. Thus, even if the shear in the gap is not a major contributor to the dispersion mechanisms, Calabrese et al. [2002] concluded that for emulsification or dispersion purposes it was necessary to have a narrow gap. They also suggested that the droplet disruption occurs on the stator surfaces and inside turbulences in the jets emerging from stator holes.

In the view of those findings, our results are not so surprising. It is probable that the gap change was not so significant, especially as the resulting gap was still really narrow (below 1 mm). Since the gap maybe not the main factor responsible for dispersion some gap increase does not affect results strongly, as can be concluded from the equation 1.6 describing a nominal shear ratio inside gap. From our observations, we can conclude that the gap can be safely doubled from the initial size (0.4 mm) without the considerable change in the dispersing efficiency of the mixing head used for a liquid metal processing. The gap size can be proportionally scaled for bigger head diameters as a presented head diameter was 22 mm.

4.3. Time influence on alumina shearing process.

The alumina shearing was done with the crossH for two different times – 4 and 10 minutes. As described before, the time 4 minutes was chosen because after this time in the mixed liquid any significant changes was not observed. Up to the time 3-4 minutes, the noise suggests that the alumina is sheared by the head. After this time, the process was smoother, and no changes were noted. To validate this observation two sheared powders were compared – 4 minutes and 10 minutes. Table 4.5. and Fig. 4.13 present the observed results – the FDPA of the alumina sheared for 10 minutes with crossH. To compare those results the inset on Fig. 4.13 shows results achieved after 4 minutes of shearing.

Table 4.5. The FDPA of the alumina processed for 10 minutes.

Particle area (μm^2)	Frequency (%)
0	50.8
5000	16.8
10000	10.1
15000	7.1
20000	5.4
25000	3
30000	2.7
35000	1.7
40000	1.3
45000	1

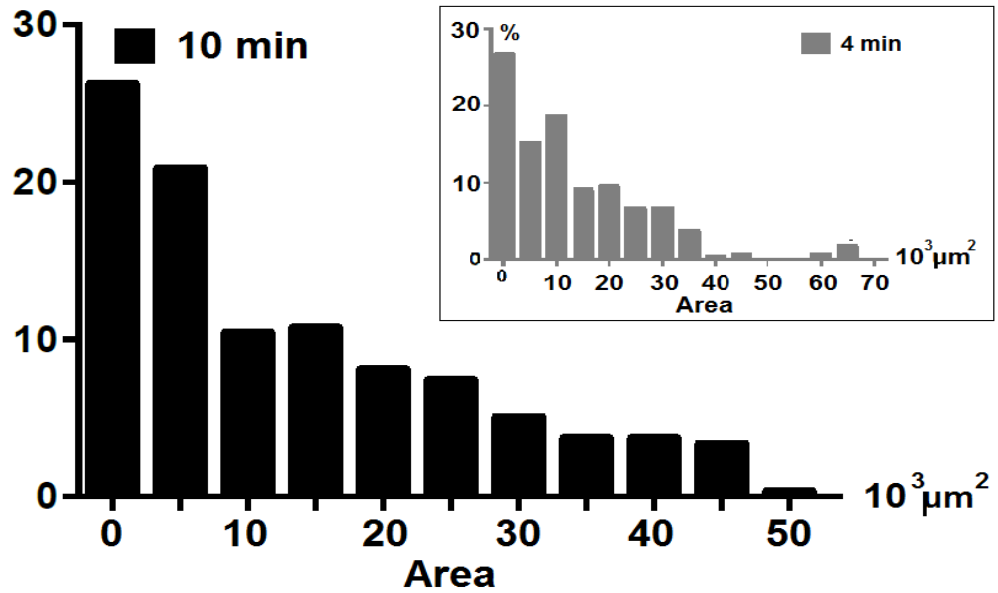


Figure 4.11. The histogram of the FDPA of the alumina after 10 minutes of shearing by the HSM. The used stator was the crossH. The inlet shows results obtained after 4 min.

Longer processing of alumina (see Figure 4.11) improves the results of shearing. In the range 0 to 5 000 μm^2 it can be found over 67% of measured sizes. With 4 minutes processing time in this range was 42% of particles. As the time was over 2 times longer, so this change is not so significant. The chosen time (4 minutes) used in previous experiments was the same for all described processes what makes the results comparable. But according to this data, extended time will still have some influence on the shearing effects.

Used time will be not comparable with the shearing time which is necessary to the oxides deagglomeration in melts. As discussed before, the shear forces which should effectively disperse oxides are much smaller than in the case of alumina particles. The time necessary to shear them is unknown but computer simulations indicate that only one pass will be effective for oxides dispersion [Tong, 2016].

Taking the Tong [2016] prediction into account, the shearing time will be optimal if all liquid will pass head at least once. That means that time should be at least equal to the time necessary to perform full agitation of liquid plus time necessary to flow all liquid through the head. As the predictions of the model cannot give us exact forecast about the mandatory time for effective oxide shearing we will obtain these results experimentally and this will be presented in the following chapters of the work.

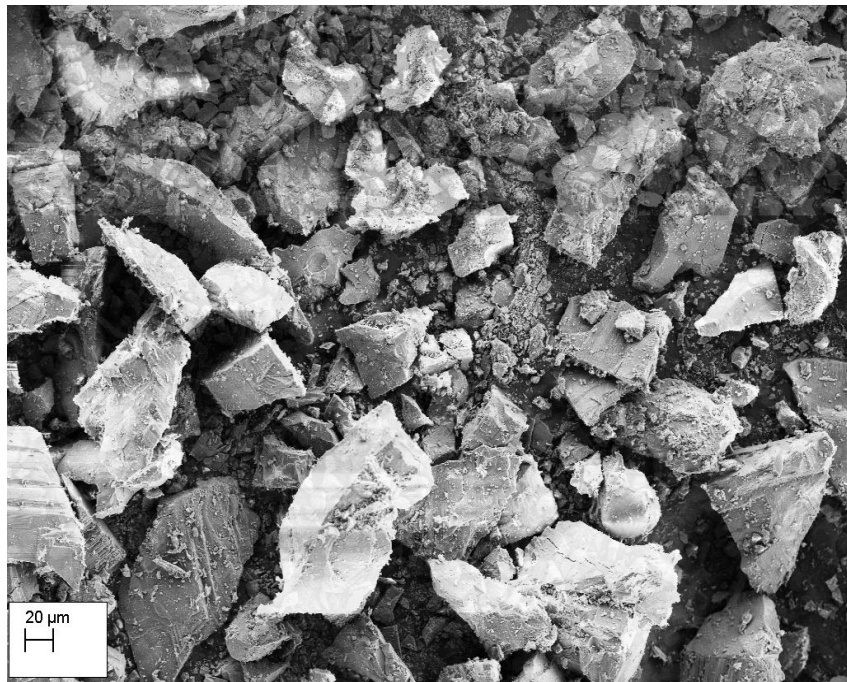
4.4. Validation of defragmentation pictures analyses.

Figure 4.2 demonstrates alumina granules before and after shearing. The area was measured from those pictures. To validate the used method and to show that after shearing we observe the fragmentation of spheres several SEM pictures were taken. One of them is presented in Figure 4.12. If we compare the SEM picture with Figure 4.2 we can clearly decide that measured objects were parts of broken alumina granules. Fragments of spheres do not strongly tend to join together, so the observed sizes reflect properly the size decrease. Measured shapes (Figure 4.2 b) with a good probability can be treated as separated parts of broken granules.

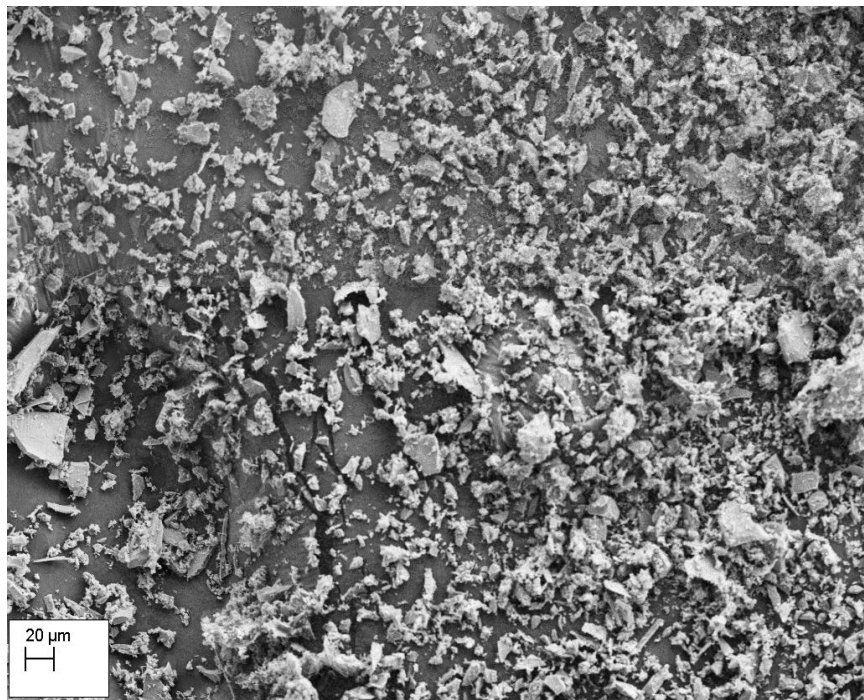


Figure 4.12. SEM picture of sheared alumina powder. We can observe some non-sheared particles of alumina and broken parts of spheres. As there are well defined so in cross-section of samples we observed sizes of single particles.

To confirm our results obtained with the alumina powder we tried to repeat some of them using MgO. Unfortunately, the magnesium oxide tends to make clusters in the epoxy kit and it is really difficult to measure particle sizes after shearing. To observe shearing effects we have to use a more accurate method, the SEM microscopy. Obtained photographs show that the sheared powder is much finer than an original one. As particles are not separated so well as before (for alumina compare with Figure 4.12) we measured areas of the biggest particles on the pictures. From Fig. 4.13 the sizes of the biggest particles were measured and the same procedure was repeated to find sizes of them after shearing (Fig.4.14).



*Figure 4.13. SEM picture of a non-sheared MgO powder.
We can observe different sizes of particles.*



*Figure 4.14. SEM picture of a sheared MgO powder.
The size decrease is well visible.*

As we measured only the biggest and well-separated particles, results presented below (Figure 4.15) should be used only for a both powders comparison and can not be used to estimate average sizes of particles.

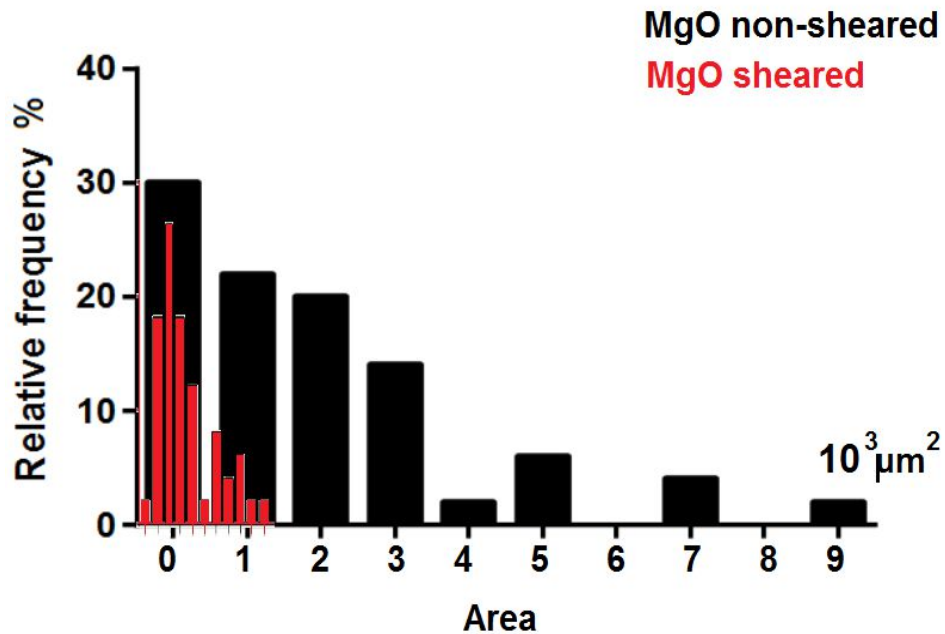


Figure 4.15. The histogram of the FDPA of MgO particles before and after shearing (results obtained with crossH, 4 min shearing).

All particles with the area bigger than $1000 \mu\text{m}^2$ are broken into smaller pieces because the bigger clusters are not present in the specimen after shearing. All biggest clusters are broken into smaller particles with the size decrease about 8 times – from maximum values about $9\,000 \mu\text{m}^2$ to maximum sizes about $1200 \mu\text{m}^2$.

Obtained results let us conclude that shearing of the magnesium oxide is really effective. The MgO it is not so hard as the alumina so the shearing effects are achieved much easier. Hence, this observation is an additional proof that the weak bonds of oxides films or agglomerates should be defragmented much more easily and quickly than the crystal alumina granules.

It is necessary to remember that in presented modelling the size reduction is the effect of the alumina granules breakage, what means that we have to break strong bonds between particles. As discussed before, liquid metals contain oxide films and clusters connected by much weaker forces. Since the process is so effective even with much

stronger bonds, it is clear, that forces applied by the HSM will be enough strong to shear and break clusters. We can assume that liquid metal processing does not require so much energy as to break alumina granules. It means that used rotational speed can be much smaller than used to break granules.

The forces inside the head decide about the shear which breaks up the particles or the agglomerates. The mechanism of breakage both can be different. 'In the experiments with the powder alumina particles, the particles inside the gap can be broken because of collisions between them as well as because of shear exerted by the flow. In the case of intrinsic particles in liquid metals which are much finer, we are not expecting so much collision between particles. The mechanism of breakage, which can be dominant, is similar as discussed by Calabrese et al. [2000, 2002]. In the case of the droplets size the shear inside the gap, where the most collisions are expected, was not predominant mechanism of the size reduction. The longitudinal shear when the drops pass the stator holes and the collisions with the stator openings are believed to play the more important role. The intrinsic oxide particles will not be broken during the HSM processing since they are small already. But any agglomerates or films will not survive the shear and, similarly to droplets considered by Calabrese et al. [2000, 2002], will be broken by longitudinal shear even if no so much collisions is expected. Due to the same reason, the volume concentration of oxide particles will not influence the results of the fragmentation significantly.

The observations with the indigotin dye and FDPA analyses help us to find that:

- 1) The cluster or film have to be brought by flow into the head and pass the stator at least one time.
- 2) The sheared oxide have to be distributed uniformly in all vessel. The high shear dispersion of agglomerates requires two important steps. The first step is the shearing of agglomerates inside the head and the second is the distribution step when sheared particles are uniformly moved by the flow. The dispersion and the distribution happen at the same time when the high-shear mixer operates.
- 3) It is proven that the HS processing of liquid metals is a really potent method to achieve the defragmentation of agglomerates as the defragmentation of the

alumina occurs in all presented experiments. The defragmentation potency of the HSM was validated too by experiments with MgO with good results.

- 4) The shape of holes in the stator has a strong influence on the defragmentation potency and the best results were obtained with square holes. However, the defragmentation potency with round holes for oxides present in the melt is proven experimentally and can be predicted from the basic physical rules and from computer simulations.
- 5) The gap size can be doubled as compared to the standard value without a significant change in the head defragmentation potency.
- 6) Changing of the holes arrangement of the stator (crossH) improves the defragmentation potency, which can be the result of a significant improvement in the flow uniformity.

Chapter 5. Distributive characterisation of mixing.

As shown by the computer modelling [Chapter 3] and experimental practice [Section 1.5] small oxide particles can play the role in the nucleation. The sufficient grain refiners usually have small sizes (up to about 10 μm) and should be dispersed and distributed uniformly in the liquid metal. Chapter 4 shows that the HSM is a very potent tool for defragmentation of particle clusters and agglomerates. To play a role in nucleation those small fragments of films and clusters should be distributed evenly in the volume of a liquid processed by the HSM. The uniform distribution results from the flow movement. Thus, the next step to reach the best conditions for effective liquid metal processing with the HSM is the improvement of a flow motion. The full agitation means that all films or clusters will have a chance to pass at least once the mixing head within a required time. Chapter 5 addresses the conditions that should be chosen to maintain the full liquid agitation.

5.1. Pseudo cavern size modelling.

5.1.1. Pseudo-cavern radius.

As described in Chapter 2 from observations made with the SiO_2 physical model and the same amount of powder used each time (8 cm^3), we can determine pseudo-cavern radii by measurements of the pseudo-cavern trace on the tank bottom. Averaged measurements for different rotational speed are presented below in Table 5.1.

Table 5.1. SiO_2 pseudo-cavern radii for a different N (crossH).

N [rpm]	R_{si} [mm]
1000	44 ± 1
2500	60 ± 1
3000	70 ± 1
4000	84 ± 2
5000	107 ± 2
6000	127 ± 3
7000	179 ± 3

The pseudo-cavern radius grows up with N increase. We can find R dependency on N in the graph (Figure 5.1).

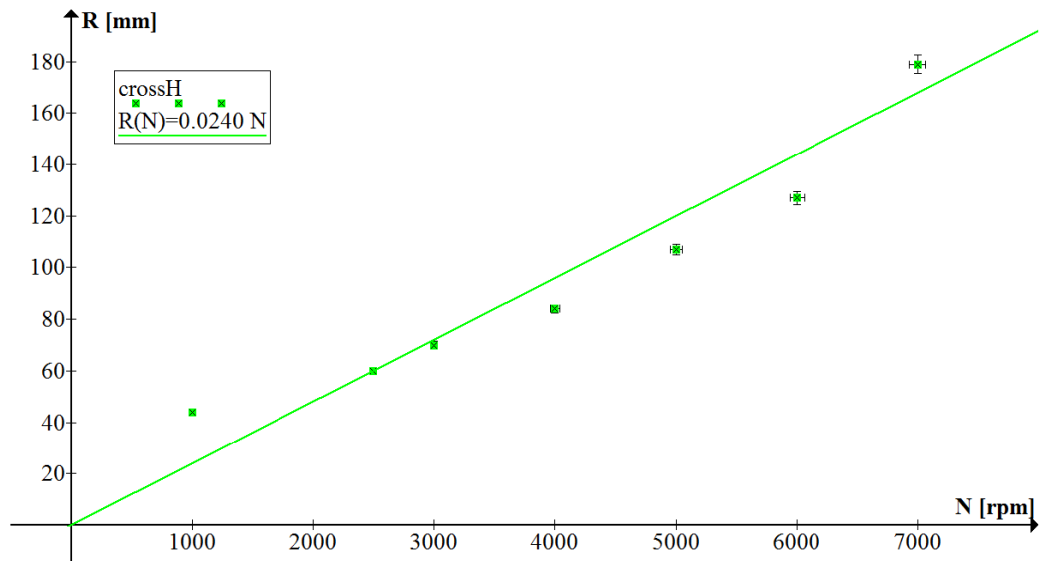


Figure 5.1. The measured pseudo-cavern radius as a function of the rotational speed.

The dependence seems to be linear and can be approximated by the trend line $R(N)$. From presented results we can describe the $R(N)$ function for the crossH (Figure 5.1):

$$R(N) = 0.024 \cdot N \quad \text{(Equation 5.1)}$$

The formula is valid for N (a rotational speed) given in rpm and R (a pseudo-cavern radius) in mm. It is important to remind that this equation is valid only for crossH and will be further used to establish a more general formula.

The linear dependence of the well-mixed region on N can be related to circulation which occurs in the flow (Section 1.2.1). Without disturbing by walls, the velocity of jets decreases along the way and flow circulates due to a centrifugal action of the rotor which acts as a pump [Paipetis, Kostopoulos, 2012; Gülich, 2014]. The circular loop observed in the flow is the effect of two forces. The first one pushes out the liquid out of the head through the stator openings, giving to jets (shown by red colour in Figure 1.8) the initial velocity which allows the jet to travel towards the tank wall (the radial velocity component, starting from the head centre along the head radius direction). The second force – the effect of the pressure difference, is the “sucking” force. In simulated figures, we can

observe this pumping force below the head (Figure 1.8). The sucking mechanism is a little bit more complicated as besides the flow coming from the bottom into the head along the head longitudinal axis, it can cause the movement of the fluid through the stator opening back into head behind the jets. When the fluid from the bottom of the tank is sucked up into the head, the pressure differences cause jet recirculation and flow movement back into the head. As a result, we have the complex vortex flow pattern shown in Fig. 1.17. As in cross-section plane, the flow movement is almost circular (see Fig. 1.18), it means that both forces are balanced. The jets initial velocity will vanish but the sucking force will give to the fluid the velocity which causes the flow redirection. Since the movement of the fluid is approximately circular, this motion can be described as the motion with a constant linear value of the speed (the resultant speed given by all forces present in the system). Since the both forces are balanced, the amount of liquid which is pushed out the stator holes travelling first as the jet is later going with the similar resultant velocity back into the head. This means that if the initial velocity increases, the jet length will increase too. If the fluid is pushed out faster the pressure changes will happen faster too, which is reflected in the faster movement of the liquid into the head. The circulation loop will be established, but with the initial velocity increase, the jet length increases too, which means that the radius of the circular loop will be proportionally larger. The jet length in the same system depends only on the rotational speed of the impeller as this speed is responsible for giving the initial speed to the liquid pushed out the stator holes. The prediction of the fluid motion circular characterization (Section 1.2.1) confirms our results, as we experimentally found a linear dependence of the pseudo-cavern size on the rotational speed N . These findings are with good agreement with a previous research. Mortensen et al. [2011] made PIV measurements of the flow caused by the rotor-stator batch mixer inside and outside the stator holes. The position of the PIV light sheet plane in Mortensen et al. [2011] research is perpendicular to plane recorded in our laboratory. Mortensen [2011] focused on the flow around stator holes and inside the head. It has been concluded in their work that “the calculated jet velocities and flow rates through the stator openings were found to be proportional to the rotor speed while energy dissipation rate scaled with the cube of rotor speed”. Since the initial jet velocities are proportional to the rotor speed (N), the pseudo-cavern size will be proportional to N as found from our experiments.

The observed values of pseudo-cavern radii depend not only on the rotational speed but on the geometrical properties of the mixing head as well. This should be taken into account and some scale-up criteria will be given in the following part. It is important

to remember that the constant value 0.024 given in the function $R(N)$ is found experimentally for the used crossH impeller. Thus, the geometric conditions in the system are reflected in this value. Results can be taken as the characterisation of the crossH and should be scaled for different heads. Since the geometry of the head is set and the vessel is big enough to treat flow as independent on the vessel shape (jets are not scattered from walls), the value of the pseudo-cavern radius is dependent only on N and rest of conditions can be described by one constant found experimentally. If other types of stators are used, this constant can be taken as an approximation what will be further discussed in Chapter 6 (Section 6.2.2.2).

5.1.2. Measured pseudo-cavern height (argon gas model).

To find the second size – a pseudo-cavern height (H), more experiments were done with the additional physical model. The argon gas model allows us to observe the reversed pseudo-cavern shape and measure the pseudo-cavern sizes not only in the x direction (R) but in the y direction (H) too (compare Figure 2.10). Measured sizes are given in Table 5.2.

Table 5.2. Argon gas pseudo-cavern sizes for the different N .

N [rpm]	R_g [mm]	H [mm]
2000	20 ± 1	28 ± 1
3000	24 ± 1	35 ± 1
4000	33 ± 1	63 ± 1
5000	44 ± 1	70 ± 1
6000	53 ± 2	84 ± 1
7000	95 ± 2	107 ± 2

All measurements were done for argon gas bubbles and sizes of the pseudo-cavern are different than obtained from the SiO₂ model. It can be visible if we check measurements of the pseudo-cavern radius presented below for both models (R_{si} - radii measured with the SiO₂ model, R_g – radii measured with the argon gas model, Table 5.3). The ratio of them is calculated to show the sizes difference.

Table 5.3. Radii of the pseudo-cavern measured for both models, the sizes comparison.

N [rpm]	R_{si} [mm]	R_g [mm]	R_{si}/R_g
2000	59±1	20±1	2.9
3000	70±1	24±1	2.9
4000	84±2	33±1	2.6
5000	107±2	44±1	2.4
6000	127±3	53±2	2.4
7000	180±3	95±2	1.9
Average:			2.5

The averaged ratio of the measured radii is equal 2.5 what means that sizes of both pseudo-caverns are completely different. The pseudo-cavern observed with the argon gas is consistently smaller than that observed with the SiO₂. Since the SiO₂ model is comparable with the real liquid metal processing (see Section 2.1.3), the sizes measured with the argon gas have to be scaled. The comparison of presented measurements allows us to calculate the missing height of the pseudo-cavern for the SiO₂ model. The used modelling procedure has two main assumptions. The first: pseudo-cavern sizes of both models grow up proportionally each to another. Thus, the observed growth is influenced only by the N, not by forces present in the initial system. Second: the pseudo-cavern grows up proportionally along both x and y-axis when the N increases. Hence, the ratio of both pseudo-cavern dimensions is constant.

To find an explanation of the first assumption we have to analyse particles velocities in each system. First, let us consider the movement of the SiO₂ particle inside

the flow. When the rotor-stator device is turned off and the SiO_2 particle is at any point of the tank it will move down because of the gravitational force. Thus, in this point at chosen time the particle will have the velocity given by gravitation shown in Figure 5.2 a. Without forces applied to the fluid by the HSM, all particles will tend to move down along a y-axis and settle on the bottom of the tank. When the HSM is turned on (constant N), the flow starts to move the fluid and particles. Jets are pushing particles along the x-axis and the sucking force brings them into the head again. In each point of the tank, the resultant flow velocity v is attached to the particle. The movement of particles is the result of two velocities – given by the gravitational force (v_g) and given by the flow (v_f). The velocity given by the flow is proportional to the N. This process is shown in Figure 5.2 b.

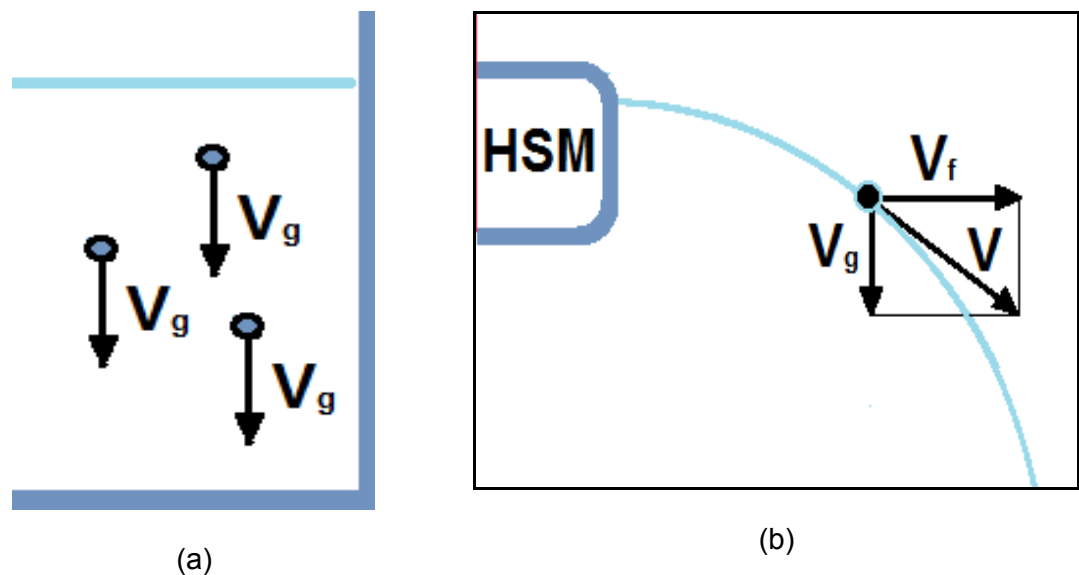
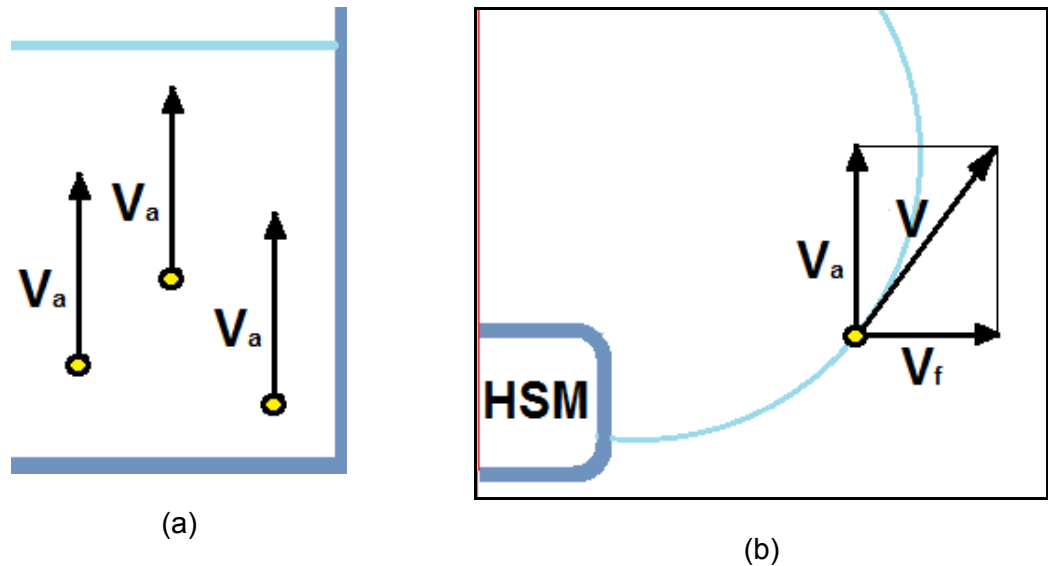


Figure 5.2. (a) SiO_2 particles without mixing forces present in the system move downwards due to the gravitational force with a velocity equal the v_g
 (b) The resultant velocity of the particle in the presence of mixing forces is the effect of movement with a flow velocity v_f , scaled by the vector v_g .

Let us consider the second physical model. The argon gas without flow forces moves up due to density difference. The Archimedes law describes this phenomenon. If we simplify the situation, the velocity due to this density differences is given to gas bubbles upwards, along the y-axis, as shown in Figure 5.3 a. If the HSM works, flow velocities change the situation of gas bubbles. On the bubble acts two main forces – the

buoyancy force giving the velocity v_a upwards, and second, the resultant force of the flow which results in the velocity of the flow, v_f . If the N is the same as when SiO_2 particles were mixed, the resultant flow velocity v_f (as depends on the N) will be identical in both models.



*Figure 5.3. (a) Argon gas bubbles without mixing forces present in the system move upwards due to the buoyancy force with velocity equal v_a
 (b) The resultant velocity of the bubble in the presence of mixing forces is the effect of movement with a flow velocity v_f , scaled by the vector v_a .*

When the HSM head is not working all particles or bubbles move along y-axis only. In both systems, we can not observe any natural forces which will move particles or bubbles along the x-axis. It is why the movement along the x-axis is only the effect of the flow velocity. Secondly, vectors of flow velocities are scaled in both cases by the vectors of v_g and v_a . Resultant velocities in both cases are different because of this scaling and the displacement of particles will be different too. Finally, the observed displacement with the argon gas bubbles is smaller and measured pseudo-cavern sizes are smaller too. As mentioned before, the gas bubbles without flow are moving only upwards, so the circular movement is the effect of the rotor speed. The same with SiO_2 , particles without an HSM flow will move down and observed and measured circulation loop is the effect of forces applied by the HSM.

Therefore, the sizes of the pseudo-cavern (circulation loops) are the effect of the flow caused by the HSM and their sizes are in both cases changed by constant forces (the buoyancy or gravitational force). Thus, sizes of resultant pseudo-cavern can be compared between models since only increasing of the N causes the increase of the pseudo-cavern diameter.

The second assumption states that the pseudo-cavern size grows up proportionally along x and y -axis when the N increases. Thus, the ratio of the radius and height is constant. The pseudo-cavern effect is not yet well described and is difficult to find any sizes predictions. But the cavern effect (the similar effect observed with open impellers) was a subject of an intensive research. The cavern shape is proven to be elliptical (effect of the torus shape of the vortex flow) by models and experiments. It was found that the impeller type determines the aspect ratio of the elliptical torus. Thus, the ratio of both sizes of the torus (along x and y -axis) is relatively constant for a given HSM shape [Wilkens et al., 2005]. Since our measurements are done with one type of impeller, the ratio of the measured D and H is constant. It is our second assumption, which allows us to calculate the height of the pseudo-cavern for the SiO_2 model.

5.1.3. Calculated pseudo-cavern height (the SiO_2 model).

Up to now, we used symbols R and the H to describe the pseudo-cavern sizes as those dimensions were measured experimentally. To find both pseudo-cavern sizes for the SiO_2 model system we have to approximate the shape of the pseudo-cavern as the ellipsoid, as described in Chapter 1.2.2. This ellipsoid in a cross section is an ellipse (compare the photograph of the cavern, Figure 1.18). On Figure 5.4 is shown the elliptical shape of the pseudo-cavern cross-section and measured sizes as well as commonly used symbols to describe both half-axis (symbols a and b). In the following part of work, we have to compare the both sizes of the pseudo-cavern and it is more logical to compare both half-axis rather than R and H as they do not give us clear information about ellipsoid shape changes (comparison of the one full axis with the half-axis). Therefore, R and H symbols are replaced in the following sections by the uniform a and b symbols.

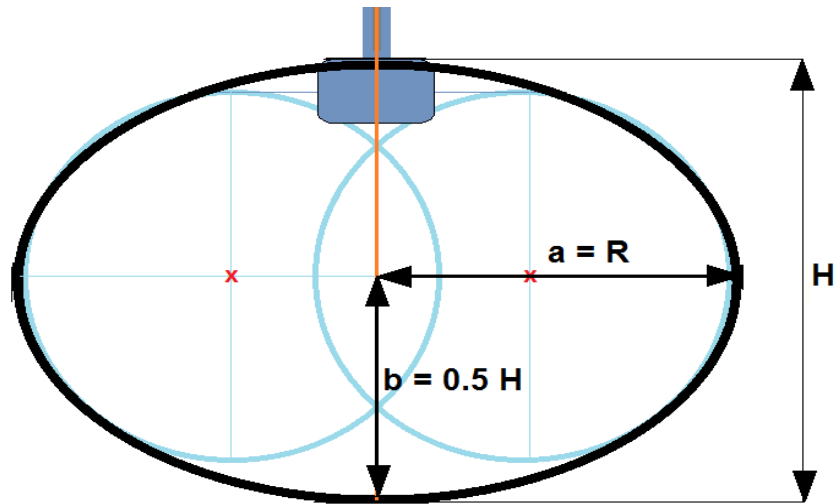


Figure 5.4. The cross-section of the ellipsoid (the pseudo-cavern shape around the blue head). Light blue circles show circulation loops (a compressed torus). Measured sizes R and H are compared with conventional half-axis symbols a and b .

From the second assumption, the ratio a and b is constant in each system. Table 5.4 gives a and b calculated from measurements of R and H (argon gas) and the ratio a to b .

Table 5.4. The ratio of both pseudo-cavern half-axis.

N [rpm]	a [mm]	b [mm]	ab^{-1}
2000	20 ± 1	14 ± 1	1.43
3000	24 ± 1	18 ± 1	1.33
4000	33 ± 1	32 ± 1	1.03
5000	44 ± 1	35 ± 1	1.26
6000	53 ± 2	42 ± 1	1.26
7000	95 ± 2	54 ± 2	1.76
Average:			1.35

From our first assumption, the existence of a pseudo-cavern is in both cases caused only by the flow movement due to the HSM processing. Thus, the pseudo-cavern sizes grow up in both systems proportionally and $ab^{-1} = 1.35$ is constant in both models. The b is equal:

$$b = 0.74 a \quad \text{(Equation 5.2)}$$

The physical argon gas model was only an additional model. It was used because the direct measurements of b -size with the SiO_2 model were much more difficult than with the argon gas model. With the established a/b relation, we can now estimate the pseudo-cavern sizes for the SiO_2 model. It is necessary as SiO_2 model reflects more properly the situation in the real melt and can be used to describe the well-mixed region of the liquid metals. Since the value of $a = R$ was measured experimentally, the b value for the SiO_2 model is calculated from Equation 5.2 and given in Table 5.5.

Table 5.5. SiO_2 pseudo-cavern sizes measured (size a) and calculated (size b) for the different N .

N [rpm]	a [mm]	b [mm]
1000	44 ± 1	31
2500	60 ± 1	42
3000	70 ± 1	49
4000	84 ± 2	59
5000	107 ± 2	75
6000	127 ± 3	89
7000	180 ± 3	126

5.1.4. Pseudo-cavern volume calculations.

As was found from the experimental data, the pseudo-cavern size depends on the rotational speed and can be described by Eq. 5.1 for the SiO₂ model. We decided to take the ellipsoid approximation of the pseudo-cavern shape as really close to the real shape. The volume of an ellipsoid is given by the equation:

$$V = \frac{4}{3} \pi abc \quad \text{(Equation 5.3)}$$

The a , b and c from Eq. 5.3 are all half-axis of the ellipsoid shape. The pseudo-cavern shape is regular and the c size of the ellipsoid is equal the a size (see Fig. 1.17, a and c are the sizes along x and z -axis on that figure). It will change our equation to the form:

$$V = \frac{4}{3} \pi a^2 b \quad \text{(Equation 5.4)}$$

If we compare Eq. 5.4 with Eq. 5.2 we can simplify:

$$V = 0.7 \frac{4}{3} \pi a^3 \quad \text{(Equation 5.5)}$$

Thus, it is 0.7 of the volume of a sphere with radius equal a (or measured values R). As sometimes the cavern size is approximated by a sphere [Solomon et al., 1981], this equation allows us to find the discrepancy which is connected with a spherical approximation.

Further reductions will give the simple equation:

$$V = 2.93 a^3 \quad \text{(Equation 5.5)}$$

From Equation 5.5 we can see that volume is dependent on the size of the pseudo-cavern radius (the size a). As we found that this radius can be written as a function of the N (Equation 5.1), the pseudo-cavern volume can be found as dependent on the N too. Thus, for the impeller with the crossH, the mixed volume can be described as:

$$V(N) = 2.93 (0.024 N)^3 \quad [\text{mm}^3] \quad \text{(Equation 5.6)}$$

Because the a was given in mm for N in rpm, the volume will be given in mm^3 . As the crucible volume is usually given in litres, so Eq.5.5 can be rewritten to describe volume in litres (dm^3). Finally, we have the useful formula:

$$V(N) = 40.5 \cdot 10^{-12} N^3 \quad [\text{dm}^3] \quad \text{(Equation 5.7)}$$

The mixed volume depends on the rotational speed and has the ellipsoidal shape. From the physical model, the mixed volume can be estimated for the given N . Inside the mixed volume energy is dissipated, proportional to the rotational speed. If we change the vessel or the impeller clearance, the flow will be changed because of reflections from walls or a bottom. But the amount of dissipated energy will be the same as we have the same power and the same rotational speed.

Thus, independently of conditions, the well-mixed volume will be the same. We can change the shape of the vessel that will change the shape of the pseudo-cavern, but not the well-mixed volume as the energy used for mixing (if we treat energy loss as negligible) will be the same. This prediction is calculated for one type of liquid and the application of the model to other fluids with a different viscosity needs a further experimental research.

The stirred volume dependence on the rotational speed N is shown in the graph, in Figure 5.5.

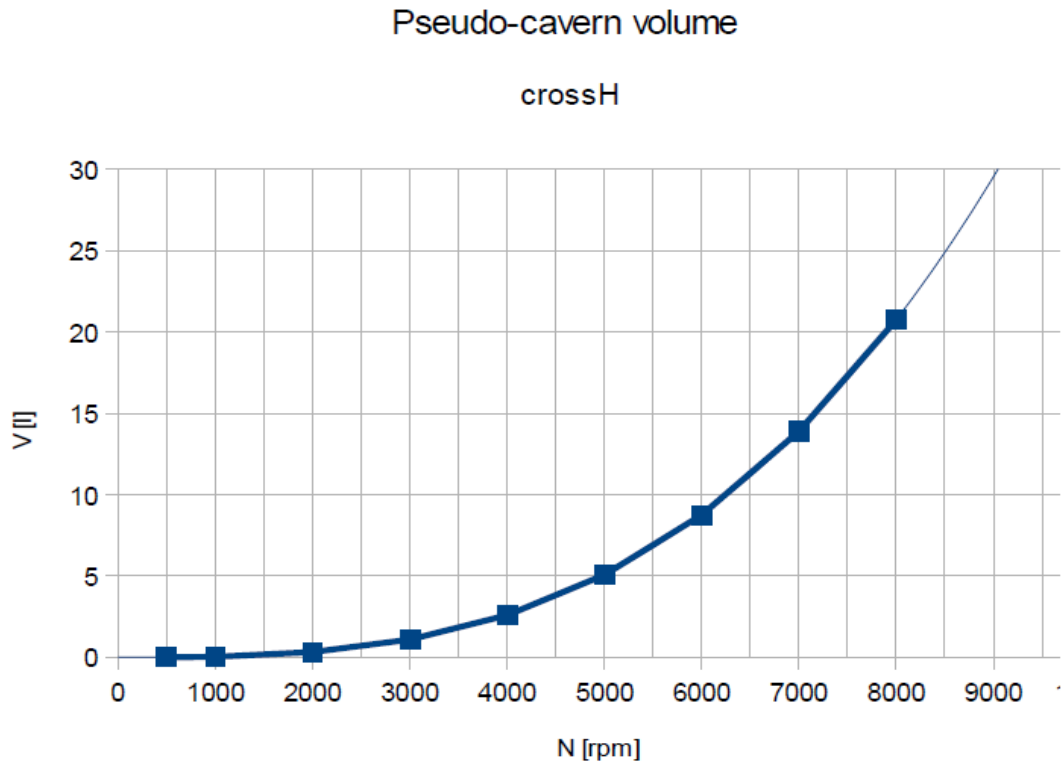


Figure 5.5. The pseudo-cavern volume for the crossH as a function of the rotational speed N [rpm].

5.1.5. The model validation by PIV experiments.

To confirm a described model we made measurements of pseudo-cavern sizes from photographs obtained by a PIV system (see Section 4.2.2). The system set-up decides that we can measure the pseudo-cavern size at rotational speeds up to 5000 rpm. This limit is the result of the bordered dimensions of the observation plane. If the flow is not disturbed, the jet turns back and the loop can be clearly observed. The measurements were done with the advised by Silverson clearances 30 to 50 mm. Usually at least some part of the flow is reflected from the bottom. Thus, after flow analyses, the importance of the point where jets are reflected from the bottom of the tank was found. As

it is the place where the elliptical jet is reflected, we can find one of the well-defined points of the ellipse. The second point was set-up on the top border of the head, as jets emerging from the stator holes define the pseudo-cavern shape (the circulation loops starts at this point). The symmetry axis of the elliptical shape of pseudo-cavern is equal to the main axis of the mixing HSM head. When drawing the ellipses (a cross-section of the full pseudo-cavern size) on pictures taken by the PIV system, these constant rules were applied, and the best shape of the ellipse was chosen to mimic the flow of fluid indicated by coloured vortices. The rules applied for ellipses drawing and measurements are illustrated in Figure 5.6.

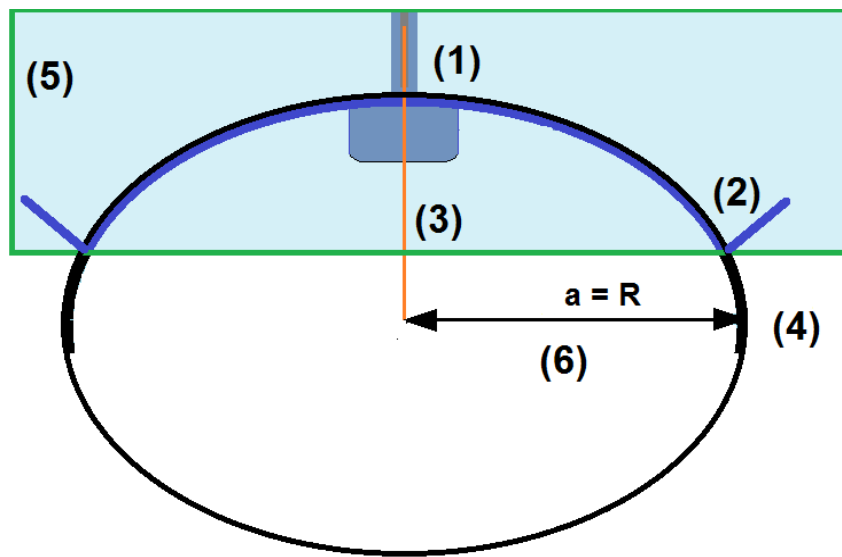


Figure 5.6. The a size measurement rules from PIV photos:

(1) the ellipse starts where the jets are emerging from the top stator holes, (2) the point where the jet is reflected by the bottom of the tank belongs to the ellipse border, (3) one of the ellipse axes is known to be equal to the head main axis, (4) the full ellipse shape is drawn to fulfil the rules 1-3 and to mimic in the best way the natural shape of the jet recorded by PIV system, (5) the tank walls are far enough to avoid the jet scattering from the walls, (6) the size a is measured from drawn elliptical shapes.

From those drawn ellipses, we measured the size a of the ellipse. The red outline shows the head position. On the sequence of photographs (Figure 5.7), we can observe that the pseudo-cavern diameter increases with the N . The PIV results are recorded at

two different heads positions (clearance 30 or 50 mm) and the pictures with the best-defined jet curvature are presented in Fig. 5.7 and 5.8 (the same scale for a reference). The size a is found from pictures and is given in Table 5.6.

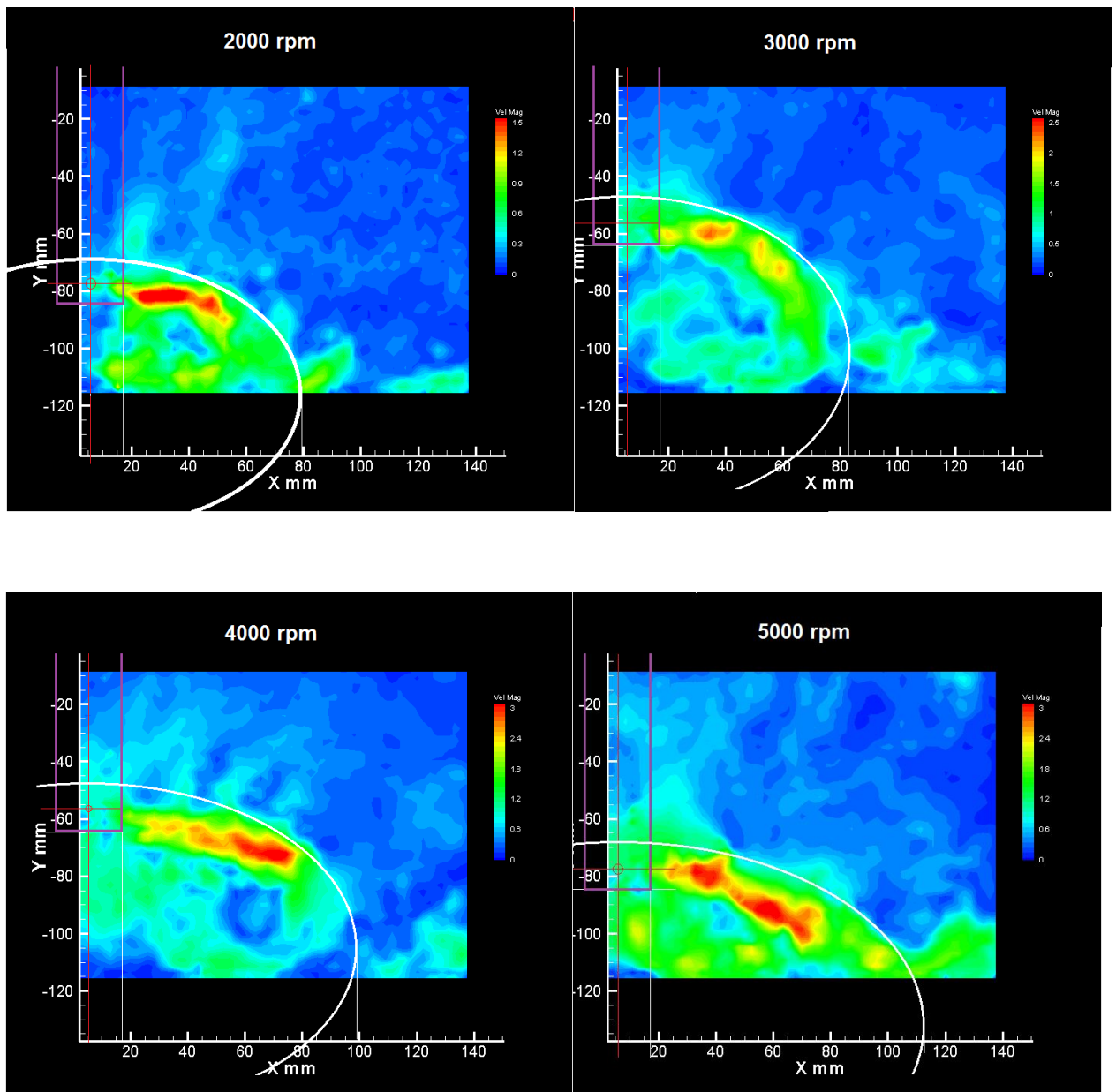


Figure 5.7. The pseudo-cavern development with the N increases. Velocities are given in m/s. Pseudo-cavern shapes are approximated by ellipses and sizes a were found. Pictures are given with the scale which is the best to represent the local flow.

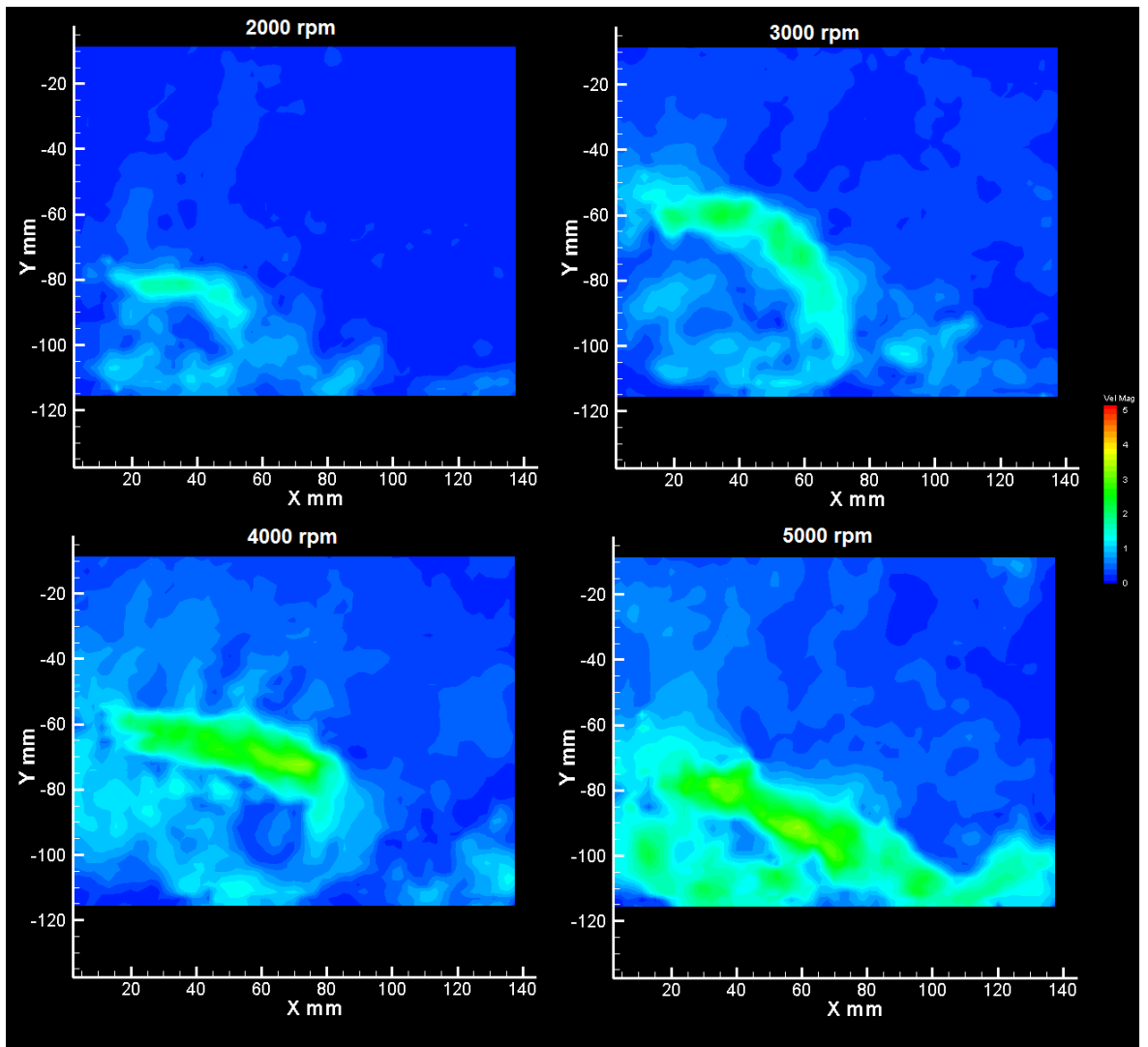


Figure 5.8. The pseudo-cavern development with N (given in the same scale for reference).

To compare the results with those measured with the SiO_2 model, the pseudo-cavern sizes are given in Table 5.6. If we make a graph of the a dependence on N we will again receive the estimated a as the function of N . Figure 5.8 shows this graph and an indicated function.

Table 5.6. The measured pseudo-cavern size from PIV results
(given as a) and in the SiO₂ model (given as R).

N (rpm)	a (mm)	R (mm)
2000	74±1	59±1
3000	76±1	70±1
4000	94±2	84±2
5000	109±2	107±2

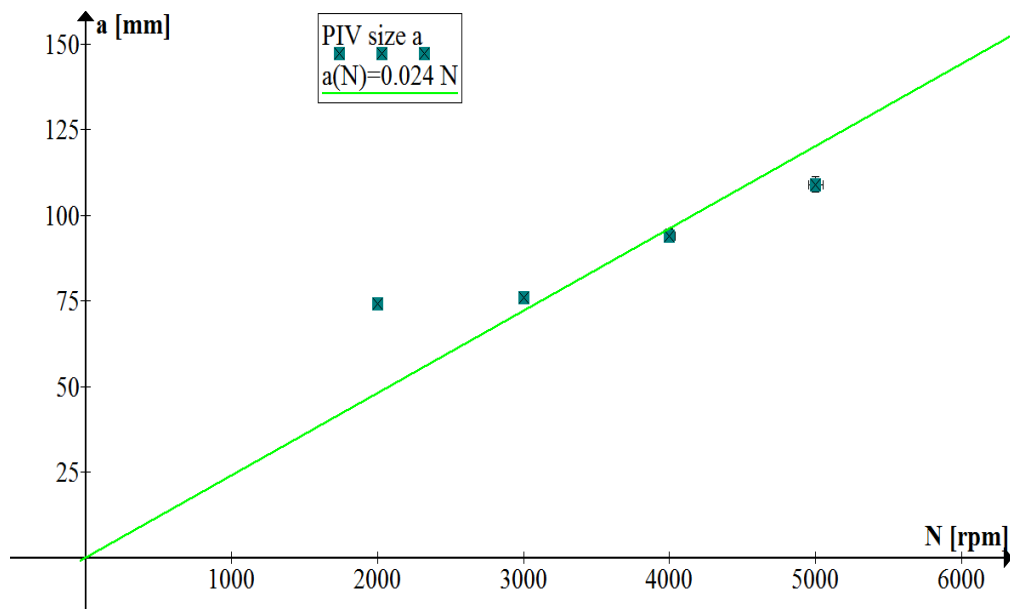


Figure 5.9. The pseudo-cavern size a as the function $a(N)$ estimated from PIV results.

The pseudo-cavern model presented before (Section 5.1.1 – 5.1.4) is in very good agreement with values measured by the PIV in the range up to 5000 rpm. The $a(N)$ estimation is described by the same formula as $R(N)$ before and is:

$$a(N) = 0.024 N \quad \text{(Equation 5.8)}$$

if N is given in rpm and a in mm.

5.2. Universal model - scale up rules.

Two main scale-up criteria of stirred tanks are widely used. The first is a constant tip speed criterion and the second is a constant value of power per unit volume criterion. We have chosen the constant tip speed criterion as it is found to give more realistic predictions [Edwards et al., 2013] and advised as applicable to the rotor-stator systems [Mortensen, 2011]. Additionally, this criterion is based on the geometrical properties of the impeller which is consistent with our approach used in the physical modelling described previously in this thesis, since viscosity is treated as constant.

To scale up the stirred system by the constant tip speed criteria, we have to compare the tip of blade speed for each rotor. If we consider two identical, except the diameter, impellers, we can write the tip speed as:

$$v_1 = \pi d_1 N_1 \quad \text{(Equation 5.9)}$$

$$v_2 = \pi d_2 N_2 \quad \text{(Equation 5.10)}$$

To describe two different situations with the same tip speed, we can write down:

$$d_1 N_1 = d_2 N_2 \quad \text{(Equation 5.11)}$$

Thus, if we scale up the rotor diameter to observe the same mixing, the rotational speed have to be decreased by the ratio of both impeller diameters:

$$N_2 = \frac{d_1}{d_2} N_1 \quad \text{(Equation 5.11)}$$

Consider the model situation. We used the small head for modelling purposes, with the rotor diameter $d_1 = 21$ mm. In a metallurgical laboratory, the bigger impellers are commonly used, with diameter $d_2 > d_1$. The model shows that the pseudo-cavern size depends on N as in Equation 5.1. Thus, if we assume:

$$a_1(N) = 0.024 N_1 \quad \text{(Equation 5.12)}$$

Then for the head with a diameter d_2 we can write:

$$a_2 (N) = 0.024 \frac{d_2}{d_1} N_2 \quad \text{(Equation 5.13)}$$

After using the constant value $d_1 = 21$ mm we can calculate:

$$a_2 (N) = 1.14 \cdot 10^{-3} d_2 N_2 \quad \text{(Equation 5.14)}$$

Where: d_2 it is the diameter of a bigger head than the one used in modelling and N_2 it is the used rotational speed in the new system, a_2 is the pseudo-cavern diameter, observed when the head d_2 works in free mixing conditions (no jets scattering) with the rotational speed equal the N_2 .

The a size can be described as a function of two variables d and N :

$$a (N,d) = 1.14 \cdot 10^{-3} d N \quad \text{(Equation 5.15)}$$

Of course, all linear dimensions have to be given in mm and the rotational speed is in rpm.

To find the mixed volume by the larger head it is necessary to repeat calculations done before but with new dependence $a(N,d)$. When we use this value a in Equation 5.5 and repeat all calculations we can find:

$$V(N,d) = 4.3 \cdot 10^{-15} d^3 N^3 \quad [\text{dm}^3] \quad \text{(Equation 5.16)}$$

The $V(N,d)$ is given in litres (dm^3) if we insert linear dimensions in mm and the N in rpm.

Equation 5.16 is a general formula which can be used to find the stirred volume of a processed liquid-metal for a given diameter of the head and a certain rotational speed.

Chapter 6. Optimisation of design and process conditions.

Chapter 3 of this thesis shows that oxides can play the positive role in the nucleation process. It is well supported not only by the computer simulation (chapter 3) but by experimental results as well (Section 1.5). In the following parts of this work, the defragmentation potency of HSMs and the distributive characterisation of mixing were checked. As oxides films and agglomerates should be broken into small particles and later distributed uniformly in the mixed volume of the fluid, two main problems were considered. Chapter 4 focuses on proving that the chosen method is really potent to use for particles deagglomeration. Chapter 5 focuses on the distribution process and describes the method to find sizes of the well-mixed region. The next part will give an answer about other factors which can influence on the mixing efficiency. As we know how to optimise the mixing by an adequate choice of a mixed volume of a liquid metal, we will consider other conditions which influence on the mixing, such as the head positioning or the rotor-stator design. The influence of the stirring time is checked experimentally and results are presented.

6.1. Impeller position.

The rotor-stator position has an influence on the flow observed in a vessel. When pseudo-cavern observations were made, the clearance had some influence on the pseudo-cavern size and the maximum size was measured after the first position approximations. To find more exactly the role of a clearance more experiments were done. The flow was analysed according to two main points. First, the presence of turbulences was checked. Second, the general flow behaviour in comparison to expected from theoretical predictions was analysed (Section 1.2.1).

To find how the clearance affects the possibility of a vortex formation a number of clearances were checked in a cylindrical vessel. The side vortex (see Section 1.2.1) can

be seen when the air is sucked by the vortex into water. When it happens, the air bubbles are visible in the vortex flow. Observations of flow give a clear information what conditions cause the vortex effect. Results recorded for crossH are presented in Table 6.1.

Table 6.1. The vortex presence in a cylindrical vessel with $T=84$ mm, $h=120$ mm for different clearances C , 1 – presence of vortex / turbulence, 0 – vortex not observed.

N(rpm)/Re		2000/ 16000	3000/ 24000	4000/ 32000	5000/ 40000	6000/ 48000	7000/ 56000	8000/ 64000	9000/ 72000
C(mm)	C(d)								
100	$4d \approx$ about d below the surface	0	0	1	1	1	1	1	1
75	3d	0	0	0	1	1	1	1	1
50	2d	0	0	0	0	1	1	1	1
20	$d \approx 1/6h$	0	0	0	0	0	1	1	1

According to those observations we assume that the probability of turbulences (the vortex creation) is growing with moving the head up off the bottom of the tank (increasing the clearance means that the position of the head is closer to the surface).

The advised head position is usually $1/6 h$ (h - the water level in a vessel) [Walas et al., 2005]. Since the vessel diameter is 84 mm, the volume of the vessel (about 0.7 l) is fully agitated at 2 500 rpm as calculated from Equation 5.7. The full agitation does not necessarily cause turbulences, but if too much energy is associated with the process, or if the head is close to the surface, turbulences can occur. It is important to find the best conditions which allow us to avoid a vortices creation what can introduce the air into the liquid.

Table 6.1 indicates that the probability of turbulence is strongly dependent on the clearance. Thus, the higher clearances should be avoided, especially if the speed is increased. If the head is positioned close to the surface, the minimum agitation speed calculated according to Chapter 5 should be used. Each decrease of the clearance about

the head diameter (d) allows increasing the N about 1 000 rpm without the risk of the air vortex. Clearances were checked from 20 mm above the bottom (close to the rotor diameter) up to 20 mm below the water surface (about d below the surface). Further increasing of the clearance caused visible surface turbulences, so should be avoided definitely.

Presented results are in a good agreement with the previous findings. A first approximation of the clearance size differs according to sources from $T/3$ [Kresta, 2004] or $h/6$ [Walas et al., 2005] or is given as specific value (up to 50 mm by Silverson). So in our case advised clearances range between 20-50 mm. As seen from Table 6.1 that range of clearances allows avoiding the flow instabilities even with a quite high speed (the speed can be doubled safely if clearances are kept in this range). Those results are well supported by previous research. For example, Myers et al. [1997] found that at the lower clearance favours more stable flow fields. With higher clearances, the observed flow exhibits instabilities as a vortex creation.

Avoiding turbulences is important but is not the main point of the process, which is focused rather on the effective dispersion and distribution of oxides in the bulk liquid. To find effects of increased clearances, a flow was checked by the PIV system.

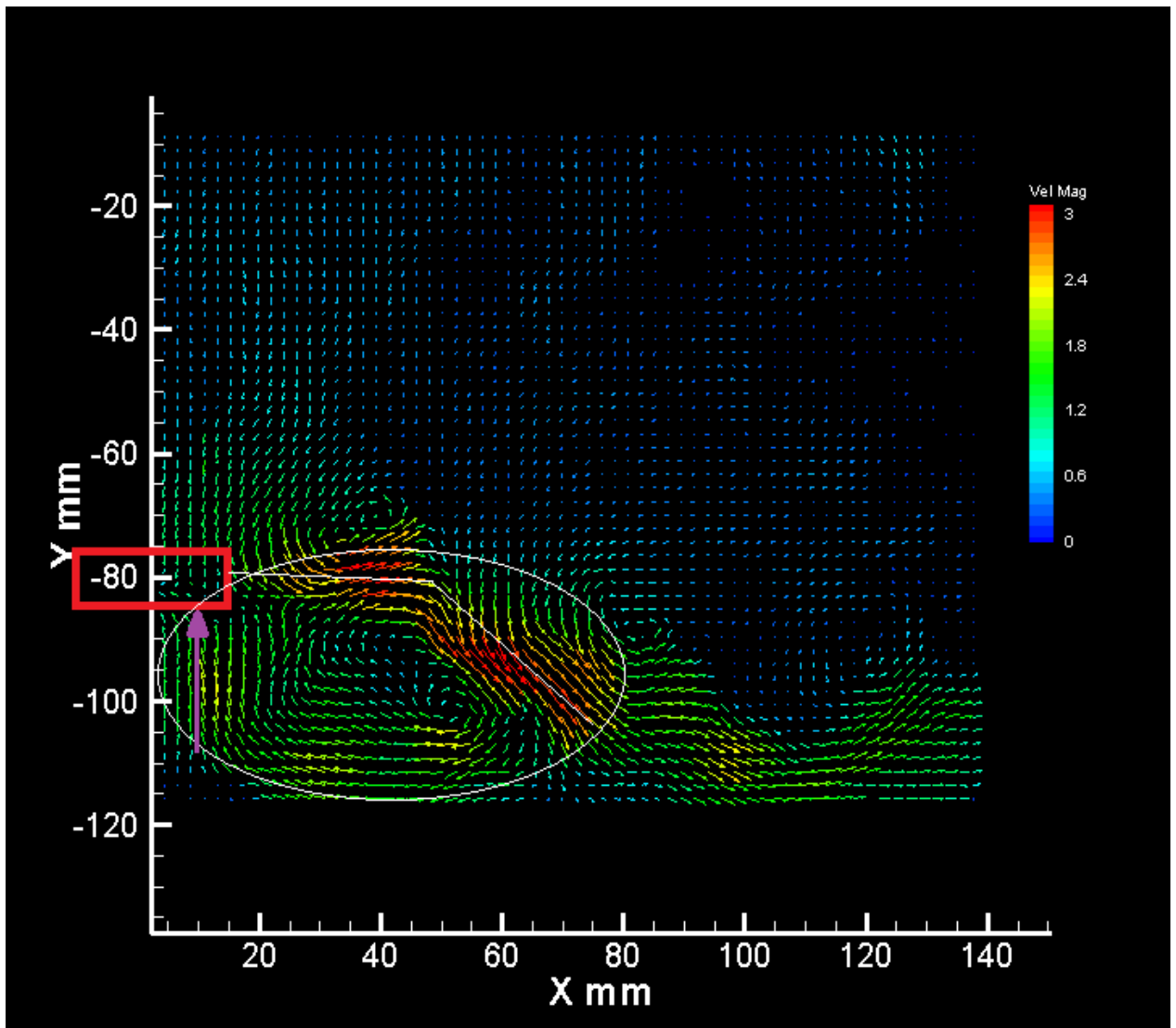


Figure 6.1. A flow pattern around the crossH (shown by the red rectangular). The clearance $C = 30$ mm, $N = 5\,000$ rpm. The circulation loop and the jet are shown by white lines, the sucking force direction is shown by the purple arrow.

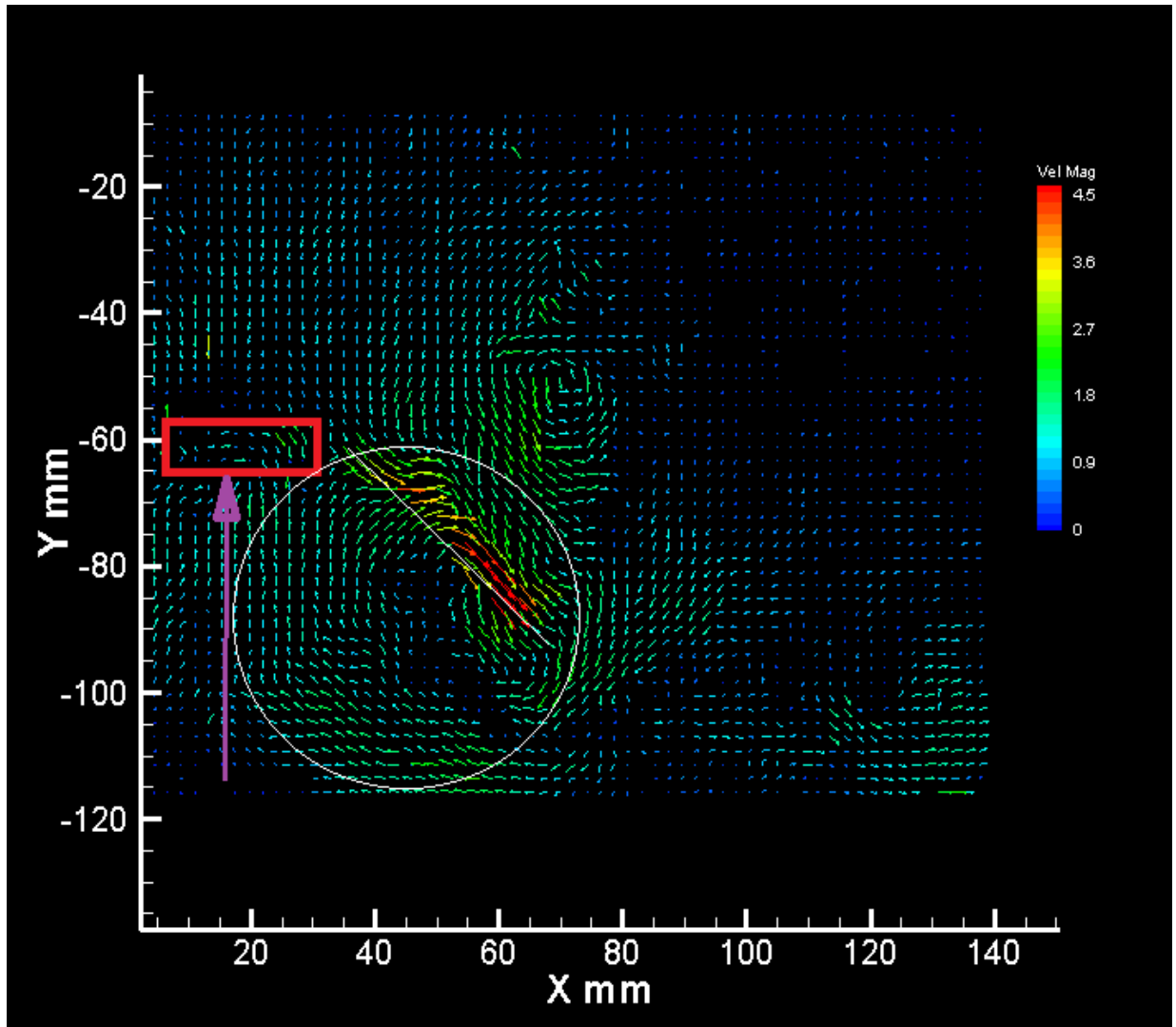


Figure 6.2. A flow pattern close to the crossH (shown by the red rectangular). The clearance $C = 50$ mm, $N = 5\,000$ rpm. The circulation loop and the jet are shown by white lines, the sucking force direction is shown by the purple arrow.

As seen from PIV photos the loop (shown by white round shapes) is more intensive if the clearance is lower (30 mm). In this case, the loop is more ellipsoidal because of the reflection of flow from the bottom. When the clearance is increased to 50 mm the loop is more circular but we observe a weaker flow and the jet (shown by a white

line in Fig. 6.1 and 6.2) on the whole way is directed towards the bottom. Velocities in the jet ($C = 50$ mm) are maximally 4.5 m/s. For the smaller clearance ($C = 30$ mm), the jet velocities are smaller (up to 3 m/s) but the mixed region seems to be agitated more uniformly inside the loop. The sucking force (shown by the purple arrow) can also be compared between both cases.

For the smaller clearance maximum velocity in this region is about 2.5 m/s. This velocity is given by the sucking force which moves flow from the bottom up to the head. When the clearance is bigger the maximum velocity equals 1.8 m/s. Bringing the particles from the bottom towards the head is more effective with smaller clearances since particles have a shorter distance to overcome.

In both cases, the amount of energy dissipated around the head is the same because the N is the same. If we compare the velocity pattern, we observe that in the case of larger clearances the energy is mostly dissipated in the jet region. When clearances are smaller (close to the diameter of the head) the energy is dissipated more uniformly inside the loop, the sucking force giving higher velocities to the particles. Both observations take place in the not fully agitated vessel. In the fully agitated vessel, we can expect the jet scattering from the walls what causes intensification of the mixing.

The jet observed with a smaller clearance ($C = 30$ mm) has a length of about 120 mm and at that point is reflected from the bottom. For $C = 50$ mm the observed jet length is about 60 mm and the jet almost disappears before reaching the bottom. From those observations, we can conclude that the lower clearances favour the intensification of the loop and more uniformly dissipated energy. As the sucking force effects are weaker if clearances are larger, so the particles which tend to settle on the bottom will be more effectively dispersed when the clearance is smaller. It is in agreement with previous observations. We can remind, for example, the research described in Section 1.2.1, done by Sharma & Shaikh [2003]. They found that the energy available for particle suspension decreased when increasing the distance of the impeller from the vessel base. A smaller clearance needs less energy to suspend the particles and favours a dispersion. When the rotor-stator system is designed for dispersion purposes this fact should be taken into account.

Observations made with the PIV system are consistent with the data obtained from the physical SiO_2 modelling system. Observed pseudo-cavern sizes were smaller with the increased C . Results are shown in Table 6.2.

Table 6.2. Pseudo-cavern radii for different N (SiO₂ system, crossH) and established from PIV photos.

N [rpm]	R[mm]	R[mm]	R[mm]
	C=30 mm	C=50 mm	From PIV
2000	59±1	35±1	74±1 (*)
3000	70±1	38±1	76±1 (**)
4000	84±2	46±1	94±2 (**)
5000	107±2	63±2	109±2 (*)
6000	127±3	78±2	-----
7000	180±3	102±2	-----

(*) C=30 mm, (**) C=50 mm

That observation can be explained by PIV results. Sucking force effects depend on the clearance and when C = 50 mm the sucking force is not enough strong to bring up particles placed further. The range of this force is visibly smaller. If the agglomerates of oxides tend to settle on the bottom, the clearance will play an important role. From presented research, smaller clearances (up to 2d) were found as the best from two reasons. First, the probability of the flow instabilities is smaller than with larger clearances. Second, the flow is more uniform and sucking force effects are better when clearances are kept on a low level.

6.2. Mixing head design.

The rotor-stator head consists the rotor and the stator. In addition to the changing rotor diameter (see Section 5.2), it is also possible to find different designs of stators (see Table 1.1). Two main changes can be done in the simple design of the rotor-stator. First, the gap size can be changed. Second, the shape and arrangement of stator holes can differ. The influence of both design modifications is described in the following part.

6.2.1. Gap size modifications.

A number of gap sizes were checked by the PIV technique to see how the design change influences on the flow pattern. Average and maximum velocities recorded with different gaps are given in Table 6.3. The original gap was 0.4 mm and it was increased to 0.6 mm and then to 0.8 mm.

Table 6.3. Recorded average (V_{ave}) and maximum (V_{max}) velocities for different gap sizes with the crossH stator.

Gap	0.4 mm		0.6 mm		0.8 mm	
	V_{max} [m/s]	V_{ave} [m/s]	V_{max} [m/s]	V_{ave} [m/s]	V_{max} [m/s]	V_{ave} [m/s]
N [rpm]						
3 000	2.3	0.4	'3.0	0.4	2.6	0.4
5 000	3.5	0.7	3.8	0.8	'4.0	0.6
8 000	'5.0	1.0	'5.0	1.0	'6.0	1.1

The energy of the rotor motion is transmitted into the fluid and the averaged velocity reflects the N increase. Thus, the averaged velocity reflects the amount of energy dissipated in the examined region. There is no significant change in average velocities. Maximum values of velocities increase slightly when the gap is increased. Thus, some part of the energy previously used for another process (probably the shear of liquid inside the head) is dissipated into the liquid surrounding the head. In effect, the jet velocity increases. Even if the mean velocities are similar, we can observe completely different flow pattern around the head. Let us check this closer.

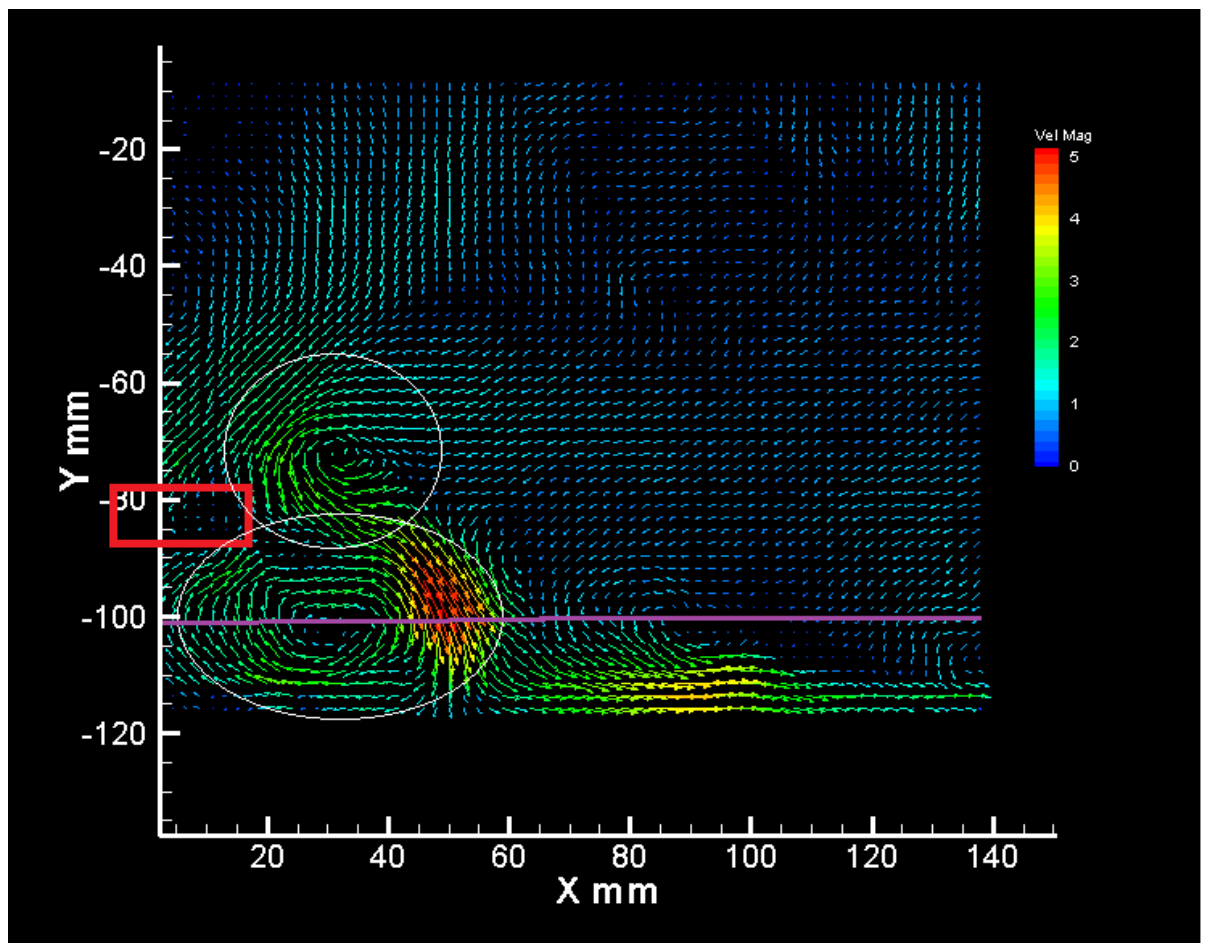


Figure 6.3. A flow around the crossH with the 0.4 mm gap, $N = 8\,000$ rpm, $Re=64000$. The head position is shown by the red rectangular and flow loops are shown by white round shapes. The purple line is drawn across the loop to show the analysed direction.

Figure 6.3 demonstrates a flow pattern in the case of the 0.4 mm gap. One can see the loop under the head and the second loop partially created by scattered flow. Some energy is dissipated to a bulk region because of a reflected flow along the bottom of the tank. To compare the velocity pattern from Figure 6.3 velocities along the purple line were extracted. The purple line is drawn across the loop, contains a central point of the loop and is parallel to the x-axis. The velocities were extracted from Figure 6.3 and the graph in Figure 6.4 shows the velocity change along chosen axis (a purple line, the axis of the loop).

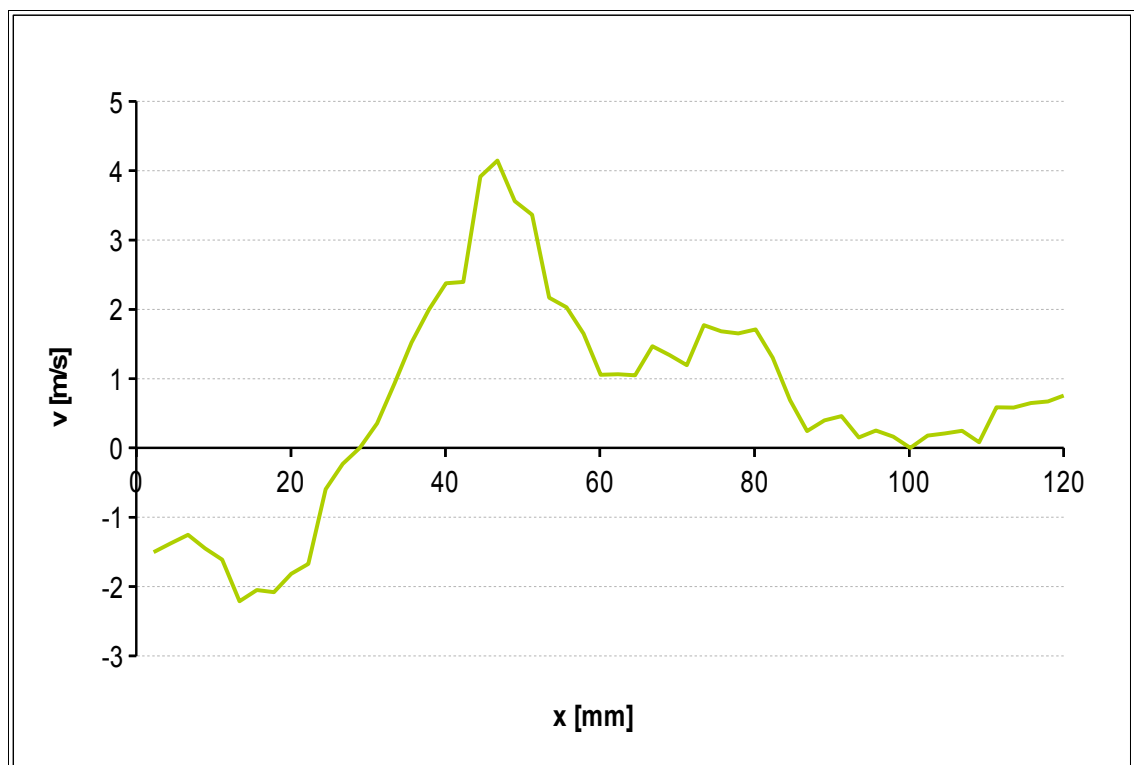


Figure 6.4. The velocities profile along the loop axis for the 0.4 mm gap (crossH).

The velocities observed under the head are equal to about 2 m/s and are the result of the sucking force. In the jet region, the velocities grow up from 0 (in the centre of the loop) up to 4 m/s. In the case of 0.4 mm gap we can observe the second loop so only part of the energy is dissipated in the analysed region, since a part is used for the second

loop creation. The velocities under the head are two times smaller than in the jet region. The jet region is localised close to head (maximal peak of velocities close to 50 mm on the x-axis). The jets flow is reversed by the sucking force and flows again into the head. The reversed velocities have a minus sign.

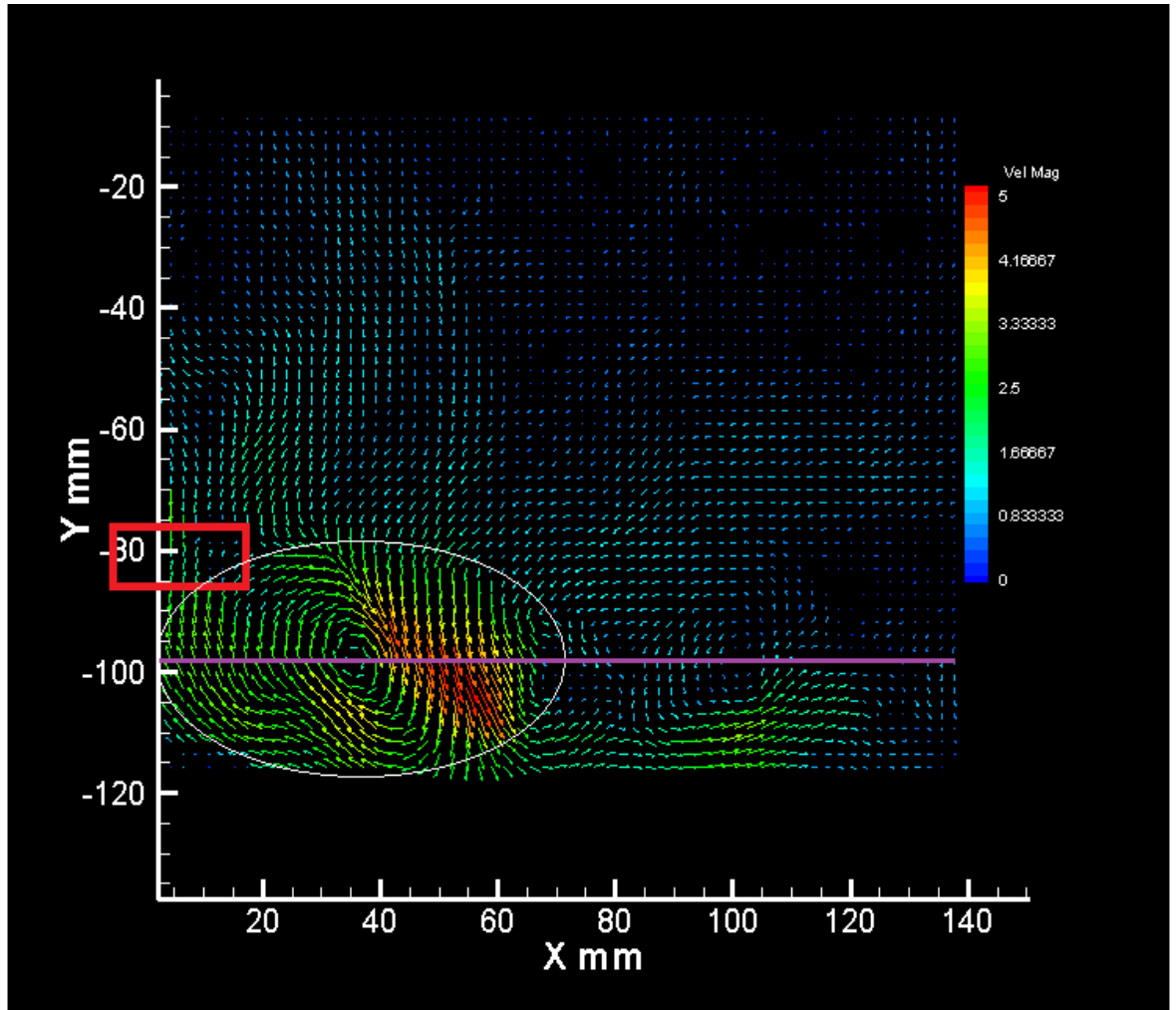


Figure 6.5. Flow around the crossH with the 0.6 mm gap, $N=8\ 000\ \text{rpm}$, $Re=64000$. The head position is shown by the red rectangular and flow loops are shown by white round shapes. The purple line is drawn across the loop to show the analysed direction.

Figure 6.5. shows a flow pattern in the case of the 0.6 mm gap. Only the one loop is created around the head. To compare the velocity pattern from Figure 6.5 velocities along the purple line were extracted. The purple line is drawn across the loop, contains a central point of the loop and is parallel to the x-axis. Rounded velocities extracted from

Figure 6.5 were used to prepare the graph in Figure 6.6 which shows the velocity change along chosen axis.

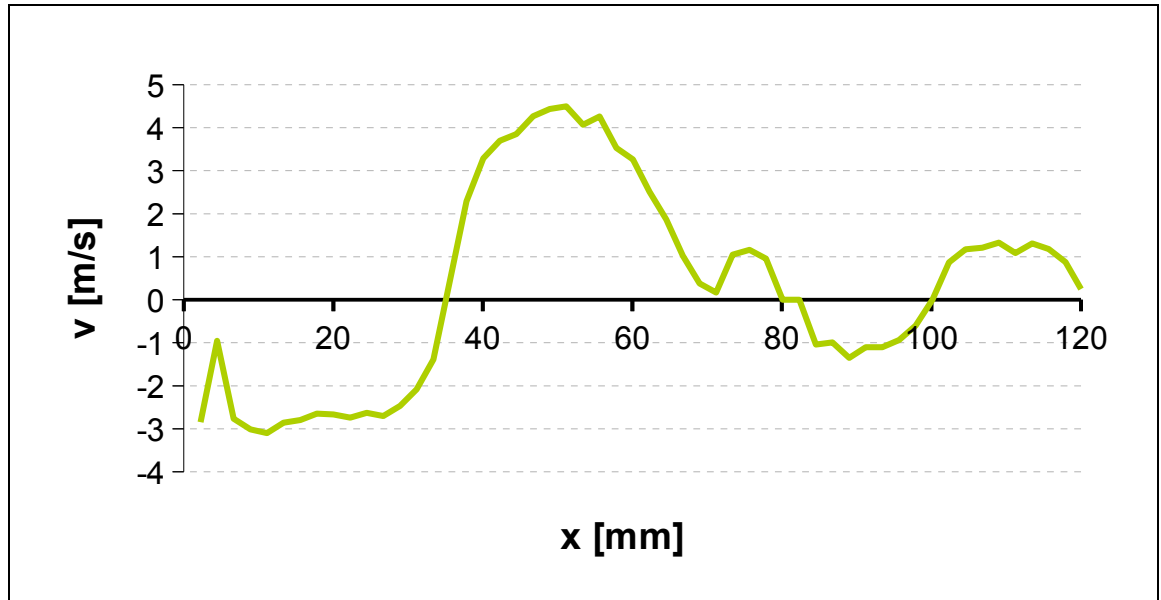


Figure 6.6. The velocities profile along the loop axis for the 0.6 mm gap (crossH).

The jet region is increased in comparison to the previous one. The peak of the velocity profile is wider, what means that more particles have velocities close to maximum. The velocity difference under the head is about 3 m/s and a jets region is observed as the velocity peak, up to about 4 m/s. The force which pushes liquid out from stator slots has a similar value to the sucking force since both forces are moving liquid with comparable velocity differences. The sucking force gives the negative velocities to a fluid at the distance to about 35 mm on the x-axis. Velocities are positive (the jet region) at the similar distance (from 35 mm to 70 mm along the x-axis). Thus, in the case of the 0.6 mm gap, the observed flow is more uniform in the analysed region. Unfortunately, one loop created in the case of the 0.6 mm gap can not be fully compared with a previous velocity profile since with the 0.4 mm gap we observed the two loops pattern. A further gap increase (up to 0.8 mm) results in the one-loop pattern (Figure 6.7) and can be fully compared with obtained for the 0.6 mm gap.

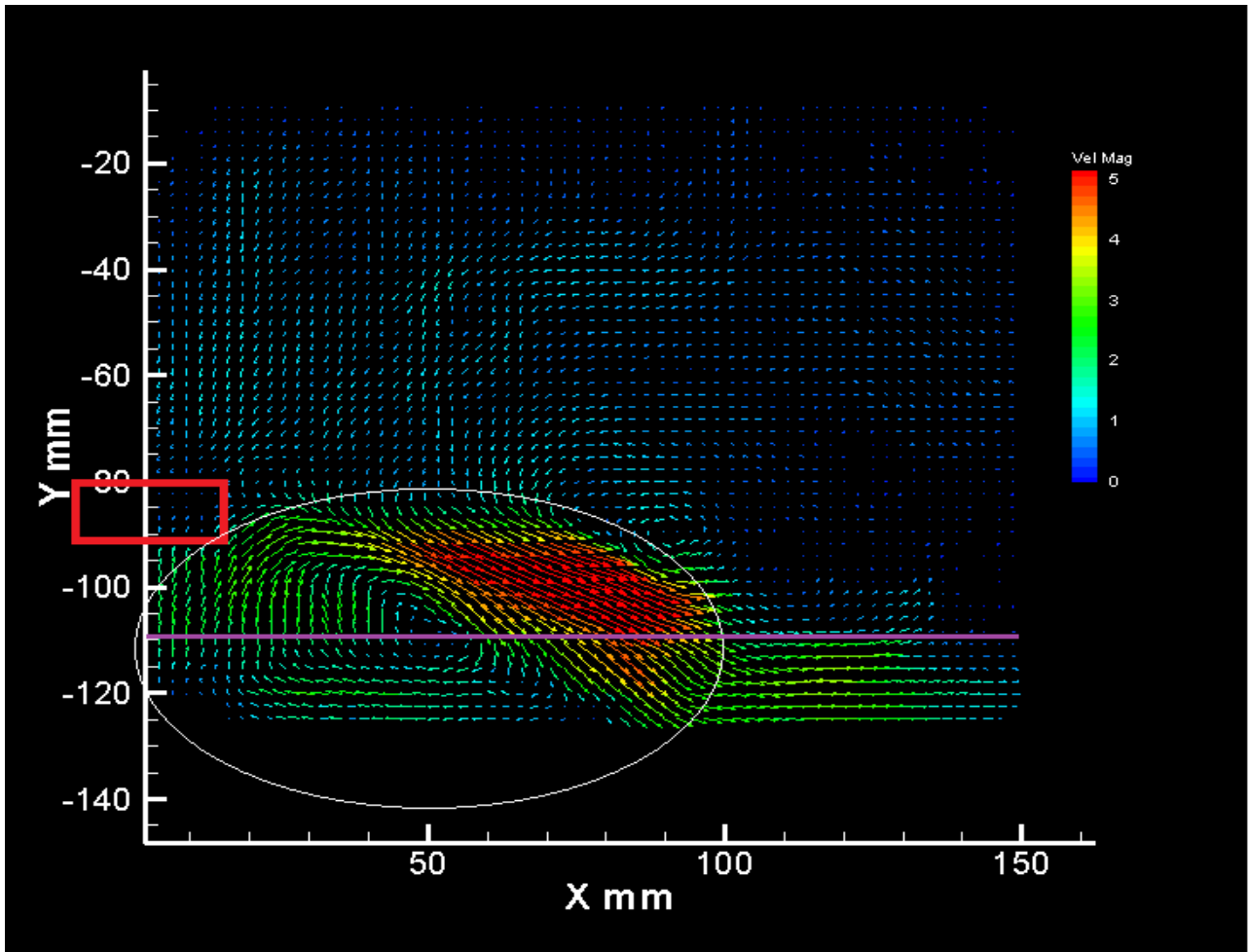


Figure 6.7. A flow around the crossH with the 0.8 mm gap, $N=8\ 000$ rpm, $Re=64000$.
 The head position is shown by the red rectangular and flow loops are shown by white round shapes. The purple line is drawn across the loop to show the analysed direction.

Figure 6.7 demonstrates a flow pattern in the case of the 0.8 mm gap. Again, only one loop is created around the head. The velocity profile from Figure 6.7 along the purple line (the loop axis) was determined. Rounded velocities extracted from Figure 6.7 are given in the graph in Figure 6.8 which shows the velocity profile along chosen axis.

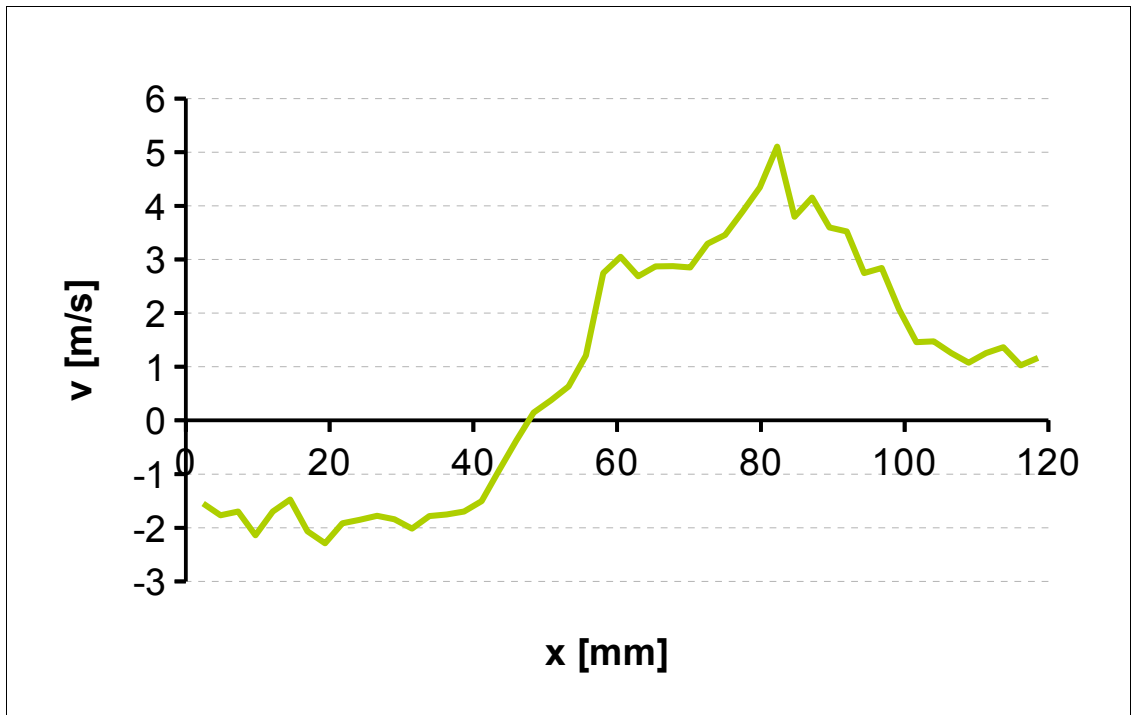


Figure 6.8. The velocities profile along the loop axis for the 0.8 mm gap (crossH).

Further increase of the gap size obviously causes the jet intensification. Not only the velocity peak in the jet region is higher than before, but also the jet region is extended up to over 120 mm. Since the observation plane crosses the jet this value can be only used to compare results with observed before. Positive velocities increase up to 5 m/s from 0 observed in the loop centre. The sucking force causes the velocity change under the head from 0 to minus 2 m/s. The jets region seems to be stronger than the sucking force range. Thus, the loop creation will be not so effective as in the case of the previously observed flow (0.6 mm gap). Stronger jets should improve the bulk region stirring but this positive effect cannot compensate the possible uniformity losses. The nonuniformity problem accompanied with the strong jets will be discussed in following sections. Three different gap sizes were investigated. The gap increase can change the flow pattern and smaller amount of energy will be spent on recirculation. Presented data shows stronger jets (as reported earlier by Calabrese, from LDA observations, 2002) and smaller efficiency in a creation of flow loops after increasing a gap size. To check the dependence of the full pseudo-cavern size on the gap size, measurements of the pseudo-cavern were made. As the sizes measured with the SiO₂ physical model were almost identical for different gap sizes with the same N, we decided to check the results by the second model (argon-gas model), which is easier to record. The photographs were

taken and exact measurements were done by ImageJ software to find differences. Two gap sizes were checked and the comparison of pseudo-cavern sizes is given in Table 6.4. The difference between measured pseudo-cavern sizes is small especially when the rotational speed increases.

Table 6.4. Values of the pseudo-cavern size a measured with a different gap (crossH).

N	a for gap 0.4 mm	a for gap 0.8 mm
2000	16 ± 0.9	24 ± 1.0
3000	31 ± 1.4	28 ± 0.9
4000	37 ± 2.4	34 ± 1.7
5000	45 ± 2.7	45 ± 3.7
6000	67 ± 2.4	64 ± 2.9

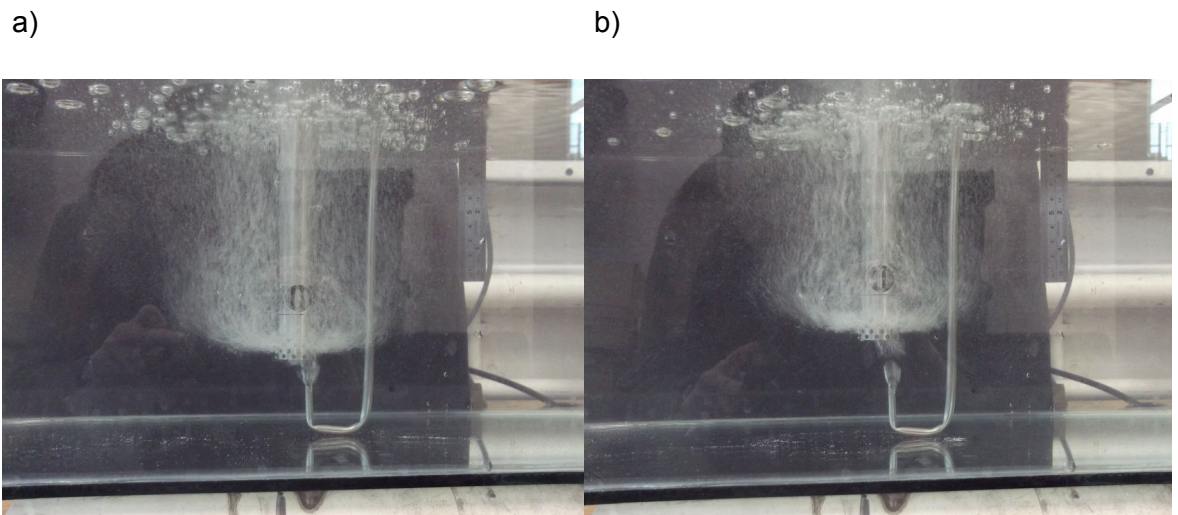


Figure. 6.9. The pseudo-cavern observed with the argon gas ($N = 6000$ rpm, crossH) for the (a) 0.4 mm, (b) 0.8 mm gap size.

Figure 6.9 compares the pseudo-cavern sizes for $N = 6000$ rpm (size about 65 mm according to Table 6.4). For smaller rotational speeds it is observed that the size increases when the gap increases, but for higher speeds, the pseudo-cavern size is almost identical for both gap sizes.

From presented experiments, we can conclude that the gap increase does not result in the increase of the well-mixed region. The gap enlargement from 0.4 to 0.6 mm is accompanied by the transition from two loops pattern to one loop pattern what can decrease the agitation above the head. It is in good agreement with numerical predictions (Calabrese, 2002; Utomo, 2005) since keeping of the narrow gap was advised by these authors.

We can conclude that the gap should be kept narrow, for example, 0.4 mm for the 22 mm rotor and scaled up proportionally when sizes of the head are increased.

6.2.2. Stator design.

Two main problems were checked. The process of the liquid alloy mixing should be done in the stable and uniform conditions, not only because of safety reasons but also to avoid air entertainment into the melt. Uniformity of mixing improves the dispersion and the distribution of oxides in the bulk liquid. To check the usability of different shapes of stator holes in the considered melt conditioning process, the comparison of the mixing efficiency was done. The overall mixing efficiency is decreased by flow instabilities. The mixing efficiency increases when the size of the well-mixed region grows up and is stirred uniformly in all volume. Analyses were done for a number of stator shapes.

6.2.2.1 Flow instabilities with different stator designs.

Flow instabilities evidenced by the vortex observed with air bubbles were analysed in full agitated conditions. The commercial Silverson stators were checked before newly designed heads were prepared for modelling purposes. After observations of instabilities, the design of stator was chosen for physical modelling, since turbulences or the air entrained into the melt should be avoided in the processing of liquid alloys. The results are summarised in Table 6.5.

Table 6.5. The observed maximal speed possible to use without the air vortex formation for different heads.

Stator name	N_{\max} [rpm]	Results of observations
General Purpose Disintegrating Head	2 000	Not applicable for liquid alloys treatment, strong vortexing effect.
Slotted Disintegrating Head	2 000	Not applicable for liquid alloys treatment, strong vortexing effect.
Square Hole High Shear Screen™	4 000	Design considered for liquid alloys processing.
RH	6 000	The stators used for physical modelling purposes have similar design and differences in the shapes of holes do not affect the vortex creation probability.
SqH	6 000	
CrossH	6 000	

The observed maximal speed (N_{\max}) which can be used in a mixing vessel shows how the stator design can influence on the possibilities of flow instabilities. The disintegrating head, as well as the slotted head, cause strong turbulences (from about 2 000 rpm), which can be seen even on the liquid surface. The square holes, as well as round holes itself, do not change the possibility of vortex creation, as can be seen also in the case of RH and SqH. Both heads differ only by the holes shape and the air vortex was only observed above the same value of N (6 000 rpm).

Observations indicate that the vortex creation is influenced by the stator opening size. Both, the disintegrating head and slotted head have the diameter of the holes about 8 mm and it is much bigger than other stators openings (about 3 times if compared with 2.5 mm RH openings). As mentioned before (Section 1.2.1) the vortex tends to touch the mixing head, usually the stator openings or the gap. Since smaller holes are distributed more randomly across the stator area, the stirring uniformity is better with narrow holes. If the holes are bigger, the jet is wider and areas without holes on the stator surface are wider too. Thus, the jet emerging from a stator hole is in contact with a more stagnant fluid. On the border between the jet and this fluid, some instabilities are expected [Söderberg, 2003]. In the case of more randomly distributed smaller stator holes, jets are weaker but agitate the liquid more uniformly and the flow instabilities are avoided.

The disintegrating head has 6 big holes which are the starting points of strong jets, so the agitation seems to be more effective especially for the user who can observe only the surface turbulences. However, the surface turbulence is the effect of the flow instability which excludes this design from the application in the liquid alloy processing (see Table 6.8). Both shapes of smaller and, in the consequence, more randomly distributed holes can be considered – square or round shapes.

To decide which design is better for the mixing efficiency, the pseudo-cavern sizes were checked for different designs of the stators.

6.2.2.2. Pseudo-cavern sizes with different stator holes designs.

To compare pseudo-cavern volumes observed with different stator holes designs the pseudo-cavern trace (with SiO₂) was measured and results are presented in Table 6.6. The SqH and the RH were used as both of them differ only by the shape of the holes.

Table 6.6. Values of the pseudo-cavern size *a* measured with different stator holes.

N [rpm]	Square holes	Round holes
	a_{SqH} [mm]	a_{RH} [mm]
2000	69±1	40±1
2500	74±1	82±1
3000	82±1	94±1
3500	85±1	105±2
4000	98±2	115±2
4500	101±2	128±2
5000	112±2	159±2
5500	118±2	164±3
6000	126±2	177±3

Figure 6.10 shows the pseudo-cavern diameter dependence on the N for both heads with a linear estimation. The size difference is about 40 % for the highest checked value of the N .

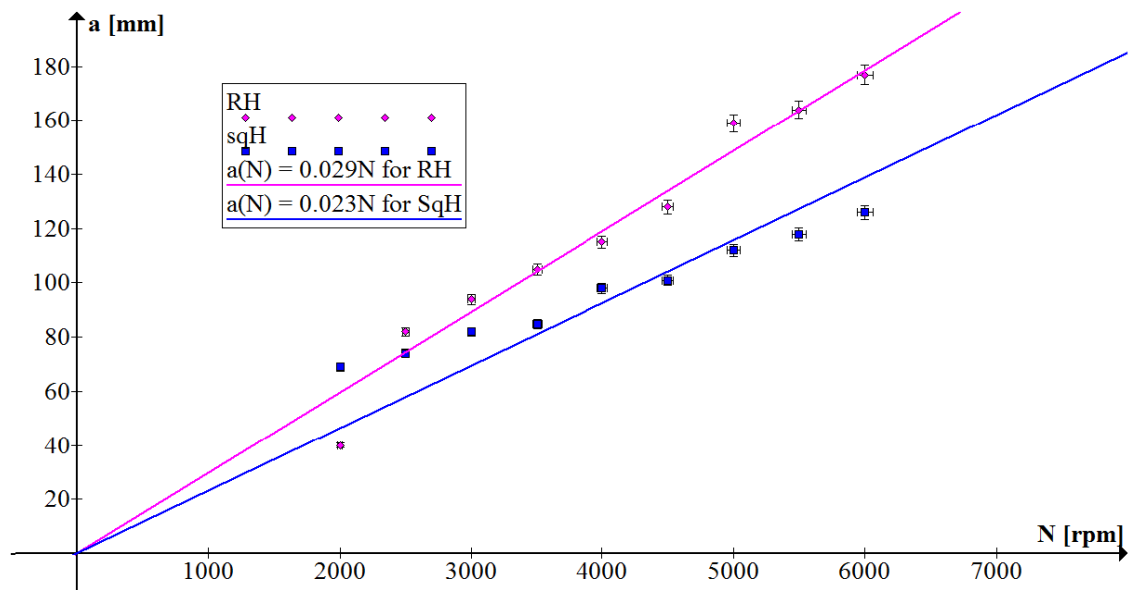


Figure 6.10. The pseudo-cavern diameter dependence on the N for stators with round and square holes with linear estimation.

The pseudo-cavern size is smaller when the holes are square shaped than when they are round. The reason of this can be explained by the jets impairment on the hole border. Round holes do not disturb jets and allow them to move more freely than the square ones. The free jets tends to acquire a cylindrical shape which is the effect of the surface tension holding droplets together. If no other forces present, the free jet maintains its shape for a specific length and will be broken in droplets into air (see Figure 6.11 and 6.12, after Eggers and Villermaux; [2008]) or will change from the concentrated form of the jet into turbulence of the fluid [Gohil et al., 2010]. Before this happens, just after passing the hole, the contraction can be observed and the jet diameter will become smaller than the hole aperture [Brodkey and Hershey; 2003]. Thus, the jet shape is

always close to the cylinder. The square hole will change this natural shape by mechanical reflections of fluid and the observed “square jet” becomes less stable. This can be seen in Figure 6.13 for two different Reynolds numbers as predicted by computer simulation [Gohil et al., 2010]. The jet at the end loses the stability and forms droplets in the air [Rayleigh, 1891; Abb’e Nollet, 1749; after Eggers and Villermaux; 2008]. In the fluid, the turbulence is observed [Gohil et al., 2010]. The “round jet” is more stable than the “square jet” as the square holes disturb the natural jet shape and the turbulence occurs faster [Gohil et al., 2010]. It is a simple reason for physical observation presented in Fig. 6.10 and explains why the mixed volume is bigger for RH since the expected jets are longer with the round holes design. That causes the pseudo-cavern size increase.

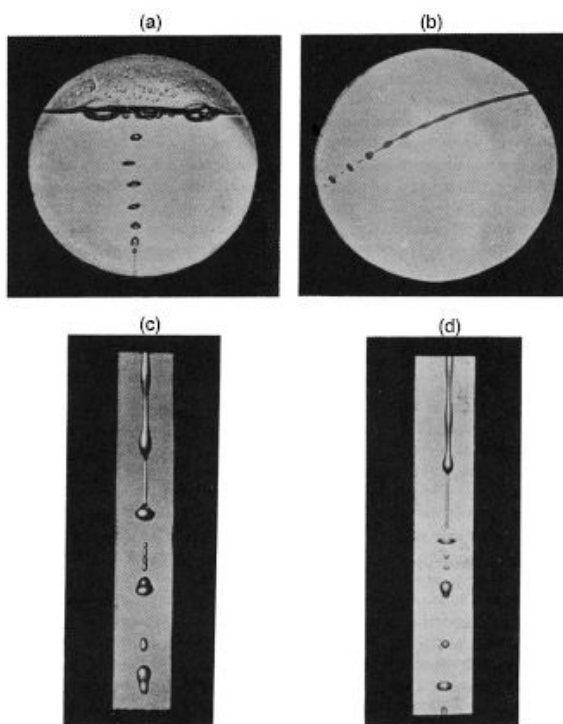


Figure 6.11.

Plate I of Rayleigh’s ‘some applications of photography’ showing the destabilization of a jet of air into water (a) and of a water jet in air (b,c,d); [Rayleigh, 1891].



Figure 6.12

Abbot Nollet demonstrating how a charged water jet disintegrates [from Abb’e Nollet, 1749].

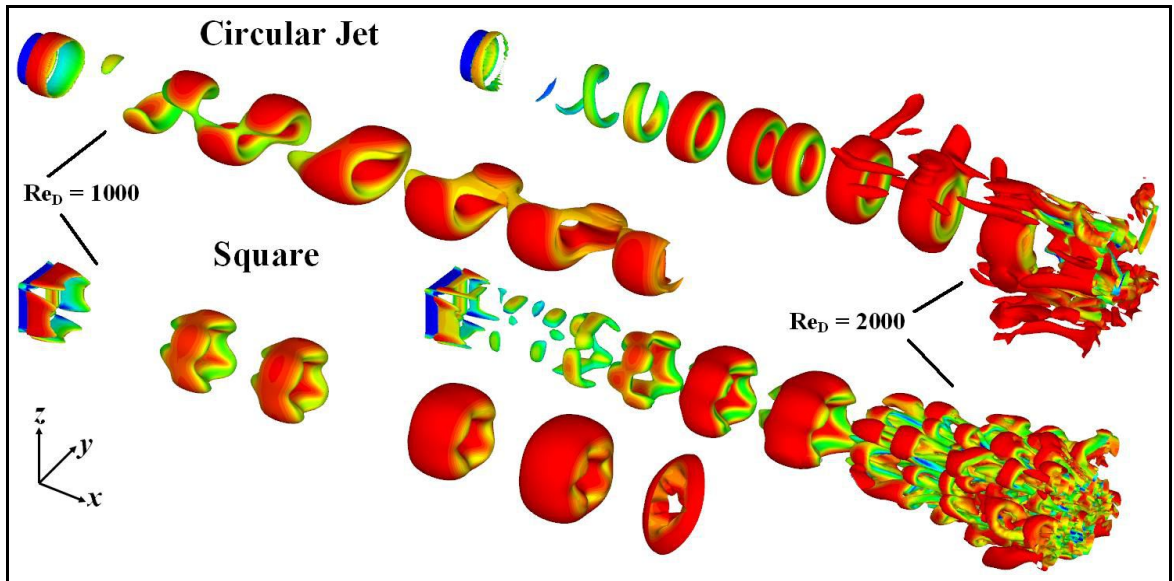


Figure 6.13. Isosurfaces of the velocity gradient tensor for circular and square jets at a Reynolds number of 1000 and 2000. The turbulence in the end of the jet occurs earlier in the case of the square jet [Gohil et al., 2010].

Our results are in good agreement with historical observations and with numerical predictions. The circular jets (from circular openings) are more concentrated and can travel longer in the jet form. Square openings disturb this motion and a turbulence occurs earlier what results in the shorter way of the laminar jet. Thus, the pseudo-cavern size as dependent on the jet length will be bigger with round-holes in comparison with square holes.

Since heads compared in Fig. 6.10 have the same design except the holes shape, in the chosen N the same amount of the energy is given by the moving rotor into a fluid. As the mixed region seems to be smaller for the SqH, it means that the part of energy is used for a process other than mixing, or the mixing inside the pseudo-cavern is more intensive. To find an explanation of this pseudo-cavern sizes difference we need to compare a flow around both heads. The flow pattern observed with a PIV system is shown in Figures 6.14 and 6.15 for each type of holes.

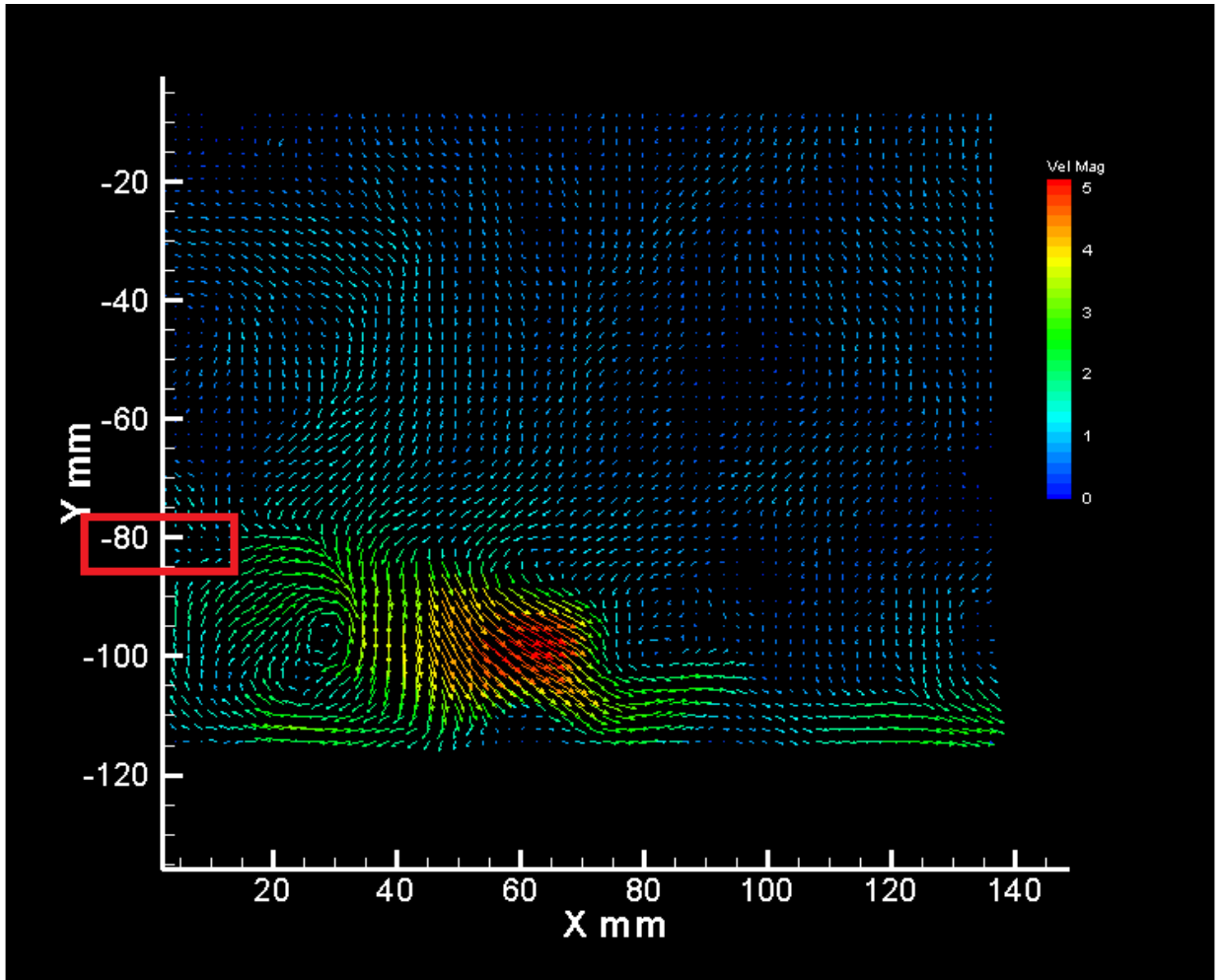


Figure 6.14. A flow around the head with square holes, $N = 7\,000$ rpm, $Re=56000$.
The head position is shown by the red rectangular.

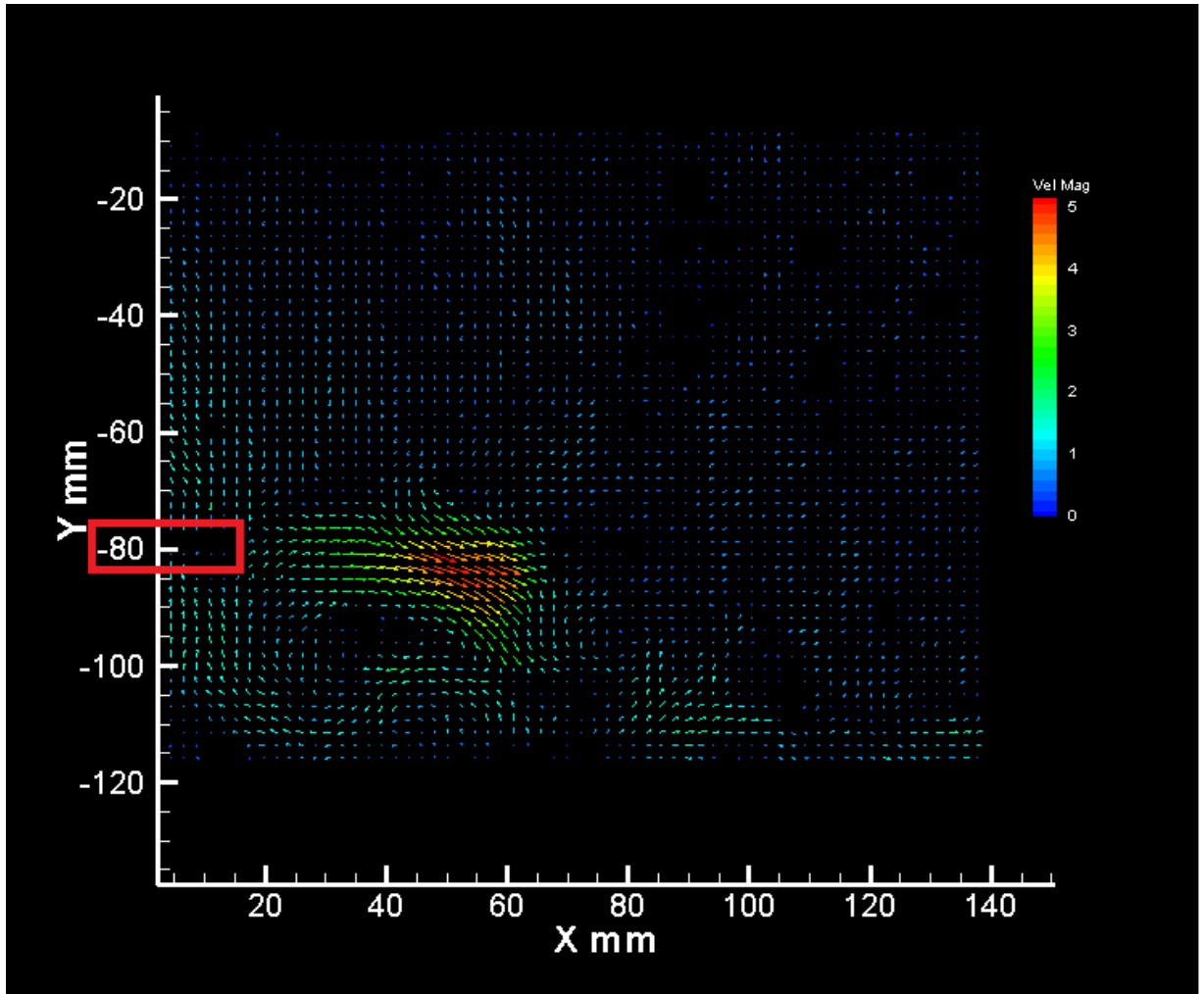


Figure 6.15. A flow around the head with round holes, $N = 7\,000$ rpm, $Re=56000$.
The head position is shown by the red rectangular.

The differences in the flow are obvious. One can expect the strong jets observed with RH (Figure 6.15). For an attentive reader, the explanation of weak flow observed in Fig. 6.15 will be clear. The observations were done in one plane in front of the mixing head (see Section 2.1.2). Between the jets, the flow can be weak and between the strong jets, we can even expect the reversed flow (see Figure 6.16). The observation plane reveals only part of the jet and part of the flow (2D photographs). The weaker flow recorded around RH is the proof that the mixed region around RH is less uniform than around SqH. The picture (Fig. 6.15) reveals the weak flow between strong jets. The fragment of the jet is crossing the observation plane in one place only and appears as the highest velocity zone. Even if the expected jets in other planes are strong (stronger than

observed in this plane), the flow in Figure 6.15 indicates that parts of liquid are not well stirred due to non-uniformity of agitation. Similar observations can be found in the Mortensen's et al. research [2011]. The used slotted head was investigated by PIV system close to the head. Of course, the slot shape is not comparable with holes shapes used in our physical modelling but the PIV photograph of the flow in the plane perpendicular to observed by us, reveals a strong jet surrounded by reversed fluid with much smaller velocities (Figure 6.16). Since our observation plane was perpendicular to shown in Fig. 6.16, we can complement our knowledge by these findings. According to published results of Mortensen [2011], it can be expected that strong jets are accompanied by regions of stagnation or weaker reversed flow which is the result of a fluid inertia. It is not surprising that the RH stator with rows of round holes causes the same effect as observed by Mortensen [2011] since the round holes are the beginnings of the strong jets.

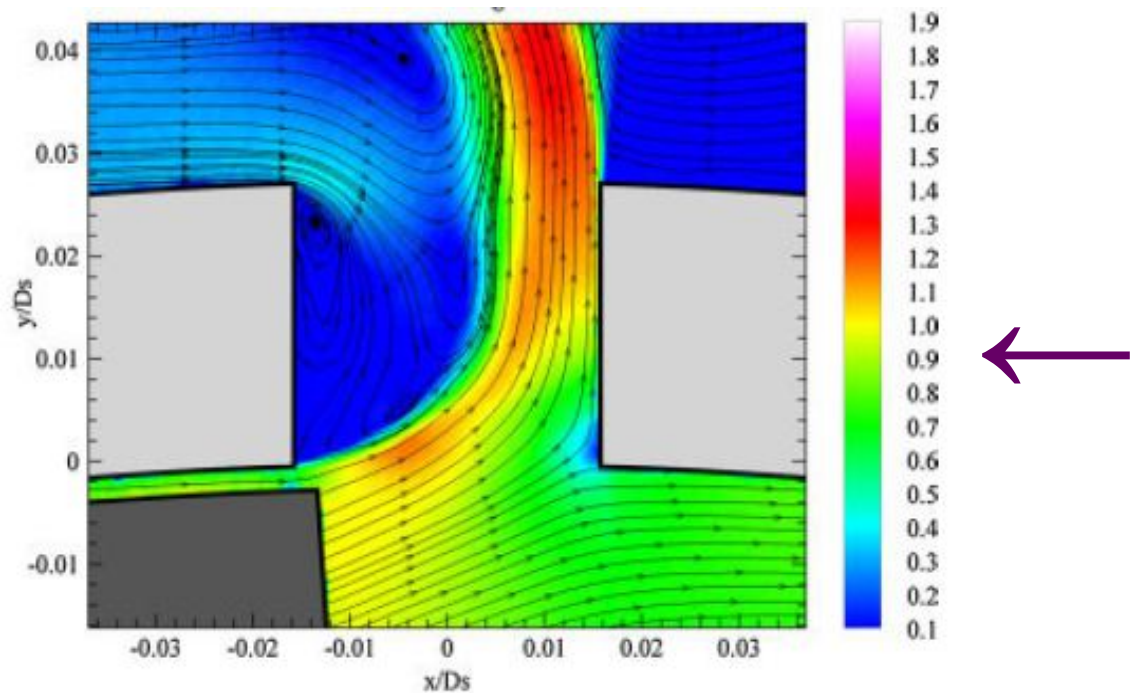


Figure 6.16. The flow close to the slotted head (the stator is light grey, the rotor is dark grey), visible: reversed velocities behind the jet. The jet is strong and well concentrated [Mortensen et al., 2011]. Top view of the head horizontal cross-section is shown. The point of view used in this thesis is shown by an arrow.

The square-holes stator provides more uniform mixing since the jets are not so well concentrated as in the case of round jets. The turbulence at the edges of jets occur earlier in the case of square jets (see Fig. 6.13). The jets will not travel as far as with round holes but the velocity pattern is more uniform because the energy is transferred by this turbulence into the fluid surrounding the jet. The better agitation can be seen from Fig. 6.14 and 6.15 as the flow observed with SqH stator is more similar to the expected one-loop flow pattern. As the velocities in pictures seem to be higher and more uniformly distributed in the stirred region with the SqH stator we have to check this closer. Table 6.7 compares averaged velocities in a flow around both heads for different N.

Table 6.7. Mean velocities for different heads (RH and SqH) and comparison between them in percents.

N [rpm]	Mean velocity [m/s]		$V_{RH} \sim V_{SqH} (^*)$
	V_{RH}	V_{SqH}	[%]
2 000	0.29	0.31	6
3 000	0.44	0.48	8
4 000	0.6	0.64	6
5 000	0.62	0.78	21
6 000	0.73	0.83	12
7 000	0.72	1	28
8 000	0.72	1.29	44

- Relatively, calculated as $100\% \cdot [(V_{RH} / V_{SqH}) - 1]$.

Mean velocities differ by as much as 44% when the value of the N increases. With the N increases, the difference increases too. The mixing is more intensive and more uniform in the case of the SqH stator. It is interesting to find this from the PIV photos as the pseudo-cavern trace (SiO₂ physical model) was observed to be bigger for the RH. The RH is causing strong jets which travel further, visibly increasing the pseudo-cavern trace on the bottom of the tank. Unfortunately, the uniformity of the mixing in this region is poor (Figure 6.15) as discussed above, which is indicated by smaller averaged velocities around the RH than around the SqH.

After analyses from PIV results, we can conclude, that the increase in the radius of pseudo-cavern with the round holes against to square holes is accompanied by the decrease of the uniformity and intensity of agitation inside the pseudo-cavern volume. The intensity of agitation was previously checked for few Silverson stators by the computer simulation [Utomo, 2009] and Table 6.8 present the simulated energy dissipation.

Table 6.8. The amount of energy dissipated in various regions in the vessel calculated by the computer simulation [Utomo, 2009].

Stator	Rotor swept region	Hole region	Jet region	Rest of the tank
Disintegrating head	47.1%	8.4%	23.7%	20.8%
Slotted head	54.9%	14.6%	25.4%	5.1%
Square-hole head	60.3%	12.0%	26.5%	1.2%

In Table 6.8, we can find information that in the case of the square-hole head from Silverson about 28% of energy is dissipated in the jet region and in the rest of tank. For disintegrating head in the similar region, the amount of energy dissipated equals 43%. Thus, the jet energy and a tank agitation are on the higher level with wide round holes (8 mm diameter). In the case of narrower (1.6 mm wide slots with the length 11 mm) and square-shaped holes (2.5 mm), about 18% more energy is dissipated in the rotor swept region and in the holes region than in the case of the disintegrating head. That means that more energy is used for the shearing process which occurs inside the head and in the holes region than in the case of the disintegrating head. Of course, the RH (Figure 2.3) differs from the disintegrating head (Table 1.1), but some similarity can be found. The holes of the RH are smaller but the same round shape will be promoting the free jets emanating from stator holes. Therefore, more energy will be transferred outside the head by jets. If we compare only the jets region (part of the tank agitated by the jets, which can be compared with the pseudo-cavern region defined in Section 1.2.2) it can be seen that the agitation is slightly less for the disintegrating head. It can be explained by the non-uniform agitation of this region. Similar results are observed in our research for RH as the averaged velocities are smaller in this region than with SqH stator.

Our observations are in good agreement with results of computer simulation done by Utomo [2009] since square holes, according to PIV results, are accompanied by a more uniform and concentrated flow inside the pseudo-cavern. Utomo [2009] also described that the energy dissipated around the square holes head is more intensive inside the jet region than observed with other stators. Additionally, for square holes, only 1% of energy is transferred into rest of tank what indicates the pseudo-cavern intensification (especially when compared with 20% of energy transferred by the disintegrating head).

In this moment we have to remind that the model described in Section 5.1.1 has been established for the crossH design and using this model for other stators is believed to be valid as an approximation which reflects reality. As just analysed, the RH causes not uniform mixing even the pseudo-cavern diameter (a) seems to be larger. The SqH stator causes uniform mixing and the pseudo-cavern diameter is similar to obtained for crossH. The a dependence on N can be described as (see Fig. 6.10):

$$a(N) = 0.023 N \quad \text{Equation 6.1}$$

The value 0.023 calculated from measured data which describes mixing conditions around the SqH is close to value obtained for crossH equal 0.024 (see Eq. 5.1). Therefore, the model described in Chapter 5 can be treated as valid for SqH. The pseudo-cavern diameter achieved with RH stator is larger but between the jets the agitation is weak. If we use the approximation described by Eq. 5.1 (or in the consequence Eq. 5.15 and Eq. 5.16) the round jets reach the walls earlier than in the case of other stators (crossH, SqH) and the scattered flow should improve the uniformity of mixing. Therefore, the model can be used for all presented types of the stators to establish uniform and fully agitated conditions of stirring.

In the case of the liquid Al alloys processing, the head has to be made from ceramic materials. According to the presented results, the square holes are giving better pseudo-cavern uniformity and mixing intensification. Since ceramic materials are hard and it is difficult and expensive to prepare more complicated hole shapes than round ones [the communication with prof. Z. Fan, 2012], the square holes are not used in ceramic heads intended to liquid alloys processing. Thus, if possible, the flow uniformity should be improved by other design changes, without using the square-shaped holes. The new design of head has been proposed and next part of the work will show how the new stator design influences on the uniformity of the flow agitation.

6.2.3. Stator holes arrangement.

Commonly used in BCAST head (RH) has a design similar to the Silverson disintegrating head. Holes are arranged in the rows (see Fig. 2.3). Thus, the flow jets are not uniformly distributed around the head. The square holes disturb jets providing turbulence and more uniform energy dissipation in the mixed region while round holes cause the strong jets able to travel far but without full agitation of mixed region. The bulk liquid is agitated mostly along jet lines, which are arranged in rows. As a result there is strong agitation in one direction.

Since the square holes can not be used with ceramic heads because of technical difficulties, it is a necessity to overcome this problem. There exists a method to improve the uniformity of mixing with using the round holes with simple arrangement changes and crossH construction has been specially designated for this purpose. To make this easier for understanding, Figure 6.17 shows jets which can be observed with both types of the head (RH and crossH).

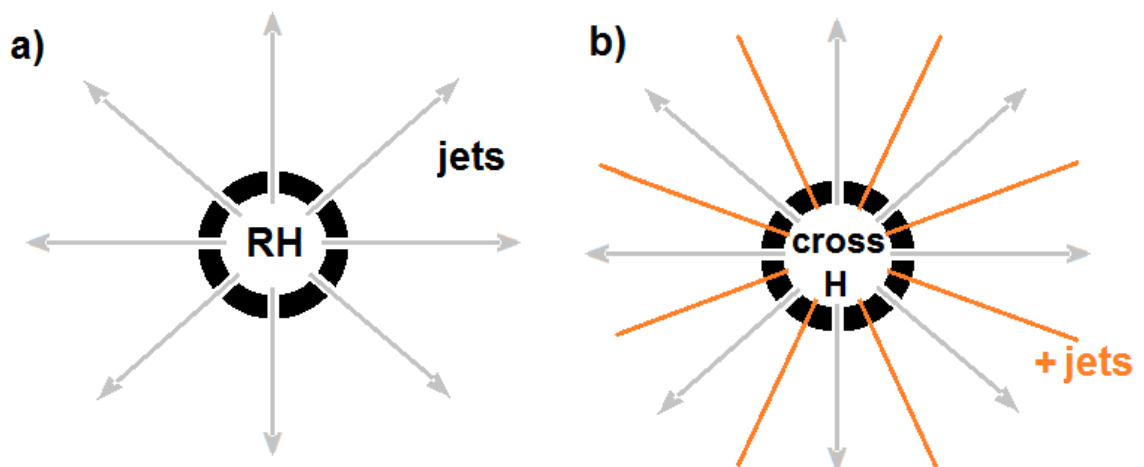


Figure 6.17. Positions of jets around a stator with round holes arranged in rows (RH) and around a crossH design. Additional red positions of jets are the effect of the holes rearrangement on the stator which improves the uniformity.

The result of the holes arrangement of crossH is observed as uniformly distributed jets and more uniform distribution of dispersed substances. Figure 6.18 demonstrates jets observed in 3D. To observe them only the bottom of the head was immersed into water. The sucking force brought a liquid to the head and spread it out as the jets which travelled in the air.

Chapter 2 outlined some difficulties in the pseudo-cavern trace measurement done with different stators. The observed trace of the pseudo-cavern has the “star” or the “flower” shape (see Fig. 2.10 b). This effect was usually observed with the RH stator or with the disintegrating head. As the emulsor screen (Silverson) has a lot more equally distributed holes, the pseudo-cavern trace was more regular with a shape closer to the circle as compared to other heads. To improve a uniformity of an agitation a crossH design is proposed in this work.



Figure 6.18. Jets around a new stator (crossH) are arranged uniformly in the space what improves the uniformity of a fluid agitation.

To check how the new design influences the flow pattern, Figure 6.19 shows the results obtained by PIV for $N = 7\,000$ rpm.

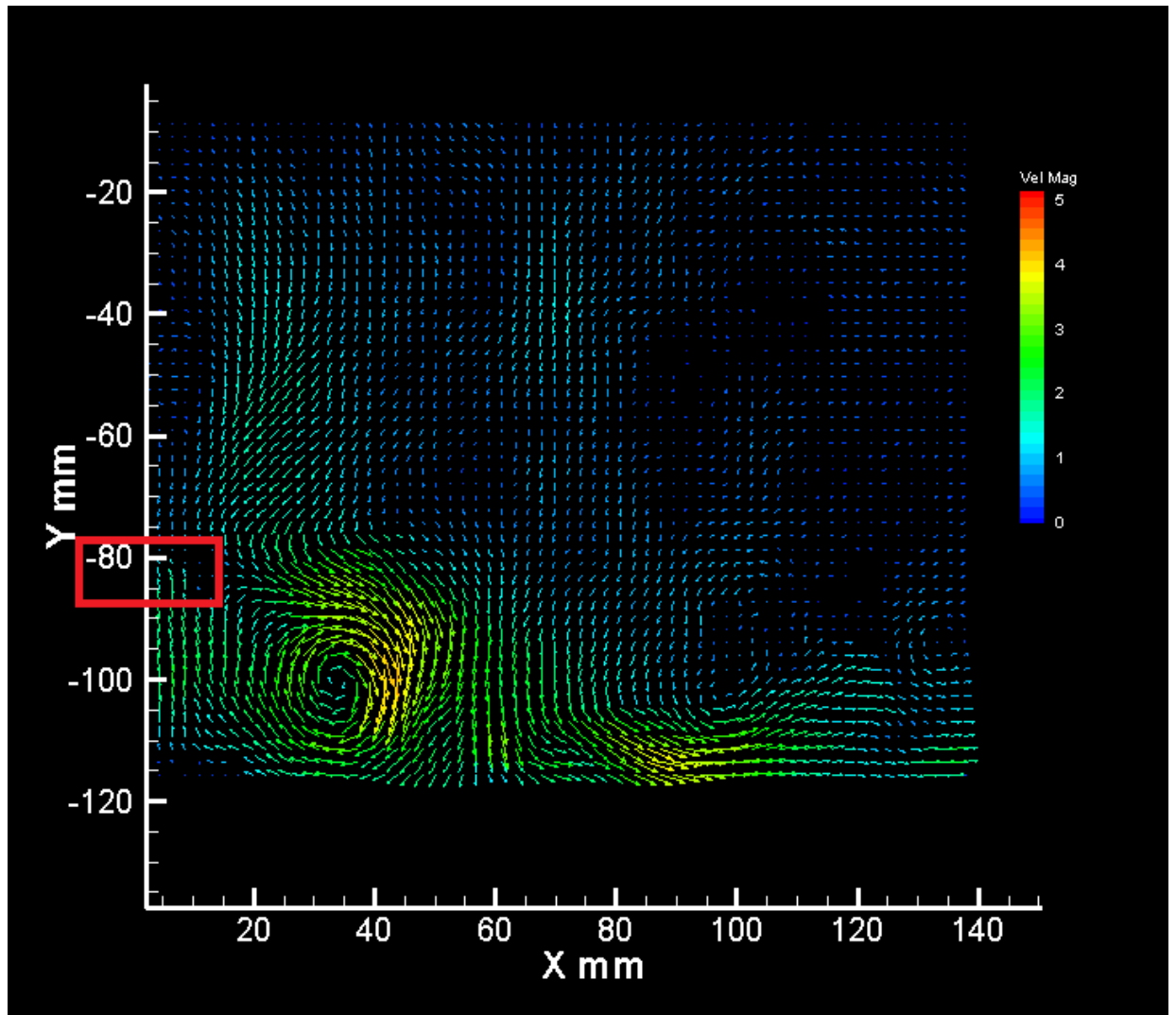


Figure 6.19. A flow around the head with round holes arranged in cross lines (crossH), $N = 7\,000$ rpm, $Re=56000$. The head position is shown by the red rectangular.

As the rotational speed in each case (Figures 6.14, 6.15, 6.19) is the same, we can compare results. The flow pattern is similar to that obtained with SqH rather than with the RH. We observe not only jets (Figure 6.19) but also a circulation loop. The agitation

by crossH (Fig. 6.19) seems to be more uniform than with the RH (Fig. 6.15). The maximum velocity of the fluid is about 4 m/s against the maximum velocity equal 5 m/s observed for RH or SqH. Thus, we will try to find if the flow intensity is decreased or not.

Averaged velocities in the stirred region are shown in Table 6.9 for a wider range of the N than the results presented in previous figures (6.14, 6.15, 6.19).

Table 6.9. Averaged velocities around the RH and the crossH and comparison between them in percent's.

N (rpm)	Mean velocity (m/s)		$V_{\text{CrossH}} \sim V_{\text{RH}} (^{\circ})$
	V_{RH}	V_{crossH}	(%)
2 000	0.29	0.25	-16
3 000	0.44	0.4	-10
4 000	0.6	0.5	-20
5 000	0.62	0.7	11
6 000	0.73	0.85	14
7 000	0.72	0.95	24
8 000	0.72	1.04	31

- Relatively, calculated as $100\% \cdot [(v_{\text{CrossH}} / v_{\text{RH}}) - 1]$.

•

The velocity of the crossH is treated as 100% and the differences are shown against velocities obtained for the RH design. The minus means that the velocity observed with a new design is smaller in a comparison with the RH design.

Over 5 000 rpm, the averaged velocity in the checked region is higher than that observed with the RH stator and this tendency seems to grow up with N. From recorded mean velocities it is difficult to decide how the new design (crossH) influences on the mixing intensity since results are different for different N.

To find a possible reason for a velocity decrease we have to check the influence of the design changes. As the holes in the RH are placed in rows, thus, in one plane all four holes will agitate flow by 4 jets. The crossH improves the uniformity around the head in 3D space. In the single plane across the head, we have only two holes and only 2 jets

agitates flow in the one plane. The observation plane is parallel to the head axis and both observations were made in the same cross plane. Thus, the flow observed close to the crossH can be weaker than observed with the RH. The maximum velocity of the jet can be smaller since the jets do not join together because of relocation and mixing is expected to be more uniform in 3D despite the velocity of the jets in one plane. Two jets are relocated into another plane and probably this influences on the observed flow strength (see the graphical explanation in Figures 6.20 and 6.21).

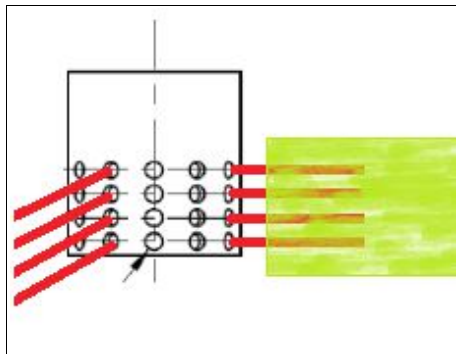


Figure 6.20. The laser light overexposes one plane and reflects existence 4 jets in one plane. Visible red jets and a green observation plane.

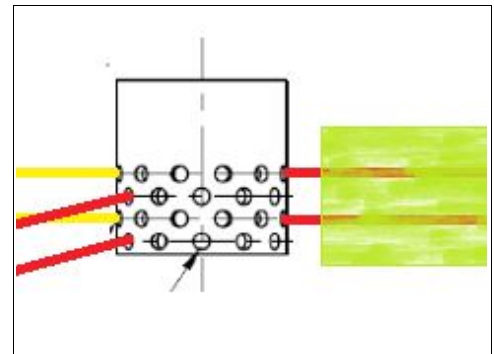


Figure 6.21. The laser light overexposes one plane and reflects existence 2 jets in one plane. Visible red jets and a green observation plane. Two yellow jets are relocated into another plane.

To validate presented explanation a 3D PIV system is required. Since only 2D results were possible to record with the PIV system available, it is impossible to decide what causes this change in mean velocities. The suggested explanation is in agreement with previous research of Utomo [2009]. The predicted flow pattern with different stators (Figure 6.22) is simulated in the plane perpendicular to the recorded by us, which can complete our findings.

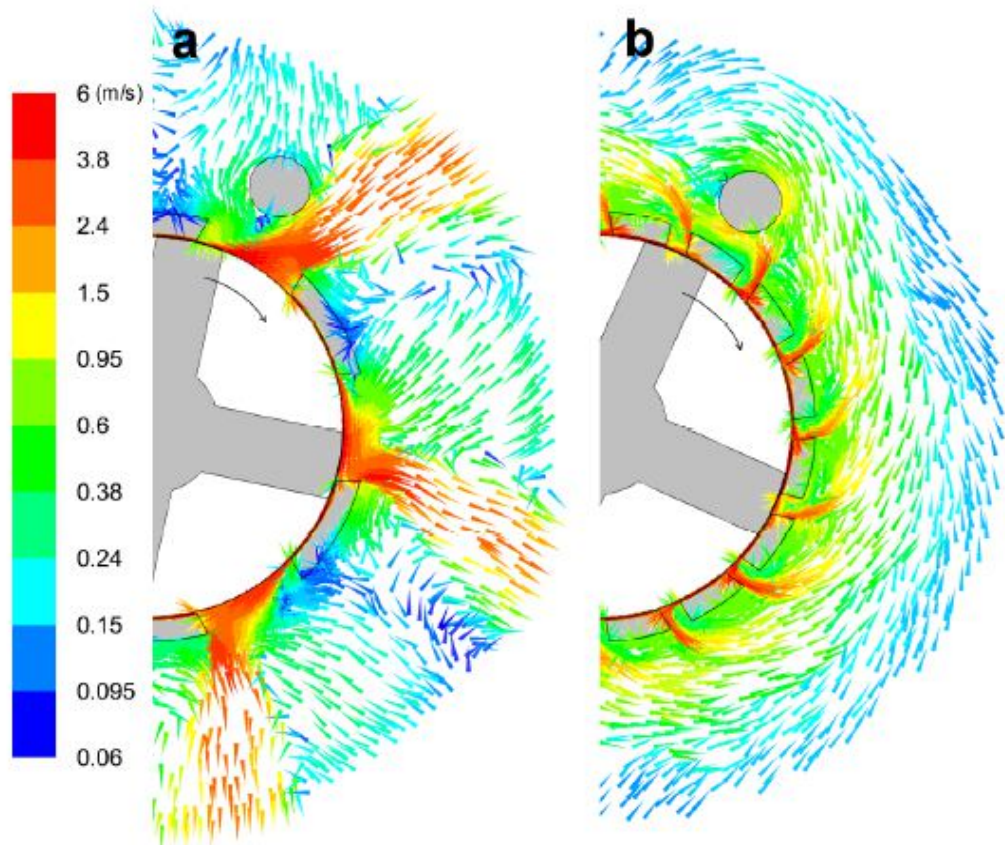


Figure 6.22. Flow patterns around (a) disintegrating head, (b) slotted head [Utomo, 2009].

The examined stators design is different but the disintegrating head has a smaller number of openings and jets are observed only in 6 planes (3 red jet planes in Fig. 6.22 a). The slotted head (Fig. 6.22 b) has much more openings. Independently of the shape of the holes, the agitation by more jets arranged around the head gives a more uniform flow pattern. The stagnant (blue) or reversed velocities are not present around the stator. The probability that any plane perpendicular to the simulated plane (Fig. 6.22) will be not well agitated is almost zero for the slotted head but it is much bigger for the disintegrating head. Stronger agitation of a fluid occurs between the jets as the number of jets increases (Fig 6.22 b). Therefore, if uniformity of stirring is high we do not expect the flow pattern like presented before in Figure 6.15. The flow pattern recorded by PIV system for the crossH shows more uniform, one-loop flow pattern. It can be taken as a proof of uniformity of mixing by this head.

The flow intensity should be further examined if necessary, but the previously made sheared powder analysis (Chapter 4) indicates that efficiency of mixing by the crossH is even better than achieved with the RH. Thus, the flow has to be strong and

uniform enough to bring the particles back into the head. Since the observed results are better than those achieved with a strong jet caused by RH, we are sure that the flow agitation is better.

In conclusion, the change in the head design improves the uniformity of mixing and from this reason can be treated as a good replacement of the SqH. The verification of findings was done by direct measurements of the mixing uniformity.

Measured pseudo-cavern traces exhibit some nonuniformity observed as non-circular shapes, named in this work as „flower” or ”star” shapes. The „star arms” are the reflection of jets emerging from stators. The „star body” is the effect of the sucking force which moves the particles up from the bottom. With different designs of the stator, the difference between radii of arms and a body was observed (see Figure 6.22).

To validate our findings by a more direct method we used the SiO₂ physical model. The non-uniform mixing can be observed on the pseudo-cavern trace. If the jets travel further (strong jets and weak flow between them) the pseudo cavern shape has a form of the star with longer arms than the radius of the “star body” (which reflects the uniform agitated liquid). Thus, the radii difference (ΔR) is taken as the nonuniformity coefficient for the observed pseudo-cavern shape (Figure 6.23, 6.24). Values of ΔR were measured experimentally and are given in Table 6.10 for the different stator designs.

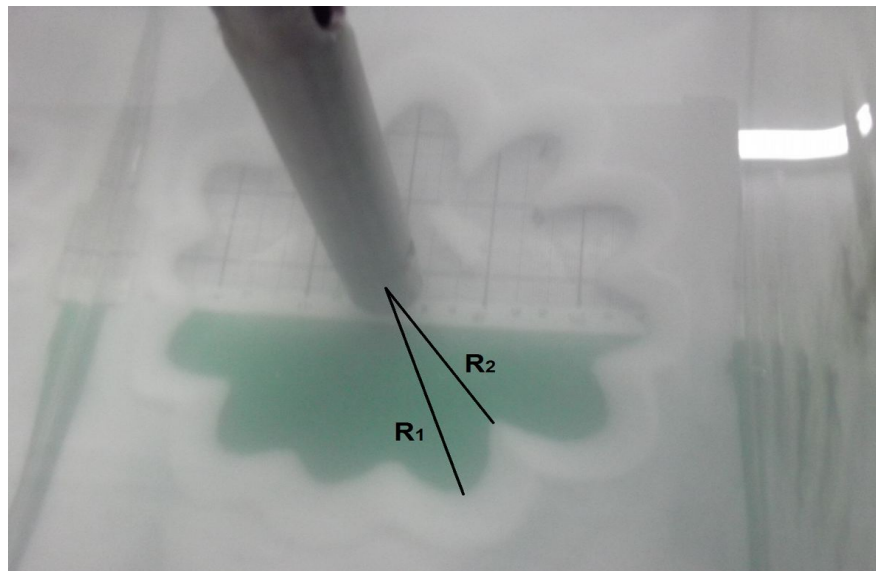
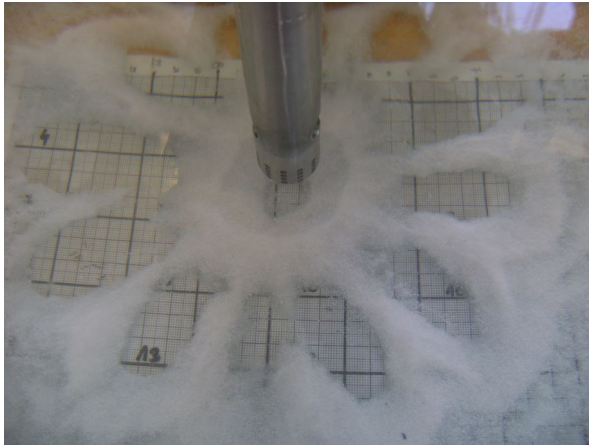
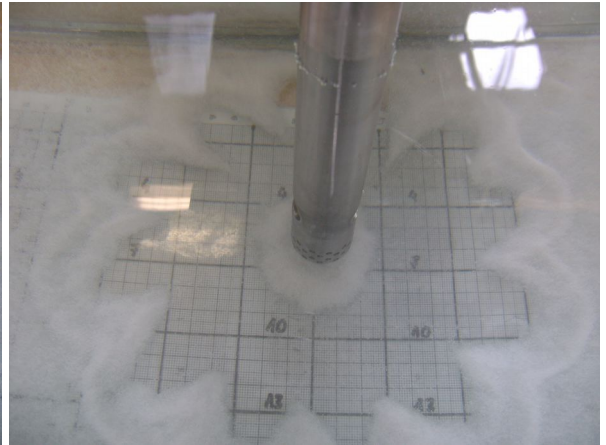


Figure 6.23. The „star” shape observed as the effect of mixing nonuniformity.

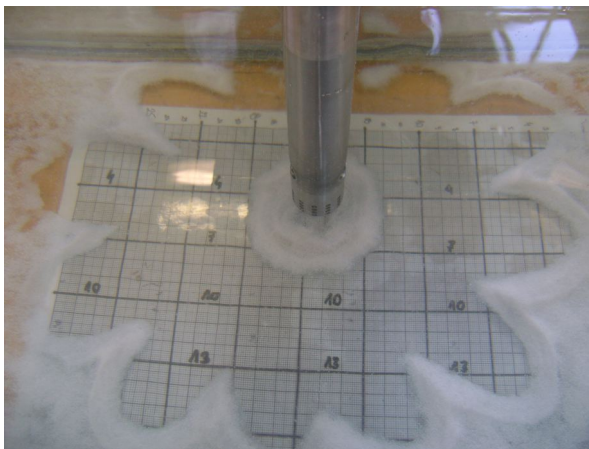
*The difference between measured radii is taken as
the nonuniformity coefficient $\Delta R = R_1 - R_2$.*



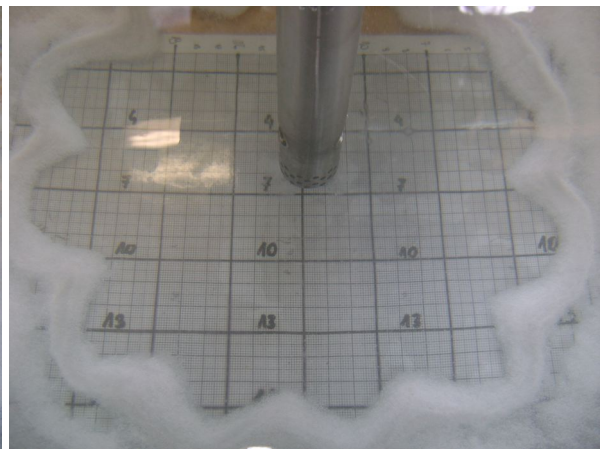
(a) RH, 3000 rpm



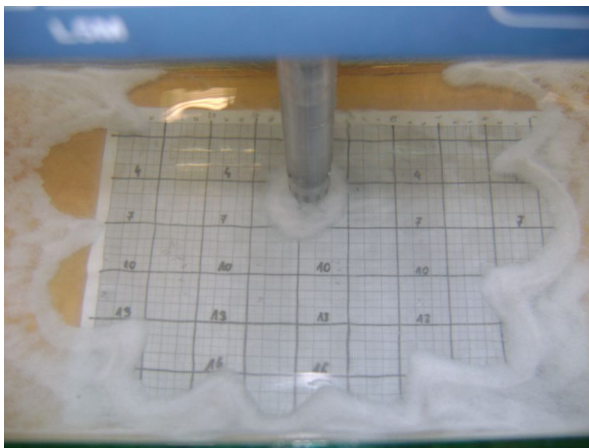
(b) crossH, 3 000 rpm



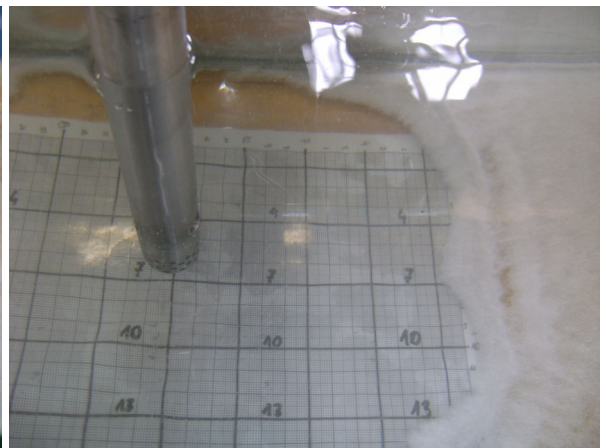
(c) RH, 4000rpm, $Re=32000$



(d) crossH, 4000 rpm, $Re=32000$



(e) RH, 5000 rpm, $Re=32000$



(f) crossH, 5000 rpm, $Re=32000$

Figure 6.24. The nonuniformity of mixing observed for RH and crossH stator.

Table 6.10. The nonuniformity coefficient ΔR measured experimentally (SiO₂ model system) with different stator designs in a wide range of the N.

N	ΔR for RH	ΔR for crossH	ΔR for SqH
	[mm]	[mm]	[mm]
2000	10±2	5±1	10±2
2500	15±2	5±1	5±1
3000	10±2	5±1	5±1
3500	10±2	5±1	3±1
4000	10±2	5±1	0±1
4500	15±2	3±1	0±1
5000	10±2	2±1	0±1
5500	5±1	0±1	0±1
6000	5±1	0±1	0±1
6500	5±1	0±1	0±1

Values of the ΔR coefficient decrease with the increase of the N. The tendency to nonuniformity of the pseudo-cavern shape caused by the non-uniform flow is stronger for the RH in comparison to other designs. For both, the SqH and the crossH, the values of the non-uniformity are smaller, about 5 mm and the nonuniformity decreases strongly with the N. The flow inside the pseudo-cavern around the RH is not uniform due to presence high velocities in the jet region against the weaker flow in other places of the pseudo-cavern as observed in Figure 6.14 . The crossH design compensates this effect by the more random jets distribution in the pseudo-cavern region. This holes arrangement can improve mixing conditions. The crossH still does not achieve so uniform flow as the SqH since values of the ΔR for the sqH are close to zero over 4 000 rpm. Obviously, the

jet is scattered on the holes border and turbulences which occur earlier [Gohil et al., 2010] cause a more uniform agitation. In the crossH case, the presence of additional planes with jets between rows agitate bulk liquid similarly.

The pseudo-cavern volume can be calculated with Equation 5.5 for measured values of a (Table 6.10). Figure 6.25 shows predicted volumes of the pseudo-cavern for a different N calculated with using measured values $R = a$ for different stators.

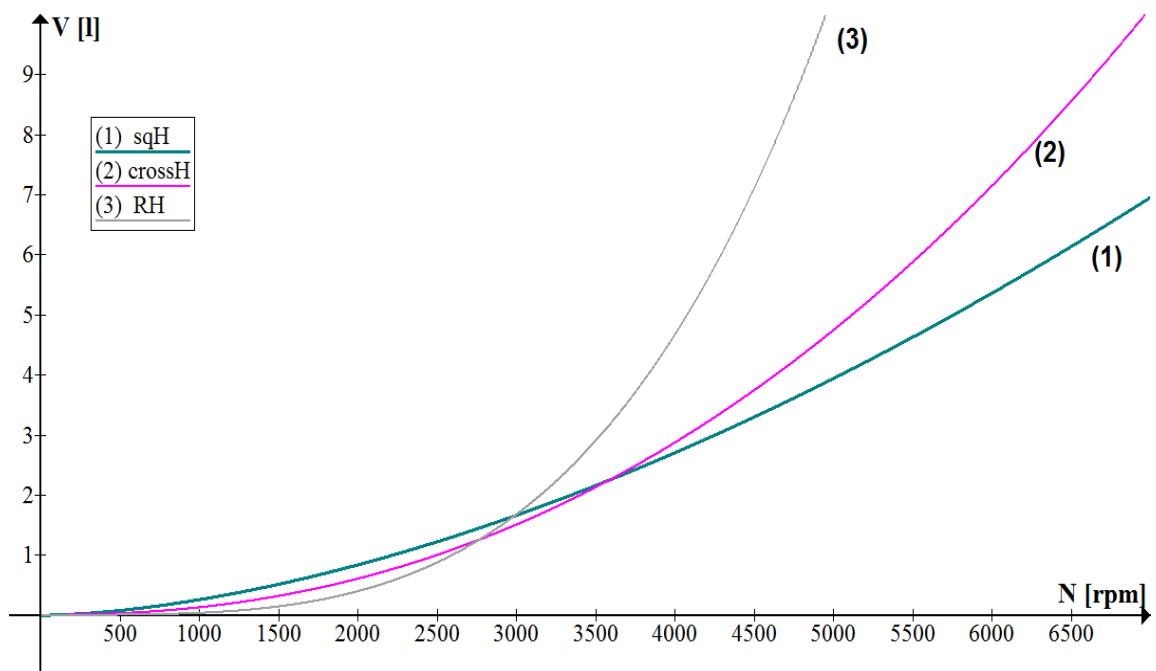


Figure 6.25. Predicted volumes of the pseudo-cavern observed with different stators for a wide range of the N .

The well-mixed volume predicted with the model for RH seems to be the biggest but as indicated from PIV results and the ΔR measurements, the mixing inside this region is not uniform. The crossH improves the uniformity of mixing and still the stirred volume is bigger against to the SqH.

Finally, the crossH:

- improves the uniformity of mixing in the pseudo-cavern volume;
- the well-mixed volume is slightly bigger than for the sqH;
- the fragmentation efficiency is better than achieved with used up to now the RH.

Since the square-holes design is too expensive and in ceramic heads is replaced by round holes, the holes rearrangement should be considered to improve the mixing uniformity.

6.3. Shearing time influence.

In the published research there are some correlations for open impellers to predict mixing time if the impeller design and physical properties of the fluid are known [Sharratt, 2007] but no such data exists for high-shear rotor-stator devices. To establish the optimum mixing time the experiment observations are necessary. The main question is what will be the minimum or optimum time that we need to disperse and distribute oxides in a vessel. Theoretical mixing time is defined as the time taken to blend a tracer into the bulk liquid until the variation in concentration fluctuations measured at a given point has reached the minimum. When we operate with a specific fluid – a molten metal, for example - the key point is to check the time influence on the real process. In metallurgy the measurements of the system homogeneity during liquid metal processing are difficult. Instead of real time homogeneity measurements, we can compare results of the oxide dispersion. As given before (Section 1.4) the dispersed oxides play a role of nucleation sites what can be seen as grain size decrease. So a number of grains and differences in their sizes can give us information on how effective is the processing by the HS device for a chosen time.

To establish the critical time in the first experiment we checked the range of time from 1 to 10 minutes. The used Al-3%Mg alloy has been processed at 660°C. The average grain size is presented in Table 6.11. Before the system reached full agitated conditions (N = 3000 rpm) the molten metal was processed for 2 minutes with smaller N (500 rpm). Thus, first we took samples of the metal processed in conditions when the pseudo-cavern did not occupy the whole vessel, and later the time influence in a fully agitated vessel was experimentally checked and results are presented in Table 6.11.

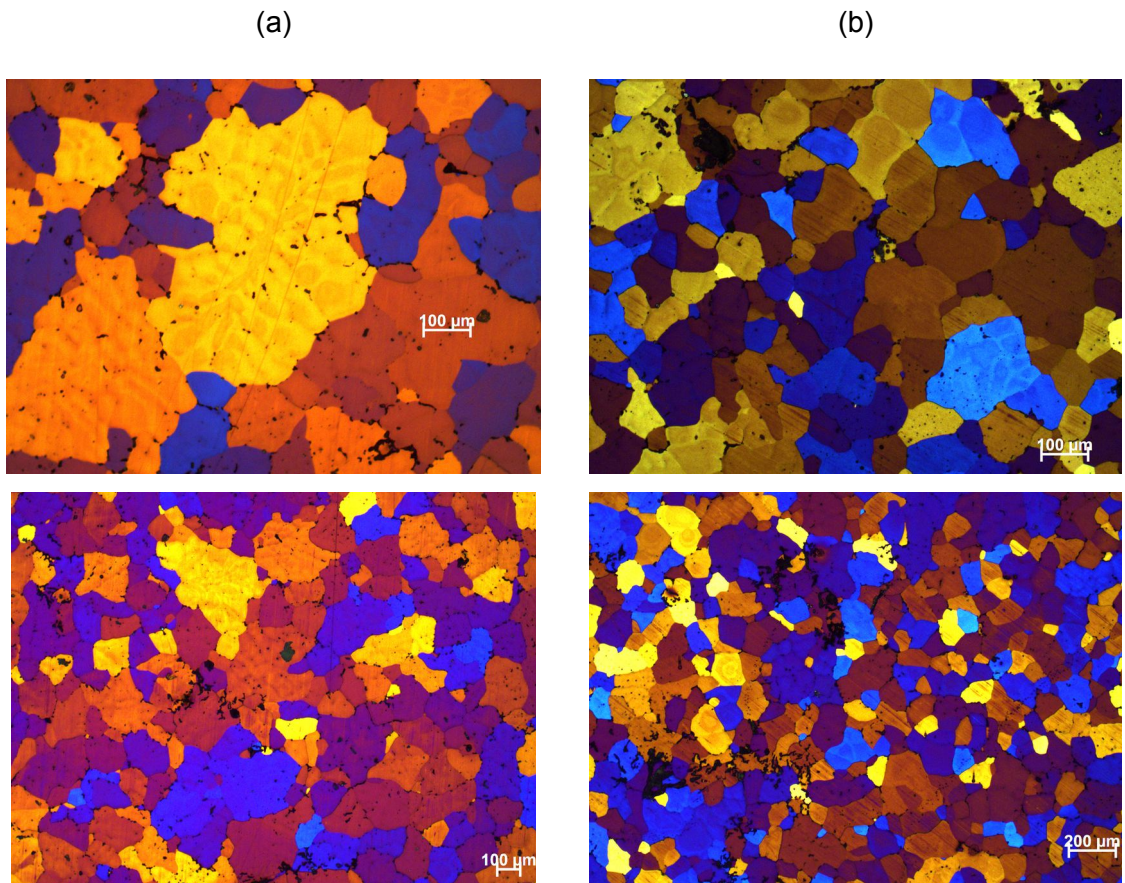
Table 6.11. Grain sizes of an Al-3%Mg alloy in dependence on the time of shearing at N = 3000 rpm after shearing stage without full agitation (N = 500 rpm).

Time of shearing (minutes)	Rounded average grain size (μm)
1	490 \pm 34
3	410 \pm 31
5	310 \pm 22
8	310 \pm 35
10	320 \pm 28

After some specific time shearing effects are similar. Only in few first minutes (less than 5 minutes), we observe the change in the grain size. A few more experiments have been done to check process during first few minutes and confirm results from the first experiment. The diameter of the crucible A16 (18.4 cm) was carefully chosen to achieve full mixing conditions with the suitable rotational speed 2500 rpm. All samples were taken in TP1 moulds and prepared in the same way to check microstructures. The rotational speed was kept at a constant level from beginning with respect to the set-up possibilities. The observed grain sizes are given below in Table 6.12.

Table 6.12. Grain sizes of an Al-3%Mg alloy in dependence on the time of shearing.

Time of shearing (min)	Rounded average grain size (μm)
2	178 \pm 23
3	156 \pm 20
4	97 \pm 14



*Figure 6.26. The grain size of Al-3%Mg alloy decrease with a time (pictures are given for two magnifications);
(a) after 2 minutes of shearing
(b) after 4 minutes of shearing.*

Figure 6.25 gives the grain structures observed after 2 and 4 minutes of shearing by the rotor-stator device. From both experiments, the process effect is the best after about 4 minutes of shearing in fully agitated conditions. Thus, the minimum time of dispersion and distribution of oxide clusters is expected between the 3rd and 4th minute of shearing.

We can assume that in fully agitated conditions the oxide films and clusters should be dispersed and the number of agglomerates should decrease up to moment when it reaches some equilibrium. In the ideal situation after this specified time, there will be no more clusters to be dispersed and a liquid with a dispersed oxide will be just stirred without big changes in a local homogeneity [Kresta, 2004]. Unfortunately, the exact predictions of time necessary to break the bonds of clusters and films are not yet available. The Tong [2016] simulation indicates that only one pass of fluid by the head is required and the completed research by him can be really useful for further analyses. However, the experimentally found time equal to 4 minutes reflects not only the time necessary for defragmentation. It is a time needed for full agitation and a time in which the fluid will pass the head enough times to cause the cluster defragmentation. Thus, this experimentally observed value can be treated as a guideline for a user, but the exact explanation of the process needs more research, for example, the completed computer simulation of cluster breakage.

Chapter 7. Proof of concept with liquid metals.

As shown by the computer modelling small oxide particles can play the role of nucleation sites. Grain refiners have small sizes and usually are well dispersed to achieve best results. Chapter 4 shows that the HSM has a high defragmentation and a deagglomeration potency. Chapter 5 focuses on the uniform particles distribution. The new physical model was presented. With the model is possible to predict sizes and a volume of the well-mixed region. The effective distribution of oxides happens only inside this region, named a pseudo-cavern. Other factors which can influence on the flow uniformity inside the well-mixed region were checked experimentally to complete the model. According to presented findings, a new design of the stator was presented in Chapter 6. A new design improves the mixing uniformity. The head defragmentation potency is kept on a similar level.

Presented in this work findings were compared with a real liquid metal processing. From formulated in Chapter 5 equations the pseudo-cavern size was calculated for the ceramic head (BCAST design). For a rotor diameter 32 mm and with equation 5.16 the pseudo-cavern volume can be calculated as:

$$V(N) = 1.4 \cdot 10^{-10} N^3 \quad [\text{dm}^3] \quad \text{(Equation 7.1)}$$

The function $V(N)$ is shown in Figure 7.1 below.

V(N) for 32 mm head

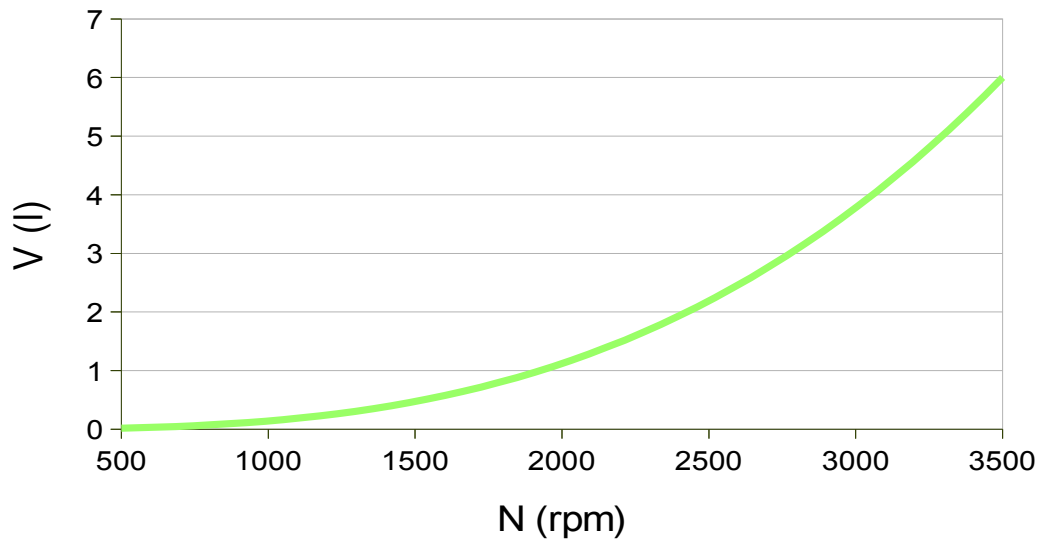


Figure 7.1. The volume as a function of N predicted the physical model for the 32 mm ceramic rotor.

Two facts were checked experimentally as the model verification. The first conclusion from the model is a necessity of liquid metal processing in full agitated conditions described by the model. Only in that condition, the effective dispersion of oxides is expected. Secondly, the model is believed to be useful independently of the vessel shape, as long the head depth under the water level is more than the head diameter, to avoid the air vortex creation. Of course, the best shape will be close to the natural shape of the pseudo-cavern but small changes in the shape or proportions shouldn't affect the mixing results. These statements were checked experimentally to validate presented model and the results are described in the following sections.

For verification how the processing of melts in non-sufficient conditions (which are defined by the new model described in this work) influences the measured grain sizes the first experiment was done in the same crucible (A20) but with different N. A smaller rotational speed was chosen to cause the mixing without full agitation and further speed increase resulted in the full agitation without the pseudo-cavern shape changes (the same vessel).

In the second experiment, the crucible was changed to A16 (different diameters, the crucible A16 had a diameter of 184 mm and the crucible A30 had a diameter of 232 mm). The second experiment shows the effects of not full agitation against full agitated results, but the effects demonstrated in a different size of the crucible than the first experiment. The pseudo-cavern proportions (R/H is forced by the vessel shape) were different and the experimental results demonstrated the applicability of the model to the changed conditions (shape).

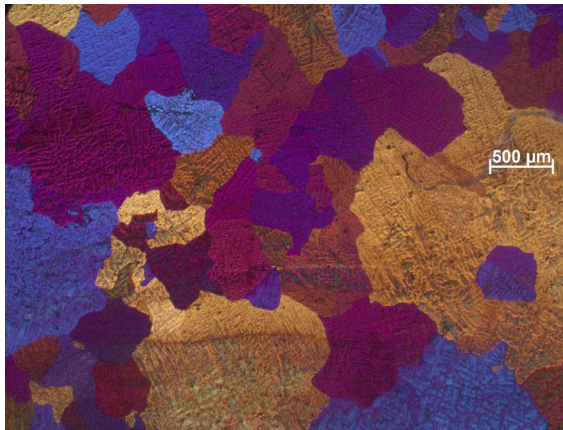
7.1. Not fully agitated conditions – a verification.

Not full agitated conditions (N = 500 rpm) and fully agitated conditions (N = 3000 rpm) as calculated from the physical model were checked. The mixed liquid volume was 2.7 l and the used N = 500 rpm was too small (compare Figure 7.1) to agitate this volume. The N increase to 3000 rpm results in full agitation (In Figure 7.1 we can see that this speed can agitate the volume about 3.5 l). In pictures below microstructures are shown to reveal grain sizes (Figure 7.2). In Table 7.1 are given measured sizes for both cases. The processing time with and without full mixing was 180 s.

Table 7.1 Measured grain sizes after the 3 min s shearing with and without a full volume agitation (crucible A20).

N = 700 rpm (without a full agitation)	N = 3000 rpm (with a full agitation)
512±35 µm	298±30 µm

(a)



(b)

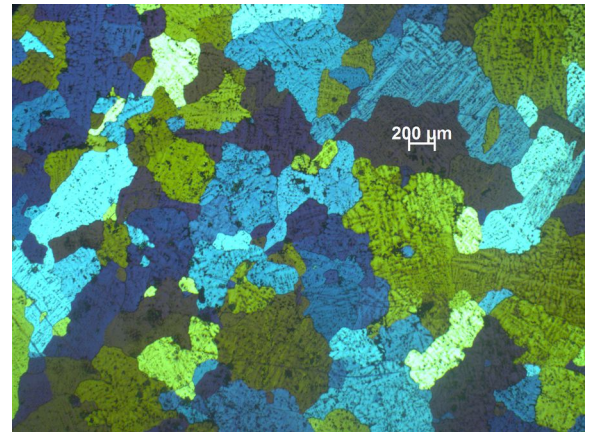


Figure 7.2. Grain sizes of Al-3%Mg alloy observed after 3 min shearing (crucible A20)

(a) without a full agitation ($N = 700$ rpm) and

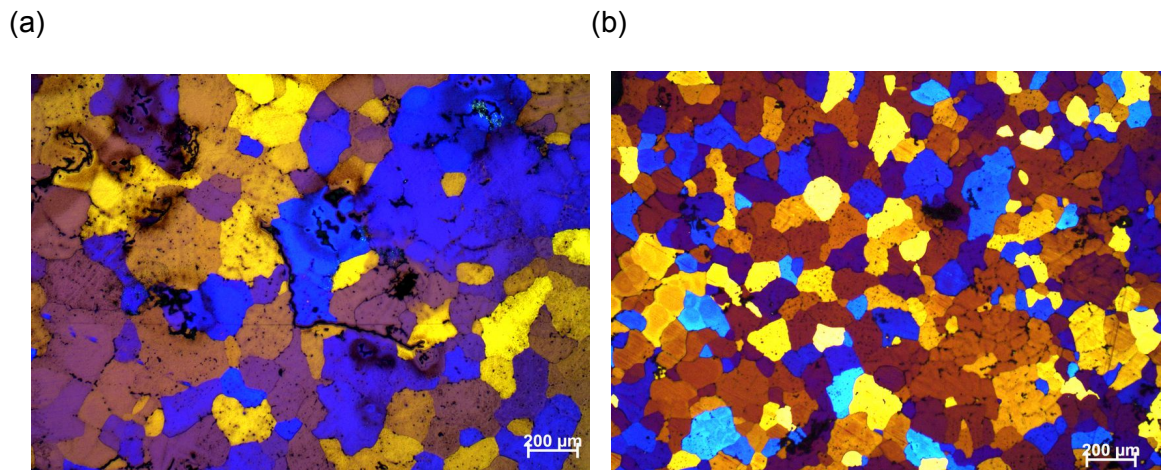
(b) with a full agitation ($N = 3000$ rpm)

Grain sizes after mixing in full mixing conditions decreased and are about 1.7 times smaller than before. The shearing in not fully agitated conditions does not give the expected results since the grain sizes are quite big and observed grains are coarse.

The full agitation results in the grain size decrease what was predicted by the model. In not fully agitated conditions, only a part of oxides agglomerates were sheared since the HSM processed the melt for 180 s. The model well predicts the best mixing conditions that result in grain sizes decrease. In this experiment, we used the rotational speed slightly higher than the minimum value required for full agitation (about 2600 rpm). In the next experiment, the used N was set at a minimal value. Although the grain size was bigger than expected in this conditions (maybe due to the specific impurity level or the local cooling rate), the trend in the grain size is constantly resulting in the decreased grain size after processing in the full agitated conditions.

7.2. Not fully agitated conditions – a verification in different vessel.

To check the possibility of the model application independently of the shape of the vessel (crucible), the shearing was done in a different crucible than before. In particular the ratio the crucible diameter to the height of alloy level is different than before (A16 instead A20). Additionally, to improve effects the next experiment was done with the optimum time of processing according to the previous research (Section 6.4). Results were checked by a typical TP-1 procedure. The micrographs of samples are presented in Figure 7.3 and measured grain sizes are given in Table 7.2.



*Figure 7.3. Grain sizes of Al-3%Mg alloy observed after 4 min shearing
(a) without a full agitation ($N = 500$ rpm, crucible A30) and
(b) with a full agitation ($N = 2500$ rpm, crucible A16)*

Table 7.2. Measured grain sizes after the 4 min shearing without and with a full volume agitation (Al-3%Mg alloy).

N = 500 rpm (without a full agitation, crucible A30)	N = 2500 rpm (with a full agitation, crucible A16)
181±46 μm	97±14 μm

This time, the full mixing was done in a smaller crucible with 180 mm diameter by using rotational speed about 2500 rpm. The volume of liquid was 2 l and we used the minimal value of the N calculated to agitate this liquid volume. Since the diameter of the crucible was changed, the ratio between the diameter and the height of the liquid in the vessel was different than in the previous experiment. The model predicts that the well-mixed region has a constant volume, independent of the vessel shape since the natural pseudo-cavern volume is found by analyses of the free pseudo-cavern shape observed in a big volume of liquid with respect to impeller sizes.

Thus, in this different conditions, we expect that used procedure will still give good dispersion and distribution of oxides. This time, we are using the minimal value of N what will be the exact validation of predictions calculated by the physical model. The shearing time was longer to observe the shearing effect more clearly. Grain sizes of the melt processed in new conditions were measured and results are presented. For reference purposes the same alloy was processed in not fully agitated conditions, so we can compare grain sizes presented in Table 7.2.

The shearing effect is still very good since the grain sizes are two times smaller than observed after a shearing in not fully agitated conditions. As the speed during the shearing process was set on the minimal value necessary to agitate this volume of the alloy, thus the second verification shows that physical model predictions are in good agreement with experimental observations. Since both experiments were done in different crucibles, the shape of pseudo-cavern in both cases was different (different ratio between diameter and height of pseudo-cavern). In both cases, the shearing effects influenced on the grain sizes, and the grain size decreases about two times. That indicates the independence of shearing effect from the crucible shape if the model conditions are fulfilled (the main criterion is the mixed volume).

Both experimental results show a good agreement with physical model predictions with reality. Thus, the model can be used widely for the best conditions selection.

Chapter 8. Conclusions.

Results of a computer simulation give a good prediction that a new technology of liquid metal processing can be based on shearing the oxides present in the melts that can play a positive role in nucleation. At the interface between ceramic-like oxides with small misfit and liquid aluminium, the ordering happens. As this ordering is giving rise to crystal growth, the oxides can be treated as grain refining particles. Thus, the uniform distribution of oxides should improve the quality of alloys.

The physical modelling proved that the HS processing of liquid metals is a really potent method to achieve the defragmentation of agglomerates as the defragmentation of the alumina occurs in all presented experiments. The defragmentation efficiency is strongly influenced by the stator holes shape and the best results were obtained with square holes. However, the defragmentation potency of round holes for oxides present in the melt was proven experimentally and can be predicted from the basic physical rules and from computer simulations. The defragmentation potency does not depend strongly on the gap size.

The effective dispersion is dependent on the flow behaviour and requires the full vessel agitation. The well-mixed region has bordered sizes and new model which describes the sizes and the volume of this region were presented. The model was checked by the PIV observations and by direct experiments in the liquid metals and it was found to be in good agreement with reality.

The uniformity of mixing inside the well-mixed region was checked for different mixing conditions and according to the results, a new design of the stator was proposed for treating liquid aluminium. This design improves the uniformity of mixing in the pseudo-cavern volume and has the dispersion efficiency higher than the design used up to now by BCAST.

The optimal mixing conditions were described, the especially necessity to:

- keep small holes to avoid the fluid instabilities,
- keep the narrow gap to avoid the fluid mixing non-uniformity.
- keep the minimum time of shearing at 4 minutes in fully agitated conditions.

Chapter 9. Future work.

Forced convection generated by HSM is the reason of uniform field of temperature and chemical composition. In this work, the uniform distribution of oxides is discussed, but the temperature field still needs more analysis.

The breakage mechanism of particles and agglomerates is still an open question. Some simulation works are pending now, and research done on this topic can be beneficial to understand the liquid metals processing by HSM.

The validation of the model was done by the experiments with melts. Some basic experiments were done with water. The volume described by Equation 5.7 was checked in water experiments with the silicon dioxide on the bottom of the tank. With N described by that equation, the specific volume seems to be fully agitated – the silicon dioxide was not present on the bottom of the tank when HSM operates. Those simple experiments were done only as preliminary verification before the melt experiments. More water experiments, in different conditions, with PIV recording, will be beneficial to supplement the knowledge about the HSM processing method.

The model was made for the specific conditions present in the light liquid metals. If another setup will be chosen, the analytical steps can be used to establish mixed volume in other fields than metallurgy.

The PIV photos were made in 2D setup. After the experiments, we obtained the radial velocities in the system. The 3D PIV system or only azimuthal direction of PIV photos can be used to better describe the flow. With that observation will be possible to analyse the uniformity and verification the influence of the stator holes arrangement discussed in Section 6.2.3. Unfortunately, the PIV system was loaned on the specific time and it was no possibility of verification and supplement the findings of the experiments done during this time.

REFERENCES:

A

[Adler-Nissen et al., 2004] J. Adler-Nissen, S.L. Mason, C. Jacobsen, Food and Bioproducts Processing 82, 311–319, (2004).

[Agema, 1989] K. S. Agema, D. J. Fray, “Preliminary Investigation on the Deformation Behaviour of an Oxide Scale on Molten Aluminium”, Department of Material Science and Metallurgy, University of Cambridge, (1989).

[Amanullah et al., 1998] A. Amanullah, S. A. Hjorth, A. W. Nienow, Chemical Engineering Science 53, 455–469, (1998).

[Armstrong, 1970] R.W. Armstrong, Metallurgical and Materials Transactions, 1 , 1169-1176, (1970).

[Armstrong, 2014] R.W. Armstrong, Materials Transactions, Vol. 55, No. 1, pp. 2 to 12, (2014).

[Assael et al., 2006] M.Assael, K.Kakosimos, R. Banish, J. Brillo, I. Egry, R. Brooks, P. Queded, K.Mills, A. Nagashima, Y. Sato, W. Wakeham, Journal of Physical and Chemical Reference Data 35 (1) 285–300, (2006).

[Averbukh et al., 1988] Y.N. Averbukh, A.O. Nikoforov, N.M. Kostin, A.V. Korshakov, Journal of Applied Chemistry of the USSR 61, 396–397, (1988).

B

[Bader, 1987] F. G. Bader, Biotechnol. Bioeng., 30: 37–51, (1987).

[Barailler et al., 2006] F. Barailler, M. Heniche, and P. A. Tanguy, Chemical Engineering Science 61: 2888-2894, (2006).

[Bowen, 1986] R. Bowen, Chem. Eng. 9 (June) 55–63, (1986).

[Brandes, 1983] E. A. Brandes, Smithells metals reference book; 6th edition, Butterworths , (1983).

[Brodkey and Hershey; 2003]

R. S. Brodkey, H. C. Hershey; Transport Phenomena: A Unified Approach, Brodkey Publishing, (2003).

[Brook et al., 2011]. E. Brooke, E. Flammang, G. V. Lauder, D. R. Troolin, T. E. Strand, *Biology letters*, Volume: 7 Issue: 5 , (2011).

[Busciglio et al., 2011] A. Busciglio, F. Grisafi, F. Scargiali, M. L. Davì, A. Brucato; 10th International Conference on Chemical and Process Engineering, Volume: 24 , (2011).

C

[Caceres and Selling, 1996] C. H. Caceres, B. I. Selling, *Materials Science and Engineering A*, 220, 109-116, (1996).

[Calabrese et al., 2000] R.V. Calabrese, M.K. Francis, V.P. Mishra, S. Phongikaroon, in: *Proc. 10th European Conference on Mixing*, Delft, The Netherlands, (2000).

[Calabrese et al., 2002] R. V. Calabrese, M. K. Francis, K. R. Kevala, V. P. Mishra, G. A. Padron, and S. Phongikaroon, *Proc. 3rd World Congress on Emulsions*, Lyon, France, (2002).

[Calabrese and Padron, 2008] R. V. Calabrese, G. A. Padron, *Sixth International Symposium on Mixing in Industrial Process Industries*, Niagara on the Lake, Niagara Falls, Ontario, Canada, August 17–21, (2008).

[Calderbank et al. ,1959] P. H. Calderbank, M. B. Moo-Young, *Chem. Eng. Res. Des.* 37,26–33, (1959).

[Campbell, 2000] J. Campbell, *Castings*, Butterworth-Heinemann, Oxford, (2000).

[Campbell, 2003] J. Campbell, *Castings*, 2nd Edition, Elsevier Ltd., Oxford, (2003).

[Candia et al., 1999] J-L. F. Candia, W. D. Deckwer, vol. 5, pp. 2695–2711, Wiley, New York, (1999).

[Cantor, 2003] B. Cantor, *Phil. Trans. R. Soc. Lond. A*, vol. 361, pp. 409–17, (2003).

[Cao and Campbell., 2002] X. Cao, J. Campbell: in *Advances in Aluminum Casting Technology II*, ed. M. Tiryakioğlu, J. Campbell, ASM International, pp.135-146, (2002).

[Conrad, 2004] H. Conrad, *Metallurgical and Materials Transactions A*, 35, 2681, (2004).

[Couper et al., 2005] J. R. Couper, W. R. Penney, J. R. Fair; Chemical Process Equipment (Second Edition) Selection and Design, Pages 277–328, (2005).

[Curtin, 1987] W.A. Curtin, Phys. Rev. Lett. 59, 1228–1231, (1987).

D

[Das et al., 2014] D. Das, N. Khanna, C. N. Dasgupta, Biohydrogen Production: Fundamentals and Technology Advances, CRC Press, (2014).

[Davies , 1985] J.T. Davies, Chemical Engineering Science 40 (1985) 839–842.

[Davies , 1987] J.T. Davies, Chemical Engineering Science 42,1671–1676, (1987).

[Davis, 1993] J.R. Davis, ASM Speciality Handbook, 199-230, (1993).

[Dickey,1984] D.S. Dickey, In Handbook of Chemical Engineering Calculations, McGraw-Hill, New York, (1984).

[Dignam 1962] M. J. Dignam, Journal of the Electrochemical Society, 109, 184-19, (1962).

[Doucet et al., 2003] L. Doucet, G. Ascanio, and P. A. Tanguy, 53rd Canadian Chemical Engineering Conference, Hamilton, Canada, (2003).

[Doucet et al., 2005] L. Doucet, G. Ascanio, and P. A. Tanguy, Trans IChemE, Part A, Chemical Engineering Research and Design, 83(A10): 1186–1195, (2005).

E

[Eckert Jr., 1992] C. E. Eckert, Proceeding of 3rd International Conference on Molten Aluminium Processing, AFS, Florida, (1992).

[Edwards et al., 2013] M.F. Edwards, N. Harnby, J.C. Middleton, Fluid Mixing II: A Symposium Organised by the Yorkshire Branch and the Fluid Mixing Processes Subject Group of the Institution of Chemical Engineers and Held at Bradford University, 3-5 April 1984, Elsevier, (2013).

[Eggers and Villermaux; 2008] J. Eggers and E. Villermaux, Rep. Prog. Phys. 71 ; 036601 (79pp), (2008).

[El-Jaby et al. , 2008] U. El-Jaby, M. Cunningham, T. Enright, T.F.L. McKenna, Macromolecular Reaction Engineering 2, 350–360, (2008).

F

[Fan, 2011] Z. Fan, In this proceedings, 29, (2011).

[Fan, 2012] Z. Fan, Metallurgical and Materials Transaction A2013, 44 , 1409 – 1418, (2012).

[Fan et al., 2009] Z. Fan, Y. Wang, M. Xia, S. Arumuganathar, Acta Mater; 57:4891, (2009).

[Falkovich, 2011] G. Falkovich, Fluid Mechanics, Cambridge University Press, (2011).

[Fisher, 1980] J. Fischer, M. Methfessel, Phys. Rev. A 22, 2836–2843, (1980).

[Francis, 1999] M.K. Francis, Ph.D. Dissertation, University of Maryland, College Park, Maryland, (1999).

[Fuoco et al., 1999] R. Fuoco, E. R. Correa, L. S, Escudero, AFS Transactions, 107, 287-294, (1999).

G

[Geiger and Poirer, 1973] G. H. Geiger, D. R. Poirier, Transport phenomena in metallurgy, Addison-Wesley Pub. Co., (1973).

[Galindo and Nienow, 1992] E. Galindo, A. W. Nienow, Biotechnology Progress 8, 233–239, (1992).

[Galletti et al. 2003] C. Galletti, E. Brunazzi, M. Yianneskis, A. Paglianti, Chemical Engineering Science, Vol. 58, pp. 3859-3875, (2003).

[Galletti et al. 2005 a] C. Galletti, K. C. Lee, A. Paglianti, M. Yianneskis, Chemical Engineering Communications, Vol. 192, pp. 516-531, (2005).

[Galletti et al. 2005 b] C. Galletti, A. Paglianti, M. Yianneskis, Chemical Engineering Science, Vol. 60, pp. 2317-2331, (2005).

[Galletti and Brunazzi, 2011] C. Galletti and E. Brunazzi, Flow Instabilities in Mechanically Agitated Stirred Vessels. INTECH Open Access Publisher, (2011).

[Geankoplis, 2003] C. J. Geankoplis, Transport Processes and Separation Process Principles, 4nd edition, Allyn and Bacon Inc., (2003).

[Geysersmans et al., 2000] P. Geysersmans, D. Gorse, V. Pontikis, J. Chem. Phys. 113, 6382–6389, (2000).

[Gingras et al., 2005] J.-P. Gingras, P.A. Tanguy, S. Mariotti, P. Chaverot, *Chemical Engineering and Processing* 44, 979–986, (2005).

[Gohil et al., 2010] T. B. Gohil, A.K Saha, and K. Muralidhar, *Journal of Visualization*, 13, pp. 141, (2010).

[Grandfield et al., 2013] J. Grandfield, D. G. Eskin, I. Bainbridge *Direct-Chill Casting of Light Alloys: Science and Technology*, John Wiley & Sons, (2013).

[Greer et al., 2000] A.L. Greer, A.M. Bunn, A. Tronche, P.V. Evans, D.J. Bristow, *Acta Mater.* 48, 2823–2835, (2000).

[Greer, 2006] A.L. Greer, *Nature Mater.* 5, 13–14, (2006).

[Guang-wen et al., 2005] C. Guang-wen, S. Yun-hua, C. Jian-ming, C. Han, *Chemical Industry and Engineering Progress* 24, 545–549, (2005).

[Gupta, 1996] D. Gupta, A. Lahiri, *Metallurgical and Materials Transactions B*, 27B, 757–764, (1996).

[Gülich, 2014] J. F. Gülich; *Centrifugal Pumps*, Springer, 24 Oct 2014, (2014).

H

[Haginoya and Fukusako, 1983] I. Haginoya, T. Fukusako, *Transactions of the Japan Institute of Metals*, 24, 613-619, (1983).

[Hall, 1951] E. O. Hall, *Proceeding of the Physical Society B*, 64(9) pp. 747-753, (1951).

[Hall et al., 2011 a] S. Hall, M. Cooke, A.W. Pacek, A.J. Kowalski, D. Rothman, *Canadian Journal of Chemical Engineering* 89, 1040–1050, (2011).

[Hall et al., 2011 b] S. Hall, M. Cooke, A. El-Hamouz, A.J. Kowalski, *Chemical Engineering Science* 66, 2068–2079, (2011).

[Harnby et al., 1997] N. Harnby, M. F. Edwards, A. W. Nienow, *Mixing in the process industries*, 2nd edition, Oxford, UK: Butterworth-Heinemann, (1997).

[Hassan et al., 2010] A. Hassan, E. Bagherzadeh, R.G. Anthony, G. Borsinger, A. Hassan, US 20100183486A1, H.R.D. Corporation, (2010).

[Hashibon et al., 2001] A. Hashibon, J. Adler, M.W. Finnis, W.D. Kaplan, *Interface Sci.* 9, 175–181, (2001).

[Hashibon et al., 2002] A. Hashibon, J. Adler, M.W. Finnis, W.D. Kaplan, *Comp. Mater. Sci.* 24, 443–452, (2002).

Hayduk and Neale, 1978] W. Hayduk, G. Neale, *Can. J. Chem. Eng.*, 56: 544–549, (1978).

[Hemrajani et al., 1988] R. R. Hemrajani, *Proc. 6th European Conference on Mixing*, Pavia Italy, May; 24–26, pp. 259–265, (1988).

[Hildebrand et al., 1976] J.H. Hildebrand, R.H. Lamoreaux, *Proc. Nat. Acad. Sci. USA* Vol 73, No 4 , pp. 988-989, April 1976 *Chemistry*, (1976).

[Hoffmann et al., 1995] J. Hoffmann, K. Buescher, D.C. Hempel, *Chemie Ingenieur Technik* 67, 210–214, (1995).

I

[Iida and Guthrie, 1988] T. Iida, R. Guthrie, *The Physical Properties of Liquid Metals*, Oxford University Press, Oxford, (1988).

[Il'inskii and Keldysh, 2013] Y. A. Il'inskii, L. V. Keldysh , *Electromagnetic Response of Material Media*, Springer Science & Business Media, (2013).

[Impey et al., 1988] S. A. Impey, D. J. Stephenson, J. R. Nicholls, *Materials Science and Technology*, 4, 1126-1132, (1988).

[Impey et al., 1991] S. A. Impey, D. J. Stephenson, J. R. Nicholls, *Proceedings of the First International Conference*, the University of Cambridge, (1991).

J

[Jakse et al., 2013] N. Jakse, A. Pasturel, *Sci. Rep.* 3, 3135, (2013).

[Jeurgens et al., 2002] L. P. H. Jeurgens, W. G. Sloof, F. D. Tichelaar, E. J. Mittemeijer, *Thin Solid Films*, 418, 89-101, (2002).

K

[Kainer, 2007] K. U. Kainer, *Proceedings of the 7th International Conference on Magnesium Alloys and Their Applications*, John Wiley & Sons, 2 Jan 2007 - Science, (2007).

[Kaplan and Kauffmann, 2006] W.D. Kaplan, Y. Kauffmann, *Annu. Rev. Mater. Res.* 36, 1–48, (2006).

[Karbstein and Schubert, 1995] H. Karbstein, H. Schubert, *Chem. Eng. Proc.* 34, 205–211, (1995).

[Karcz and Szoplik, 2004] J. Karcz and J. Szoplik, *Chem. Pap.* 58(1)9|14, (2004).

[Kauffmann and Koch, 2011] Y. Kauffmann, S.H. Oh, C.T. Koch, A. Hashibon, C. Scheu, M. Rühle, W.D. Kaplan, *Acta Mater.* 59, 4378–4386, (2011).

[Kaufman and Rooy, 2004] J. G. Kaufman, E. L. Rooy, “Aluminum Alloy Castings: Properties, Processes, and Applications”, ASM International, (2004).

[Kauffmann et al., 2005] S.H. Oh, Y. Kauffmann, C. Scheu, W.D. Kaplan, M. Rühle, *Science* 310, 661–663, (2005).

[Kelton and G., 2011] K.F. Kelton and A.L. Greer, *Nucleation in Condensed Matter*, Elsevier, Oxford, (2011).

[Kevala et al., 2005] K.R. Kevala, K.T. Kiger, R.V. Calabrese, in: APS Division of Fluid Dynamics 58th Annual Meeting (DFD05), Chicago, IL, (2005).

[Khopkar et al., 2009] A.R. Khopkar, L. Fradette, P.A. Tanguy, *Chemical Engineering Research and Design* 87 (2009) 1631–1639.

[Kim and Cantor, 1994] W.T. Kim, B. Cantor, *Acta Metall. Mater.* 42, 3115–3127, (1994).

[Kowalski et al., 2011] A. J. Kowalski, M. Cooke, and T. L. Rodgers, School of Chemical Engineering & Analytical Science, The University of Manchester, Unilever R&D, Wiley Online Library, (2011).

[Kresta et al., 2004] E.L. Paul, V.A. Atiemo-Obeng, S. M. Kresta, *Handbook of Industrial Mixing Science and Practice*, John Wiley & Sons, (2004).

[Kumar et al., 2011] S. Kumar, N. Hari Babu, G.M. Scamans, and Z. Fan, *Metallurgical and Materials Transactions*, vol 42A, 3143, (2011).

L

[Lee and Kim., 2011] S. B. Lee and Y. M. Kim, *Acta Mater.* 59, 1383 (2011).

[Li, 2011] H.T. Li. Ph.D. Thesis, Brunel University, (2011).

[Li et al., 2011] H.T. Li, Y. Wang, M. Xia, Y. Zuo and Z. Fan, Brunel University Press, p 93-110, (2011).

[Li et al., 2011a] H.T. Li, Y. Wang, M. Xia, P. Jarry, G.M. Scamans, Z. Fan, Brunel University Press, p 93-110, (2011).

[Li et al., 2011b] H.T. Li, M. Xia, Y. Zuo and Z. Fan, Journal of Crystal Growth 314, 285–292, (2011).

[Li et al., 2012a] H.T. Li, Y. Wang, Z. Fan, 2012 IOP Conf. Ser.: Mater. Sci. Eng. 27, 012047, (2012).

[Li et al., 2012b] H.T. Li, Y. Wang, Z. Fan, Acta Materialia 60, 1528–1537, (2012).

[Liu et al., 2003] L. Liu, A. M. Samuel, F. H. Samuel, H. W. Doty, S. Valtierra, Journal of Materials Science, 38, 1255-1267, (2003).

M

[Ma et al., 1992] W.-J. Ma, J.R. Banavar, J. Koplik, J. Chem. Phys. 97, 485–493, (1992).

[Maa and Hsu, 1996] Y.-F. Maa, C. Hsu, Journal of Controlled Release 38, 219–228, (1996).

[Mak, 1992] A. T. Mak, Ph. D. thesis, University of London, (1992).

[Makarov et al., 1999] S. Makarov, D. Apelian, R. Ludwig, AFS Transactions, 107, 727-735, (1999).

[McMullen and Oxtoby, 1987] W.E. McMullen, D.W. Oxtoby, J. Chem. Phys. 86, 4146–4156, (1987).

[Men and Fan, 2012] H. Men and Z. Fan, IOP Conference Series: Materials Science and Engineering, 27, conference 1 (The 3rd International Conference on Advances in Solidification Processes): Article no. 012007, (2012).

[Men et al., 2010] H.Men, B.Jiang, Z. Fan, Acta Mater. 58, 6526, (2010).

[Merwe and Frankand, 1949] ; F.C. Frank and J.H. Van der Merwe: Proc. R. Soc. Lond. A, 1949, vol. 198, pp. 216–25.

[Metzner and Otto, 1957] A.B. Metzner, R.E. Otto, AIChE J3, 3–10, (1957).

[Mi et al., 2003] J. Mi, R. A. Harding, M. Wickins, J. Campbell, Intermetallics, 11, 377-385, (2003).

[Morrison, 2012] F. A. Morrison, Cambridge University Press, (2012).

[Mortensen et al., 2011] H. H. Mortensen, R. V. Calabrese, F. Innings, L. Rosendahl, Can. J. Chem. Eng. 89:1076–1095, (2011).

[Myers et al., 1997] K. J. Myers, R. W. Ward, A. A. Bakker, Journal of Fluid Engineering, Vol. 119, pp. 623-632, (1997).

[Myers et al., 1999] K. J. Myers, M. F. Reeder, D. Ryan, G. Daly, Chem. Eng. Prog., **95**: 33-42, (1999).

N

[Nash, 1998] W. A. Nash, Schaum's Outline of Theory and Problems of Strength of Materials, McGraw-Hill Professional. p.82., (1998).

[Naumann, 2008] Robert J. Naumann, Introduction to the Physics and Chemistry of Materials, CRC Press, (2008).

[Nienow, 1968] A. W. Nienow, Chemical Engineering Science, Vol. 23, pp. 1453-1459, (1968).

[Nollet, 1749] A. Nollet, *Recherches Sur les Causes Particulières des Phénomènes Électriques* (Paris: les Frères Guerin), (1749). [After Eggers and Villermaux; 2008].

O

[Oh et al., 2006] S.H. Oh, C. Scheu, M. Rühle, Korean J. Electron Microscopy Special Issue 1, 19–24, (2006).

[Özcan-Tas et al., 2009] N.G. Özcan-Tas, kin, G. Padron, A. Voelkel, Chemical Engineering Research and Design 87, 468–473, (2009).

P

[Padron, 2001] G.A. Padron, M.S. thesis, University of Maryland, College Park, (2001).

[Padron, 2005] G.A. Padron, Ph.D. Dissertation, University of Maryland, College Park, Maryland, (2005).

[Paipetis, Kostopoulos, 2012] A. Paipetis, V. Kostopoulos; Springer Science & Business Media, 13 Sep 2012, p114-116, (2012).

[Palafox and Laird, 2011] J.P. Palafox-Hernandez, B.B. Laird, M. Asta, *Acta Mater.* 59, 3137–3144, (2011).

[Patel et al., 2013] J. Patel, Y. Zuo, A. Fan, *Proceedings of the 2013 International Symposium on Liquid Metal Processing and Casting*, John Wiley & Sons, (2013).

[Patterson et al., 2004] G.K. Patterson, E.L. Paul, S.M. Kresta, A.W. Etchells, in: E.L. Paul, V.A. Atiemo-Obeng, S.M. Kresta (Eds.), *Handbook of Industrial Mixing: Science and Practice*, John Wiley & Sons, Inc, New Jersey, pp. 755–867, (2004).

[Parsegian, 2006] V. A. Parsegian , *Van der Waals Forces – A Handbook for Biologists, Chemists, Engineers, and Physicists*, Cambridge University Press, (2006).

[Phongikaroon , 2001] S. Phongikaroon, Ph.D. Dissertation, University of Maryland, College Park, MD, (2001).

[Phongikaroon , 2004] S. Phongikaroon, R.V. Calabrese, K. Carpenter, *Journal of Coatings Technology and Research* 1, 329–335, (2004).

[Perry et al., 2007] R. H. Perry, D. Green, *Perry's Chemical Engineers' Handbook*, 8th edition, McGraw-Hill, (2007).

[Petch, 1953] N. J. Petch, *Journal of the Iron and Steel Institute*, 174 pp. 25-28, (1953).

Q

[Quested and Greer, 2004] T. E. Quested, A. L. Greer, *Acta Mater.* 52:3859, (2004).

[Ouzineb et al., 2006] K. Ouzineb, C. Lord, N. Lesauze, C. Graillat, P.A. Tanguy, T. McKenna, *Chemical Engineering Science* 61, 2994–3000, (2006).

R

[Raffel et al., 2007] M. Raffel C. Willert, S. Wereley , J. Kompenhans, *Particle Imaging Velocimetry – A Practical Guide*, 2nd edn. Berlin, Germany: Springer, pp. 1–448, (2007).

[Ray, 1993] S. Ray, *Journal of Materials Science*, 28 pp. 5397-5413, (1993).

[Rayleigh, 1891] Rayleigh Lord, *Nature* 44 249–54, (1891). [After Eggers and Villermaux; 2008].

[Reilly and Cantor, 1995] K.A.Q. O'Reilly, B. Cantor, *Acta Metall.* 43, 405–417, (1995).

[Reynolds, 1883] O. Reynolds, *Philosophical Transactions of the Royal Society*, **174** (0): 935–982, (1883).

[Reynolds, 1895] O. Reynolds, *Philosophical Transactions of the Royal Society of London. A*, v. 186, pp. 123-164, (1895).

[Reza, 2015] M. R. Pahlavani, *Selected Topics in Applications of Quantum Mechanics*, CC BY 3.0 license, (2015).

[Rielly et al., 2007] C. D. Rielly, M. Habib, J.P. Sherlock, *Trans. I. Chem. E.*, 85, 953-962, (2007).

[Robertson et al., 1987] B. Robertson, J.J. Ulbrecht, *American Institute of Chemical Engineers*, New York, pp. 72–81, (1987).

[Rohatgi et al., 2005] P. K. Rohatgi, R.B. Thakkar, J. K. Kim, A. Daoud, *Materials Science and Engineering A*, 398 pp. 1-14, (2005).

[Roesler et al., 2007] J. Roesler, H. Harders, M. Baeker, *Mechanical Behaviour of Engineering Materials: Metals, Ceramics, Polymers, and Composites*, Springer Science & Business Media, (2007).

[Rott, 1990] N. Rott, *Annual Review of Fluid Mechanics*, 22 (1): 1–11, (1990).

S

[Scamans et al., 2012] G. Scamans, H. Li and Z. Fan, 13th International Conference on Aluminum Alloys (ICAA13) Edited by: H. Weiland, A. Rollett, W. Cassada TMS (The Minerals, Metals & Materials Society), (2012).

[Schenker et al., 2013] M.C. Schenker, M.J.B.M. Pourquié, D.G. Eskin, B.J. Boersma, *Ultrason Sonochem*; 20(1):502-9, (2013).

[Schiotz et al., 1998] J. Schiotz, F.D. D. Tolla, K.W. Jacobsen, *Nature*, 391, 561-563, (1998).

[Sharma and Shaikh, 2003] R. N. Sharma, A. A. Shaikh, *Chemical Engineering Science*, Vol. 58, pp. 2123-2140, (2003).

[Sharratt, 2007] P. N. Sharratt, Handbook of Batch Process Design, Blackie, London, (1997).

[Sikkenk et al., 1987] J.H. Sikkenk, J.O. Indekeu, J.M.J. van Leeuwen, E.O. Vossnack, Phys. Rev. Lett. 59, 98–101, (1987).

[Silva and Talbot, 1988] M. P. Silva, D. E. J. Talbot, Light Metals, 1988 edit by P.G. Campbell, The Minerals, Metals and Materials Society, 1035-1040, (1998).

[Singh et al., 2007] K.K. Singh, S.M. Mahajani, K.T. Shenoy, A.W. Patwardhan, S.K. Ghosh, Chem. Eng. Sci. 62 (5), 1308–1322, (2007).

[Sleppy, 1961] W. C. Sleppy, Journal of the Electrochemical Society, 1097-1102, (1961).

[Smirnov, 1992] B.M. Smirnov, **Cluster Ions and Van Der Waals Molecules**, CRC Press, (1992).

[Smith,1994] E.H. Smith, Mechanical engineer's reference book , Oxford: Butterworth Heinemann, (1994).

[Smith et al, 2010] W. Smith, T.R. Forester, I.T. Todorov: DL_POLY_3, version 3.10, Daresbury Laboratory,UK, (2010).

[Solomon et al., 1981] J. Solomon, T. P. Elson, A. W. Nienow, G. W. Pace, Chemical Engineering Communications 11, 143–164, (1981).

[Sossa, 2007] J. A. Sossa M.Sc. thesis, Universidad Industrial de Santander, Colombia, (2007) .

[Söderberg, 2003] L. D. Söderberg, Journal of Fluid Mechanics, 493, pp 89-119, (2003).

[Stokes, 1851] G. Stokes, Transactions of the Cambridge Philosophical Society, **9**: 8–106, (2014).

T

[Thapar, 2004] N. Thapar, Ph.D.Dissertation, Cranfield University, Cranfield Bedfordshire, (2004).

[Thiele, 1962] W. Thiele, Die Oxydation von Aluminium- und Aluminiumlegierungs-Schmelzen, 38, 708-786, (1962).

[Temam, 2001] R. Temam, Navier–Stokes Equations, Theory and Numerical Analysis, AMS Chelsea, pp. 107–112, (2001).

[Tennekes and Lumley, 1992] H. Tennekes, J. L. Lumley, A first course in turbulence (14. print. ed.). Cambridge, Mass: MIT Press, (1992).

[Tong, 2016]

M.M. Tong, Presentation given in the project meeting for RecycAl, BCAST, 30 March , (2016).

[Totten et al., 2003] G. E. Totten, D. S. MacKenzie, Handbook of Aluminum: Vol. 1: Physical Metallurgy and Processes; CRC Press, (2003).

[Tzamtzis et al., 2011] S. Tzamtzis, H. Zhang, M. Xia, N. Hari Babu, Z. Fan, Mater. Sci. Eng. A, 528, 2664-9, (2011).

[Tzamtzis, 2011] S. Tzamtzis, Ph.D. Thesis, Brunel University, (2011).

U

[Ulbrecht, 1985] J. J. Ulbrecht, G. K. Patterson, Mixing of Liquids by Mechanical Agitation, Chemical Engineering Series: Concepts and Reviews, Volume 1, Gordon and Breach Science Publishers, London, (1985).

[Utomo, 2009] A. T. Utomo, Ph.D thesis, University of Birmingham, (2009).

V

[Vergano, 2006] D.Vergano, USA Today, September 10, (2006).

[Viček et al, 2016] P. Viček, B. Kysela, T. Jirout, I. Fořt, Chemical Engineering Research and Design , Volume 108 , 42 – 48, (2016).

[Volmer and Webber., 1926] M. Volmer and A. Webber: Z. Phys. Chem., vol. 119, pp. 277–301, (1926).

W

[Walas et al., 2005] S. M. Walas, Chemical Process Equipment: Selection and Design, Second Edition, Elsevier B.V., (2005).

[Wang, 1991] C. Y. Wang, Annual Review of Fluid Mechanics 23: 159–177, (1991).

[Wang et al., 2010] J.S. Wang, A. Horsfield, P.D. Lee, P. Brommer, Phys. Rev. B 82, 144203, (2010).

[Webb et al., 2003] E.B. Webb III, G.S. Grest, D.R. Heine, Phys. Rev. Lett. 91, 236102, (2003).

[Wei, 1991] J. Wei, J. L. Anderson, K. B. Bischoff, Advances in Chemical Engineering, Vol.17, p. 44, Academic Press, (1991).

[Werfers and Misra, 1987] Werfers K., Misra, C., Alcoa Technical paper, 1987 edited by Cao, X., PhD Thesis, University of Birmingham, (2001).

[Wilkens et al., 2005] R.J. Wilkens, J.D. Miller, J.R. Plummer, D.C. Dietz, K.J. Myers, Chemical Engineering Science 60, 5269 – 5275, (2005).

X

[Xu et al., 1998] D. Xu, W. K. Jones Jr., J. Evans, Metallurgical and Materials Transactions B, 29B, 1281–1288, (1998).

Z

[Zhang et al., 2002] L. Zhang, S. Taniguchi, K. Matsumoto, Ironmaking and Steelmaking 29 (5), 326–336, (2002).

[Zhang et al., 2005] M.X. Zhang, P.M. Kelly, M. Qian, J.A. Taylor, Acta Mater. 53, 3261–3270, (2005).

[Zhang et al., 2007] L. Zhang, S. Taniguchi, K. Matsumoto, Metallurgical and Materials Transactions B, 38B, 63–83, (2007).

[Zhang et al., 2013] L. Zhang, A. Allanore, C. Wang, Yurko, J.Crapps, Materials Processing Fundamentals, John Wiley & Sons, (2013).

[Zhao and Rice, 2011] M. Zhao, S.A. Rice, J. Phys. Chem. A 115, 3859–3866, (2011).

[Zope and Mishin, 2003] R.R. Zope, Y. Mishin, Phys. Rev. B 68, 024102, (2003).

[Zuo et al., 2012] Y. B. Zuo, B. Jiang, Y. Zhang, Z. Fan, IOP Conf. Ser.: Mater. Sci. Eng. 27, 012043, (2012).